JOURNAL OF APPLIED PHYSICS

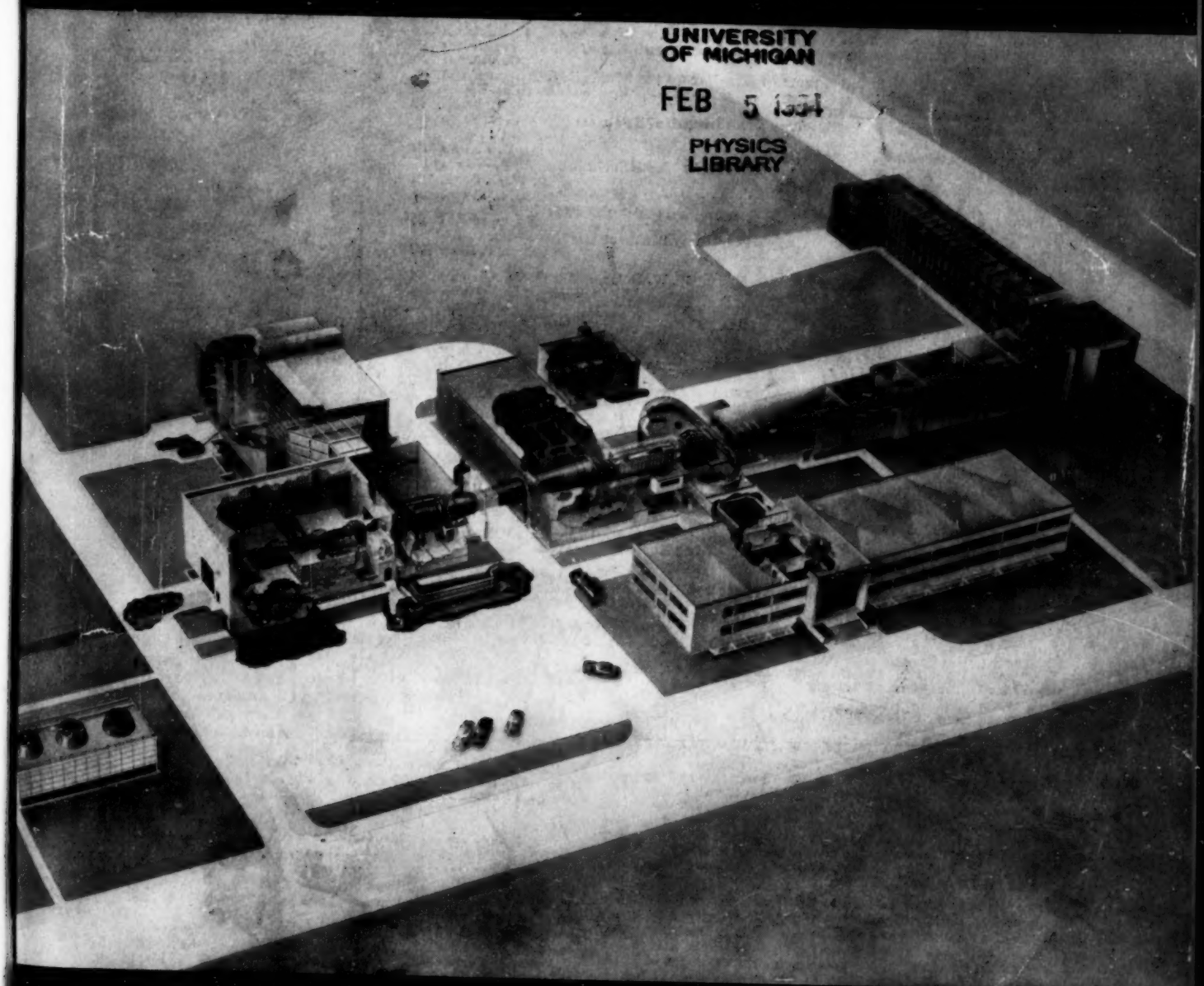

UNIVERSITY
OF MICHIGAN
FEB 5 1954
PHYSICS
LIBRARY

JOURNAL OF APPLIED PHYSICS

Vol. 25, No. 1 JANUARY, 1954

In This Issue

	Page
Electrical Properties of Selenium. III. Microcrystalline Selenium Metal Doped H. W. Henkels and J. Maczuk	1
Thickness-Shear and Flexural Vibrations of Contoured Crystal Plates R. D. Mindlin and M. Forray	12
Thickness-Shear Vibrations of Piezoelectric Crystal Plates with Incomplete Electrodes R. D. Mindlin and H. Deresiewicz	21
Suppression of Overtones of Thickness-Shear and Flexural Vibrations of Crystal Plates R. D. Mindlin and H. Deresiewicz	25
Ion Trajectories in the Omegatron Clifford E. Berry	28
Space Charge Waves in Inhomogeneous Electron Beams Gordon Kent	32
On a Property of a Family of Equiangular Spirals and its Application to Some Problems of Wave Propagation K. Landecker	41
Effect of Gas Slip on Unsteady Flow of Gas Through Porous Media J. S. Aronofsky	48
Cylindrical Shock Waves Produced by Instantaneous Energy Release Shao-Chi Lin	54
Thermal Diffusivity of Metals at High Temperatures P. H. Sidles and G. C. Danielson	58
Brightness Waves and Transitory Phenomena in the Quenching of Luminescence by Alternating Electric Fields G. Destriau	67
Direct Determination of the Flow Curves of Non-Newtonian Fluids. III. Standardized Treatment of Viscometric Data Irvin M. Krieger and Samuel H. Maron	72
On the Detection of Sure Signals in Noise R. C. Davis	76
Effect of Inelastic Collisions on the Slowing-Down Length of Neutrons in a Hydrogenous Mixture Howard C. Volkin	83
Preparation of Aerosols for Electron Microscopy Ernest H. Kalmus	87
Velocity Attenuation of Explosive-Produced Air Shocks Jacob Savitt and R. H. F. Stresau	89
Method of Measuring Magnetostriction A. W. Cochardt	91
On the Stability of Fluid Flows with Spherical Symmetry M. S. Plesset	96
Some Problems in the Diffusion of Minority Carriers in a Semiconductor S. Visvanathan and J. F. Battey	99
Some Magnetostriction Relations in Materials Possessing Preferred Domain Orientations George T. Rado	102
Field Emission Current-Density Distribution W. P. Dyke, J. K. Trolan, W. W. Dolan, and F. J. Grundhauser	106
On the Summation of Infinite Series in Closed Form Albert D. Wheelon	113
On Reciprocity Theorems in Electromagnetic Theory T. H. Crowley	119
Simplified Calculation for Dolph-Tchebycheff Arrays G. J. van der Maas	121
Letters to the Editor:	
Electrical Characteristics of MnSe and MnTe Wilfred Palmer	125
Sudden Change in the Arrangement of Crystallites in Thin Evaporated Bismuth Films Lorn L. Howard	125
Further Remarks on the Nature of the Statistical Observer David Middleton	127
Information Loss Attending the Decision Operation in Detection David Middleton	127
Discussion of "Statistical Criteria for the Detection of Pulsed Carriers in Noise I, II" D. Middleton, W. W. Peterson, and T. G. Birdsall	128
Method for Generating Strong Shock Waves A. Hertzberg and W. E. Smith	130
Electrical Conductivity Induced by Ionizing Radiation in Some Polymeric Materials A. J. Warner, F. A. Muller, and H. G. Nordlin	131
Dispersion Formula for Plasma Waves L. R. Walker	131
Comments on Summation of Slowly Converging Series Julian H. Braun	132
Further Comments on Summation of Slowly Converging Series Igor Gumowski	133
Note on Helix Impedance Measurements Using an Electron Beam D. A. Watkins and A. E. Siegman	133
Comment on "The Summation of Series Involving Roots of Transcendental Equations and Related Applications" G. Kuerti	133
Metal Whiskers S. Eloise Koonce and S. M. Arnold	134
Some Remarks on Thermal Effect in an Electron Beam on the Gain of Traveling-Wave Tubes Kanehisa Udagawa and Masao Sumi	135
Erratum: Thermal Effects in Point Contact Rectifiers H. L. Armstrong	136
Erratum: A Note on the Analysis of First-Order Glow Curves Leonard I. Grossweiner	136
Errata: A Study of the Propagation Mode for Metallic Vapors in Shadow Casting by Vacuum Evaporation of Au^{198} and Cr^{51} Luther E. Preuss	136
Erratum: On the Propagation Constant in Gentle Circular Bends in Rectangular Wave Guides—Matrix Theory A. T. de Hoop	136
Announcement	24
Index to Advertisers	xxii

ELMER HUTCHISSON, *Editor*

EARLE C. GREGG, *Assistant Editor*

Board of Editors
MAURICE A. BIOT
RAY E. BOLZ
WALLACE J. ECKERT
ROBERT D. HEIDENREICH
LOUIS A. PIPES
ROMAN SMOLUCHOWSKI
W. R. SMYTHE
ARTHUR V. TOBOLSKY
A. M. WEINBERG

Publication of the American Institute of Physics

OFFICERS
GEORGE R. HARRISON, *Chairman*
GEORGE B. PEGRAM, *Treasurer*

GOVERNING BOARD
J. W. BUCHTA
KARL K. DARROW
G. J. DIENES
S. A. GOUDSMIT
GEORGE R. HARRISON
FREDERICK V. HUNT
DEANE B. JUDD
HUGH S. KNOWLES
C. C. LAURITSEN
WILLIAM F. MEGGERS
PHILIP M. MORSE
BRIAN O'BRIEN
GEORGE B. PEGRAM
I. I. RABI
DUANE ROLLER
FREDERICK SEITZ
WILLIAM SHOCKLEY
RICHARD M. SUTTON
J. H. VAN VLECK
MARK W. ZEMANSKY

Consultant on Printing
MELVIN LOOS

ADMINISTRATIVE STAFF
HENRY A. BARTON, *Director*
WALLACE WATERFALL, *Executive Secretary*
THEODORE VORBURGER, *Advertising Manager*
RUTH F. BRYANS, *Publication Manager*
EDITH I. NEFTEL *Circulation Manager*
KATHRYN SETZE *Assistant Treasurer*

The JOURNAL OF APPLIED PHYSICS, published monthly at Prince and Lemon Sts., Lancaster, Pa., is devoted to physics in its role as the science basic to other natural sciences and to the arts and industries. Previous to 1937 this publication was known as PHYSICS. The JOURNAL OF APPLIED PHYSICS publishes editorials and reviews, as well as technical papers of applied physics. Articles appearing in it are indexed regularly, according to their field, by Physics Abstracts, Chemical Abstracts, Engineering Index, Inc., Industrial Arts Index, etc.

Manuscripts should be submitted to Elmer Hutchisson, Editor, Case Institute of Technology, Cleveland 6, Ohio. Unless otherwise stated, submission of a manuscript is a representation that it has been neither copyrighted, published, nor submitted for publication elsewhere. The authors' institutions are requested to pay a **publication charge** of $8 per page which, if honored, entitles them to 100 reprints without further charge. Instructions will be sent with galley proofs.

Subscriptions, renewals, and orders for back numbers should be addressed to the American Institute of Physics, 57 East 55 Street, New York 22, New York.

Subscription Price	U.S. and Canada	Elsewhere
To members of the American Institute of Physics and Affiliated Societies	$10.00	$11.00
To all others	12.00	13.00

Back Number Prices

Yearly back number rate when complete year is available: $14.00. Single copies: $1.25 each.

Changes of address should be sent to the American Institute of Physics; **corrected proofs** should be sent to the Publication Manager, American Institute of Physics. **Advertising rates** supplied on request. Orders, advertising copy, and cuts should be sent to the American Institute of Physics.

Entered as second class matter January 22, 1937, at the Post Office at Lancaster, Pennsylvania, under the Act of March 3, 1879. Accepted for mailing at the special rate of postage provided for in paragraph (d-2), section 34.40, P. L. & R. of 1948, authorized May 2, 1932.

Copyright 1954, by the American Institute of Physics

Physics

Journal
of
Applied Physics

Volume 25, Number 1 January, 1954

Electrical Properties of Selenium. III. Microcrystalline Selenium Metal Doped*

H. W. Henkels† and J. Maczuk
University of Pennsylvania, Moore School of Electrical Engineering, Philadelphia, Pennsylvania
(Received April 24, 1953)

The thermoelectric powers and dc and 200-mc resistivities of pure and metal-doped selenium have been studied as functions of temperature. The properties of materials in the two important microstructures (colony and equiaxed) were distinguished. The influences of the metals Na, Cu, Ag, Mg, Zn, Cd, Hg, Ga, In, Tl, Pb, Sb, Bi, Te, Fe, Ni, Co, and Ce were noted.

A working model of the selenium semiconductor was developed. In this model there is an acceptor level <0.15 ev from the full band caused by nonmetals and possibly lattice defects. In strained crystals or material in the colony structure a second acceptor level 0.27 ev from the full band is postulated from the behavior of dc and ac resistivity curves as a function of temperature. The density of the first level varies in the range 10^{14}/cm³ to 6×10^{16}/cm³ with amount of nonmetal impurity. The density of the second level depends on the crystal structure, decreasing as the colony structure recrystallizes to the equiaxed. In the specimens crystallized at 110°C the density was about 2×10^{16}/cm³. Both metals and nonmetals are largely segregated at grain boundaries. Metals produce effective donor levels at these places.

The dc properties reflect the presence of internal barriers produced by the segregation. The donor levels enhance barriers existing in the purest selenium tested increasing resistivities and thermoelectric powers.

With increase in temperature >160°C the density of acceptor levels decreases as defects are removed by structural changes in the lattice.

IN three previous papers[1–3] the electrical properties of liquid, single crystal, and microcrystalline selenium, pure, and doped with impurities of O_2, I_2, and S to 0.1 atomic percent were presented. Carrier densities (holes) and effective mobilities were calculated from basic data on thermoelectric powers and resistivities. (The range of carrier densities was also checked by the bias variation of capacity of rectifiers.) The dependence of the effective mobilities on frequency was also demonstrated. From this information a picture of the microcrystalline aggregate was developed.

The purpose of the present paper is to report the general influence of a large number of metals on the electrical properties of selenium in different crystalline conditions in the light of the initial development of a model included in reference 3.

The experimental techniques employed were the same as those in the above reference and in addition included determinations of the temperature dependences of resistivities at high frequencies.

MATERIALS AND PROCEDURES

Chemically pure selenium shot from the Canadian Copper Refiners, Limited was used in all experiments. The analyses (colorimetric by the laboratories of the company) for Te, Cu, Pb, and Fe were in fractional parts per million. The laboratory purification procedure (not using HCl as reducing agent) and the results of experiments reported in reference 1 indicate that the material is free of halogens. The selenium was heated molten in vacuum for several hours to remove oxygen. Alloying agents consisted of selenides, and in some cases, of free metals.

Two control samples of pure selenium were taken at different periods in the pouring procedure to check on the amount of oxygen picked up during the alloying steps. One sample of each impurity concentration was inserted into an oven preset at approximately 110°C and heated for three hours. The second was crystallized at 210°C for one hour. These periods of crystallization are somewhat arbitrary, but were chosen with foreknowledge of the distinct types of microstructures (discussed later) it was desired to achieve. Thus, it was possible by

* This work was done under Contract DA-36-039sc-5426 with the U. S. Signal Corps Engineering Laboratory, Fort Monmouth, New Jersey.
† Now at Westinghouse Electric Corporation, Materials Division, 7325 Penn Avenue, Pittsburgh 8, Pennsylvania.
[1] H. W. Henkels, J. Appl. Phys. 21, 725–731 (1950).
[2] H. W. Henkels, J. Appl. Phys. 22, 916 (1951).
[3] H. W. Henkels, J. Appl. Phys. 22, 1265–1278 (1951).

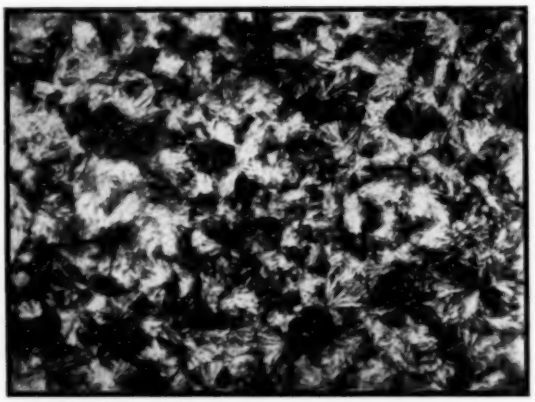

(a)

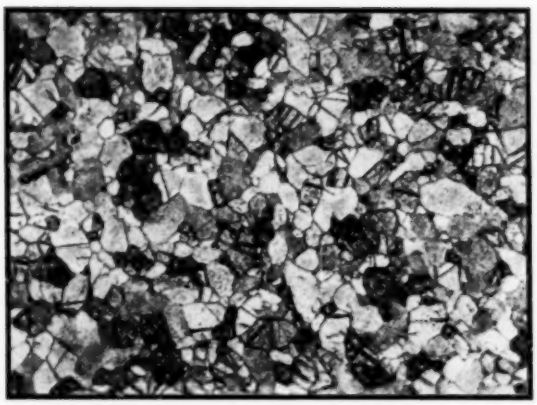

(b)

FIG. 1. Microstructures in selenium (666×).

studying both 110°C and 210°C specimens of metal-doped selenium to differentiate between the influence of the metal in retarding crystallization and in altering the electrical properties in a more direct manner by introducing acceptor or donor levels.

The methods of measuring dc resistivity and thermoelectric power simultaneously were described in reference 3. The high-frequency technique, also described, was modified by enclosing the Q-meter terminals in a cryostat. Measurements were made in the absence of light and in a rough vacuum. The temperature was varied from 170°K to 488°K over a period of hours and the 200 mc and dc resistivities noted alternately.

From the basic data on the temperature dependences of thermoelectric powers and dc and ac resistivities effective mobilities, carrier densities and activation energies were computed. The effective mobility (of single carriers) follows from the definition provided the thermoelectric power is large:

$$b_h = 1/\rho e n.$$

This condition was always fulfilled (i.e., the conduction was predominantly by holes).

Carrier densities were determined from the thermoelectric power according to the relation

$$Q = -\frac{k}{e}\left(2 - \ln \frac{nh^3}{2(2m\pi kT)^{\frac{3}{2}}}\right).$$

This assumes the existence of a scalar free path independent of energy as well as an electronic mass for single carriers. Since the Debye temperature for selenium is well below the lowest temperature employed, the assumption of a free path is valid. Its independence of energy is the usual assumption in the high-temperature region. The scalar nature of the free path is assumed for simplicity but is not correct in view of the anisotropy of the selenium lattice. Recent data‡ give an anisotropy ratio for resistivities perpendicular and parallel to the c axis of 3.5 to 4.0 (both ac and dc). The mass of holes in selenium is unknown. Therefore, the calculation may be expected to give the absolute value of effective carrier densities $n/(m/m_e)^{\frac{3}{2}}$ to within order of magnitude and relative magnitudes somewhat better. Further assumptions in the explanation of the results will be reserved for the discussion, these relying on subsidiary data to some extent and representing a further extension on the basis of a particular model.

NEW DATA

Crystal Structures

Undercooled or amorphous selenium is quite stable at temperatures to 60° or 70°C. However, while undercooling, the material nucleates to some extent. The rate of nucleation depends on temperature and purity. The maximum nucleation rate occurs in the vicinity of 100°C. Many materials, most important of which are the nonmetals, accelerate nucleation, while a few inhibit crystallization (notably phosphorus). The subsequent crystallization rate after nucleation increases with temperature to within a few degrees of the melting point.

The crystallites grow in radial clusters from the nucleation centers until the entire mass has crystallized (Fig. 1(a)). This material then recrystallizes at temperatures above about 150°C to the equiaxed structure shown in Fig. 1(b). The regions of contact of different radial colonies undergo the transition to a very fine equiaxed structure first. Then the recrystallization proceeds toward the nuclei of the colonies. On further heating the grains grow a factor of about 10 in linear extension. (Although a complete quantitative discussion of the rates involving critically the purities and temperatures is out of order at this time, an idea of the time scale can be obtained by the observation that pure selenium containing oxygen from contact with air has the structure 1(a) after heating one hour at 110°C, the structure 1(b) (with smaller grain size) in about 10 minutes at 210°C.)

‡ Unpublished.

Crystallization at 110°C

Despite any possible acceleration of crystallization or recrystallization the specimens prepared at 110°C were found to behave in the manner distinctive to the colony structure. The specimens prepared at 210°C also formed a distinct group, but the behavior was, in a few cases, that of an intermediate type of structure. Alloys with mercury were definite exceptions in that the typical metallic behavior was not exhibited in any case. However, for ease in consideration the properties of selenium with metal impurities will be discussed in categories dictated by the method of preparation (i.e., crystallized at 110°C or 210°C).

Resistivities

Figure 2 presents data on the 200-mc and dc resistivities as a function of temperature of one of the pure selenium control samples. The extent of reproducibility of the data is illustrated in Table I where two probes of the same specimen and two different specimens (taken at different periods in the pouring procedure) are compared. The behavior of all the samples crystallized at 110°C can be roughly expressed in terms of the parameters listed in the table, i.e., the temperature coefficients above and below the inflection point, the temperature of the latter, and the resistivities at this point, all with dc and 200-mc fields. Table I also presents the data for the alloys, in groups corresponding to those of the periodic table. It should be recalled that the nonmetals did not alter the resistivities in this type of microstructure (see reference 3).

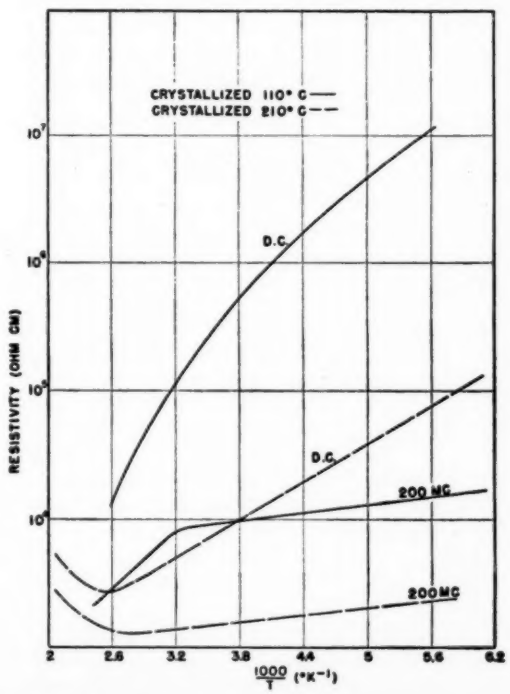

FIG. 2. Ac and dc resistivities of selenium in colony and equiaxed structures as functions of temperature.

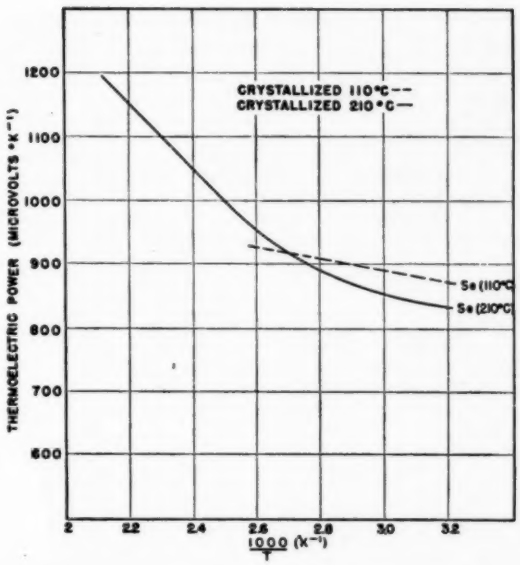

FIG. 3. Thermoelectric power of selenium in colony and equiaxed structures as functions of temperature.

Thermoelectric Powers

The thermoelectric powers at 50°C are listed in Table II. The temperature dependence was noted from room temperature to 130°C in all cases, but the behaviors were similar to those previously reported in reference 3.

Carrier Densities and Mobilities

Table II also lists the average carrier densities, these varying little with temperature. With constant carrier densities we are, as in the references on both single crystals and nonmetal-doped microcrystalline selenium, presented with the fact that the effective mobilities increase exponentially with the temperature. The exponents depend, however, on the frequency of the field decreasing at higher frequencies toward very small values. On the other hand, the kink becomes more evident at high frequencies. The explanation of these behaviors is given in the discussion. The exponents at lower temperatures are the same as those in Table I.

Crystallization at 210°C

Figure 2 also presents data on the dc and 200-mc resistivities of a pure control sample crystallized at 210°C. The thermoelectric power as a function of temperature is shown in Fig. 3, together with that for selenium crystallized at 110°C. The average carrier densities are the same for the two types of pure selenium within the precision of measurement. The resistivities at the temperature (370°K) where the measured values were equal are compared in the following table.

Comparison of the ac curves of Fig. 2 below 385°K shows that on recrystallization to the equiaxed structure, the effective mobilities increase, the kink disappears and the temperature coefficients [φ in $\rho=\rho_0 \exp(q\varphi/kT)$]

TABLE I. Resistivities of pure selenium control samples crystallized at 110°C—3 hours.

Group	Specimen	Dc resistivity at kink (ohm cm)	Kink temp. (°K)	Temperature coefficient φ in $\rho=\rho_0\exp(\varphi q/kT)$ (ev) above kink point	(ev) below kink point	Ac resistivity at kink (ohm cm)	Kink temp. (°K)	Temperature coefficients φ in $\rho=\rho_0\exp(\varphi q/kT)$ (ev) above kink point	(ev) below kink point
VI_b	1 probe 1	8.1×10^4	313	0.285	0.189	7.8×10^3	308	0.130	0.0181
	1 probe 2	6.6	313	0.293	0.168	7.1	328	0.176	0.0246
	[a]2 probe 1	13	313	0.332	0.164	7.8	318	0.149	0.0237

Resistivities of metal-doped selenium samples crystallized at 110°C—3 hours.

Group	Impurity added	Atomic percentage of metal	Dc resistivity at kink (ohm cm)	Kink temp. (°K)	Temperature coefficients φ in $\rho=\rho_0\exp(q\varphi/kT)$ (ev) above	(ev) below	Ac resistivity at kink (ohm cm)	Kink temp. (°K)	Temperature coefficients φ in $\rho=\rho_0\exp(q\varphi/kT)$ (ev) above	(ev) below
I_a	Na_2Se	0.00955	7.1×10^4	318	0.315	0.20	7.6×10^3	339	0.225	0.047
		0.0764	8.2	318	0.365	0.185	7.7	345	0.29	0.034
I_b	CuSe	0.0126	8.7	328	0.315	0.185	9.5	328	0.185	0.0465
		0.254	24 000	299	0.41	0.165	57	[b]...	[b]...	[b]...
	Ag_2Se	0.011	50	312	0.27	0.140	25	299	0.140	neg.
		0.095	6000	299	0.36	0.115	60 (at 312)	[c]...	neg.	neg.
II_a	MgSe	0.0191	7	339	0.30	0.175	13	328	0.24	0.023
II_b	ZnSe	0.128	7	339	0.365	0.155	8.4	345	0.285	0.039
	CdSe	0.00650	10	319	0.245	0.190	12	323	0.215	0.049
		0.0710	10	312	0.315	0.170	22	328	0.30	0.085
	HgSe	0.00715	12	318	0.397	0.260	11	331	0.123	0.0316
		0.0682	100	313	0.390	0.214	22	345	0.237	0.0285
III_b	Ga	0.100	11	318	0.30	0.19	10.5	334	0.27	0.026
	In	0.00875	10	328	0.296	0.175	8.2	328	0.145	0.034
		0.0795	7	328	0.39	0.195	8.7	328	0.290	0.0165
	Tl	0.00745	[d]2 000 000	(?)	...	...	15	303(?)	0.0095	0.0095
		0.0665	2 000 000	(?)	...	...	60	303(?)	0.09	...
IV_b	PbSe	0.0109	11	323	0.245	0.175	14	313	0.160	0.034
V_b	Sb_2Se_3	0.0086	20	322	0.43	0.175	27	322	0.255	0.017
		0.070	100	312	0.365	0.255	39	312(?)	0.76(?)	0.0035
	Bi_2Se_3	0.00745	37	313	0.37	0.155	28	333	0.30	...
		0.0740	600	303	0.465	0.145	38	333	...	...
VI_b	SeO_2					(See reference (3))				
	Te	0.0108	12.5	328	0.415	0.160	9.5	328	0.145	0.0175
		0.095	95	328	0.405	0.180	17	313	0.150	0.0155
VII_b						(See reference (3))				
VIII	NiSe	0.00845	6	339	0.385	0.185	9.5	339	0.265	0.0415
		0.0750	8	339	0.405	0.173	9.5	339	0.185	0.0465
	CoSe	0.0104	6	333	0.325	0.175	9.0	328	0.210	0.0335
		0.112	8	323	0.325	0.180	11	323	0.205	0.0165
Rare earth	Ce	0.099	7	333	0.285	0.170	10	333	0.20	0.0305

[a] Poured first and should be relatively more free of oxygen from air contamination during sample pouring.
[b] Only rough measurements were possible with the *Q*-meter technique, but no kink was evident.
[c] Larger negative temperature coefficients above room temperature.
[d] The column units are still valid, i.e., the resistivities exceed 2×10^{10} ohm cm.

below room temperature decrease somewhat. At temperatures between room temperature and 385°K, the higher temperature coefficients characteristic of the colony structure have disappeared.

Comparison of the behaviors shows that, whereas below 385°K the positive temperature coefficients (i.e., the slopes of the log resistivity curves *versus* reciprocal absolute temperature) were greatly reduced, the negative coefficients above that temperature were not changed at higher frequencies.

TABLE II. Thermoelectric powers and carrier densities of metal-doped selenium samples crystallized at 110°C—3 hours (measured at 50°C except where noted in parentheses).

Group		Atomic percent metal	Thermoelectric powers at 50°C (μV/°C)	Dc resistivity at 50°C (ohm cm)	Ac resistivity at 50°C (ohm cm)	Average carrier densities at 50°C (cm^{-3})
I_b	Cu	0.254	1240 (112°)	518 (113°)$\times 10^4$	5.7×10^4	0.154 (112°C)$\times 10^{15}$
	Ag	0.011	1040	41	3.8	1.175
		0.095	1300 (112°)	320 (104°)	8.0	0.0770 (112°C)
II_a	Mg	0.0191	890	12.4	1.3	6.92
II_b	Zn	0.128	870	8	0.94	8.71
	Cd	0.00650	...	...	1.1	8.71
		0.0710	870	9.4	1.8	8.71
	Hg	0.00715	935	22	1.4	4.17
		0.0682	1090	83	2.4	6.93
III_b	Ga	0.100	910	7.5	1.1	5.61
IV_b	Pb	0.0109	870	10	1.1	8.76
V_b	Sb	0.0086	1000	18	2.3	1.91
		0.070	1190	72	3.8	0.213
	Bi	0.00745	1060	36	3.2	1.048
		0.0740	1270 (100°C)	175	3.8	0.0870 (100°C)
VI_b	Se	...	882	4.8	0.7	7.76
	Te	0.0108	910	8.6	0.95	5.48
		0.095	1090	100.0	1.7	0.676
VIII	Co	0.0104	865	5.8	1	9.33
		0.112	865	7.4	1	9.33
Rare earths	Ce	0.099	830	11	1	13.8

Indeed in many cases with metal additions the negative temperature coefficients increased in magnitude at higher frequencies. The hysteresis effect characteristic of the temperature cycling remained evident at high frequencies. This ac behavior gives further support to the idea (presented in reference 3) of structural changes occurring in the selenium near the melting point with decrease in number density of acceptors.

The kink in the ac resistivity curves is not apparent in most of the specimens containing metals and crystallized at 210°C. Exceptions are samples containing 0.1 percent Sb and 0.1 percent Hg. The kink in the dc resistivity is still apparent in a larger number of samples, i.e., those containing 0.1 percent Tl, Ag, Sb, Hg, and to a small extent in a number of other specimens. The hysteresis effects were in general larger than in the 110°C samples.

Group I_a—Na

The thermoelectric power and its temperature dependence were essentially unchanged by the addition of sodium in amount less than 0.1 atomic percent. The resistivities were raised by a factor of almost two at temperatures below 385°C. Above this temperature negative temperature coefficients were reduced in magnitude at high frequencies and did not occur in dc measurements except above 476°K (within 20°C of the melting point).

Hysteresis loops were reduced in size.

Group I_b—Cu, Ag

The prime data on alloys containing silver or copper is presented in Fig. 4. The carrier densities and ac and dc resistivities at 50°C are compared in Table IV.

The average carrier densities thus vary by a factor 40, the dc resistivity by a factor 2200, the ac resistivities by a factor of 10. The temperature coefficients decrease with frequency as observed in the pure specimens. Negative temperature coefficients do not occur at higher temperatures in the dc curves while small negative coefficients are observed in all the ac data. Hysteresis effects are less apparent than in pure specimens.

Group II_b—Zn, Cd, Hg

Data on the temperature dependences of dc and ac resistivities of specimens containing metals of Group II_b are contained in Fig. 5. The thermoelectric powers from 313°K to 483°K generally increased in the order of increase of resistivities, but the over-all variation with

TABLE III. Resistivities of selenium specimens having equal average carrier densities but different structures.

Temperature of crystallization	Structure	Resistivities at 3770°K (ohm cm) dc	ac
110°C	Colony	20×10^3	3.5×10^3
210°C	Equiaxed	2.8×10^3	1.2×10^3

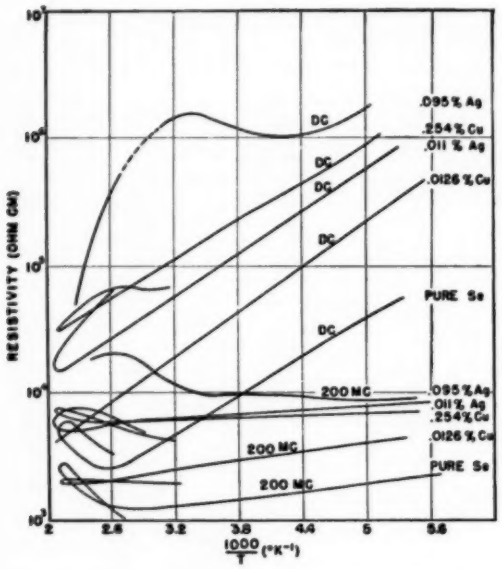

FIG. 4. Ac and dc resistivities of selenium with impurities of silver and copper as functions of temperature.

impurities of 0.1 percent was small. Table V compares carrier densities and resistivities at 50°C.

It should be noted that the kinks noted in the specimens crystals at 110°C remain pronounced in the specimen containing 0.065 percent atomic Hg at 200 mc whereas a similar behavior is detectable in specimens with 0.007 atomic percent Hg, 0.07 atomic percent Cd. In these specimens the carrier densities did not decrease with temperature to the same extent as in pure selenium. The hysteresis was slightly less than in the control sample.

Group III_b—In, Ga, Tl

Figure 6 presents the ac and dc resistivities as functions of temperature. The thermoelectric powers of samples containing gallium and indium were in the same range as that of pure selenium.

The thermoelectric power of samples with thallium, measurable only near the melting point, was very small

TABLE IV. Resistivities and carrier densities of selenium specimens having impurities of group I_b.

Alloy	Carrier density (cm^{-3})	Resistivity dc (ohm cm)	Resistivity ac (ohm cm)	Temperature coefficient dc (ev)	Temperature coefficient ac (ev)
Pure Se	12×10^{15}	0.22×10^{4}	0.13×10^{4}	0.08 0.0845	0.0265
Cu 0.0126	6.1	1.17	0.24	0.1	0.022
Cu 0.254	4.6	18.3	0.6	0.1 0.095	0.0125
Ag 0.011	2.6	12.0	0.6	0.1	0.020
Ag 0.095	0.27	480	1.3		slightly negative

(about 100 μv/°K or lower). The ac resistivities were low for alloys of all these metals including Tl. It is remarkable that the resistivity of the sample containing 0.0665 atomic Tl percent decreased in resistance by such a large factor in high-frequency fields (at 50°C the resistivity dropped a factor of 70 000). The negative temperature coefficients noted at 200 mc above 70° were abnormally large in magnitude.

Group IV_b—Pb

Specimens doped with lead did not exhibit negative temperature coefficients in the dc resistivity curves at any temperature. The dc and ac resistivities and thermoelectric powers as functions of temperature are shown in Fig. 7.

Table VI compares the carrier densities, resistivities

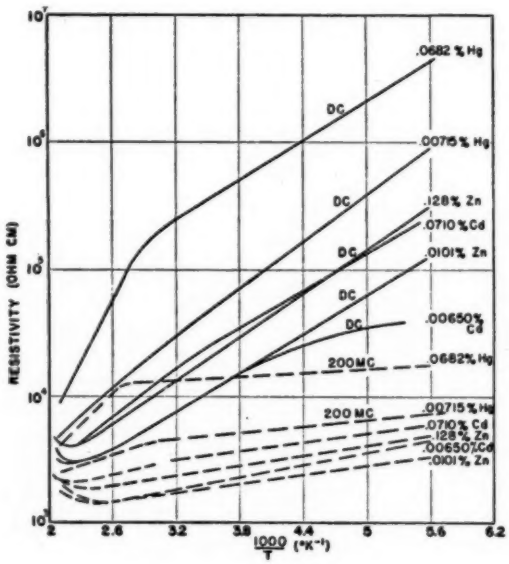

FIG. 5. Ac and dc resistivities of selenium with impurities of mercury, cadmium, and zinc as functions of temperature.

and temperature coefficients. Hysteresis effects were small.

Group V_b—Sb, Bi

With impurities of antimony and bismuth, the hysteresis effects were greatly exaggerated. In addition, with the sample containing bismuth several reproducible maxima and minima in the temperature 200-mc resistivity curves occurred. The antimony doped specimens showed kinks as observed in samples crystallized at 110°C.

Table VII below gives a representative range of the values of carrier densities, resistivities and temperature coefficients at 50°C.

Negative temperature coefficients were observed at higher temperatures in specimens containing bismuth, but not in those containing antimony.

Group VI$_b$—Te

Data are given in Fig. 8 and Table VIII. The hysteresis effects (not shown) were large. In this case the range of ac resistivities corresponded at 50°C, roughly with the range of carrier densities.

Group VIII—Ni, Co, Fe

The behaviors of thermoelectric powers and resistivities of specimens with Ni, Co, and 0.0158 percent Fe were identical with that of the pure control sample. The 0.17 atomic percent Fe sample had somewhat increased ac and dc resistivities.

Rare Earths—Ce

The ac and dc resistivities were increased very slightly in order of increasing amounts of cerium. The thermoelectric power at 50°C was unaltered.

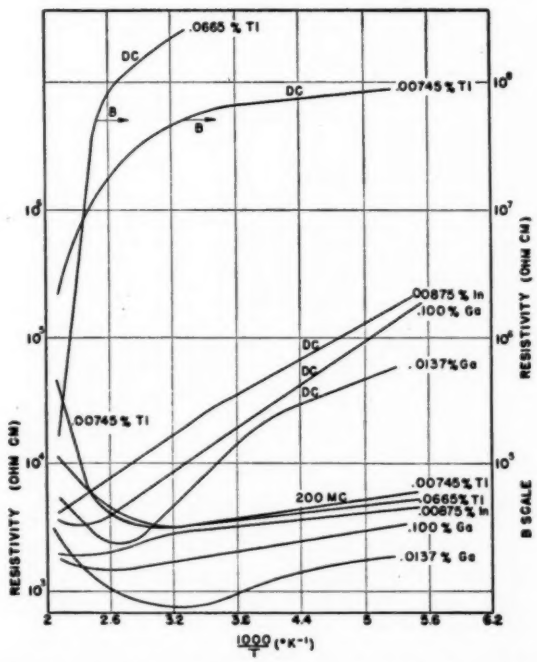

FIG. 6. Ac and dc resistivities of selenium with impurities of thallium, indium, and gallium as functions of temperature.

Group II$_a$—Mg

At 50°C the thermoelectric powers increased but slightly in the same order as the increases in resistivities. The unusual resistivities are compared in Fig. 9. Hysteresis effects were quite small.

DISCUSSION

Microcrystalline specimens have been used in the studies because of the fact that crystals of selenium will not grow with impurities of metals or nonmetals. This behavior has been previously discussed in reference 1. On the other hand the crystals studied possessed many anomalous properties in common with the microcrystalline specimens. Further high frequency studies of single crystals will be reported in another paper. The picture of the microcrystalline aggregate was developed with knowledge of behavior of pure single crystals.

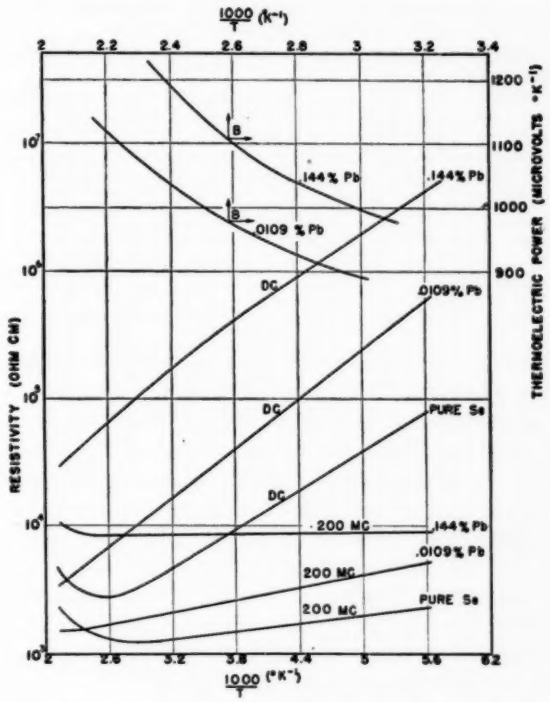

FIG. 7. Thermoelectric power, dc and ac resistivities of selenium with impurities of lead as functions of temperature.

Chemically Pure Selenium

The chemical analyses for certain metals in selenium fall in the range of fractional parts per million as noted. The new data have shown that additions of as little as 0.0126 percent Cu, 0.0101 percent Mg, 0.00715 percent Hg, 0.0109 percent Pb, 0.0086 percent Sb, or 0.00745 percent Bi, alter the properties of selenium crystallized at 210°C to a significant extent, while 0.011 percent Ag and 0.00745 percent Tl markedly change the properties.

Nonmetals were not analyzed, but the method of reduction and the previous experiments with liquid selenium indicate that halogens are not present. The absence of data on the influence of traces of phosphorus and nitrogen represents unfortunate lacuna in our

TABLE V. Resistivities and carrier densities of selenium specimens having impurities of group II$_b$.

Alloy	Carrier density (cm^{-3})	Resistivity dc (ohm cm)	Resistivity ac (ohm cm)	Temperature coefficient dc (ev)	Temperature coefficient ac (ev)
Pure Se (210°C)	$12\times10^{+15}$	0.22×10^{4}	0.133×10^{4}	0.084	0.027
Zn 0.0101	↑	0.64	0.16	0.10	0.024
0.128		1.1	0.22	0.11	0.025
Cd 0.00650		0.64	0.17	0.11	0.033
0.0710		1.4	0.3	0.11	0.027
Hg 0.00715		2.5	0.45	0.13	0.018
0.0665	4.3	21	1.3	0.10	0.011

TABLE VI. Resistivities and carrier densities of selenium specimens having impurities of lead.

Alloy	Carrier densities (cm^{-3})	Resistivities dc (ohm cm)	Resistivities ac (ohm cm)	Temperature coefficients dc (ev)	Temperature coefficients ac (ev)
Se	12×10^{15}	0.22×10^{4}	0.13×10^{4}	0.084	0.027
Pb					
0.0109	8.4	1.3	0.20	0.13	0.030
0.144	2.6	24	0.86	0.12	0.003

knowledge of the element. The necessity of preparing series of alloys in air has lead to the introduction of oxygen into the specimens during the alloying procedure. Thus the properties of the base material used in this and previous work can be assumed to be those of selenium with small impurities of oxygen or possibly nitrogen. (The influence of oxygen was noted in reference 3). It is thus necessary to have selenium of purity at least 99.998–9 percent with respect to a number of common metals before the properties of the selenium itself can be studied. This fact makes much of the older work on selenium of doubtful meaning.

Properties of Pure Selenium

The forbidden band gap in undercooled liquid selenium is 2.31 ev[4] whereas in hexagonal selenium having the same coordination numbers, but with distances between nearest neighbors considerably smaller (especially in neighboring chains) the gap is smaller. Furthermore the electron affinities and extrinsic activation energies of the two materials may be expected to be different. With this situation the electrical properties of selenium during the transition may be expected to be quite complex. As a further complication it has been found that selenium crystallizes first in colony structure (see Fig. 1a), then recrystallizes into an equiaxed metallic structure. The properties during the transition would be of little immediate interest at the present state of development of the theory of semiconductors and solid state electronic devices except for the fact of the stability of the different forms. In attempts to ascertain the fundamental electrical properties of the element and in the processing of selenium rectifiers and photocells, it therefore is necessary to retain parameters describing past histories besides those describing purity. In reference 3 the period and temperature of crystallization were together described in terms of a parameter of extent of crystallization. Photomicrographic examinations since that time have confirmed the fact that the same stages in the crystallization process are followed at any temperature in the transition from undercooled to hexagonal selenium.

Our interest has been in the stable materials crystallized at 110°C and 210°C. The lower temperature was chosen as one giving a stable form of selenium in a reasonable time (about 3 or 4 hours) representing a colony structure. The latter temperature is the one employed in producing low resistivity selenium with properties most metal-like. The resistivity of pure selenium crystallized at 110°C depends very little upon the period of crystallization after the minimum in the resistivity-period of crystallization curve has been reached, whereas that of selenium crystallized at 210°C increases with time of heat treatment beyond that corresponding to a minimum resistivity. After recrystallization the grain size in this type of selenium increases slowly with time. There remains some question concerning the reasons for the slow increase in resistivity with time of heat treatment. Schweichert[5] has demonstrated by direct analysis of halogen content that the resistivity rise depends on the expulsion of halogen. However, the two effects, i.e., the increase in grain size and the expulsion of halogen are interconnected as

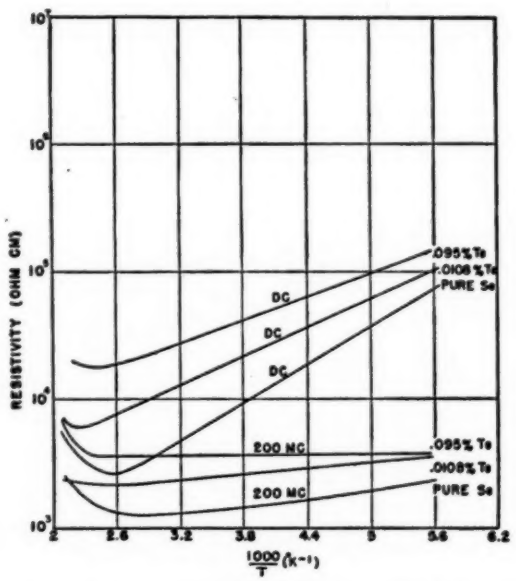

FIG. 8. Dc and ac resistivities of selenium with impurities of tellurium as functions of temperature.

TABLE VII. Resistivities and carrier densities of selenium specimens having impurities of group V_b.

Alloy	Carrier density (cm^{-3})	Resistivities dc (ohm cm)	Resistivities ac (ohm cm)	Temperature coefficients dc (ev) below	dc (ev) above	ac (ev) below	ac (ev) above
Se	12×10^{15}	0.22×10^{4}	0.13×10^{4}	0.084		0.027	
Sb							
0.0086	In range	5.5	0.7	0.088	0.15	0.0065	0.043
0.070	4.8	20	1.5	0.077	0.20	0.003	0.055
Bi							
0.0075	to	8	0.8	0.097		0.005	
0.074	1.5	10	1.2	irregular		irregular	

[4] Thermal ionization energy from report "Electrical properties of liquid selenium. I" by H. W. Henkels and J. Maczuk, J. Appl. Phys. 24, 1056–1060 (1953).

[5] H. Schweichert, Z. Physik 128, 47–55 (1950).

deduced from comparison of the behavior of the resistivity *versus* time of heat treatment with parameters of quench procedure reported in reference 6.

However, since these increases are small compared with those under consideration, they will be neglected in obtaining an overall view of the influence of metals on selenium.

Neglecting for the moment the theoretically insensitive (in this temperature range) variation of mobilities with temperature the ac behavior of the resistivities as functions of temperatures may be interpreted in the following manner. It has been found that some specimens exhibit small negative temperature coefficients, others zero or small positive coefficients. Single crystals have practically zero temperature coefficients.§ Therefore, to a first approximation the carrier densities will, in the appropriate corresponding temperature regions,

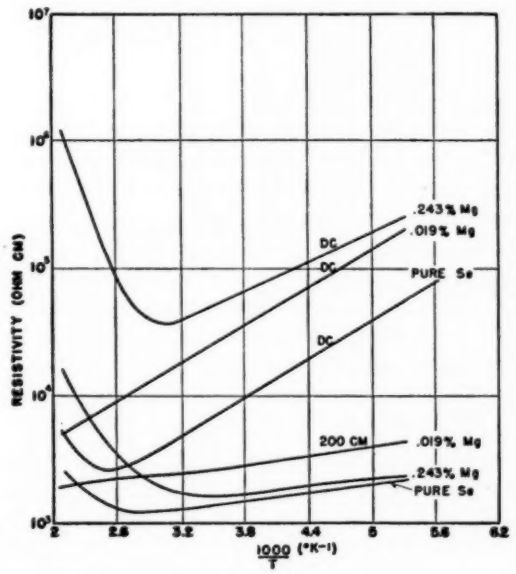

FIG. 9. Dc and ac resistivities of selenium with impurities of magnesium as functions of temperature.

be taken as constant (i.e., it will be assumed that any slight positive slope in the resistivity curves represents the combined effects of slight variations in mobilities or the existence of internal barriers which have not quite been capacitatedly shunted).

I. The crystallites of all types of selenium, regardless of microcrystalline condition (colony structure, equiaxed structure, single crystals), have carrier densities at temperatures from 147°K to somewhat above room temperature which are constant, indicating the exhaustion of an acceptor level lying within 0.15 ev of the full band. In making the calculation the Fermi level was found as a function of temperature assuming electronic mass carriers of densities given by the thermoelectric powers. The forbidden band gap was assumed to be 1.6 ev. From the fact that selenium does not become intrinsic below the melting point, the mass can possibly be somewhat over 10 times the electronic mass. The density of acceptor levels varied from 10^{14} in single crystals to 10^{16} in microcrystallic selenium containing considerable unavoidable oxygen. In previous experiments[3] with intentional impurities of nonmetals O_2 and I_2 the densities ranged up to about 6×10^{16}.

TABLE VIII. Resistivities and carrier densities of selenium specimens having impurities of tellurium.

Alloy	Carrier density (cm^{-3})	Resistivities dc (ohm cm)	Resistivities ac (ohm cm)	Temperature coefficients dc (ev)	Temperature coefficients ac (ev)
Se	12×10^{15}	0.22×10^{4}	0.13×10^{4}	0.084	0.027
Te 0.0108		1.5	0.21	0.07	0.015
0.095	4.8	14	0.42	0.06	0.002

II. Selenium with colony structures and strained crystals exhibit a kink in the log resistivity versus reciprocal temperature curve somewhat above room temperature indicating the presence of a second acceptor level lying 0.27 ev from the full band. The estimation of the depth of the level was made as follows. A rough estimation of the small residual internal barrier resistance at 200 mc was made. After correcting for such a residual resistance a temperature coefficient above room temperature of 0.128 ev was obtained which was constant to a temperature of about 150°C. The kink temperature had to fall close to 316°K. After determining the Fermi level as function of temperature graphically the hole densities could be calculated. With the assumption of 5×10^{15} acceptors in the lowest level 1.5×10^{16} acceptors in the second level and the activation energy of 0.27 ev given above, a temperature coefficient above room temperature was calculated. The parameters chosen gave a temperature coefficient of 0.125 ev which was constant in the temperature range desired. Furthermore, the average carrier densities in this range were about $7\text{–}8\times10^{15}$ in agreement with measured values.

On recrystallization the density of acceptors of the second type decreases with a consequent decrease in the temperature coefficients above room temperature (see Fig. 7 of reference 3).

There is reason to believe from our measurements on single crystals at lower frequencies and from Schaller's measurements that the second levels are aggregated to large extent and are possibly associated with strains or slight changes in axis direction in the selenium.

III. At temperatures above about 110° or 120°C the resistivities both ac and dc of microcrystalline selenium increase with temperature at a rate depending on the crystal structure and both the metal and nonmetal content of the selenium, indicating a decrease in density of acceptor levels arising from structural changes in the selenium. This does

[3] H. W. Henkels, "Resistance measurements during crystallization of selenium," Technical Report 14, Contract NObs 34144, December 1, 1948.

§ Data to be published.

not occur in our single crystals. It has previously been demonstrated that this behavior is most prevalent in specimens which are quenched in any way during preparation. (The selenium in this report was undercooled to room temperature and then crystallized as noted. Any undercooling is regarded as a quench.) With highly nonmetal-doped selenium (see Figs. 14 and 15 of reference 3), the effect is more pronounced. The thermoelectric powers reflect the same behavior. In single crystals the decrease in acceptor levels calculated is small compared with that occurring in heavily nonmetal doped microcrystalline specimens. A perfection of the lattice at higher temperatures is expected from the work of Brill and Krebs. Moreover, both the decrease in acceptor levels and the perfection of the lattice may be associated with the fact that the lattice is becoming more molecular. (The individual chains of selenium are separating, the c/a ratio decreasing from about 1.136 to 1.118.)

Hysteresis effects are most prevalent in specimens in which more imperfect structures have been produced by nucleating the selenium by undercooling the liquid. Another previous report has shown that the hysteresis loops in resistivity at high temperatures are reflected in similar changes in the thermoelectric power. These facts point again to the structural change postulated above. The hysteresis effects and negative temperature coefficients occur even at high frequencies, leading us to the conclusion that they are associated to some extent with structural changes in the interior of the crystallites.

IV. The higher temperature coefficients observed in dc measurements on single crystals and microcrystalline specimens reflect the presence of internal barriers at grain boundaries or at places where the direction of the c-axis shifts slightly. The number of parameters involved in the detailed calculation of the resistance of simple internal barriers is very large including those of carrier mobilities, defect densities, grain sizes and sizes of regions of altered defect densities. In the present situation the problem is more complex in that the electron affinities, extrinsic and intrinsic activation energies at grain boundaries are unknown. The problem of the treatment of very densely aggregated defects associated with grain boundaries or dislocations has not been attacked except in the general terms of surface states.

To rough approximation the barriers may be viewed as being produced by the variation in work function across a sandwich of the segregated impurities between selenium with a uniform, but small, acceptor density distribution. The resistance of half of such a barrier was first described by Schottky. With such an abrupt barrier the resistance depends on temperature through a factor $\exp(Vq/kT)$ where V is the peak electrostatic potential above that in the uncharged material. Other barrier shapes will alter this result only in quantitative detail. By adding electrostatic potential energies to the Fermi levels calculated in connection with the determination of the position of the two acceptor levels given above and incorporating a parameter describing grain sizes the carrier densities can be calculated. Again assuming constant mobilities, the form of the dc resistivity curves can be reproduced in the two cases of colony and equiaxed structures. At higher frequencies successively larger portions of the electrostatic barriers are capacitatively shunted so that the peak electrostatic potential to be used in calculating temperature coefficients depends on the frequency of the applied field. It is necessary to account for the ready occurrence of such barriers in selenium, which apparently are not a serious problem in the other elemental semiconductors. The explanation is readily found in the low carrier densities in selenium. These low densities can arise from two causes: (1) the insolubility of foreign atoms in selenium (already clearly demonstrated) for non-metals in reference 3 and inferred for metals from the phase diagrams; (2) the depth of donor levels formed. With the resulting acceptor densities in the range 10^{14}/cm to 10^{16}/cm^3 the thickness of barrier layers can be quite large for small variations in the work functions (approximately 0.1–0.2 ev) caused by the segregation assumed. In the same way the early discovery and use of selenium in large area rectifiers is explained. The very small grain size (up to about 10^{-4} cm in the colony structure) enhances the influence of such barriers. In the colony structure of Se with the smaller grain sizes the effective or dc mobilities can be very small (approximately 0.001 cm^2/volt sec) while in single crystals the dc mobilities are much higher (as high as 4 cm^2/volt sec for conduction parallel to the c axis at higher temperatures).

Properties of Metal-Doped Selenium

General examination of all the data on thermoelectric powers shows that the average carrier densities are either decreased or unaffected by metal additions. Again, however, as in the case with non-metals the variation in carrier densities are relatively very small compared with those observed in other semiconductors. The range of carrier densities extended from 1.2×10^{16}/cm^3 for selenium containing some oxygen to about 2×10^{14}/cm^3 for silver doped selenium. The purest microcrystalline specimen previously prepared had carrier densities of the order of 2×10^{15}/cm^3, the single crystals 2×10^{14}/cm^3 at the same temperature. The resistivities on the other hand were greatly increased when the thermoelectric powers were high. We are again lead to the conclusion reached in the case of nonmetals, namely, that the impurities in selenium are largely segregated. Since sulfur and selenium are distinctly electronegative with respect to all the materials alloyed (except Te) it is not at all surprising that the limits of solubility are very small.

Assuming then that most of the metal impurity atoms are segregated, probably at grain boundaries, the following general picture of the effect of metal impurities is reached.

V. All elements electropositive with respect to selenium produce localized energy levels in the forbidden band which are closer to the empty band. With aggregated levels of this type, the barriers already existing (in the purest selenium yet tested) are enhanced by the shifting of the Fermi level closer to the empty band. Thus the resistivities and thermoelectric powers increase. An expression for the thermoelectric power of two materials with different work functions, mobilities, and acceptor and donor densities in parallel junction has been developed, but the large number of undetermined parameters does not allow a unique solution. However, with enhanced barriers the average carrier densities should decrease in the manner observed.

VI. The efficiency of the metals in any insoluble group (i.e., excepting Group VI$_b$, and V$_b$ which may be partially soluble and is better discussed in conventional terms) in altering the properties of selenium increases with the size of the atom. Thus Ag is more effective than Cu, Hg more effective than Cd, Tl more effective than In.

Colony Structures

The temperature dependence of resistivity of selenium in the colony structure, regardless of impurities of any metal or nonmetal shows the presence of two acceptor levels. The dc resistivities increase in the range indicated by increase in the thermoelectric power, but exact correspondence between calculated carrier densities and resistivities is not obtained. However, such a correspondence would not be expected since the impurities are segregated and much more complicated formulas should be used in computing carrier densities. The small variation (factor of 10) in ac resistivities points up the small solubility of most materials in selenium.

Aside from the metals Sb and Bi which may be partially soluble in selenium and Te which in larger concentrations forms a solid solution, the lighter metals did not alter the resistivities or thermoelectric powers. All the heavy metals tested were effective in creating donor levels, these including Cu, Ag, Hg, Tl. On the other hand in the purest selenium studied the dc resistivities were much higher than the ac although both were less than those in metal-doped specimens. Residual unanalyzable metal impurities could have contributed to the formation of barriers, but we feel it more reasonable to attribute the barriers in the purest selenium to aggregated geometric defects associated with strains. The number of these decreases as the material recrystallizes.

Equiaxed Structures

On the formation of the equiaxed structure the second acceptor density decreases to an unimportant level. The length of time required for the recrystallization depends on the purity and reflects the stabilizing influence of certain metals. In addition, however, the average acceptor densities were reduced in the completely recrystallized materials indicating the formation of localized donor levels as explained.

The hypothesis of localized donor levels has received support from the production of *n*-type selenium in liquid selenium where solubility problems are avoided.[4] Thus, Bi, Sb, As impurities in selenium make the material *n* type below the intrinsic region. Preliminary data on Tl-doped liquid selenium also show reversals in the thermoelectric power to negative values. The electron mobility is much smaller than that of holes so that with the low solubilities of metal impurities in hexagonal selenium the over-all thermoelectric power remains positive indicating hole conduction.

Thickness-Shear and Flexural Vibrations of Contoured Crystal Plates*

R. D. MINDLIN AND M. FORRAY
Department of Civil Engineering, Columbia University, New York, New York
(Received May 7, 1953)

An approximate method is devised for calculating frequencies of thickness-shear and flexural vibrations of crystal plates of varying thickness. Applications are made to plates having the shape of a double wedge and to plates with beveled edges.

INTRODUCTION

IN previous papers,[1] equations of motion were derived and illustrative problems were solved for the thickness-shear and flexural vibrations of isotropic, crystalline, and piezoelectric plates of uniform thickness. The investigations are now extended to include contoured, crystal plates, i.e., plates of varying thickness.

As might be expected, the equations of motion of contoured plates are not easy to solve. Even when they are specialized to contours and motions depending on but one spatial coordinate, as in this paper, they reduce only to equations of the fourth order with variable coefficients; and these are of a type for which there do not appear to be solutions in terms of tabulated functions.

There are two major physical factors which contribute to the complexity of the equations. One is the variation in thickness, which we wish to retain. The other is the coupling between the flexural and thickness-shear modes, each of which is an infinite system. This coupling occurs also, of course, in uniform plates, so that it is appropriate to examine solutions for uniform plates in an effort to devise simplifying approximations for contoured plates.

In II and III there were given the frequencies of thickness-shear and flexural vibrations of AT-cut, quartz plates of uniform thickness. The spectrum obtained is shown in Fig. 1. The data for these curves were calculated from the roots of a transcendental equation: the secular equation obtained from applying boundary conditions to an appropriate solution of the equations of motion. At the points of intersection of the curves for the even and odd modes (identified by circles and squares in Fig. 1) the transcendental equation degenerates to an algebraic formula. As a result, it was possible to find simple algebraic equations for two families of curves whose alternate intersections are at the circled and squared points. The algebraic curves are shown in Fig. 2. Now, as the coupling is diminished, the loops in Fig. 1 spread and approach as limits, for zero coupling, the curves in Fig. 2. This is illustrated, for a portion of the spectrum, in Fig. 3.

It was shown, in II, that the portions of the curves in Fig. 1, which are nearly parallel to the curves n = constant in Fig. 2, correspond to motions which are predominately thickness-shear. Also, the portions of the curves in Fig. 1, which are nearly parallel to the curves r = constant in Fig. 2, correspond to motions which are essentially flexural. Thus, in the limit, for zero coupling, the curves of Fig. 2 give the true frequencies not only at the alternate intersection points but also throughout; i.e., the curves n = constant and r = constant give the frequencies of the uncoupled thickness-shear and flexural modes, respectively. This situation is typical of the coupling of two infinite sets of modes.

It would be useful to be able to write separate equa-

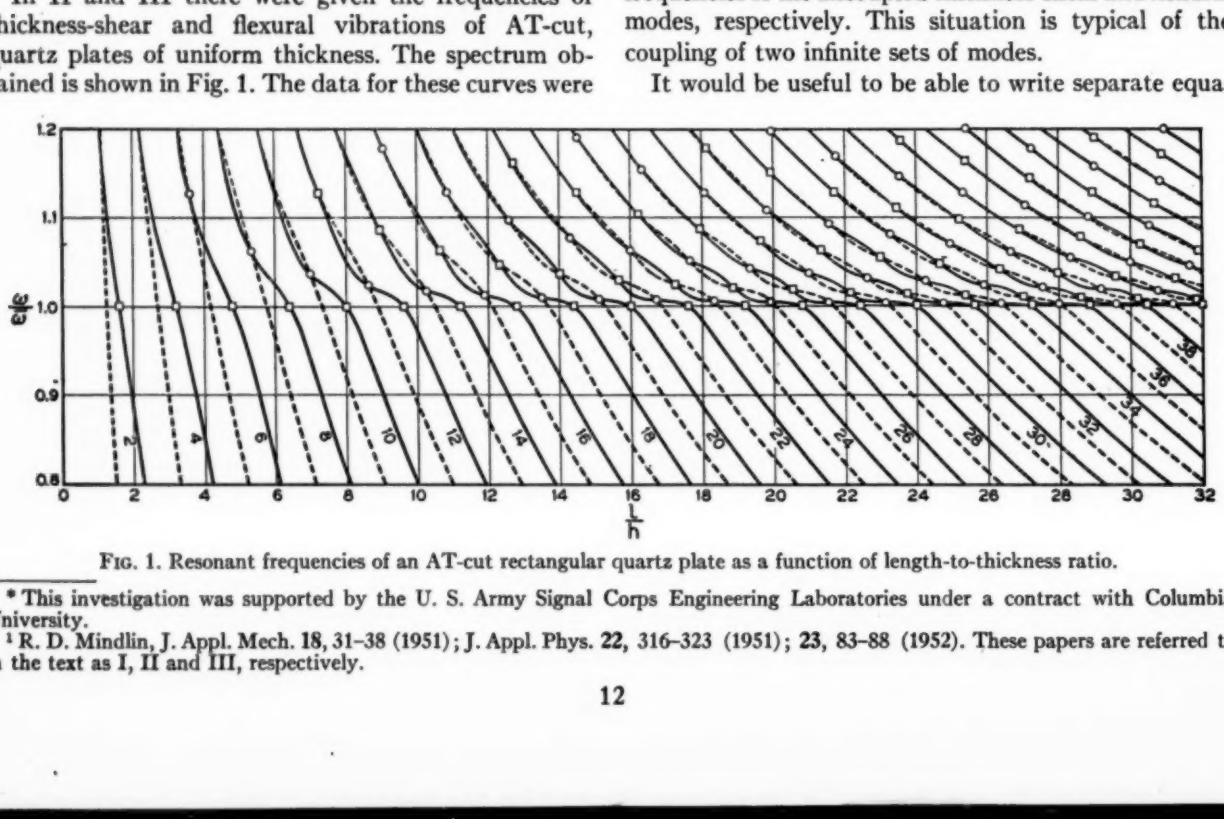

FIG. 1. Resonant frequencies of an AT-cut rectangular quartz plate as a function of length-to-thickness ratio.

* This investigation was supported by the U. S. Army Signal Corps Engineering Laboratories under a contract with Columbia University.

[1] R. D. Mindlin, J. Appl. Mech. 18, 31–38 (1951); J. Appl. Phys. 22, 316–323 (1951); 23, 83–88 (1952). These papers are referred to in the text as I, II and III, respectively.

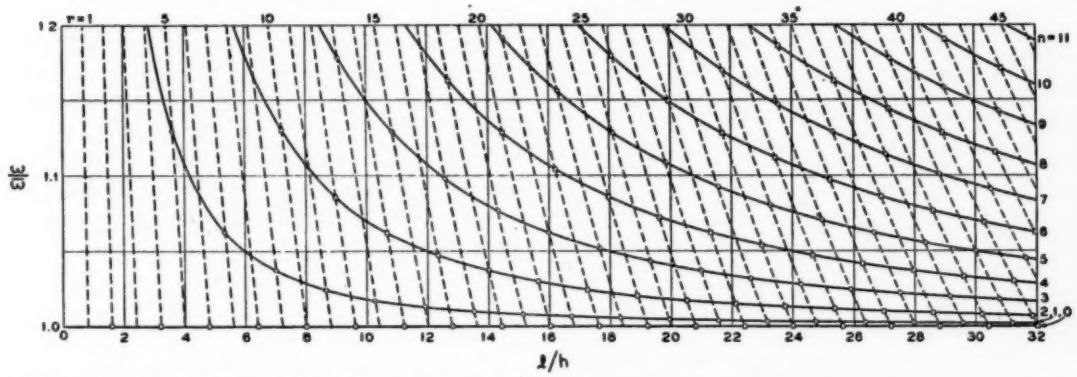

FIG. 2. Frequencies of uncoupled thickness-shear and flexural modes of an AT-cut rectangular quartz plate. The circled and squared points are those from the upper half of Fig. 1.

tions of motion, for the thickness-shear and flexural modes, which would lead directly to the curves in Fig. 2; but this does not appear to be possible. However, based on a physical interpretation of the coupling phenomenon, it is possible to write separate sets of equations of motion which lead approximately to the desired, uncoupled frequencies. These equations are, of course, much simpler than the equations which include the coupling. The thickness-shear equations are obtained by dropping the flexural-rigidity terms from the full equations and the flexural equations are obtained by dropping the thickness-shear deformation and rotatory inertia terms. In each case an arbitrary parameter is inserted in the transverse inertia term of the resulting equations. The values of these parameters are obtained by comparing the solutions of the separated equations, for the case of a uniform plate, with the known solution of the coupled equations. Calculations of the coordinates of the intersection points of Fig. 2 from the solutions of the coupled and uncoupled equations are thus made to agree very closely.

Consequently, we have two sets of uncoupled equations of motion which, for the uniform plate, give the curves of Fig. 2 with adequate precision. These equations are then solved for the case of a contoured plate having the shape of a double wedge. This is the simplest case which shows the effects of a greater thickness at the center of the plate than at the edge. It is found, for example, that the frequency of the first thickness-shear mode of a wedge is not much higher than the corresponding frequency of a uniform plate whose thickness is the same as the maximum thickness of the wedge. This result is closely associated with the fact that the thickness-shear motion is localized near the center of the wedge. In the thickness-shear overtones, however, a larger proportion of the wedge participates and, consequently, there is a greater spread in the frequencies of the overtones in a wedge than in a uniform plate. On the other hand, the flexural motion is predominant at the thin edges of the wedge and, with this, is associated the result that, in a given frequency range, there are approximately twice as many flexural modes in a wedge as in a uniform plate.

The thickness-shear equations are next solved for the case of a beveled plate, i.e., one with a portion of uniform thickness between the two wings of the double wedge. It is shown that a very small uniform portion serves to bring the frequency of the first thickness-shear mode very close to that of a uniform plate. This is in conformity with the finding that the thickness-shear motion is localized near the center.

PLATE EQUATIONS

The plate is referred to an x, y, z system of rectangular coordinates, with $y=0$ as its middle plane and the x axis as the axis of symmetry of a monoclinic crystal. The varying thickness, h, is then a function of x and z. For thickness-shear and flexural motions, the plate-stress equations take the same form as in II. These become, after introducing a factor $\exp(i\omega t)$:

$$\begin{aligned} \partial M_x/\partial x - Q_x + \partial M_{xz}/\partial z + \rho h^3\omega^2\psi_x/12 &= 0, \\ \partial Q_x/\partial x + \partial Q_z/\partial z + \rho h\omega^2\eta &= 0, \\ \partial M_{xz}/\partial x - Q_z + \partial M_z/\partial z + \rho h^3\omega^2\psi_z/12 &= 0, \end{aligned} \tag{1}$$

where

$$\begin{aligned} M_x &= D_1\partial\psi_x/\partial x + D_2\partial\psi_z/\partial z, \\ M_z &= D_2\partial\psi_x/\partial x + D_3\partial\psi_z/\partial z, \\ M_{xz} &= D_5(\partial\psi_z/\partial x + \partial\psi_x/\partial z), \\ Q_z &= D_4(\psi_z + \partial\eta/\partial z), \\ Q_x &= D_6(\psi_x + \partial\eta/\partial x), \end{aligned} \tag{2}$$

and

$$\begin{aligned} D_1 &= (C_{11} - C_{12}^2/C_{22})h^3/12, \\ D_2 &= (C_{13} - C_{12}C_{23}/C_{22})h^3/12, \\ D_3 &= (C_{33} - C_{23}^2/C_{22})h^3/12, \\ D_4 &= \pi^2(C_{44} - C_{24}^2/C_{22})h/12, \\ D_5 &= C_{55}h^3/12, \\ D_6 &= \pi^2 C_{66}h/12. \end{aligned} \tag{3}$$

The boundary conditions are prescribed by specifying one member of each of the three products

$$M_x\psi_x, \quad M_{xz}\psi_z, \quad Q_x\eta, \tag{4}$$

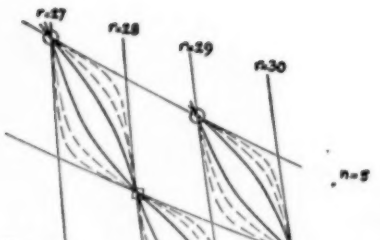

FIG. 3. Illustrating variation of coupling between thickness-shear and flexural modes.

at each point of the edges of the plate, where the normal is ν and the tangent is s.

MOTION INDEPENDENT OF z

In this paper, the problems considered involve contouring and motion independent of z, i.e.,

$$h=h(x), \quad \psi_x=\psi(x,t), \quad \psi_z=0, \quad \eta=\eta(x,t). \tag{5}$$

As a result, upon elimination of the moments and shears through the use of Eq. (2), the equations of motion (1) reduce to

$$\begin{aligned}(D_1\psi')'-D_6(\psi+\eta')+\rho h^3\omega^2\psi/12=0,\\ [D_6(\psi+\eta')]'+\rho h\omega^2\eta=0,\end{aligned} \tag{6}$$

where $'\equiv d/dx$. The boundary conditions are similarly reduced to the specification, on edges $x=$ constant, of one member of each of the two products

$$M_x\psi \quad \text{and} \quad Q_x\eta, \tag{7}$$

where

$$M_x=D_1\psi' \quad \text{and} \quad Q_x=D_6(\psi+\eta'). \tag{8}$$

Equations (6)–(8) have the same form as those for a Timoshenko beam of varying section. There is no difficulty in eliminating one of ψ and η from Eq. (6) to obtain a fourth order equation on the other. Because of the x dependence of h, D_1, and D_6, however, the resulting equation defines, in general, functions which are not tabulated. This would be no great obstacle for the calculation of frequencies of the lower modes of vibration; but, for frequencies in the neighborhood of the lowest thickness-shear frequency, the thickness-shear motion is strongly coupled with high modes of flexure in a plate which is long in comparison with its thickness. Hence, energetic or perturbation methods are very lengthy.

RESOLUTION OF EQUATIONS

Equations (6)–(8) may be resolved into two sets of equations which govern, approximately, the thickness-shear and flexural motions separately.

To obtain the thickness-shear equations, we first set the flexural rigidity D_1 equal to zero in the first equation of (6). This restricts the equations to modes involving little flexure. To compensate, in part, for what little flexural rigidity is neglected, we modify the transverse inertia in the second equation of (6) by introducing a multiplying factor K_2 whose value will be determined later. Equations (6) then reduce to

$$\begin{aligned}12D_6(\psi_2+\eta_2')-\rho h^3\omega^2\psi_2=0,\\ [D_6(\psi_2+\eta_2')]'+K_2\rho h\omega^2\eta_2=0,\end{aligned} \tag{9}$$

where ψ_2 and η_2 are the displacements in the uncoupled shear modes. The boundary conditions reduce to the specification of one member of the single product

$$Q_x\eta_2, \tag{10}$$

on each of two boundaries $x=$ constant. Q_x is still given by the second equation of (8).

The equations of flexure are obtained from Eqs. (6)–(8) by dropping the rotatory inertia and shear deformation terms and again modifying the transverse inertia. The result is, of course, the equation of classical beam theory,

$$(D_1\eta_1'')''-K_1\rho h\omega^2\eta_1=0, \tag{11}$$

where η_1 is uncoupled flexural deflection and K_1 is a multiplying factor to be determined later. The boundary conditions remain as in Eq. (7), but now

$$\psi_1=-\eta_1', \quad M_x=-D_1\eta_1'', \quad Q_x=-(D_1\eta_1'')'. \tag{12}$$

Equations (9) and (11) must now be completed by determining K_2 and K_1. This is done by solving (9) and (11) for the case of uniform thickness, for which the solution of the full equations (6) is known, and choosing expressions for K_2 and K_1 which will make the frequencies obtained from the resolved and combined equations match as well as possible.

DETERMINATION OF K_2

For a plate of uniform thickness, h and D_6, in Eqs. (9), are constants. Eliminating ψ_2 from (9) leaves η_2 governed by

$$\eta_2''+\delta_2^2\eta_2=0, \tag{13}$$

where

$$\delta_2^2=\frac{12K_2}{h^2}\left(\frac{\omega^2}{\bar{\omega}^2}-1\right) \tag{14}$$

and

$$\bar{\omega}^2=12D_6/\rho h^3, \tag{15}$$

i.e., $\bar{\omega}$ is the frequency of the first thickness-shear mode in an infinite plate of thickness h.

Upon inserting the solution of Eq. (13) in the boundary conditions for a free edge (i.e., $Q_x=0$ on $x=\pm l/2$), the secular equation is found to be

$$\delta_2 l=n\pi, \quad n=1,2,3,\cdots, \tag{16}$$

and hence from Eq. (14),

$$\frac{\omega^2}{\bar{\omega}^2}=1+\frac{\pi^2n^2h^2}{12K_2l^2}. \tag{17}$$

This should be, approximately, the equation of the family of curves represented by full lines in Fig. 2. From II, it is known that this family of curves is given by

$$2(\omega/\bar{\omega})^2=1+kn^2h^2/l^2 +[(1+kn^2h^2/l^2)^2-4(Knh/l)^4/g]^{\frac{1}{2}} \tag{18}$$

and is represented approximately, for the small n and large l/h in which we are interested, by

$$(\omega/\bar{\omega})^2=1+kn^2h^2/l^2, \tag{19}$$

where $K^2=\pi^2/12$ and

$$k=\pi^2(1+g)/12g, \tag{20}$$

$$g=\frac{\pi^2C_{66}}{12(C_{11}-C_{12}^2/C_{22})}. \tag{21}$$

Since $k>\pi^2/12$, it is apparent that Eq. (17) gives frequencies which are too low. It will be recalled, from II, that g is the ratio of the thickness-shear modulus to the plate-flexure modulus. Now, in deriving Eq. (17), the plate flexure modulus was set equal to zero, which is the same as making g infinite. But, with g infinite, Eq. (19) reduces to Eq. (17) if $K_2=1$. Thus, the discrepancy between Eqs. (17) and (19) is due to the omission of the effect of flexural rigidity. This effect may now be replaced, approximately, by setting

$$K_2=g/(1+g), \tag{22}$$

as a result of which Eqs. (17) and (19) become identical. Thus the omission of flexural rigidity is balanced by a decrease in transverse inertia, the same for all modes. It should be observed that Eqs. (17) and (22) still do not give the thickness-shear curves of Fig. 2 exactly, but only as well as Eq. (19) does. The discrepancies which remain are discussed below in the section entitled, "Test of Procedure".

DETERMINATION OF K_1

For a uniform plate, (11) reduces to

$$\eta_1^{iv}-\delta_1^4\eta_1=0, \tag{23}$$

where

$$\delta_1^4=K_1\rho h\omega^2/D_1. \tag{24}$$

The solution of Eq. (23) with the boundary conditions for free edges leads to the well-known secular equation

$$\cosh\delta_1 l\cos\delta_1 l=1, \tag{25}$$

whose roots, for the high modes of present interest, are given very closely by

$$\delta_1 l=(2r+1)\pi/2, \quad r=1, 2, 3, \cdots. \tag{26}$$

Hence,

$$(\omega/\bar{\omega})^2=[(2r+1)Kh/l]^4/16gK_1. \tag{27}$$

This is intended to represent the dashed curves in Fig. 2, whose exact equation, from II, is

$$2(\omega/\bar{\omega})^2=1+kr^2h^2/l^2 -[(1+kr^2h^2/l^2)^2-4(Krh/l)^4/g]^{\frac{1}{2}}. \tag{28}$$

The frequencies given by Eq. (27) are higher than those given by Eq. (28). This is essentially because the approximation involves making the shear modulus infinite; and the additional stiffness raises the frequencies.

Now, the main interest is in intersections of the dashed and full curves, of Fig. 2, in the neighborhood of $\omega/\bar{\omega}=1$. Therefore, it is desirable to have the curves of Eq. (27) pass through $\omega/\bar{\omega}=1$ at the same values of l/h that are obtained from Eq. (28) by setting $\omega/\bar{\omega}=1$, i.e., at

$$l/h=\pi r[12(1+g)]^{-\frac{1}{2}}. \tag{29}$$

This is accomplished by setting $\omega/\bar{\omega}=1$ in Eqs. (27) and (28) and then eliminating l/h between the two equations, with the result

$$K_1=\frac{(1+g)^2}{g}\left(\frac{2r+1}{2r}\right)^4. \tag{30}$$

Thus, the increase in shear stiffness is balanced by an increase in transverse inertia, slightly greater for the lower modes than for the higher.

TEST OF PROCEDURE

The coordinates of the intersection points of Eqs. (17) and (27), for r and n even and r and n odd, are to be compared with the corresponding coordinates obtained from Eqs. (18) and (28). The formulas for the coordinates are found by eliminating first $\omega/\bar{\omega}$ and then l/h from the two pairs of equations. Thus, the coordinates from the uncoupled equations (9) and (11) are given by

$$2(l/h)^2=kn^2\{-1+[1+(2K^4r^2/k^2gn^2)^2]^{\frac{1}{2}}\},$$
$$\omega/\bar{\omega}=(k^2gn^2/2K^4r^2)\{1+[1+(2K^4r^2/k^2gn^2)^2]^{\frac{1}{2}}\}, \tag{31}$$

and the coordinates from the full equations (6), as obtained in II, are given by

$$(l/h)^2=K^2(gr^2-n^2)(r^2-gn^2)/g(1+g)(r^2+n^2),$$
$$(\omega/\bar{\omega})^2=g(r^2+n^2)^2/(gr^2-n^2)(r^2-gn^2). \tag{32}$$

Table I contains the coordinates, calculated from Eqs. (31) and (32), for the values of r and n at which circled and squared intersection points occur in Fig. 2. In each group of four coordinates, the lower figures are those for l/h and $\omega/\bar{\omega}$, respectively, as calculated from the approximation (31) and the upper figures are those from the "exact" formulas (32). It may be seen that correspondence is very good, especially for

TABLE I. Comparison of intersection points of frequency spectrum obtained from coupled and uncoupled equations of motion of uniform plate.

n	0		1		2		3		4		5		6		7		8		9		10	
r	l/h	ω/ω̄	l/h	ω/ω̄	l/h	ω/ω̄	l/h	ω/ω̄	l/h	ω/ω̄	l/h	ω/ω̄	l/h	ω/ω̄	l/h	ω/ω̄	l/h	ω/ω̄	l/h	ω/ω̄	l/h	ω/ω̄
1																						
2	1.601	1.000																				
	1.601	1.000																				
3																						
4	3.203	1.000																				
	3.203	1.000																				
5			3.617	1.129																		
			3.778	1.123																		
6	4.804	1.000																				
	4.804	1.000																				
7			5.329	1.062																		
			5.441	1.061																		
8	6.405	1.000																				
	6.405	1.000																				
9			6.992	1.037																		
			7.078	1.037																		
10	8.007	1.000			7.234	1.129																
	8.007	1.000			7.555	1.123																
11			8.632	1.025																		
			8.702	1.024																		
12	9.608	1.000			8.965	1.087																
	9.608	1.000			9.228	1.084																
13			10.260	1.017			9.069	1.178														
			10.319	1.017			9.636	1.167														
14	11.209	1.000			10.658	1.062																
	11.209	1.000			10.882	1.061																
15			11.881	1.013			10.851	1.129														
			11.932	1.013			11.333	1.123														
16	12.810	1.000			12.328	1.047																
	12.810	1.000			12.523	1.046																
17			13.498	1.010			12.589	1.098														
			13.543	1.010			13.009	1.095														
18	14.412	1.000			13.983	1.037			12.693	1.163												
	14.412	1.000			14.155	1.037			13.416	1.154												
19			15.111	1.008			14.298	1.077														
			15.151	1.008			14.671	1.075														
20	16.013	1.000			15.627	1.030			14.468	1.129												
	16.013	1.000			15.782	1.030			15.110	1.123												
21			16.722	1.007			15.987	1.062			14.509	1.191										
			16.758	1.007			16.322	1.061			15.489	1.178										
22	17.614	1.000			17.264	1.025			16.210	1.104												
	17.614	1.000			17.404	1.024			16.789	1.101												
23			18.331	1.006			17.660	1.052			16.314	1.155										
			18.365	1.005			17.965	1.051			17.196	1.147										
24	19.216	1.000			18.894	1.021			17.929	1.087												
	19.216	1.000			19.023	1.020			18.456	1.084												
25			19.939	1.005			19.322	1.043			18.085	1.129										
			19.970	1.005			19.602	1.043			18.888	1.123										
26	20.817	1.000			20.520	1.017			19.630	1.073			18.138	1.178								
	20.817	1.000			20.639	1.017			20.113	1.071			19.272	1.167								
27			21.546	1.004			20.975	1.037			19.830	1.109										
			21.575	1.004			21.233	1.037			20.568	1.105										
28	22.418	1.000			22.143	1.015			21.316	1.062			19.933	1.150								
	22.418	1.000			22.253	1.015			21.763	1.061			20.974	1.142								
29			23.153	1.003			22.621	1.032			21.555	1.093			19.947	1.197						
			23.179	1.003			22.861	1.032			22.238	1.090			21.341	1.184						
30	24.020	1.000			23.763	1.013			22.991	1.054			21.701	1.129								
	24.020	1.000			23.865	1.013			23.407	1.053			22.665	1.123								
31			24.758	1.003			24.260	1.028			23.264	1.081			21.763	1.169						
			24.783	1.004			24.485	1.028			23.900	1.079			23.053	1.159						
32	25.621	1.000			25.380	1.011			24.657	1.047			23.449	1.112								
	25.621	1.000			25.476	1.011			25.046	1.046			24.346	1.107								
33			26.363	1.003			25.896	1.025			24.960	1.071			23.552	1.147						
			26.386	1.002			26.106	1.024			25.555	1.069			24.753	1.139						
34	27.222	1.000			26.995	1.010			26.315	1.042			25.178	1.098			23.579	1.186				
	27.222	1.000			27.086	1.010			26.680	1.041			26.019	1.095			25.125	1.174				
35			27.968	1.002			27.527	1.022			26.645	1.062			25.318	1.129						
			27.990	1.002			27.725	1.022			27.204	1.061			26.443	1.123						
36	28.824	1.000			28.609	1.009			27.967	1.037			26.894	1.087			25.385	1.163				
	28.824	1.000			28.695	1.009			28.311	1.037			27.684	1.084			26.833	1.154				
37			29.572	1.002			29.155	1.019			28.321	1.056			27.067	1.114						
			29.593	1.001			29.342	1.019			28.848	1.055			28.124	1.110						
38	30.425	1.000			30.222	1.008			29.613	1.033			28.597	1.077			27.170	1.144				
	30.425	1.000			30.303	1.008			29.939	1.033			29.343	1.075			28.531	1.137				
39			31.176	1.002			30.781	1.017			29.989	1.050			28.800	1.102			27.207	1.178		
			31.196	1.001			30.958	1.017			30.488	1.049			29.799	1.098			28.908	1.167		
40	32.026	1.000			31.833	1.007			31.255	1.030			30.290	1.069			28.935	1.129				
	32.026	1.000			31.910	1.007			31.564	1.030			30.996	1.068			30.220	1.123				
41			32.780	1.002			32.404	1.016			31.651	1.045			30.520	1.091			29.007	1.159		
			32.798	1.002			32.572	1.016			32.125	1.044			31.466	1.088			30.612	1.150		
42	33.628	1.000			33.444	1.007			32.893	1.027			31.974	1.062			30.685	1.116			29.018	1.191
	33.628	1.000			33.517	1.007			33.187	1.027			32.645	1.061			31.902	1.111			30.978	1.178

small n and large r; i.e., for the low thickness-shear overtones of a thin plate.

The shapes of the uncoupled and coupled modes may also be compared. For example, the deflections for the uncoupled, antisymmetric thickness-shear modes are, from Eq. (13) and Eq. (16),

$$\eta_2 = A_2 \sin(n\pi x/l),$$

and, the corresponding uncoupled flexural deflections are, from Eq. (23),

$$\eta_1 = A_1[\sin\delta_1 x + \sin(\delta_1 l/2)\ \mathrm{cosech}(\delta_1 l/2)\ \sinh\delta_1 x],$$

where δ_1 is given by Eq. (26). These are to be compared with the corresponding shapes obtained from the

coupled equations [see II, Eq. (56)],

$$\eta=\eta_1+\eta_2$$
$$=A_1\sin(r\pi x/l)+A_2\sin(n\pi x/l).$$

Thus, the thickness-shear, or long wavelength, components have exactly the same shape in the two cases; but the flexural, or short wavelength, components differ.

THICKNESS-SHEAR VIBRATIONS OF A DOUBLE WEDGE

The thickness-shear equations (9) will be solved, in this section, for the case of a double wedge with free edges. The plate is of length l and its thickness (see Fig. 4) is

$$h=ax, \quad 0\leqslant x\leqslant l/2,$$
$$h=a(l-x), \quad l/2\leqslant x\leqslant l, \tag{33}$$

where $a=2h_0/l$ and h_0 is the maximum thickness of the wedge. By treating the symmetric and antisymmetric modes separately, only the first equation (33) is required.

Equations (9) are conveniently resolved into

$$12K_2h\eta_2=-(h^3\psi_2)'$$
$$D_6[h^{-1}(h^3\psi_2)']'+K_2(\rho h^3\omega^2-12D_6)\psi_2=0. \tag{34}$$

Then, with h given by the first of (33), the second of (34) becomes

$$\psi_2''+5x^{-1}\psi_2'+[\beta^2+(4-p^2)x^{-2}]\psi_2=0, \tag{35}$$

where

$$\beta^2=K_2\rho\omega^2/K^2C_{66}, \tag{36}$$

$$p^2=1+12K_2/a^2. \tag{37}$$

The solution of Eq. (35) is

$$\psi_2=Ax^{-2}J_p(\beta x)+Bx^{-2}Y_p(\beta x), \tag{38}$$

where J_p and Y_p are the Bessel functions of the first and second kinds and A and B are constants.

For the antisymmetric modes (n odd) the boundary conditions (10) are

$$Q_x(0)=0, \quad \eta(l/2)=0. \tag{39}$$

Hence, $B=0$ and

$$(1-p)J_p(\gamma)+\gamma J_{p-1}(\gamma)=0, \quad (n \text{ odd}), \tag{40}$$

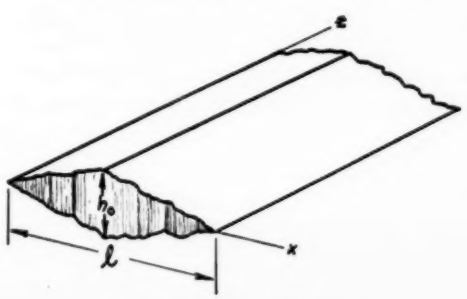

FIG. 4. Double wedge.

TABLE II. Thickness-shear frequencies of double wedge.

p	l/h_0	γ_n $n=1$	$n=2$	$n=3$	ω_n/ω^*, ($g=0.283$) $n=1$	$n=2$	$n=3$
8	9.76	9.95	12.23	14.22	1.25	1.54	1.79
16	19.64	18.31	21.09	23.35	1.15	1.32	1.46
24	29.50	26.57	29.71	32.18	1.11	1.24	1.34
32	39.29	34.78	38.22	40.86	1.09	1.20	1.28

where

$$\gamma=\beta l/2. \tag{41}$$

For the symmetric modes (n even) the boundary conditions are

$$Q_x(0)=0, \quad Q_x(l/2)=0. \tag{42}$$

Hence, $B=0$ and

$$J_p(\gamma)=0, \quad (n \text{ even}). \tag{43}$$

The frequencies are now obtained, in terms of the roots of Eqs. (40) and (43), from Eqs. (41) and (36). Introducing a reference frequency

$$\omega^*=(\pi/h_0)(C_{66}/\rho)^{\frac{1}{2}}, \tag{44}$$

i.e., the frequency of the first thickness-shear mode of an infinite plate of uniform thickness h_0, and using the expression for K_2 from Eq. (22), we have, for the frequency ω_n of the nth mode,

$$\omega_n/\omega^*=(\gamma_nh_0/l)[(1+g)/3g]^{\frac{1}{2}}. \tag{45}$$

The numbers γ_n, in Eq. (45), are the roots of Eqs. (40) and (43) taken alternately, i.e., when n is odd, γ is the $(n+1)/2$th root of Eq. (40); when n is even, γ is the $n/2$th root of Eq. (43). Table II contains the first three roots for four values of p, i.e., for four values of wedge angle. Also included in Table II are the corresponding frequencies calculated from Eq. (45) for the AT-cut of quartz, for which $g=0.283$ (see II). The thickness-shear frequencies of the first three modes are plotted as full lines in Fig. 5.

Equation (45) is the equation of a family of curves, for the wedge, which corresponds to the family of full lines, in Fig. 2, for the uniform plate. It is interesting to compare the influence of the length-thickness ratio on the frequencies in the two cases. In the case of the wedge, the frequency cannot be expressed explicitly in terms of l/h_0 because the latter is contained in the order, p, of the Bessel functions appearing in the secular equations. However, the leading terms can be found in the following manner. For the odd modes, the secular equation (40) can be written as

$$[\gamma J_p(\gamma)]'=0, \tag{46}$$

so that it is seen that the zeros of Eq. (40) lie near the stationary values of $J_p(\gamma)$. Hence, approximately, the first root of Eq. (40) is at the first maximum of $J_p(\gamma)$ which, by Watson's formula is

$$\gamma_1=p+0.8086^{\frac{1}{3}}p+O(p^{-\frac{1}{3}}) \tag{47}$$

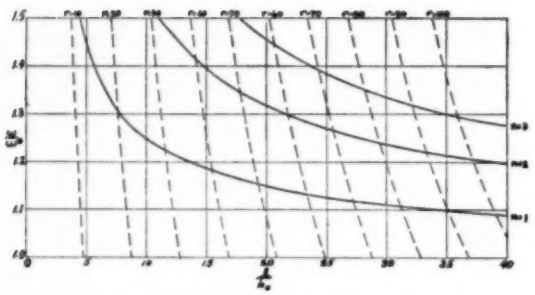

FIG. 5. Frequencies of uncoupled thickness-shear and flexural modes of a double wedge.

for large p, i.e., for large l/h_0. Inserting the expression for p from Eq. (37) and expanding, we find, approximately,

$$\omega_1=\omega^*+0.66\omega^*(kh_0^2/l^2)^{\frac{1}{2}}. \tag{48}$$

On the other hand, the frequency of the first thickness-shear mode of a uniform plate, for large l/h, is, from Eq. (18) or (19),

$$\omega_1=\bar{\omega}+(1/2)\bar{\omega}(kh^2/l^2). \tag{49}$$

In Eq. (49) the first term on the right is the thickness-shear frequency of an infinite plate and the second term gives the first order influence of the finite length of the plate. In Eq. (48) the first term on the right is the thickness-shear frequency of an infinite plate of uniform thickness equal to the maximum thickness of the wedge and the second term gives the first order influence of the ratio of length to maximum thickness. In both cases the second term is much smaller than the first but the correction term for the wedge is greater than that for the uniform plate. Hence, the thickness-shear frequency of a double wedge is only slightly greater than that of a uniform plate of thickness equal to the maximum thickness of the wedge. This is despite the fact that the average thickness of the wedge is only half that of the uniform plate, from which it might be conjectured that the wedge frequency would be double that of the uniform plate. The reason this is not so is that only the central portion of the wedge contributes to the shear motion, as will be shown below. Further, it may be seen, from the presence of the power $\frac{1}{2}$ in Eq. (48), that changes in length of the wedge have much less influence on the thickness-shear frequency than corresponding changes in length of a uniform plate. This also is due to the fact that the outer portions of the wedge do not participate in the shear motion.

Another influence of the wedge shape is on the spread of the thickness-shear frequency spectrum. To study this, we first find, approximately, the frequency of the second mode, which is obtained from the first root of Eq. (43). For large p, the first zero of $J_p(\gamma)$ is, by Watson's formula,

$$\gamma_2=p+1.8557p^{\frac{1}{3}}+O(p^{-\frac{1}{3}}), \tag{50}$$

so that, by the same procedure as before,

$$\omega_2=\omega^*+1.37\omega^*(kh_0^2/l^2)^{\frac{1}{2}}. \tag{51}$$

The corresponding frequency for the uniform plate is

$$\omega_2=\bar{\omega}+2\bar{\omega}(kh^2/l^2). \tag{52}$$

Hence, approximately, for plate and wedge of the same maximum thickness,

$$\frac{(\omega_2-\omega_1)_{\text{wedge}}}{(\omega_2-\omega_1)_{\text{plate}}}=0.47\,(l^2/kh^2)^{\frac{1}{2}}. \tag{53}$$

For example, for an AT quartz plate, $g=0.283$ and, hence, $k=3.73$. If the plate is of uniform thickness, the difference in frequencies, when $l/h=30$, is about 10 kilocycles per second for a plate one millimeter thick. By Eq. (53), the difference in frequency between the first two modes of the wedge would be about 180 kilocycles per second.

FLEXURAL VIBRATIONS OF A DOUBLE WEDGE

When $h=ax$, Eq. (11) becomes

$$16(x^3\eta_1'')''-\lambda^4x\eta_1=0, \tag{54}$$

where

$$\frac{\lambda^4}{16}=\frac{12K_1\rho\omega^2}{a^2(C_{11}-C_{12}^2/C_{22})}. \tag{55}$$

The solution of Eq. (54) is

$$x^{\frac{1}{2}}\eta_1=AJ_1(\lambda x^{\frac{1}{2}})+BJ_1(i\lambda x^{\frac{1}{2}})+CY_1(\lambda x^{\frac{1}{2}})+DY_1(i\lambda x^{\frac{1}{2}}). \tag{56}$$

For the symmetric modes, the boundary conditions are

$$M_x(0)=Q_x(0)=\eta_1'(l/2)=Q_x(l/2)=0. \tag{57}$$

Hence, B, C, and D vanish and

$$\delta J_0(\delta)-2J_1(\delta)=0, \tag{58}$$

where

$$\delta=\lambda(l/2)^{\frac{1}{2}}. \tag{59}$$

For the antisymmetric modes, the boundary conditions are

$$M_x(0)=Q_x(0)=\eta_1(l/2)=M_x(l/2)=0. \tag{60}$$

Hence, $C=D=0$, $B=AJ_1(\delta)/I_1(\delta)$ and

$$\delta I_1(\delta)J_1(\delta)-2[I_0(\delta)J_1(\delta)-I_1(\delta)J_0(\delta)]=0, \tag{61}$$

where I_0 and I_1 are modified Bessel functions.

From Eqs. (55) and (59), the frequency of the rth

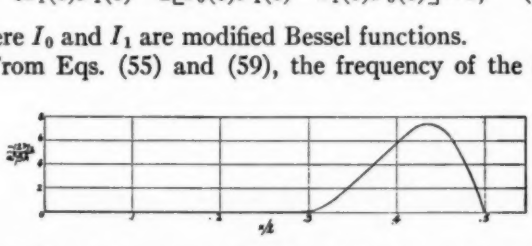

FIG. 6. Shape of transverse deflection of the first antisymmetric thickness-shear mode of a double wedge ($1/h_0=19.64$).

mode is given by

$$\frac{\omega_r}{\omega^*}=\frac{\delta_r^2 h_0^2}{12l^2(1+g)}\left(\frac{2r}{2r+1}\right)^2, \tag{62}$$

where δ_r is the $(r+1)/2$th root of Eq. (58) when r is odd; and, when r is even, δ_r is the $r/2$th root of Eq. (61).

Equation (62) is the equation of a family of curves, for the wedge, which corresponds to the family of dashed curves, in Fig. 2, for the uniform plate. The curves showing the uncoupled flexural frequencies for the wedge are the dashed lines in Fig. 5. Only every tenth mode is drawn in the figure.

For high modes, equations (58) and (61) give, approximately,

$$\delta_r=(2r+5)\pi/4. \tag{63}$$

Then, from Eqs. (30), (62), and (63), the frequencies of the high, uncoupled, flexural modes of a wedge are

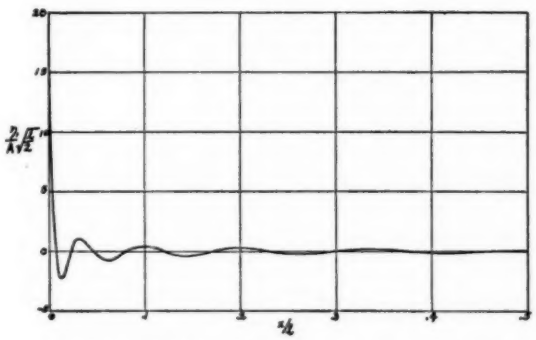

FIG. 7. Shape of transverse deflection of the tenth symmetric flexural mode of a double wedge.

given by

$$(\omega/\omega^*)^2=[(2r+5)Kh_0/2l]^4/16K_1g. \tag{64}$$

This is to be compared with Eq. (27) which gives the frequencies of the high, uncoupled, flexural modes of a uniform plate. It may be seen that the rth mode of the wedge has the same frequency as the $(r+2)$th mode of a uniform plate of (1) twice the length and of thickness equal to the maximum thickness of the wedge or (2) the same length and one-quarter the maximum thickness of the wedge. Alternatively, for a uniform plate and a wedge of the same maximum dimensions, an uncoupled flexural mode of the wedge has a frequency one-quarter that of the next-but-one higher mode of the plate. This is in contradistinction to the relation between the frequencies of the uncoupled, thickness-shear modes of plate and wedge. These were found to be about the same.

It may also be seen that, for a given l/h, the order of the flexural mode which couples with the first thickness-shear mode is about twice as high for the wedge as for the uniform plate.

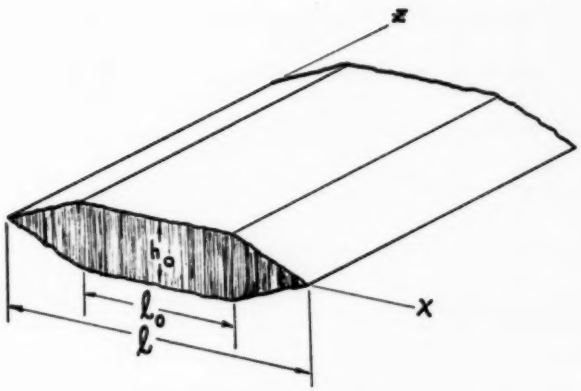

FIG. 8. Plate with beveled edges.

SHAPES OF MODES

For the uncoupled thickness-shear motion, the rotation is given by

$$\psi_2=Ax^{-2}J_p(\beta x),$$

and the deflection is given, in terms of ψ_2, by the first equation of (34). Thus, the mode shapes are described essentially by Bessel functions of the first kind of very large order (since p is very large for small wedge angles) and of small argument (since βx is small for the lower modes). A characteristic of such functions is that they are very small for an appreciable range in the neighborhood of zero argument. As illustrated in Fig. 6, for $l/h_0=19.64$, the deflection in the first antisymmetric mode is zero at the end of the wedge and is practically zero into about 60 percent of the distance to the center. Thus, only about 40 percent of the wedge (the central portion) participates in the thickness-shear motion.

On the other hand, the uncoupled flexural modes are described by Bessel functions of low order. For example, the deflection for the symmetric modes is

$$\eta_1=Ax^{-\frac{1}{2}}J_1(\lambda x^{\frac{1}{2}}).$$

The Bessel function of order unity has a diminishing amplitude with increasing argument. For example (see Fig. 7), for the tenth symmetric mode (which has twenty nodes) the amplitude at the edge of the wedge is about one hundred times as large as the amplitude at the center.

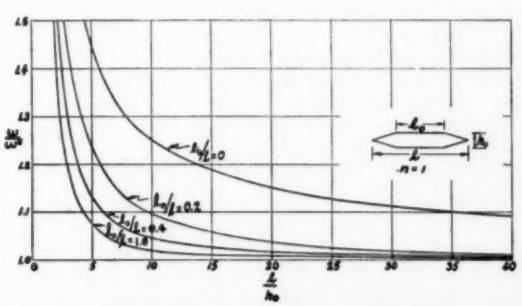

FIG. 9. Influence of length, of portion of uniform thickness, on frequency of first thickness-shear mode of a beveled plate.

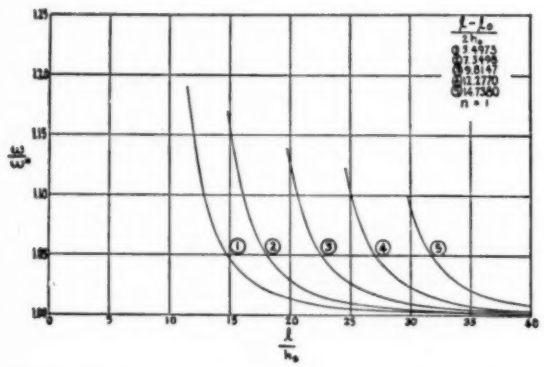

FIG. 10. Influence of wedge angle on frequency of first thickness-shear mode of a beveled plate.

Thus, while the thickness-shear motion is concentrated near the center of the wedge, the flexural motion is concentrated near the edges.

BEVELED PLATE

In this section we investigate the effect, on the thickness-shear frequencies, of a uniform portion of plate between the two wings of the wedge. The cross section of the plate is illustrated in Fig. 8, i.e., we have

$$\begin{aligned} h&=ax, \quad 0\leqslant x\leqslant (l-l_0)/2;\\ h&=h_0, \quad (l-l_0)/2\leqslant x\leqslant l/2. \end{aligned} \tag{65}$$

For the wedge portion we have, from Eqs. (34) and (38),

$$\begin{aligned} \psi&=Ax^{-2}J_p(\beta x),\\ 12K_2\beta\eta&=-(h^3\psi)'. \end{aligned} \tag{66}$$

For the uniform portion, we have from Eqs. (9) and (13), for the antisymmetric modes,

$$\begin{aligned} \eta&=B\sin\delta(l/2-x);\\ (1-\omega^2/\omega^{*2})\psi&=B\delta\cos\delta(l/2-x). \end{aligned} \tag{67}$$

The boundary conditions require that ψ and η be continuous at $x=(l-l_0)/2$, i.e., at the interface between the wedge and uniform portions. Equating the appropriate members of Eqs. (66) and (67), and eliminating A and B, we find the secular equation

$$\alpha\gamma_0 J_p(\gamma_0)\tan(C\alpha\gamma_0)=[\gamma_0 J_p(\gamma_0)]', \tag{68}$$

where

$$\begin{aligned} C^{-1}&=(l/l_0-1),\\ \gamma_0&=\beta l_0/2C,\\ \alpha&=\delta/\beta=(1-\omega^{*2}/\omega^2)^{1/2}. \end{aligned} \tag{69}$$

The solution of Eqs. (68) and (69) for the frequency of the first thickness-shear mode as a function of l/h_0, for various values of l_0/l, is shown in Fig. 9. The uppermost curve is that for the double wedge and the lowest curve is that for the uniform plate. It may be seen that a very small uniform portion causes the frequency to be much closer to that of the uniform plate than to the frequency of a double wedge. This is in conformity with the previous result that the thickness-shear motion is concentrated near the center of the plate. Since, in this case, the central portion has a uniform thickness, it follows that the frequency is very nearly that of a uniform plate.

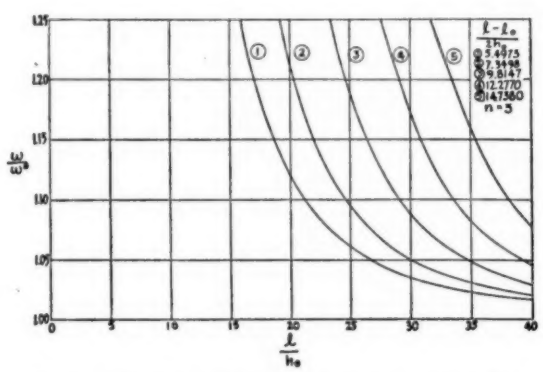

FIG. 11. Influence of wedge angle on frequency of third thickness-shear mode of a beveled plate.

Additional computations were made, from Eqs. (68) and (69), of ω/ω^* *vs* l/h_0 for 5 values of wedge angle. The results are given in Figs. 10 and 11 for the first ($n=1$) and second ($n=3$) antisymmetric modes, respectively.

JOURNAL OF APPLIED PHYSICS VOLUME 25, NUMBER 1 JANUARY, 1954

Thickness-Shear Vibrations of Piezoelectric Crystal Plates with Incomplete Electrodes*

R. D. MINDLIN AND H. DERESIEWICZ
Department of Civil Engineering, Columbia University, New York, New York
(Received May 7, 1953)

In this paper the influence of length of electrodes on thickness-shear frequencies of piezoelectric crystal plates is investigated.

IN the third of a series of papers[1] on thickness-shear and flexural vibrations of plates, solutions were obtained for the forced vibrations of rectangular piezoelectric crystal plates whose surfaces are completely coated by the electrodes. The present paper deals with crystal plates having rectangular electrodes which cover only a portion of their surfaces.

The presence or absence of electrode is equivalent to a change in the thickness-shear modulus of elasticity and piezoelectric constant. Thus, coated and uncoated portions of the plate, if separated, would have different natural frequencies of vibration even if they had the same dimensions. The full plate, then, exhibits coupling between the modes of the coated and uncoated portions. Since each of the latter contains coupling between the thickness-shear and flexural modes, the resulting frequency spectrum is very complicated. Although the secular equation is easy to obtain, the calculation of its roots is very laborious. In order to study the effect of coupling between the coated and uncoated portions, use is made of a device, developed previously (IV), whereby approximations to the thickness-shear and flexural modes may be investigated separately. The coupling phenomena between the thickness-shear modes of the coated and uncoated portions are then explored in detail. The thickness-shear frequencies of the partially coated plate are shown to be the result of coupling between two systems. One of these is a fully coated plate, in thickness-shear motion, whose length is equal to the length of the coated portion of the partially coated plate; the other is an uncoated plate, in similar motion, of length equal to that of the uncoated portion of the partially coated plate.

RESUMÉ OF EQUATIONS

Referred to a rectangular coordinate system, the faces of the plate are at $y=\pm h/2$ and only motion independent of z is considered. Then, from III, Equation (31), the equations of motion, at frequency ω, are

$$\begin{aligned} D_1\xi''-D_6(\xi+h\eta')+F_1\varphi''-F_6\varphi_0+\rho\omega^2R\xi=0,\\ D_6(\xi'+h\eta'')+F_6\varphi_0'+\rho\omega^2h\eta=0,\\ (R+4\pi C_1)\varphi''-4\pi F_1\xi''=0, \end{aligned} \tag{1}$$

where primes denote differentiation with respect to x, while ξ and η are the x and y components of displacement, and φ is the electric potential. The coefficients are given by

$$\begin{aligned} &D_1=(c_{11}-c_{12}^2/c_{22})R; \qquad F_1=(e_{11}-c_{12}e_{12}/c_{22})R,\\ &D_6=\kappa^2c_{66}; \qquad F_6=\kappa^2e_{26}, \\ &C_1=(\kappa_{11}+e_{12}^2/c_{22})R; \qquad R=h^2/12, \end{aligned} \tag{2}$$

where c_{ij}, e_{ij}, κ_{ij} are the elastic, piezoelectric, and susceptibility coefficients, respectively, and where κ is defined later. Note that F_6 differs in definition from that in III by the factor κ^2.

The moment and shear in the plate are, respectively,

$$M_x=D_1\xi'+F_1\varphi'; \tag{3}$$

$$Q_x=D_6(\xi+h\eta')+F_6\varphi_0. \tag{4}$$

In Equations (1) and (4), taken from III, wherever F_6 is found as a coefficient, φ has been replaced by φ_0. The necessity for this has been brought to the authors' attention by Dr. J. A. Lewis, and arises from considering the sequence of operations in computing the relation

$$Q_x=\int_{-h/2}^{h/2}T_6dy. \tag{5}$$

In III, the expression for T_6 in terms of ξ, η, and φ was inserted in the integrand before integration. Consequently, it was not recognized that the term φ in the resulting expression should have appeared as φ_0, i.e., the applied potential, as would have been apparent if the integration had been performed first.

A similar change is required in the expression for

$$P_y=\int_{-h/2}^{h/2}P_2dy, \tag{6}$$

but this does not affect the differential equations for the modes of motion considered here.

INFINITE PLATE: DETERMINATION OF κ^2

The pure, thickness-shear motion of an infinite plate is obtained by setting $\eta=0$ and $\xi=\xi_0$ (a constant) in (1). Hence,

$$(\rho R\omega^2-\kappa^2c_{66})\xi_0=F_6\varphi_0. \tag{7}$$

From (7), resonance in an infinite plate occurs when

$$\omega^2=\kappa^2c_{66}/\rho R. \tag{8}$$

* This investigation was supported by the U. S. Army Signal Corps Engineering Laboratories under a contract with Columbia University.

[1] R. D. Mindlin, J. Appl. Mech. **18**, 31–38 (1951); J. Appl. Phys. **22**, 316–323 (1951), **23**, 83–88 (1952); R. D. Mindlin and M. Forray, J. Appl. Phys. **24**, 12 (1953). These papers are referred to as I, II, III and IV, respectively.

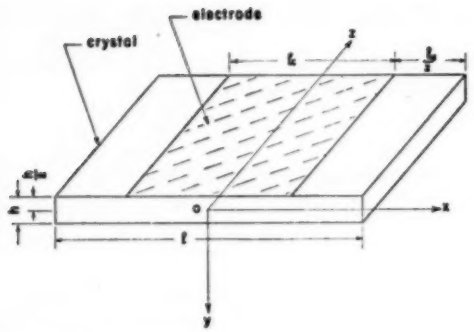

FIG. 1. Plate with electrode coating on a portion of the surface.

This is to be compared with Lawson's[2] solution of the three-dimensional equations:

$$\omega^2=\frac{4\alpha_n^2 c_{66}}{\rho h^2}\left(1+\frac{e_{26}^2}{c_{66}K_2}\right), \tag{9}$$

where

$$K_2=(1+4\pi\kappa_{22})/4\pi$$

and α_n are the roots of

$$\tan\alpha_n=\alpha_n(1+c_{66}K_2/e_{26}^2) \tag{10}$$

for a plate with coated electrodes, and

$$\alpha_n=n\pi/2 \tag{11}$$

for an uncoated plate.

Comparing (8) and (9), we find

$$\kappa_i^2=\alpha_i^2(1+e_{26}^2/c_{66}K_2)/3, \quad i=c, u \tag{12}$$

where α_c is the first root of (10) and $\alpha_u=\pi/2$. Thus, κ has different values, κ_c and κ_u, according as the plate has or has not electrode coating. Since the moduli D_6 and F_6 are proportional to κ^2, the effect of electrode coating appears in this theory as an alteration of an elastic and piezoelectric property. From (8) and (12), infinite coated and uncoated plates have natural frequencies ω_c and ω_u, respectively, given by

$$\omega_i^2=\kappa_i^2 c_{66}/\rho R, \quad i=c, u. \tag{13}$$

PARTIALLY COATED PLATE OF FINITE LENGTH

We consider, now, a plate, bounded by edges $x=\pm l/2$, with electrodes covering a portion $-l_c/2\leq x\leq l_c/2$ (see Fig. 1). The motions of the coated and uncoated portions are each governed by equations of the form (1) but with different values of the constants D_6 and F_6. In addition, $\varphi_0=0$ for the uncoated portion. The simultaneous solution of the two sets of equations must be found with boundary conditions $M_x=Q_x=0$ at $x=\pm l/2$ and M_x, Q_x, ξ and η continuous at $x=\pm l_c/2$. There is no difficulty in finding this solution and the accompanying secular equation. However, the frequency spectrum is very complicated because the motion involves fourfold coupling; i.e., between thickness-shear and flexure as well as between coated and uncoated portions. Since we are interested mainly in the effects of partial coating on the thickness-shear overtones, it is expedient to introduce an approximation whereby the thickness-shear modes may be studied independently of the flexural modes. This is a device employed previously (IV) to study plates of varying thickness. It consists, simply, of omitting the flexural resistance terms, which play only a minor role in the thickness-shear modes, and modifying the transverse inertia to compensate for the omission.

THICKNESS-SHEAR EQUATIONS

If the flexural resistance $D_1\xi'+F_1\varphi'$ is omitted from (1), these become

$$\begin{aligned} &D_6(\xi+h\eta')+F_6\varphi_0-\rho\omega^2 R\xi=0;\\ &D_6(\xi'+h\eta'')+F_6\varphi_0'+\lambda\rho\omega^2 h\eta=0, \end{aligned} \tag{14}$$

where λ is the correction factor, for transverse inertia, which we now proceed to determine by comparing solutions of (14), for fully coated and uncoated plates of finite length, with the corresponding solutions of (1).

Eliminating ξ from (14) we find, for the equation governing η,

$$\eta''+\delta_i^2\eta=0 \tag{15}$$

where

$$\delta_i^2=\frac{\lambda_i}{R}\left(\frac{\omega^2}{\omega_i^2}-1\right), \quad i=c, u. \tag{16}$$

The resonant frequencies of the antisymmetric modes of a fully coated or a fully uncoated plate, of length l, are obtained by applying the boundary conditions $Q_x=0$ at $x=\pm l/2$ to the solution, $\eta=B\sin\delta_i x$, of (15), with the result $\delta_i l=n\pi$, $n=1, 3, 5, \cdots$, or,

$$\frac{\omega^2}{\omega_i^2}=1+\frac{Rn^2\pi^2}{\lambda_i l^2}. \tag{17}$$

The corresponding solution of (1) was shown in II and III to yield, as a first approximation,

$$\frac{\omega^2}{\omega_i^2}=1+\frac{k_i n^2 h^2}{l^2}, \tag{18}$$

where

$$k_i=\kappa_i^2(1+1/g_i), \quad g_i=R\kappa_i^2 c_{66}/D_1(1+J),$$

$$J=\frac{(e_{11}-e_{12}c_{12}/c_{22})^2}{(c_{11}-c_{12}^2/c_{22})(K_1+e_{12}^2/c_{22})},$$

$$K_1=(1+4\pi\kappa_{11})/4\pi.$$

From (17) and (18), we find

$$\lambda_i=\pi^2/12k_i, \quad i=c, u. \tag{19}$$

Hence,

$$\delta_i^2=\frac{\pi^2}{k_i h^2}\left(\frac{\omega^2}{\omega_i^2}-1\right). \tag{20}$$

[2] A. W. Lawson, Phys. Rev. 62, 71 (1942).

In the absence of piezoelectric effect, $J=0$ and $\kappa^2=\pi^2/12$, so that (19) reduces to $\lambda=(1+g)/g$, as in IV.

THICKNESS-SHEAR VIBRATIONS OF A PARTIALLY COATED PLATE OF FINITE LENGTH

Equation (15), with δ_i given by (20), is now to be solved for the case illustrated in Fig. 1. Considering first the antisymmetric modes, the solution of (15) is taken as

$$\eta_c=B\sin\delta_c x,$$
$$\eta_u=C\cos\delta_u x+D\sin\delta_u x \tag{21}$$

for the coated and uncoated portions, respectively.

The boundary conditions require the evanescence of the shear at $x=l/2$ and the continuity of shear and deflection at $x=l_c/2$. These become, respectively,

$$\eta_u'(l/2)=0;$$
$$\frac{\kappa_c^2 c_{66}h}{1-\omega_c^2/\omega^2}\eta_c'(l_c/2)+\frac{\kappa_c^2 e_{26}\varphi_0}{1-\omega_c^2/\omega^2}=\frac{\kappa_u^2 c_{66}h}{1-\omega_u^2/\omega^2}\eta_u'(l_c/2); \tag{22}$$
$$\eta_c(l_c/2)=\eta_u(l_c/2).$$

Substituting (21) into (22), the secular equation is found to be

$$\kappa_u^2 k_c\delta_c\tan(\delta_c l_c/2)=\kappa_c^2 k_u\delta_u\cot(\delta_u l_u/2), \tag{23}$$

where $l_u=l-l_c$. To put this equation into a form suitable for computing its roots, let

$$\delta_u/\delta_c=a,\quad \gamma=\delta_c l_c/2,\quad r=l_c/l. \tag{24}$$

Referring to (20), and noting that $\omega_u>\omega_c$, we see that a is real when ω is outside the range of frequencies between ω_c and ω_u and that a is imaginary when ω lies between ω_c and ω_u. In the latter case, let $a=ia_1$. Then (23) becomes

$$\begin{aligned}&\tan\gamma\tan(r^{-1}-1)a\gamma=ak_u\kappa_c^2/k_c\kappa_u^2,\quad \omega<\omega_c,\ \omega>\omega_u;\\ &\tan\gamma\tanh(r^{-1}-1)a_1\gamma=a_1k_u\kappa_c^2/k_c\kappa_u^2,\quad \omega_c<\omega<\omega_u.\end{aligned} \tag{25}$$

From the first of (24)

$$\begin{aligned}&\omega/\omega_c=[g_u(k_c-k_ua^2)/(g_ck_c-g_uk_ua^2)]^{\frac{1}{2}},\\ &\qquad\qquad \omega<\omega_c,\ \omega>\omega_u;\\ &\omega/\omega_c=[g_u(k_c+k_ua_1^2)/(g_ck_c+g_uk_ua_1^2)]^{\frac{1}{2}},\ \omega_c<\omega<\omega_u;\end{aligned} \tag{26}$$

and, from the second of (24),

$$\begin{aligned}&l/h=(2\gamma/\pi r)[(g_ck_c-g_uk_ua^2)/(g_u-g_c)]^{\frac{1}{2}},\\ &\qquad\qquad \omega<\omega_c,\ \omega>\omega_u;\\ &l/h=(2\gamma/\pi r)[(g_ck_c+g_uk_ua_1^2)/(g_u-g_c)]^{\frac{1}{2}},\ \omega_c<\omega<\omega_u.\end{aligned} \tag{27}$$

Equations (25), (26), and (27) constitute the solution of the problem of finding the frequencies for the case of antisymmetric modes. For the symmetric modes, (26) and (27) remain unaltered, while in (25) tan and tanh are replaced by cot and coth, respectively, and the algebraic sign of the right-hand side of the second of (25) is changed.

In calculating the relation between ω/ω_c and l/h, in (25), (26), and (27), the elastic constants enter only in the form κ_c, g_u/g_c, and k_u/k_c. For a given plate g_i is determined by the material constants in accordance with (12) and (18). The calculations are performed by selecting a value of a or a_1, which fixes the ratio ω/ω_c by (26) and the roots, γ, of (25), for a particular ratio of electrode coating r. The values of γ are then inserted in (27) to obtain the series of plate dimensions, l/h, which have the selected frequency ratio ω/ω_c. Such computations were performed for the AT cut of quartz and $r=\frac{1}{2}$, i.e., with electrodes covering half the surface. The resulting frequency spectrum is shown in Fig. 2. In the sets of three curves, in Fig. 2, the lowest is for the fully coated, the central for half coated, and the upper for the fully uncoated plate.

VARIATION OF FREQUENCY WITH LENGTH OF COATING

The influence of the fraction of coating (r) on the frequencies of a plate of given length may be obtained as follows. Replace γ, in (25), by its expression in terms of r and l/h, according to (27). In the revised equation (25), choose a value of l/h and the corresponding set of values of ω/ω_c (or a) determined previously. For l/h and ω/ω_c, calculate the roots, r, of the

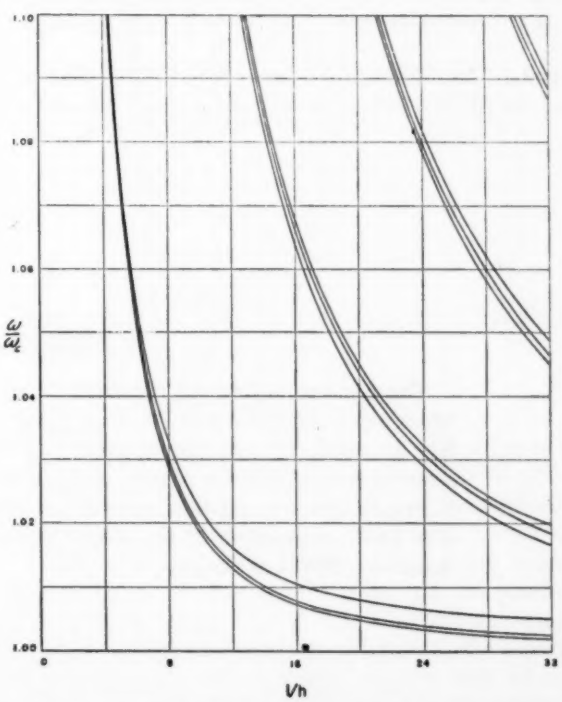

FIG. 2. Frequencies of thickness-shear vibration of a plate with various fractions of electrode coating on the surface.

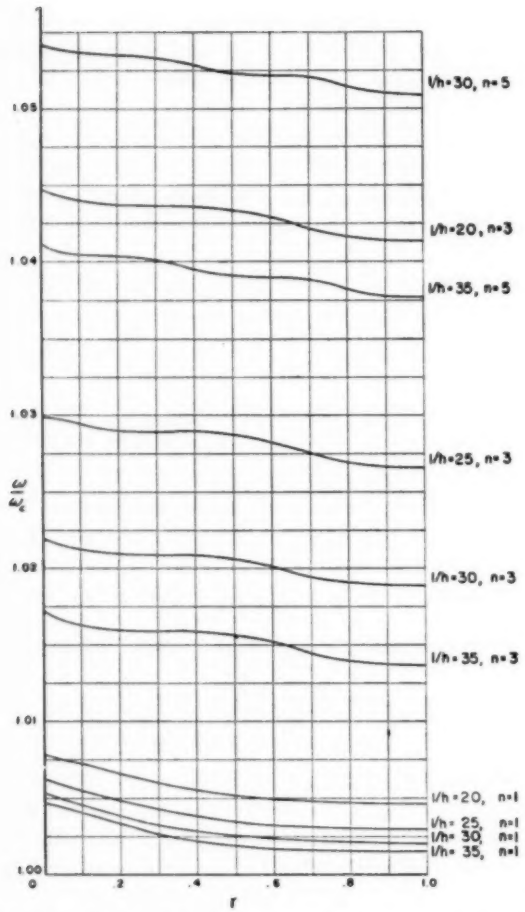

FIG. 3. Variation of thickness-shear frequencies with fraction of surface which is coated with electrode.

revised (25). This procedure yields data from which may be plotted curves of frequency (ω/ω_c) *versus* fraction of coating (r) for each value of l/h. Such curves are illustrated in Fig. 3.

UNCOUPLED THICKNESS-SHEAR MODES

Additional insight into the coupling phenomenon involved is obtained by studying the special roots of the first of (25) for which the transcendental equation degenerates to an algebraic one. We note that the first of (25) is satisfied by

$$\begin{aligned} &\gamma=n\pi/2, \quad n=1, 3, 5, \cdots; \\ &(r^{-1}-1)a\gamma=m\pi/2, \quad m=0, 2, 4, \cdots. \end{aligned} \tag{28}$$

Hence, the transcendental equation (25) for the frequencies reduces to

$$a=mr/n(1-r). \tag{29}$$

These expressions for a and γ are now inserted in (26) and (27) to obtain frequencies ω/ω_c and corresponding lengths l/h in terms of m and n; by eliminating m and n, in turn, between the formulas for ω/ω_c and l/h, there results

$$\begin{aligned} \omega^2/\omega_c^2&=1+k_c n^2h^2/l_c^2, \\ \omega^2/\omega_u^2&=1+k_u m^2h^2/l_u^2. \end{aligned} \tag{30}$$

These are the equations of the uncoupled thickness-shear modes. Comparing (30) with (18), we see that the thickness-shear overtones of a partially coated plate act as though they were produced by the coupling of two simple systems. One of these is comprised of the thickness-shear overtones of a fully coated plate whose length is that of the coated portion of the partially coated plate. The other system is comprised of the thickness-shear overtones of a completely uncoated plate whose length is the total uncoated length of the partially coated plate.

Fluid Dynamics Meeting

The regular meeting of the Division of Fluid Dynamics will be held during the Annual Meeting of the American Physical Society in New York, January 28–30, 1954. The tentative schedule of sessions includes a session on shock waves in liquids and solids, two sessions of contributed papers, and a joint session with the Institute of the Aeronautical Sciences. The annual business session of the Division will be held on January 30, 1954. The final programme of the meeting will be published in a forthcoming Bulletin of the American Physical Society.

Suppression of Overtones of Thickness-Shear and Flexural Vibrations of Crystal Plates*

R. D. MINDLIN AND H. DERESIEWICZ
Department of Civil Engineering, Columbia University, New York, New York
(Received May 7, 1953)

It is shown how electrodes, coated on the surfaces of thickness-shear plates, may be shaped so that, when the driving frequency coincides with a particular resonant frequency, only that resonant mode is excited.

INTRODUCTION

ELECTRODES, coated on the surface of a piezoelectric crystal, may be shaped with either of two purposes in view. It may be desired, in the case of filters, to suppress resonances of all modes, except one, regardless of the frequency of the driving voltage. This problem has been considered by J. J. Vormer,[1] for longitudinal vibrations of a rod, and by J. A. Lewis[2] for coupled thickness-shear and flexural vibrations. On the other hand, in the case of oscillators, it is desirable that, when the driving frequency coincides with the appropriate resonant frequency, no other modes of motion be excited. In the present paper it is shown how this may be done in the case of coupled thickness-shear and flexural vibrations of plates, within the framework of Mindlin's[3] plate equations.

PLATE EQUATIONS

The thickness (h) of the plate is taken parallel to the y direction of a rectangular coordinate system, and only vibratory motion, independent of the z coordinate, at frequency ω, is considered. As shown in III and in an accompanying paper,[4] the equations of motion are then

$$\begin{aligned} D_1\xi''-D_6(\xi+h\eta')+F_1\varphi''-F_6\varphi_0+\rho\omega^2R\xi=0;\\ D_6(\xi'+h\eta'')+F_6\varphi_0'+\rho\omega^2h\eta=0;\\ (R+4\pi C_1)\varphi''-4\pi F_1\xi''=0, \end{aligned} \tag{1}$$

where primes indicate differentiation with respect to x, ξ and η are the tangential and normal components of displacement, φ is the electric potential, and φ_0 is the potential applied at the surface electrodes. The coefficients in Eqs. (1) are given by

$$\begin{aligned} &D_1=(c_{11}-c_{12}^2/c_{22})R; \qquad F_1=(e_{11}-c_{12}e_{12}/c_{22})R;\\ &D_6=\kappa_e^2c_{66}; \qquad F_6=\kappa_e^2e_{26};\\ &C_1=(\kappa_{11}+e_{12}^2/c_{22})R; \qquad R=h^2/12;\\ &\kappa_e^2=\alpha_e^2(1+e_{26}^2/c_{66}K_2)/3;\\ &K_i=(1+4\pi\kappa_{ii})/4\pi,\ i=1,2;\\ &\alpha_e=\tan^{-1}[\alpha_e(1+K_2c_{66}/e_{26}^2)],\ (1^{st}\text{ root}) \end{aligned}$$

in which c_{ij}, e_{ij}, κ_{ij} are the elastic, piezoelectric, and susceptibility coefficients, respectively.

Eliminating φ from Eqs. (1), we have

$$\begin{aligned} \omega_e^2Rg_e^{-1}\xi''+(\omega^2-\omega_e^2)\xi-\omega_e^2h\eta'=F_6\varphi_0/\rho R;\\ \omega_e^2h\eta''+12\omega^2h^{-1}\eta+\omega_e^2\xi'=0, \end{aligned} \tag{2}$$

where

$$\omega_e^2=D_6/\rho R,$$

$$g_e=R/S(1+J), \quad S=D_1/D_6,$$

$$J=\frac{(e_{11}-e_{12}c_{12}/c_{22})^2}{(c_{11}-c_{12}^2/c_{22})(K_1+e_{12}^2/c_{22})}.$$

If η is eliminated from Eqs. (2), the equation governing ξ is found to be

$$(d^2/dx^2+\delta_1^2)(d^2/dx^2+\delta_2^2)\xi=C\varphi_0, \tag{3}$$

where

$$C=F_6\omega^2g_e/\rho R^3\omega_e^4,$$

$$2(\delta_1^2,\ \delta_2^2)=S\delta_0^4\{1+g_e\pm[(1-g_e)^2+4g_e\omega_e^2/\omega^2]^{\frac{1}{2}}\},$$

$$\delta_0^4=\omega^2/RS\omega_e^2.$$

The boundary conditions for free edges $x=\pm l/2$ are

$$\left.\begin{aligned} M_x=D_1\xi'+F_1\varphi'=0;\\ Q_x=D_6(\xi+h\eta')+F_6\varphi_0=0, \end{aligned}\right\}\text{on } x=\pm l/2$$

and these reduce to

$$\left.\begin{aligned} \xi'=0;\\ \xi''+S\delta_0^4g_e\xi=0, \end{aligned}\right\}\text{on } x=\pm l/2. \tag{4}$$

Thus, the differential equation to be solved is Eq. (3) with boundary conditions (4).

ELECTRODE SHAPE

It may be seen, from Eqs. (2), that the applied potential, φ_0, plays the mechanical role of a tangential surface traction. Suppose, now, that the electrodes do not cover the surfaces of the plate completely, but have varying widths (in the z direction). Then, strictly speaking, some z-dependent motion will be produced which will be coupled with the x-dependent motion governed by Eqs. (3) and (4). However, if we neglect this coupling, the x-dependent motion will be as if forced by an electrode potential which varies with the x coordinate in proportion to the electrode width. To

* This investigation was supported by the U. S. Army Signal Corps Engineering Laboratories under a contract with Columbia University.

[1] J. J. Vormer, Proc. Inst. Radio Engrs. **39**, 1086–1087 (1951).

[2] J. A. Lewis, Bell Telephone Laboratories, Tech. Mem. MM 52-140-22, June 25, 1952.

[3] R. D. Mindlin, J. Appl. Mech. **18**, 31–38 (1951); J. Appl. Phys. **22**, 316–323 (1951), **23**, 83–88 (1952). These papers are referred to as I, II, and III.

[4] R. D. Mindlin and H. Deresiewicz, J. Appl. Phys. **24**, 21 (1953).

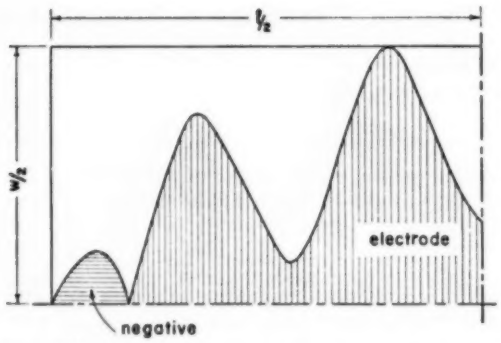

FIG. 1. Electrode shape for exciting the coupled mode comprised of the first thickness-shear mode and the ninth flexural mode ($n=1$, $r=9$; $l/h=6.992$, $\omega/\omega_c=1.037$).

this approximation, then, $\varphi_0=\varphi_0(x)$, where φ_0 is now proportional to the electrode width in the z direction.

Consider the function

$$\varphi_0=\varphi_1\cos\beta_1 x+\varphi_2\cos\beta_2 x, \tag{5}$$

where φ_1, φ_2, β_1, β_2 are constants. Substituting Eq. (5) in Eq. (3), we find that the differential equation has the particular integral

$$\xi=U_1\cos\beta_1 x+U_2\cos\beta_2 x, \tag{6}$$

provided

$$U_1=\frac{C\varphi_1}{(\beta_1^2-\delta_1^2)(\beta_1^2-\delta_2^2)},\qquad U_2=\frac{C\varphi_2}{(\beta_2^2-\delta_1^2)(\beta_2^2-\delta_2^2)}. \tag{7}$$

Now, δ_1 and δ_2 are functions of ω. Let β_1 be the value which δ_1 approaches as ω approaches a frequency ω'. Also, let β_2 be that value which δ_2 approaches as δ_1 approaches β_1. Then U_1 and U_2 approach infinity, but

$$\begin{aligned}\lim_{\omega\to\omega'}\left\{\frac{U_1}{U_2}\right\}&=-\frac{\varphi_1}{\varphi_2}\lim_{\omega\to\omega'}\left\{\frac{(\beta_2^2-\delta_2^2)}{(\beta_1^2-\delta_1^2)}\right\}\\&=-\frac{\varphi_1}{\varphi_2}\lim_{\omega\to\omega'}\left\{\frac{d\delta_2^2/d\omega^2}{d\delta_1^2/d\omega^2}\right\}\\&=\frac{\varphi_1}{\varphi_2}\frac{a^4(1+g_c)^2-g_c(1+a^2)^2}{(1+g_c)^2-g_c(1+a^2)^2},\end{aligned} \tag{8}$$

where $a=\delta_2/\delta_1=\beta_2/\beta_1$, and φ_1 and φ_2 are arbitrary for an infinite plate.

Considering, now, a finite plate of length l, the boundary conditions (4) give

$$U_1/U_2=a\sin a\gamma/\sin\gamma; \tag{9}$$

$$(a^2-g_c)\tan\gamma=a(1-a^2g_c)\tan a\gamma, \tag{10}$$

where $\gamma=\delta_1 l/2$. Hence, for a plate of finite length, it is necessary, from Eqs. (8) and (9), that

$$\frac{\varphi_1}{\varphi_2}=-\frac{a\sin a\gamma}{\sin\gamma}\frac{(1+g_c)^2-g_c(1+a^2)^2}{a^4(1+g_c)^2-g_c(1+a^2)^2}. \tag{11}$$

As shown in II and III, Eq. (10) is the secular equation for the free vibrations of the plate. The frequencies are obtained by selecting a value of a, which fixes the frequency at

$$\omega=\omega_c[1-a^2(1+g_c)^2/g_c(1+a^2)^2]^{-\frac{1}{2}}, \tag{12}$$

following which the roots, γ, of Eq. (10) are computed. Then the lengths corresponding to the chosen ω are found from

$$l/h=\gamma(\omega_c/\omega)[(1+a^2)/3(1+g_c)]^{\frac{1}{2}}. \tag{13}$$

Hence, the electrode shape

$$\varphi_0=\varphi_1\cos(2\gamma x/l)+\varphi_2\cos(2a\gamma x/l), \tag{14}$$

where φ_1/φ_2 is given by Eq. (11), excites only one normal mode, of frequency given by Eq. (12), of a plate whose length is given by Eq. (13).

The solution has been carried out for the antisymmetric modes. The same results are obtained for the symmetric modes (excited by split electrodes) except that sine and cosine are interchanged.

ALGEBRAIC FORMULAS

The secular equation (10) is satisfied by (see II and III)

$$\begin{aligned}\gamma&=r\pi/2, &&r=1,2,3,\cdots,\\ a\gamma&=n\pi/2, &&n=0,1,2,\cdots,\end{aligned} \tag{15}$$

where r and n are odd for the antisymmetric modes and even for the symmetric modes.

For the modes defined by Eqs. (15), the solution (14) takes the simple form

$$\varphi_0=\varphi_1\cos(r\pi x/l)+\varphi_2\cos(n\pi x/l) \tag{16}$$

for the antisymmetric modes and

$$\varphi_0=\varphi_1\sin(r\pi x/l)+\varphi_2\sin(n\pi x/l) \tag{17}$$

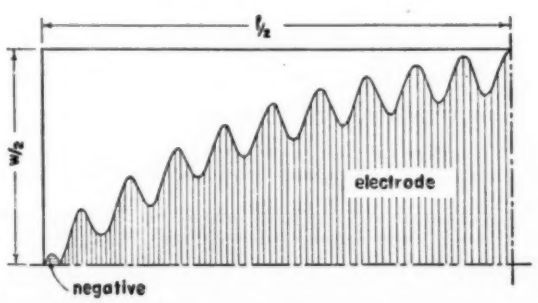

FIG. 2. Electrode shape for exciting the coupled mode comprised of the first thickness-shear mode and the thirty-ninth flexural mode ($n=1$, $r=39$; $l/h=31.176$, $\omega/\omega_c=1.002$).

for the symmetric modes, where

$$\frac{\varphi_1}{\varphi_2}\frac{n}{r}=-(-1)^{(3n+r)/2}\frac{r^4(1+g_c)^2-g_c(r^2+n^2)^2}{n^4(1+g_c)^2-g_c(r^2+n^2)^2}. \quad (18)$$

Examples of these shapes are shown in Figs. 1 and 2 for the AT cut of quartz, for which $g_c=0.283$.

The corresponding frequencies and lengths are given by

$$\omega/\omega_c=g_c^{\frac{1}{2}}(r^2+n^2)[(g_cr^2-n^2)(r^2-g_cn^2)]^{-\frac{1}{2}};$$
$$l/h=(\pi/2)[(g_cr^2-n^2)(r^2-g_cn^2)/3g_c(1+g_c)(r^2+n^2)]^{\frac{1}{2}}.$$

It may be seen that the first term in φ_0 has the mode shape of the flexural overtone and the second term in φ_0 has the mode shape of the thickness-shear overtone. That is, the first term has r half-waves and the second term n half-waves along the length of the plate. Generally, a low order thickness-shear mode is used in a thin plate. Then the coupling takes place with a high-order flexural mode, i.e., n/r is small. In this case

$$\frac{\varphi_1}{\varphi_2}\frac{n}{r}\approx-(-1)^{(3n+r)/2}\frac{(1+g_c)^2-g_c}{g_c}\ll 1,$$

so that the electrode has essentially the mode shape of the thickness-shear overtone, with its edge scalloped according to the mode shape of the flexural overtone, as illustrated in Fig. 2. For a given thickness-shear overtone (n) the amplitude of the scallop diminishes with increasing order of flexural overtone, i.e., with increasing length of the plate, as shown in Fig. 3.

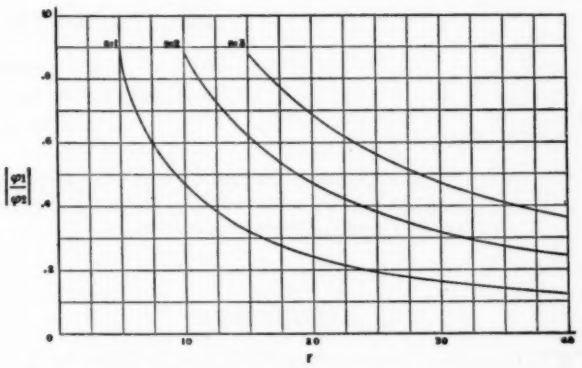

FIG. 3. Ratio of amplitudes of short and long wavelength portions of electrode shape as a function of the order (r) of flexural overtone, for various values of the order (n) of thickness-shear overtone.

ACKNOWLEDGMENT

We wish to acknowledge an illuminating discussion with Dr. J. A. Lewis.

JOURNAL OF APPLIED PHYSICS VOLUME 25, NUMBER 1 JANUARY, 1954

Ion Trajectories in the Omegatron*

CLIFFORD E. BERRY
Consolidated Engineering Corporation, Pasadena, California
(Received May 16, 1953)

The equations of motion for ions in an idealized two-dimensional Omegatron are solved for the general case of arbitrary initial velocity and arbitrary starting time. A simple picture of the paths is obtained by use of a rotating coordinate system.

I. INTRODUCTION

THE name "Omegatron"[1,2] has been given by J. A. Hipple and his co-workers to a type of mass spectrometer in which mass separation is achieved through the phenomenon of cyclotron resonance.

In the Omegatron an alternating electric field acts normal to a uniform magnetic field, so that ions having a natural frequency of rotation equal to the applied frequency receive energy from the electric field during each revolution. Ions whose natural frequency differs from the applied frequency will first gain energy, then suffer either a phase retardation or phase advance with respect to the applied electric field during each revolution; such ions will thus gain energy for a certain number of revolutions, then lose energy, then gain, etc. A resonant ion will travel in an orbit of continually increasing radius, whereas a nonresonant ion will travel in an expanding and contracting spiral orbit of limited size. An ion collector at suitable distance from the point of origin of the ions will collect only the resonant ions if all nonresonant ions are restricted to maximum excursions less than the distance from origin to collector.

The Omegatron obviously resembles the cyclotron; however, there is one important difference. Instead of accelerating the particles twice each revolution at the gaps between "Dee" electrodes, the Omegatron utilizes an essentially uniform electric field throughout the accelerating region. This eliminates harmonic effects and causes all particles of given mass to "bunch" in space, regardless of their starting phase.

This paper derives in detail the respective trajectories of resonant and nonresonant ions in the Omegatron, and points out a simple physical interpretation of the mathematical results.

II. SOLUTION OF THE EQUATIONS OF MOTION

In order to derive the trajectories of the ions in an Omegatron, a uniform alternating electric field with positive direction along the positive x axis, and a uniform magnetic field along the z axis will be assumed.† The uniformity of the fields implies zero forces in the z direction, so that only motions in the $x-y$ plane need be considered. The coordinate system used is shown in Fig. 1. The following symbols, in the mks system, are used:

B = magnetic field strength in webers per meter².
ω_0 = angular frequency of applied electric field in radians per second.
E = peak amplitude of electric field in volts per meter. The instantaneous electric field is $E\sin\omega_0 t$.
M = mass of an ion in kilograms.
e = the charge of the electron in coulombs (only singly charged ions will be considered).
ω = the natural frequency in radians per second of a particle with mass M, charge e, in a magnetic field strength of B. This is equal to eB/M radians per second.
u = initial velocity of a particle in the x direction in meters per second.
v = initial velocity of a particle in the y direction in meters per second.
$V=u+iv$ (initial velocity vector in the $x-y$ plane).
r = the radial distance from the origin to the collector in meters.
ϕ = the phase angle relating the time of origin of a particle to the phase of the applied electric field.
$\epsilon=\omega-\omega_0$ (the difference frequency).

The differential equations for the motion of a charged particle in the $x-y$ plane are readily found to be:

$$M\ddot{x}=eE\sin\omega_0 t+eB\dot{y} \tag{1}$$

$$M\ddot{y}=-eB\dot{x}, \tag{2}$$

where the dots represent time derivatives. These can be simplified by defining a quantity $\alpha=eE/M$, having units of meters per second². Further, it is noted that $eB/M=\omega$. Thus the equations can be rewritten

$$\ddot{x}=\alpha\sin\omega_0 t+\omega\dot{y}, \tag{3}$$

$$\ddot{y}=-\omega\dot{x}. \tag{4}$$

If we use as initial conditions $x=y=0$, $\dot{x}=u$, $\dot{y}=v$, for $\omega_0 t=\phi$, these equations can be readily solved in a straight-forward manner. Considerable simplification in writing the results, and in interpretation, is achieved by using complex notation; the complete solution is

* A preliminary version of this paper was presented at the American Physical Society meeting at Berkeley, California, December 27–29, 1951. See Phys. Rev. 85, 765 (1952).
[1] Hipple, Sommer, and Thomas, Phys. Rev. 76, 1877 (1949).
[2] Sommer, Thomas, and Hipple, Phys. Rev. 82, 697 (1951).
† A problem closely related to this one was solved by Truell in Proc. Inst. Radio Engrs. 46, 1249 (1948) and Proc. Inst. Radio Engrs. 37, 1144 (1949).

found to be

$$x+iy=i\frac{V}{\omega}[e^{-i\omega(t-\phi/\omega_0)}-1]$$
$$-i\frac{\alpha}{\omega_0^2-\omega^2}\left[\frac{\omega}{\omega_0}\cos\omega_0 t-i\sin\omega_0 t\right]$$
$$+i\frac{\alpha}{\omega_0^2-\omega^2}\left[\frac{\omega_0}{\omega}\cos\phi-i\sin\phi\right]e^{-i\omega(t-\phi/\omega_0)}$$
$$-i\frac{\alpha}{\omega_0\omega}\cos\phi. \quad (5)$$

The first term of Eq. (5) clearly is due to the initial velocity of the particle at the time of ionization. This term represents a circular path of radius $|V|/\omega$, passing through the origin, and tangent to the vector V. The second term represents an elliptical motion about the origin, with angular frequency ω_0, which is independent of the phase angle, and which approaches a circle as $\omega_0\rightarrow\omega$. The third term represents a circular motion about the origin, with angular frequency ω, the amplitude and phase of which depend upon the relative magnitudes of ω and ω_0, and upon the phase angle ϕ. The fourth term can be considered simply as a static shift, along the y axis, of the center of rotation. Since all of the terms are either constant or periodic in time, the maximum amplitude of the motion is bounded.

Equation (5), as it stands, does not describe the motion of a particle in resonance, i.e., one for which $\omega=\omega_0$. The path of a resonant particle can be derived explicitly either by solving Eq. (3) and (4) again with $\omega=\omega_0$, or by finding the limit of Eq. (5) as $\omega_0\rightarrow\omega$. The latter is perhaps preferable, since simultaneously a simple expression for the paths of particles nearly in resonance is obtained. Setting $\epsilon=\omega-\omega_0$ in Eq. (5) and rearranging, there results

$$x+iy=[(iV)/(\omega_0+\epsilon)][e^{-i(\omega_0+\epsilon)(t-\phi/\omega_0)}-1]$$
$$+\frac{i\alpha}{(2\omega_0+\epsilon)\epsilon}\left\{\left[1-\left(1-\frac{\epsilon e^{i\phi}\cos\phi}{\omega_0+\epsilon}\right)e^{-i\epsilon(t-\phi/\omega_0)}\right]e^{-i\omega_0 t}\right.$$
$$\left.+(\epsilon/\omega_0)(\cos\omega_0 t)-[(2\omega_0+\epsilon)\epsilon/(\omega_0+\epsilon)\omega_0](\cos\phi)\right\}. \quad (6)$$

If we expand $\exp\{-i\epsilon(t-\phi/\omega_0)\}$, which occurs within the square bracket in Eq. (6), in a power series in ϵ, the apparent singularity disappears, and the equation for a resonant particle is found to be

$$x+iy|_{\omega_0=\omega}=(iV/\omega_0)(e^{-i\omega_0(t-\phi/\omega_0)}-1)$$
$$-[\alpha/(2\omega_0^2)][\omega_0 t-\phi-ie^{i\phi}\cos\phi]e^{-i\omega_0 t}$$
$$+(i\alpha/2\omega_0^2)(\cos\omega_0 t)-(i\alpha/\omega_0^2)(\cos\phi). \quad (7)$$

In Eq. (7), a rigorous expression for the path of an ion in resonance, the first term is identical to that for the general case and represents simply a superimposed circular motion due to initial velocity. The second term represents a spiral motion due to the appearance of t in the amplitude of the exponential. It is apparent that after a few cycles, the other terms within the bracket become negligible compared to $\omega_0 t$. The third term is simply a small sinusoidal oscillation of the center of rotation along the y axis, and the last term represents a small shift of the apparent center of rotation along the y axis. These latter terms are likewise negligible after a few cycles, so that, neglecting the initial velocity, the motion of a particle in resonance closely approaches an Archimedes spiral.

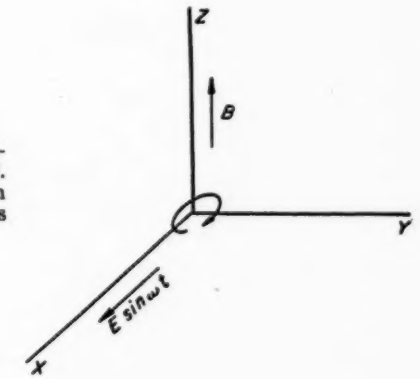

FIG. 1. The coordinate system used. The sense of rotation for a positive ion is shown.

It is interesting to note in Eq. (7) that no harmonic effects exist; i.e., no ions other than those having a unique mass defined by Eq. (7) can continue to gain energy without limit. In the cyclotron, by contrast, particles not only of mass m, the resonant mass, but also $3m$, $5m$, etc., can appear at the accelerating gaps at the proper times to receive energy. The lack of harmonic effects in the Omegatron can be attributed to the fact that the particles are in the accelerating field at all times.

III. CONDITIONS NEAR RESONANCE

In the vicinity of resonance, where $\omega_0\approx\omega$, i.e., $\epsilon\ll\omega_0$, Eq. (6) can be reduced to a simple form. If we consider particles of zero initial velocity, there results

$$x+iy|_{\epsilon\ll\omega_0}\cong\{i\alpha/[(2\omega_0+\epsilon)\epsilon]\}(1-e^{-i\epsilon(t-\phi/\omega_0)})e^{-i\omega_0 t}. \quad (8)$$

If, now, the motion is considered with reference to a coordinate system rotating clockwise with angular velocity ω_0, the particle is seen to take a circular path tangent to the origin, with angular frequency ϵ. For ϵ positive ($\omega>\omega_0$) the center of the circle is on the positive y axis of the rotating system, and for ϵ negative ($\omega<\omega_0$) the center is on the negative y axis. If we take the limit in Eq. (8) as resonance is approached ($\epsilon\rightarrow 0$), and neglect the phase angle, the motion *in the rotating system* is seen to be

$$x+iy=-\alpha t/2\omega_0, \quad (9)$$

which represents a uniform velocity along the negative

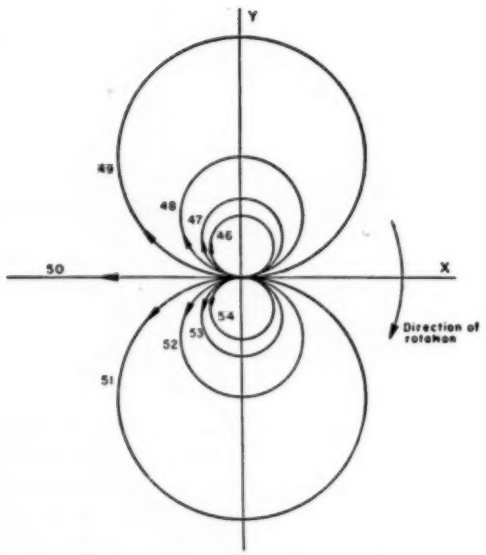

FIG. 2. The paths of a number of ions in the rotating coordinate system when ions of mass 50 are in resonance.

x axis. Reference to the coefficient of the linear term in t in Eq. (7) shows that Eq. (9) is correct.

The foregoing approximate treatment thus provides a simple picture of the operation of the Omegatron. In a coordinate system rotating with the frequency of the applied electric field, ions in resonance travel at uniform velocity along the x axis, lighter ions (higher frequency) travel in circular paths centered on the positive y axis and tangent to the origin, while heavier ions travel in similar circles centered on the negative y axis (Fig. 2). Varying the applied frequency continuously from a value below the resonant frequency will cause the radius of the circular path to increase from a finite value to inifinity at resonance, and then to decrease to a finite value on the other side of resonance. At the same time, as resonance is crossed, the center of the circular path moves from one side of the origin to the other.

IV. FORMATION OF "SPOKES"

If we return to Eq. (7), and again neglect the initial velocity, it is apparent that particles of a given phase angle can be considered as having radial motion in a coordinate system rotating with angular velocity ω_0, and oscillating slightly in the y direction with frequency ω_0 about a center determined by the phase angle. Since $\omega_0 t$ eventually becomes large relative to all other terms, all resonant particles rotate about the origin in a well-defined region analogous to a spoke in a wheel. A simple illustration of this fact is obtained by evaluating Eq. (7) at an instant in time corresponding to an integral number of revolutions, and finding the relative positions of particles of different phase. If we set $\omega_0 t = 2n\pi$, it is found that

$$x|_{\omega_0 t=2n\pi} = -(\alpha/2\omega_0^2)(2n\pi - \phi + \cos\phi \sin\phi) \quad (10)$$

$$y|_{\omega_0 t=2n\pi} = (\alpha/2\omega_0^2)(\cos\phi - 1)^2. \quad (11)$$

Similar calculations for other instants in time give results which differ only in detail. Figure 3 shows the configuration of the "spoke" at four instants during one cycle.

It is significant that all resonant ions formed during a single cycle reach a given amplitude within the time interval of one period; in other words, no given time of formation is less advantageous than another.

By the same reasoning, nonresonant ions of given mass but differing phase angle are seen to lie in a roughly circular bundle. In Eq. (6) ions of a given phase angle can be considered as taking a circular path in a coordinate system rotating with angular frequency ω_0, and oscillating in the y direction at the same frequency about a center position dependent upon the phase angle. The diameter of the circle along which each ion moves is a function of its phase angle. Thus the circular paths corresponding to different phase angles have different radii and different centers, becoming more nearly coincident as resonance is approached. Figure 4 illustrates these paths for the case $\epsilon = 0.11\omega_0$.

V. EFFECT OF A SUPERIMPOSED DC FIELD

If a dc field of strength E' volts/meter is superimposed upon the alternating field, a cycloidal motion obviously will be superimposed upon the trajectory given in Eq. (5). If E' is small compared with E, the principal effect of the dc field is to cause all ions, regardless of mass, to drift down the negative y axis at an average velocity of E'/B meters/second. If we substitute for α and ω_0 in Eq. (7), the rate of increase in radius of a particle in resonance is exactly $E/2B$, so that if $E' < E/2$, resonant ions will continue to move outward along the positive y axis. If a collector is placed on the positive y axis, resonant ions can be collected on it while all nonresonant ions continuously drift away in the opposite direction. Thus the use of a small superimposed dc field in the Omegatron offers a

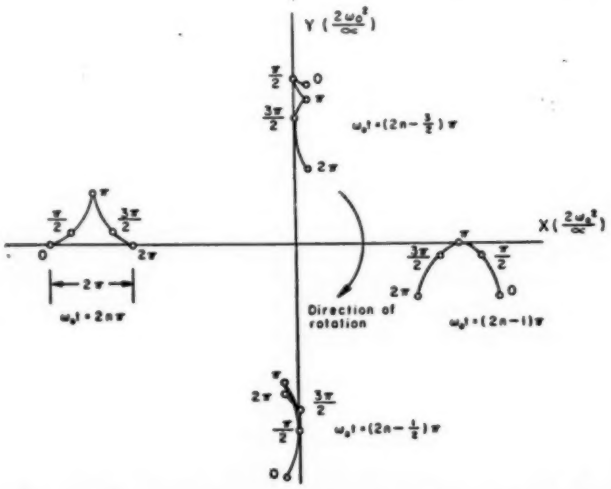

FIG. 3. Positions of resonant ions formed at various times during one period of the alternating field, shown at quarter-cycle intervals.

practical means of continuously removing ions from the ionizing region so as to prevent the buildup of a large space charge.

VI. OTHER PROPERTIES OF THE OMEGATRON

Sommer, Thomas, and Hipple[2] have given expressions for resolving power, path length, and number of revolutions of a resonant particle. For completeness, these will be derived here from the foregoing expressions for the particle trajectories. To simplify the problem, particles will be assumed to have zero initial velocity and zero phase angle.

The resolving power ρ is defined as $M/\delta M$ or $\omega_0/\delta\omega$, where δM or $\delta\omega$ corresponds to the base width of a peak in appropriate units. Ions of a given mass will be collected throughout a frequency range of $\omega_0-\epsilon$ to $\omega_0+\epsilon$, so long as the maximum amplitude of their motion, $2\alpha/(2\omega_0+\epsilon)\epsilon$, from Eq. (8) is equal to or greater than r, the distance to the collector. Clearly, $\delta\omega=2\epsilon$, so that $\delta\omega$ is determined by

$$r=2\alpha/(2\omega_0+\epsilon)\epsilon\cong 2\alpha/\omega_0\delta\omega, \tag{12}$$

in which it is assumed that $\epsilon\ll 2\omega_0$. Then, from the definition of ρ,

$$\rho\cong r\omega_0^2/2\alpha \tag{13}$$

or, upon substitution for α and ω_0,

$$\rho\cong reB^2/2EM. \tag{14}$$

The effect of initial velocity on resolving power can be found in similar manner. Since initial velocity can take any direction, the maximum amplitude, $|2V|/(\omega_0+\epsilon)$, of the first term of Eq. (6) can be added directly to the maximum amplitude given by Eq. (8). Then it is found that

$$\rho\cong(r-2|V|/\omega_0)\omega_0^2/2\alpha. \tag{15}$$

Thus, the effect of initial velocity is to diminish the physical radius by an amount equal to the diameter of the circular path due to initial velocity.

The approximate number of turns, N, required for a resonant particle to reach the collector is obtained by setting the time-dependent amplitude term of Eq. (7) equal to the radius r:

$$r=\alpha t/2\omega_0. \tag{16}$$

If we set $\omega_0 t=2N\pi$,

$$r=\alpha N\pi/\omega_0^2, \tag{17}$$

from which

$$N=\omega_0^2 r/\alpha\pi. \tag{18}$$

If we substitute from Eq. (15),

$$N=2\rho/\pi. \tag{19}$$

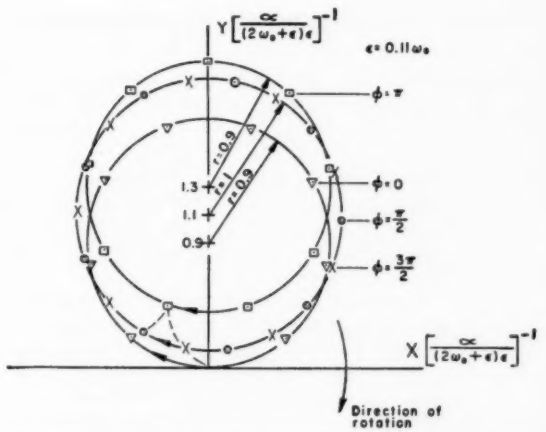

FIG. 4. Positions of a group of nonresonant ions of the same mass but differing phase angles, showing bunching action. The dotted line is the locus of all particles formed during one period of the alternating field.

In other words, the number of turns required for resonant particles to reach the collector is equal to roughly $\frac{2}{3}$ the resolving power.

The approximate path length L can likewise be expressed in simple form. To a first approximation, the length of an Archimedes spiral is equal to the average circumference times the number of turns. In the Omegatron, the average circumference is πr, so that

$$L\cong N\pi r. \tag{20}$$

If we substitute for N from Eq. (19),

$$L\cong 2r\rho. \tag{21}$$

Thus the path length is approximately equal to the product of the diameter and the resolving power.

VII. CONCLUSION

The foregoing mathematical treatment gives in detail the trajectories of ions in a two-dimensional Omegatron, describes a simple interpretation of the trajectories, and derives various properties of the device. While a practical Omegatron is a three-dimensional device, in which means for axial trapping of the ions must be provided,[2] it is felt that the treatment presented here will be useful in designing instruments and in interpreting experimental results.

ACKNOWLEDGMENTS

The author is indebted to Dr. P. A. Shaffer for his suggestion of the use of complex notation, to Drs. H. W. Washburn, C. F. Robinson, and W. M. Brubaker for many helpful discussions, and to Miss Betty Walkey for critical review of the manuscript.

JOURNAL OF APPLIED PHYSICS VOLUME 25, NUMBER 1 JANUARY, 1954

Space Charge Waves in Inhomogeneous Electron Beams

GORDON KENT
Cruft Laboratory, Harvard University, Cambridge, Massachusetts
(Received May 19, 1953)

A magnetically confined sheet electron beam filling the space between two plane parallel electrodes is discussed. It is assumed that the average electron space charge is not neutralized by positive ions so that the potential at the center is depressed, and the beam is inhomogeneous in velocity and charge density. The objective of this theoretical treatment is to determine whether or not exponentially growing space charge waves can be supported by such a beam.

For small inhomogeneity and continuous behavior of all quantities as functions of the inhomogeneity, it is shown that growing waves are not possible. This conclusion is supported by discussion of the analogous adjacent beam problem and the analogous velocity distributed filamentary beam. Although the adjacent beams can support growing waves, it is argued that the analogy is not valid because the adjacent beams cannot be obtained by a continuous perturbation of a single homogeneous beam. The analogy of the velocity distributed beam does not suffer from this deficiency. In this case it is shown that growing space charge waves cannot exist unless the distribution function has more than one relative maximum.

I. INTRODUCTION

IN the published literature on space charge waves in electron beams[1-3] of the sort employed in velocity modulated electronic tubes, it has been assumed that the average space charge density of the electrons is neutralized by the presence of positive ions in the beam. For *CW* tubes employing grids at the ends of the drift space, persuasive argument can be advanced to justify this assumption, but for gridless tubes and pulsed tubes the absence of positive ions appears to be a better assumption. Without grids, there is no ion trapping so that the ions tend to drift out of the beam to the cathode, and for pulsed tubes there may be insufficient time for the formation of a positive ion core.

Without positive ion neutralization, the potential at the center of the beam is depressed by the electron space charge with the result that the velocity at the center is less than the velocity at the edges. It was claimed by A. V. Haeff[3] that this inhomogeneity of the beam would lead to exponentially growing space charge waves of the same sort that occur in the two beam electron wave tube, but to the knowledge of this author, a satisfactory analytical affirmation or denial of Dr. Haeff's assertion has not as yet been published. Since the question of whether or not growing waves can be supported by the inhomogeneous beam is of some importance in connection with electron wave tubes, as well as to problems of beam instability and noise, it is the author's primary purpose to determine the kind of wave propagation constants which can be found.

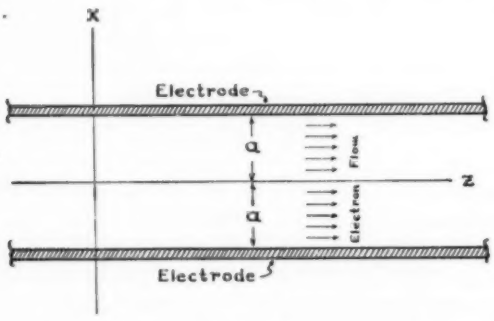

FIG. 1. Geometry of the inhomogeneous beam.

II. FORMULATION OF THE PROBLEM

Rather than attempt to discuss the electron beam in a typical tube, a highly simplified model is used in order to make the analysis tractable. As shown in Fig. 1, a sheet beam, infinite in the y and z directions, completely filling the space between two perfectly conducting plane electrodes located at $x=a$ and $x=-a$, is postulated. The electron flow is assumed to be in the z direction only. In order that such a beam can exist, it must be assumed that a very large magnetic field is applied in the z direction so that the beam is magnetically confined. The dc current density of the beam is assumed to be constant while the dc potential, charge density, and velocity may be functions of x alone. Velocities are taken to be non-relativistic. For the rf terms, it is assumed that some sort of coupling devices are located at two values of z.

It is useful in the analysis to admit the presence of positive ions in the beam, in which case it is assumed that the positive ions have the same spacial distribution as the electrons and that they are immobile. The parameter σ is introduced as the measure of inhomogeneity, varying from zero for the neutralized beam to unity for the complete absence of ions. The magnitude of the ratio of ion density to electron density is $(1-\sigma)$.

Finally it is assumed that the difference between center and edge velocities is small compared to the center velocity, even when σ is put equal to one, and that rf quantities are sufficiently small to permit linearization of all equations.

While an exact solution for the dc quantities of the beam can be obtained, this is an irrational function of x

[1] E. Feenberg, Sperry Gyroscope Company Report No. 5221-1043 (1945).
[2] S. Ramo, Proc. Inst. Radio Engrs. 27, 757-763 (1939).
[3] A. V. Haeff, Proc. Inst. Radio Engrs. 37, 4-10 (1949).

and consequently is of little use. For this reason, the following approximate relationships will be used in subsequent analysis:

$$V(x)=V(0)[1+\sigma h_0^2x^2], \tag{1}$$

$$u(x)=u_0[1+\tfrac{1}{2}\sigma h_0^2x^2], \tag{2}$$

$$\rho_0(x)=\rho_0(0)[1-\tfrac{1}{2}\sigma h_0^2x^2], \tag{3}$$

where $V(x)$ = the dc potential, $u(x)$ = the dc velocity, and $u(0)=u_0$, $\rho_0(x)$ = the electron charge density, taken as a positive quantity, $h_0=h(0)$ = the plasma wave number $=(1/u_0)(\eta\rho_0(0)/\epsilon_0)^{\frac{1}{2}}$, η = charge to mass ratio of the electron, and ϵ_0 = permitivity of free space.

Since it is known that wave-like solutions for the rf quantities in the homogeneous or neutralized beam are found to exist, it is assumed for this case that all rf quantities may be represented by some function of x alone multiplied by $\exp[i(\omega t-\gamma z)]$, where ω is the angular frequency and γ is the propagation constant. The assumption that electron motion is one dimensional, implies that the velocity, current density, and retarded vector potential are vectors having only z components. Accordingly, the rf quantities will be denoted as follows:

Retarded scalar potential $=\phi(x)e^{i(\omega t-\gamma z)}$,
Rf electron charge density $=\rho(x)e^{i(\omega t-\gamma z)}$,
Rf velocity, z component $=v(x)e^{i(\omega t-\gamma z)}$,
Retarded vector potential, z component $=A(x)e^{i(\omega t-\gamma z)}$,
Rf current density, z component $=-[\rho_0(x)v(x)+\rho(x)u(x)]e^{i(\omega t-\gamma z)}$.

By virtue of the small signal assumption, the expression for current has been linearized by dropping second order terms in rf quantities.

Maxwell's equations are identically satisfied providing

$$d^2\phi/dx^2+(k^2-\gamma^2)\phi=\rho/\epsilon_0, \tag{4}$$

$$d^2A/dx^2+(k^2-\gamma^2)A=\mu_0(\rho_0v+\rho u), \tag{5}$$

and

$$\gamma A=(\omega/c^2)\phi, \tag{6}$$

where

c = velocity of light,
$k=\omega/c=2\pi/\lambda$,
μ_0 = magnetic permeability of free space.

The *gauge* Eq. (6) is equivalent to the equation for the conservation of charge. The dynamic equation, which completes the system (4), (5), and (6), contains both x and z components, but the assumption of a large focussing magnetic field permits one to ignore the effects of forces exerted in the x direction. The z component of the equation for nonrelativistic velocities is

$$(\omega-\gamma u)v=\eta(\omega A-\gamma\phi), \tag{7}$$

where the left-hand member, the total time derivative of the velocity, has been linearized in accordance with the small signal assumption.

Separation of dependent variables in the system (4), (5), (6), and (7) leads to the following differential equation for the scalar potential

$$d^2\phi/dx^2+(k^2-\gamma^2)[1-(h/k'-\gamma)^2]\phi=0, \tag{8}$$

where

$$k'=(\omega/u),$$
$$h^2=(\eta\rho_0/\epsilon_0u^2).$$

The coefficient multiplying $\phi(x)$ in (8), as an explicit function of σ, x, and γ, is

$$F(\sigma x^2,\gamma)=(k^2-\gamma^2)\left\{1-\frac{h_0^2(1-\frac{3}{2}\sigma h_0^2x^2)}{[k_0(1-\frac{1}{2}\sigma h_0^2x^2)-\gamma]^2}\right\}, \tag{9}$$

where second-order terms in σ have been dropped from the numerator but not from the denominator, for reasons which will become clear in subsequent discussion.

Since $F(\sigma x^2,\gamma)$ is an even function of x, it follows that the solutions of (8) may be classed as even or odd functions. The odd solutions, however, are of no physical importance because they cannot be energetically coupled to any symmetric modulating or demodulatlng structure. The desired solutions, therefore, must be even functions and must satisfy the boundary condition $\phi(\pm a)=0$, which implies that the z component of the electric field vanishes at the electrodes.

For the neutralized beam, $\sigma=0$, F becomes a function of γ only, and (8) is satisfied by $\cos\{x[F(0,\gamma)]^{\frac{1}{2}}\}$. The boundary conditions are met providing

$$F(0,\gamma)=[(2n+1)\pi/2a]^2, \quad n=0,1,2,\cdots. \tag{10}$$

For each value of n, Eq. (10) is of fourth degree in γ, and the four solutions correspond to two TM waves and two space charge waves. Assuming that $2a\ll\lambda$, the TM waves are sharply attenuated and the presence of the electron-ion plasma has only a second order effect on their propagation constants. Any inhomogeneity of the beam, therefore, can cause at most a third order effect on these waves. For the space charge waves, γ is of the order of magnitude of k', as the following relationship indicates:

$$\gamma\cong k_0\pm h_0/\{1+[(2n+1)\pi/2ak_0]^2\}^{\frac{1}{2}}. \tag{11}$$

Accordingly, for the space charge waves in the inhomogeneous beam, it is reasonable to assume that $|\gamma|\sim k'$, a condition which permits simplification of (9) by dropping k^2 from the first bracket but gives no justification for removing σ from the denominator in the second bracket. On the basis of the neutralized beam solutions, it may be further supposed that the inhomogeneous beam solutions may be characterized by a number, n, which indicates the number of zero's of the solution in the interval $(0, a)$. At a small sacrifice of generality, a facility in notation is achieved by confining the discus-

sion henceforth to inhomogeneous beam solutions having no internal zeros.

For complex values of γ having the assumed order of magnitude, $F(\sigma x^2, \gamma)$ is a complex function as will be the corresponding solution of (8). The problem, therefore, is to determine the even solution of (8), considered as an equation in the complex domain; and from the requirement that the solution vanishes at $x=a$ on the real axis but at no interior point of the interval $(-a, a)$ of the real axis, the values of γ are to be found.

III. THE APPROXIMATE DIFFERENTIAL EQUATION AND ITS SOLUTION

By the transformation $x^2=\xi$, Eq. (8) is put in a form having one elementary, one regular, and one irregular singularity; this is a confluent form of an equation having at least six elementary singularities. Since the generalized Lamé equation has only five elementary singularities, it follows that the exact solution of (8) or any transformed equivalent cannot be expressed in closed form in terms of the known functions of mathematical physics. In fact, Ince[4] has shown that the exact solution is expressible as an infinite series of Mathieu functions. For this investigation, a literal rather than numerical solution is required, and Ince's results are consequently of little use.

In view of the preceding considerations, it becomes necessary to choose some method for approximating the solution. This choice is made difficult by the fact that the singularities of the equation depend on the unknown parameter, γ, and one has insufficient knowledge of the behavior of $F(\sigma x^2, \gamma)$ to justify the assumptions necessary for application of the WKB or perturbation methods. Nevertheless, from necessary conditions contingent to the existence of a solution one can obtain some limits on the possible values of γ, and from these in addition to physical considerations a third approximation method can be justified.

First of all, it is almost a trivial observation that the poles of $F(\sigma x^2, \gamma)$ cannot occur in the closed interval of the real axis $(-a, a)$. Furthermore, when γ is complex it is easily shown that

$$\int_{-a}^{+a} F_1|\phi|^2dx=\int_{-a}^{+a}|d\phi/dx|^2dx; \tag{12}$$

$$\int_{-a}^{+a} F_2|\phi|^2dx=0, \tag{13}$$

where

$$F_1=R[F(\sigma x^2, \gamma)],$$
$$F_2=Im[F(\sigma x^2, \gamma)].$$

From these necessary conditions it follows that real values of γ are limited by

$$\left.\begin{array}{l} k_0+h_0>\gamma>k_0 \\ \\ k_1>\gamma>k_1-h_1 \end{array}\right\} \quad \text{or} \tag{14}$$

where

$$k_1=k'(a),$$
$$h_1=h(a).$$

When γ is complex having modulus Γ and argument θ, it can be shown that

$$\left.\begin{array}{l} \Gamma^2\sin^2\theta<\Gamma(h_0k_0)^{\frac{1}{2}} \\ \Gamma<k_0 \\ \\ \Gamma>k_1 \end{array}\right\} \quad \text{or} \tag{15}$$

More precise limits than are given in (14) and (15) are implied by the necessary conditions, but the task of obtaining them explicitly becomes prohibitively difficult. The relationship (15) is not sufficient to show either that $F(\sigma x^2, \gamma)$ is a slowly varying function or that it may be expanded in a Taylor series, convergent for values of x in the $(-a, a)$ interval; in fact, (15) suggests the possibility that the exact opposite is true. Nevertheless, the fact that $F(\sigma x^2, \gamma)$ has no poles on the relevant portion of the real axis implies that the function may be expressed by an interpolation formula to any desired degree of accuracy.

Of the many formulas, the most apt is the Stirling formula for center interpolation. If it be required that the approximate function, $G(\sigma x^2, \gamma)$, equals $F(\sigma x^2, \gamma)$ at the points $(-a; 0; a)$, then

$$G(\sigma x^2, \gamma)=F(0, \gamma)+[F(\sigma a^2, \gamma)-F(0, \gamma)]x^2/a^2. \tag{16}$$

Providing $F(\sigma x^2, \gamma)$ is monotonic in each half of the interval, which is true for real γ, G should be a good approximation. Since F may be interpreted as an admittance, as will be shown subsequently, it seems physically reasonable to assume such a monotonic behavior. Equation (8) may then be replaced by the approximate equation

$$\frac{d^2\phi}{dx^2}+G(\sigma x^2, \gamma)\phi=0. \tag{17}$$

Equation (17) has the form

$$\frac{d^2\phi}{dx^2}+[\beta(1-4\alpha)-\beta^2x^2]\phi=0. \tag{18}$$

The even solution of (18) is known[5] to be

$$\phi(x)=e^{-\beta x^2/2}{}_1F_1(\alpha, \tfrac{1}{2}, \beta x^2), \tag{19}$$

where the parameters α and β are determined by comparison of (17) and (18). The function ${}_1F_1$ is the confluent hypergeometric or Kummer function, defined by the series

$${}_1F_1(\alpha, \tfrac{1}{2}, \beta x^2)=\sum_{n=0}^{\infty}\frac{(2n)!(\alpha)_n}{2^{2n}(n!)^2}(\beta x^2)^n, \tag{20}$$

[4] E. L. Ince, Proc. Roy. Soc. Edinburgh **A41**, 94–99 (1923).

[5] J. R. Airey and H. A. Webb, Phil. Mag. **36**, 137–141 (1918)

where

$$(\alpha)_n = \prod_{k=0}^{k=n+1} (\alpha+k).$$

IV. EVALUATION OF THE PROPAGATION CONSTANTS

The values of γ must be determined by setting (19) equal to zero when $x=a$ and then solving this equation simultaneously with the defining relations of the new parameters. Thus the system to be solved is

$$\left.\begin{aligned} &\epsilon^{-\beta a^2/2}{}_1F_1(\alpha, \tfrac{1}{2}, \beta a^2)=0 \\ &\beta(1-4\alpha)=F(0,\gamma) \\ &(a\beta)^2=F(0,\gamma)-F(\sigma a^2,\gamma) \end{aligned}\right\}. \quad (21)$$

Since the first line of (21) contains a transcendental function which is only partially tabulated, no further progress can be made toward a determination of the propagation constants without first converting the Kummer function into some kind of rational expression.

For the homogeneous beam, $\beta\to 0$ and $\alpha\to-\infty$ in such a way that $-4\alpha\beta\to(\pi/2a)^2$, and the solution (19) becomes a cosine function. It appears, therefore, that the assumptions appropriate for small beam inhomogeneity are

$$\left.\begin{aligned} &|a^2\beta|^2 \ll 1 \\ &|\alpha| \gg 1 \\ &-4\alpha\beta\sim(\pi/2a)^2 \end{aligned}\right\}. \quad (22)$$

In the choice of the approximation method, it was hoped to avoid the assumption of the first line of (22) that the total variation of F be small, because of lack of complete *a priori* justification, but the assumption is evidently necessary unless one is to proceed by numerical methods.

If the solution (18) in a power series in β and terms of order three and higher are discarded, the top line of (21) becomes

$$f(q,\beta)=\cos q-\left(\frac{a^2\beta}{2}\right)\frac{\sin q}{q}+\tfrac{1}{2}\left(\frac{a^2\beta}{2}\right)^2 \times\left[4\frac{\sin q}{q}+\frac{\cos q}{q^2}-\frac{\sin q}{q^3}\right]=0, \quad (23)$$

where $q^2=-4\alpha\beta a^2$. In principle, (23) can be solved explicitly for q, and this result can then be developed in another power series in β, the coefficients of which may be evaluated from (23) by the rule for differentiating an implicit function. The lower order terms obtained by this procedure are

$$q=(\pi/2)-(1/\pi)(a^2\beta) +(1/\pi)[(1/3)-(3/\pi^2)](a^2\beta)^2. \quad (24)$$

When (24) is squared and higher order terms omitted, the system (21) becomes

$$\left.\begin{aligned} q^2&=(\pi/2)^2-(a^2\beta)+[(1/3)-(2/\pi^2)](a^2\beta)^2 \\ q^2+a^2\beta&=a^2F(0,\gamma) \\ (a^2\beta)^2&=a^2F(0,\gamma)-a^2F(\sigma a^2,\gamma) \end{aligned}\right\}. \quad (25)$$

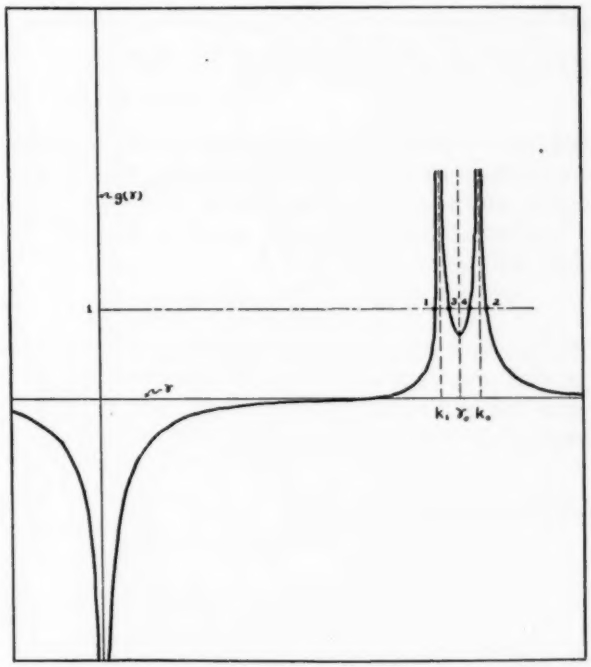

FIG. 2. Graphical representation of the roots of Eq. (26).

The elimination of q and β from (25) leads to a sixth degree equation in γ which is of the same form as the equation which occurs for two perfectly mixed beams in the same geometry. Two of the roots of this equation,

$$(1-\delta)(h_0/k_0-\gamma)^2+\delta(h_1/k_1-\gamma)^2-(\pi/2a\gamma)^2=1, \quad (26)$$

where $\delta=(1/3)-(2/\pi^2)$, correspond to field waves and are of no concern here. The remaining four roots are space charge waves. In Fig. 2, the left-hand side of (26), represented as $g(\gamma)$, is plotted as a function of γ. The intersections of this curve with the horizontal line unit distance above the axis constitute these four roots, designated γ_1, γ_2, γ_3, and γ_4. Evidently γ_3 and γ_4 are not admissible solutions as shown because they are inconsistent with (14). If γ_3 and γ_4 are to be admissible at all, the corresponding intersection points must appear in complex space. The condition for complex values of $\gamma_{3,4}$ is simply

$$g(\gamma_0)>1, \quad (27)$$

where

$$\gamma_0\cong(k_0k_1)^{\frac{1}{2}}.$$

Since $g(\gamma)$ is a monotonically decreasing function for $k_0<\gamma$ and since $g(k_0)\to+\infty$, it follows that γ_2 will be a real solution satisfying the inequality $(k_0+h_0)>\gamma_2>k_0$, providing $g(k_0+h_0)<1$. By a similar argument, $k_1>\gamma_1>(k_1-h_1)$ providing $g(k_1-h_1)<1$. Since

$$g(k_0+h_0)=1-\{\delta[1-(h_1/k_0-k_1+h_0)^2] +[\pi/2a(k_0+h_0)]^2\}, \quad (28)$$

and the bracketed term of (28) is positive, the first of the above provisions is true without restriction. At

$\gamma=(k_1-h_1)$,

$$g(k_1-h_1)=1-\{(1-\delta)[1-(h_0/k_0-k_1+h_1)^2]+[\pi/2a(k_1-h_1)]^2\}, \quad (29)$$

and the fact that the bracketed term of (29) is positive implies that the second provision is true. Thus it is seen that γ_1 and γ_2 are always consistent with (14).

To check the consistency of γ_1 and γ_2 with (22), it is observed that

$$(a^2\beta)^2=[a^2F(0,\gamma_{1,2})-(\pi/2)^2](1/\delta) \quad (30)$$

does not explicitly depend on the inhomogeneity parameter, but only implicitly through γ_1 and γ_2. If (30) is expanded in a power series in σ, the first term of the series vanishes and the second term is

$$(a^2\beta)^2\cong(2/\delta)(a\gamma_h)^2\left(\frac{k_0}{k_0-\gamma_h}\right)\times\left[\left(\frac{\pi}{2a\gamma_h}\right)^2+\frac{\gamma_h}{k_0}\right]\frac{1}{\gamma_h}\frac{d\gamma_{1,2}}{d\sigma}\bigg|_{\sigma=0}\sigma, \quad (31)$$

where γ_h = value of γ taken from (11) for the neutralized beam. Providing $\gamma_{1,2}$ is a differentiable function of σ, and there is no reason to suppose the contrary, then (31) shows that the total change of the function $F(\sigma x^2,\gamma)$ from the center to the outside of the beam may be made as small as desired by choosing σ sufficiently small. The solutions γ_1 and γ_2 are thus consistent with the assumptions of (22) and they satisfy the necessary conditions (14), permitting the conclusion that two ordinary (not exponentially growing) space charge waves exist in a beam with small inhomogeneity.

The complex propagation constants may be explicitly obtained by making use of the assumption that $\Gamma\sim\gamma_0$ and that the inhomogeneity is sufficiently small so that $[\sigma(ah_0)^2/2(1-\delta)^{\frac{1}{2}}]\ll 1$. Under these conditions, the two lowest order terms of Eq. (26) lead to a quadratic equation in γ with the complex solutions

$$\gamma_{3,4}=k_1[1+\tfrac{1}{2}\delta\sigma(ah_0)^2\pm i\tfrac{1}{2}\sigma(ah_0)^2(\delta(1-\delta))^{\frac{1}{2}}]. \quad (32)$$

The solutions appear to be consistent with the necessary conditions of (15), although it is difficult to say conclusively because of the many approximations made, but substitution of $\gamma_{3,4}$ into the expression for $(a^2\beta)^2$ gives the result

$$|a^2\beta|^2\sim 32/\sigma(ah_0)^2. \quad (33)$$

Since (33) is evidently much greater than one, the assumptions of (22) are grossly violated, and these results must be discarded as inconsistent.

Although two admissible space charge wave propagation constants have been obtained by making an assumption which renders the problem tractable, superficially there appears to be no reason why an infinity of alternate assumptions could not have been made and corresponding propagation constants determined and verified by the consistency requirement. Such a procedure, however, is mathematically prohibitive, and one must look for a method to show how many propagation constants exist. Arguments to be adduced subsequently from this part of the analysis, in addition to analysis of two similar problems, support the assertion that the assumptions of (22) are physically valid for small inhomogeneity and that as a consequence all the propagation constants have been determined in γ_1 and γ_2. In short, there can be no growing waves.

V. THE PROBLEM OF ADJACENT NEUTRALIZED BEAMS

An alternate formulation of the problem of the inhomogeneous beam can be based on a model of the beam which is constituted of laminar sheets of charge flowing between the two electrodes. The differential equation of each lamination is the equation of the neutralized beam and is soluble in terms of trigonometric functions. The boundary conditions require that the scalar potential vanish at the electrodes and that the potential and its transverse derivative be continuous across all the interfaces between laminations. The equation for the propagation constants is the determinant resulting from the boundary conditions; if the laminations are increased in number without limit, the determinant becomes infinite. Providing the charge and velocity in each lamination depend on the position of the lamination exactly as the charge and velocity in the inhomogeneous beam depend on the transverse coordinate, the infinite determinantal equation is an alternate method for determining the propagation constants of the inhomogeneous beam.

In this section, the problem of three sheet beams is discussed. The charges and velocities are chosen to make the model a crude approximation of the inhomogeneous beam. The geometry is the same as shown in Fig. 1, the center beam is of thickness a, and the two outer beams are identical each having thickness $a/2$. In both beams the electron charge is assumed to be neutralized by the presence of positive ions. The electron charge and velocity of the center and outer beams are denoted by ρ_0; u_0 and ρ_1; u_1, respectively.

The differential equation for the center and outer beams, in this order, are

$$d^2\phi_0/dx^2+(\gamma^2-k^2)[(h_0/k_0-\gamma)^2-1]\phi_0=0, \quad (34)$$

$$d^2\phi_1/dx^2+(\gamma^2-k^2)[(h_1/k_1-\gamma)^2-1]\phi_1=0, \quad (35)$$

while the boundary conditions require that

$$\left.\begin{aligned}\phi_1(a)&=0\\ \phi_1(a/2)&=\phi_0(a/2)\\ \phi_1'(a/2)&=\phi_0'(a/2)\\ \phi_0'(0)&=0\end{aligned}\right\}. \quad (36)$$

The last line of (36) is the stipulation that the potential be an even function, and it is at once satisfied by

choosing the solution

$$\phi_0(x)=A_0\cos[T_0x/a],$$
$$\phi_1(x)=A_1\cos[T_1x/a]+B_1\sin[T_1|x|/a], \quad (37)$$

where

$$\left.\begin{aligned}T_0^2&=a^2(\gamma^2-k^2)[(h_0/k_0-\gamma)^2-1]\\ T_1^2&=a^2(\gamma^2-k^2)[(h_1/k_1-\gamma)^2-1]\end{aligned}\right\}. \quad (38)$$

If one substitutes (37) into (36), one obtains three homogeneous linear equations for A_0, A_1, and B_1. In order that these equations possess a non-trivial solution, the determinant formed from the coefficients must vanish, and there results the relation,

$$T_1^2(1+\cos T_0)(1+\cos T_1)=T_0^2(1-\cos T_0)(1-\cos T_1). \quad (39)$$

Before much use can be made of (39) it must be converted to an expression involving only rational functions of γ. Providing the charges and velocities of the inner and outer beams are very nearly equal, the reasonable assumption to make is that

$$T_0^2\sim(\pi/2)^2. \quad (40)$$

Expression (39) can be solved explicitly for T_1^2 by developing a Taylor series about the point $T_0^2=(\pi/2)^2$, and (40) provides justification for dropping higher order terms. From this procedure there results the equation,

$$T_1^2=(\pi/2)^2+[(2+\pi)/(2-\pi)][T_0^2-(\pi/2)^2], \quad (41)$$

which is evidently a rational function of γ. Inspection of (41) along with (40) shows that the assumption made implies that $|T_1^2-T_0^2|\ll 1$, which is exactly analogous to the assumptions in (22) of the last section. Moreover, when (41) is expressed explicitly in terms of γ,

$$(\tfrac{1}{2}+1/\pi)(h_0/k_0-\gamma)^2+(\tfrac{1}{2}-1/\pi)(h_1/k_1-\gamma)^2=1+(\pi/2a\gamma)^2, \quad (42)$$

it appears that (42) is, with trivial exceptions, the same equation as (26). In view of these facts, it may be concluded without further analysis that there are two solutions corresponding to field waves, two admissible real solutions corresponding to space charge waves, and two complex space charge wave solutions which are inconsistent with (40) and therefore inadmissible.

To determine whether or not different assumptions would lead to additional space charge wave propagation constants, a geometric procedure is sufficient. It is convenient for this discussion to let $y(\gamma)=T_1^2$ and $x(\gamma)=T_0^2$. In (x, y, γ) space both $x(\gamma)$ and $y(\gamma)$ describe two surfaces. One surface represented by $y(\gamma)$ passes through all values of x and those values of $\gamma<k_1$, while the other surface represented by $y(\gamma)$ passes through all values of x and those values of $\gamma>k_1$. Similarly, one surface represented by $x(\gamma)$ passes through all values of y and those values of $\gamma<k_0$; the other $x(\gamma)$ surface passes through all values of y and those values of $\gamma>k_0$. Since $k_0>k_1$, the second surface represented by $x(\gamma)$ can never intersect the first surface represented by $y(\gamma)$; but the first $y(\gamma)$ surface intersects the first $x(\gamma)$ surface, and the second $y(\gamma)$ surface intersects both the $x(\gamma)$ surfaces.

The projection on the $x-y$ plane of the three intersection lines can be deduced with the aid of the derivative in parametric form:

$$dy/dx=\frac{(h_1/k_1-\gamma)^2(k_1\gamma-k^2/k_1-\gamma)-\gamma}{(h_0/k_0-\gamma)^2(k_0\gamma-k^2/k_0-\gamma)-\gamma}. \quad (43)$$

Let $y=y_1(x)$ be the projection when $\gamma<k_1$. If we apply Descartes' rule to (43), it is easily shown that both numerator and denominator have two and only two simple real zeros. Accordingly, the slope of y_1 changes sign four times, while there are only two critical points, and the curve cannot be simple. From the definitions of x and y, it is evident that $y_1(x)$ passes through the origin twice and is asymptotic to the lines:

$$x=y,$$
$$x\cong(ak_1)^2\left[\left(\frac{h_0}{k_1\Delta u/u_0}\right)^2-1\right],$$

where

$$\Delta u=u_1-u_0.$$

When $k_1<\gamma<k_0$, let $y=y_2(x)$. In this case, the derivative is always negative. The asymptotes are the lines:

$$y\cong(ak_0)^2\left[\left(\frac{h_1}{k_1\Delta u/u_0}\right)^2-1\right],$$
$$x\cong(ak_1)^2\left[\left(\frac{h_0}{k_1\Delta u/u_0}\right)^2-1\right].$$

Let $y=y_3(x)$ when $\gamma>k_0$. The slope of y_3 is always positive, and its asymptotes are:

$$y=x,$$
$$y\cong(ak_0)^2\left[\left(\frac{h_1}{k_1\Delta u/u_0}\right)^2-1\right].$$

The curve defined by the principal branch of (39) passes through the points $(0, \pi^2)$ and $(\pi^2/4, \pi^2/4)$. In the third quadrant it is asymptotic to the line $(y=x)$. In Fig. 3 is shown a sketch of y_1, y_2, and y_3 superposed on the curve defined by (39). When $(\Delta u/u_0)$ and $(ak)^2$ are large, it is possible to find six intersections in real space between the y_1, y_2, y_3 curves and that of (39). Each intersection is the projection on the $x-y$ plane of an intersection of three surfaces in space, and it corresponds to one and only one value of γ.

For the condition $2a\ll\lambda$, assumed for the problem, points (1) and (2) would appear as intersections in complex γ space, and these are the attenuation constants for the field waves. On the other hand, points (3) and (6) are always real intersections corresponding to

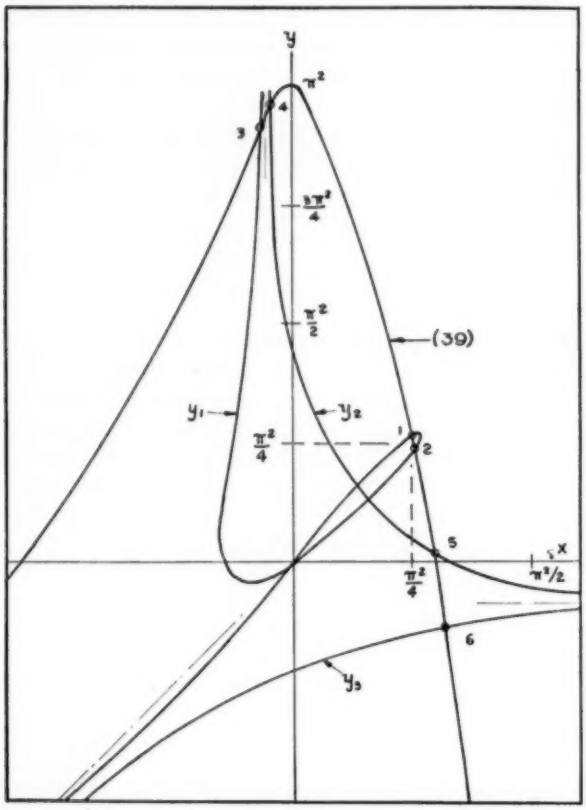

FIG. 3. Graphical demonstration of the existence of six propagation constants for the adjacent beams.

the two space charge wave real propagation constants. For a small velocity difference between the beams points (4) and (5) are intersections in complex space. These points determine the complex propagation constants of the growing space charge waves.

This geometric treatment suggests a variety of ways for determining a criterion for the existence of complex space charge wave propagation constants. A simple method is to use the linear approximation of (39), Eq. (41), together with a hyperbolic approximation of $y_2(\gamma)$ to determine a condition for no intersection of the two. The approximate condition which results is

$$(\Delta u/\bar{u})(\omega/\omega_p)<1, \tag{44}$$

where $\bar{u}$=average velocity and ω_p=average plasma frequency. (Equation (44) is the same as that derived by Haeff[3] for two unbounded mixed beams except for a factor of $\sqrt{2}$ which appears on the right in his expression).

The adjacent sheet beams here treated and the inhomogeneous beam are deceptively similar, and there is apparent justification for extrapolating the results of this section to conclude that growing space charge waves can exist in the inhomogeneous beam. The differences, however, are poignant. As will be argued subsequently, such a conclusion is an unwarranted extension of the analogy.

VI. THE VELOCITY DISTRIBUTED BEAM

The electron beam under consideration in this section is a neutralized filamentary beam characterized by a distribution function,

$$f(v, z, t)dv = \text{the number of electrons at time } t \text{ in unit volume centered at } z, \text{ having velocities in the interval } (v, v+dv). \tag{45}$$

If the function $f(v, z, t)$ is identically zero except for two discrete velocities, the model becomes that of the perfectly mixed discrete beams in the electron wave tube discussed by Haeff.

Substantial simplification of the treatment of the space charge waves may be achieved by assuming that any free space wavelength considered is much larger than the transverse dimensions of bounding electrodes parallel to the direction of electron flow, and that these dimensions in turn are much larger than the thickness of the filament. The first condition allows a quasi-static formulation of the problem and eliminates the field waves at the outset, while the latter permits the analysis to be one-dimensional. In addition, the usual small signal assumption is essential.

Let the velocity, distribution function, potential, and charge density be represented according to the scheme,

$$\begin{aligned} v&=u+v_1(u)e^{i(\omega t-\gamma z)},\\ f&=f_0(u)+f_1(u)e^{i(\omega t-\gamma z)},\\ \phi&=\phi_1 e^{i(\omega t-\gamma z)},\\ \rho&=-\rho_1 e^{i(\omega t-\gamma z)}. \end{aligned} \tag{45}$$

Since the beam is neutralized, the charge density is related to the distribution function by the integral

$$\rho_1=e\int_{u_0}^{u_1} f_1 du, \tag{46}$$

where u_0 and u_1 are, respectively, the lower and upper limits of the velocity spread. The current density in the z direction, linearized according to the small signal assumption, is

$$J=-e\int_{u_0}^{u_1}\{uf_0+[uf_1+v_1f_0]e^{i(\omega t-\gamma z)}\}du. \tag{47}$$

In the terms of (45), (46), and (47), Poisson's equation is

$$-\gamma^2\phi_1=(e/\epsilon_0)\int_{u_0}^{u_1} f_1 du, \tag{48}$$

the linearized dynamic equation is

$$v_1=-\eta\gamma\phi_1/(\omega-\gamma u), \tag{49}$$

and the equation for the conservation of charge is

$$\int_{u_0}^{u_1}[\gamma v_1 f_0-(\omega-\gamma u)f_1]du=0. \tag{50}$$

Equation (50) will be satisfied if

$$v_1=(\omega-\gamma u)f_1/\gamma f_0. \tag{51}$$

If (48), (49), and (51) are to possess a nontrivial solution, γ can take only those values which are solutions of the equation

$$1-\frac{e\eta}{\epsilon_0}\int_{u_0}^{u_1}\frac{f_0(u)du}{(\omega-\gamma u)^2}=0. \tag{52}$$

To investigate the real solutions of (52) it is convenient to represent the left-hand side of (52) by $G(\gamma)$ and examine the real zeros of this function. Assuming that $f_0(u)$ is continuous and positive in the closed interval, (u_0, u_1), and vanishes identically outside this interval, then $G(\gamma)$ has the following behavior:

(a) $\lim_{\gamma\to-\infty} G(\gamma)=1$

(b) $\lim_{\gamma\to+\infty} G(\gamma)=1$

(c) $\lim_{\gamma\to(\omega/u_1)_-} G(\gamma)\to-\infty$

(d) $\lim_{\gamma\to(\omega/u_0)_+} G(\gamma)\to-\infty$

(e) $G'(\gamma)<0$ for $\gamma<(\omega/u_1)=k_1$

(f) $G'(\gamma)>0$ for $\gamma>(\omega/u_0)=k_0$

(g) $G(\gamma)$ has an infinite number of singularities in the interval $(\omega/u_0)\geq\gamma\geq(\omega/u_1)$.

It follows from (a), (c), and (e) that $G(\gamma)$ has one and only one real zero in the range $-\infty<\gamma<k_1$, and from (b), (d), and (f) it follows that $G(\gamma)$ has one and only one real zero in the range $k_0<\gamma<+\infty$. From (g), there can be no real zeros in the interval $k_1\leq\gamma\leq k_0$. Therefore, (52) has two and only two real solutions under the conditions of the assumptions made on $f_0(u)$.

To discuss the possible complex solutions of (52), assume that $f_0(u)$ is everywhere continuous, is positive in the open interval, (u_0, u_1), and vanishes identically at the end points and outside the interval. In addition, it is necessary to assume that $f_0'(u)$ is continuous in the open interval, vanishes identically outside the interval and has one and only one zero at u' inside the interval.

By virtue of the continuity of $f_0(u)$ and its vanishing at the end points, a change of variable in (52) and one partial integration leads to

$$1+\int_a^b\frac{g(\tau)d\tau}{(\tau-\gamma/\omega)}=0, \tag{53}$$

where

$$a=1/u_1,$$

$$b=1/u_0,$$

$$g(\tau)=f_0'(1/\tau)e\eta/\epsilon_0\omega^2.$$

When one puts $(\gamma/\omega)=\alpha+i\beta$, equation (53) may be separated into its real and imaginary parts. These are the following simultaneous equations for α and β:

$$1+\int_a^b\frac{g(\tau)(\tau-\alpha)d\tau}{(\tau-\alpha)^2+\beta^2}=0 \tag{54}$$

and

$$\int_a^b\frac{g(\tau)d\tau}{(\tau-\alpha)^2+\beta^2}=0, \tag{55}$$

assuming $\beta\neq0$. If it is supposed that (55) is satisfied, (54) may be simplified to

$$1+\int_a^b\frac{\tau g(\tau)d\tau}{(\tau-\alpha)^2+\beta^2}=0. \tag{56}$$

From the assumptions about $f_0'(u)$, it follows that $g(\tau)\leq0$ for $1/u_1<\tau\leq1/u'$, and $g(\tau)\geq0$ for $1/u'\leq\tau<1/u_0$. As a result, the subsequent inequalities may be written:

$$\left.\begin{aligned}\int_a^{1/u'}\frac{\tau g(\tau)d\tau}{(\tau-\alpha)^2+\beta^2}&>\frac{1}{u'}\int_a^{1/u'}\frac{g(\tau)d\tau}{(\tau-\alpha)^2+\beta^2},\\ \int_{1/u'}^b\frac{\tau g(\tau)d\tau}{(\tau-\alpha)^2+\beta^2}&>\frac{1}{u'}\int_{1/u'}^b\frac{g(\tau)d\tau}{(\tau-\alpha)^2+\beta^2}.\end{aligned}\right\} \tag{57}$$

If one adds the two and applies (55) to the right side, one gets:

$$\int_a^b\frac{\tau g(\tau)d\tau}{(\tau-\alpha)^2+\beta^2}>0. \tag{58}$$

Since (56) and (58) are incompatible, there can be no complex solutions of (52) under the conditions of the assumptions on $f_0(u)$ and $f_0'(u)$.

At first glance the assumptions placed on $f_0(u)$ may appear to be so restrictive that the results are meaningless, but this is not the case. Any distribution function is positive or zero within the interval and identically zero outside, and because of the velocity spread of thermal electrons, it must be continuous. The restrictions on the end point behavior are details introduced for the sake of the mathematics and need introduce no conflict with physical reality. If $f_0(u)$ has but one relative maximum, there is present essentially one beam. Under these conditions, it has been shown that two, and only two, real propagation constants exist and no complex propagation constants are possible.

The mixed beam which is analogous to the inhomogeneous beam has the distribution function

$$f_0(u)=2J_0/u^2,\quad u_0<u<u_1. \tag{59}$$

The details of the end points can be modified to satisfy the assumptions above without materially changing (59). One may conclude, therefore, that no growing waves are possible.

VII. CONCLUSIONS

In the previous discussion of the ion neutralized sheet beam, it was pointed out that there are four values of γ for each mode; two of these are propagation constants for space charge waves and the others are attenuation constants for TM field waves. Although the presence of the beam has only a second order effect on the field waves, they are essential for a complete solution of the problem. If the drift space between the electrodes is bounded longitudinally by ideal grids for example, then there are four boundary conditions to be satisfied at these planes. The scalar potential must vanish at both the entrance and exit grids, and at the entrance plane the charge as well as the velocity may be arbitrarily fixed. These four conditions require the four integration constants associated with the four waves. If the drift space is not bounded by grids but is like that of a gridless Klystron, the conditions at the two gaps are more complicated because the potential, charge, and velocity are no longer independent, but the four integration constants are still needed.

When two sheet beams are made to flow in the drift space, whether they are mixed or separate, two more initial plane conditions are introduced, two more values of γ are required, and as shown in Haeff's paper as well as in Sec. V above, they do appear. From this fact, one may conclude by induction that the number of values of γ for the fundamental mode will always be just twice the number of beams present in addition to the two field wave propagation constants. While this statement eludes proof, physical experience dictates few if any doubts.

Conceptually treating the inhomogeneous beam as one beam, two beams, or a continuum of beams implies that four, six, or a continuum of propagation constants exist. Each of these models behaves properly in the limit as the inhomogeneity vanishes, but there are evidently vast differences in the results derived. This fact points to the necessity for a multiplicity criterion which will make possible a more realistic and unique choice of model. Moreover, if results are to be experimentally verifiable, the criterion must be one which lends itself to an experimental determination. In the analysis of the velocity distributed beam, a possible criterion which is sufficient for the problem under consideration is suggested. The number of beams present in any aggregate of beams is equal to the number of relative maxima of the distribution function (45), when it is generalized to include the transverse coordinate. The neutralized sheet beam, which is obviously single, can be perturbed without changing its singleness according to the criterion, but not all perturbations have this property. The perturbation which produces the adjacent beams is a specific example of one which does not. This measure of multiplicity makes it possible to determine experimentally the number of beams by making a velocity analysis.

The inhomogeneous beam obviously satisfies the stated condition for singleness. From the assertion on the number of propagation constants necessary, it follows that all the values of γ for the fundamental mode were determined in the preceding analysis. Further support for this conclusion may be adduced from the discussions of both Secs. V and VI. In V it was shown that the behavior of the adjacent beams with respect to the existence or non-existence of growing space charge waves was essentially the same as the behavior of the perfectly mixed beams discussed by Haeff. Therefore, as far as this question is concerned, the analogy between the inhomogeneous beam and the velocity distributed beam should be exact and the conclusions of Sec. VI must be applicable to the inhomogeneous beam.

A remaining paradox is the remarkable similarity between the inhomogeneous beam and the adjacent beams in the face of the unlike conclusions. For infinitesimal velocity differences it is unthinkable that the two situations could be significantly different, and fortunately, the validity of this physical intuition is conserved by the multiplicity criterion. When the velocity difference between the center and outer beams is less than a figure of the order of the thermal velocity spread of the electrons, the distribution function has only one maximum and there is only one beam. Therefore, the given formulation of the adjacent-beam problem is incorrect for infinitesimal velocity differences.

When the velocity difference is large enough to justify the multiple-beam formulation, there are poignant differences between this and the inhomogeneous beam. For the latter, the assumptions (22) can be physically justified from the fact that $F(\sigma x^2, \gamma)$ has the significance of an admittance connecting the potential and the z component of total current accordlng to the relation

$$I_z = (k/\gamma)(\epsilon_0/\mu_0)^{\frac{1}{2}} F(\sigma x^2, \gamma)\phi(x). \tag{60}$$

From physical considerations it is intuitively evident that the total change in F between the center and edge of the beam must increase continuously from zero as the inhomogeneity is increased, and it must be possible to choose the inhomogeneity sufficiently small to make this variation as small as desired. For the adjacent beams, this argument cannot be made with equal persuasiveness even if the velocity difference is permitted to be infinitesimal. With the given formulation of the problem, an infinitesimal velocity difference implies spacial discontinuities in the velocity and charge so that the admittance, which is functionally dependent on these quantities as well as on γ, also becomes discontinuous. As the velocity difference goes to zero uniformly, all the discontinuities vanish, but there is no particular reason why the discontinuity of the admittance should vanish uniformly. In short, one may say that there is no

completely continuous way to make the qualitative transition from the single neutralized beam to the adjacent beams. Accordingly, the assumption (40) is hardly justifiable.

Supposing for the moment that the inhomogeneous beam would support growing waves, one would expect that beam noise would increase exponentially with beam length, for no beam is completely homogeneous. Furthermore, the close connection between beam instability and growing waves implies that most electron beams would be on the verge of oscillation. Since these conditions are not generally found in practice, there is further physical evidence in support of the conclusion that the growing space charge waves cannot exist in a single beam.

VIII. ACKNOWLEDGMENT

The author is indebted to Professor Marvin Chodorow of Stanford University for fruitful discussions throughout the course of the research, which was carried out as a Ph.D. dissertation under Dr. Chodorow's direction.

This work was made possible by the financial support of the Microwave Laboratory of Stanford and a fellowship sponsored by the Sperry Gyroscope Co. Assistance with the manuscript was generously provided by the Institute for Advanced Study, Princeton, New Jersey.

JOURNAL OF APPLIED PHYSICS VOLUME 25, NUMBER 1 JANUARY, 1954

On a Property of a Family of Equiangular Spirals and its Application to Some Problems of Wave Propagation

K. LANDECKER
School of Physics, University of Sydney, New South Wales, Australia
(Received May 18, 1953)

It is shown that all the normals drawn from any point in the plane to the members of a family of equiangular spirals may be simply located geometrically. The locus of all the end points of the normals is a circle. It is also shown that the standing wave pattern in a uniformly attenuating medium may in simple cases (as with an attenuating transmission line) be represented by a vector diagram using a symmetrical pair of spirals. Then the foregoing theorem makes it possible to determine the voltage and current maxima and minima by constructing the locus circle referred to. This is illustrated by several examples. Finally it is pointed out that the locus circle may also be projected into the "Smith Chart."

INTRODUCTION

MOST of the known properties of equiangular spirals were discovered by early geometers, a great many of them apparently by Jacob Bernoulli.[1] The following theorem relating to a family of spirals does not appear to be recorded in the literature. We shall first state and prove the theorem, discuss its consequences, and finally show its bearing on certain problems of wave propagation.

1. THEOREM OF EQUIANGULAR SPIRALS

Let a family of equiangular spirals $r=\exp[k(\varphi+\delta)]$ be drawn about a point A as center (asymptotic point) and let δ be the parameter of the family. A specimen $\delta=$const is shown in Fig. 1. A radius vector drawn from a point B to a (running) point P of the spiral will then clearly, with increasing φ, go through a succession of maxima and minima.

The problem is to determine for the specimen drawn, and for all the other members of the family, the end points of the radius vector when the latter is a maximum or a minimum, respectively; i.e., *to find all the normals to the family passing through B.*

This question is completely answered by the following theorem:

"The second locus of all maxima and all minima of the radius vector BP for every turn of one particular spiral and for all members of the family is a circle (L in Fig. 1) which may be constructed as follows: Draw a perpendicular bisector to AB. Draw a straight line through A inclined at an angle $\psi=$ arc cot k to AB. The intersection of this line with the bisector determines the center of the circle L

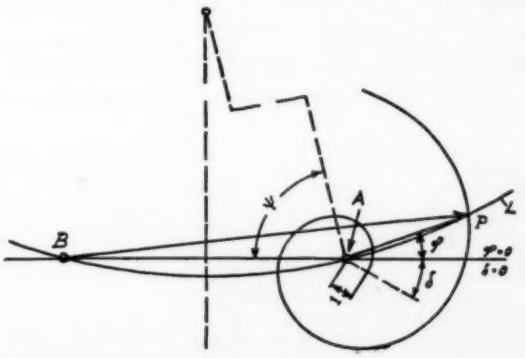

FIG. 1. A specimen $\delta=$const of a family of equiangular spirals $r=\exp[k(\varphi+\delta)]$.

[1] G. S. Carr, *Synopsis of Mathematics* (London, 1886), p. 724; Jacob Bernoulli, *Opera* (Geneva, 1744), p. 497 ff. (Bernoulli's original work was not accessible to the writer.)

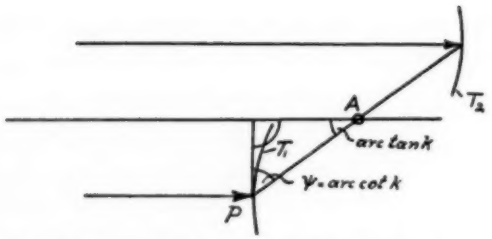

FIG. 2. The normals to two spiral turns for $AB \to \infty$.

through A and B which is the required second locus. The first locus is of course the particular spiral itself."

A proof of this proposition is as follows: Let us suppose first that in Fig. 1. $AB \to \infty$. Then all normals from B will be parallel to AB, as shown for two symmetrical spiral turns T_1 and T_2 in Fig. 2. This means that in order to find the end points of the normals in this special case we must lay off AP at an angle arc tan k from A, as shown. This is because the radius vector r from A must intersect the tangent at P a tan angle arc cot k. This is the fundamental property of equiangular spirals and follows immediately by differentiating the above equation of the family with respect to φ, keeping δ constant.

If AB is finite, i.e., if B is in a position as shown in Fig. 3, construct the normal for $AB \to \infty$ as before. Then describe an arc about A through B to intersect the normal for $AB \to \infty$ in B', and connect A to B'. Turn the *shaded* figure $APB'Q$ until AB' coincides with AB. The figure is then in the dotted position $AP'BQ'$. The apex P' is now *not* in contact with the spiral turn T_1. In order to bring P' into contact with the spiral, i.e., in order to make $P'Q'$ a tangent, P' must be shifted in such a way that the angles $\sphericalangle BP'Q' = \sphericalangle B'PQ = 90°$ and $\sphericalangle AP'Q' = \sphericalangle APQ = \psi$ remain unaltered in magnitude. Therefore P' must be shifted along a circular arc passing through A, B, and P'. This must hold for any spiral turn intersecting AB. To find the center of this arc L, let P' approach A along the arc until the chord AP' finally becomes a tangent to it. But any normal to AP' is inclined at an angle arc tan k against $P'Q'$ and this latter becomes a normal to AB in A. Therefore the first locus of the center of the wanted arc is a straight line drawn through A at an angle arc cot k to AB. The second locus clearly is the perpendicular bisector of AB.

If a spiral turn does not intersect AB internally (as, e.g., T_2 in Fig. 2) the extension of the above proof is easily carried through. This is shown in Fig. 4 with an obvious modification of the notation of Fig. 3, and is self-explanatory. It is seen that the end points of the normals through B still lie on the same arc L. We therefore conclude that all normals from B to any spiral of the family have their end points on L. The whole configuration is shown on a smaller scale in Fig. 5 so that the entire locus circle can be seen.

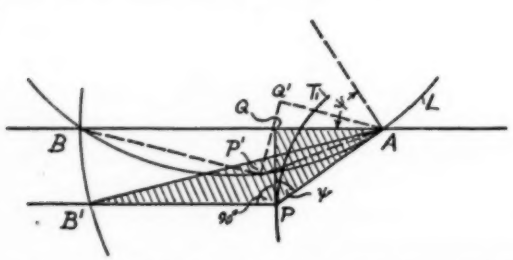

FIG. 3. Construction of the locus circle L when a spiral turn intersects AB internally.

The following consequences result immediately from the theorem. In general the number of possible normals to any one spiral of the family is not unlimited because, with increasing φ, a state will be reached in which the spiral turn does not intersect the locus circle L any more. A linear plot of the magnitude of the radius vector BP versus the angle φ will then exhibit initially a succession of maxima and minima and finally only inflections, with a monotonic increase of magnitude. In the limit the plot will approach the exponential function $BP \sim \exp[k(\varphi+\delta)]$. In other words for large values of φ the radius vector from B can no longer be distinguished from the radius vector r from A.

Finally for $AB \to \infty$, the L circle degenerates into a straight line drawn through A at an angle arc tan k against the direction AB.

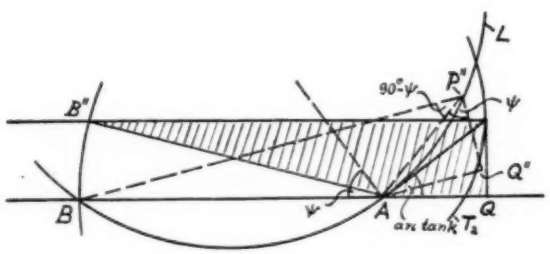

FIG. 4. Construction of the locus circle L when a spiral turn intersects AB externally.

It follows that for this special case the number of maxima and minima is infinite and they occur now alternately for $\varphi = (\text{arc tan} k) \pm \kappa\pi$, where κ is an integer.

In the following section we show that this theorem is very useful for a convenient and instructive graphical representation of waves emanating from a source, attenuated in a uniform but arbitrary way along their path and reflected or absorbed by a termination.

2. REPRESENTATION OF WAVE PROPAGATION BY MEANS OF SPIRAL DIAGRAM

The waves we wish to represent graphically may be of a quite general type as, e.g., light waves passing through an attenuating medium, waves in organ pipes, or wave guides, etc. However, initially we deal in the following with the simplest type of wave propagation, namely propagation along a transmission line with an arbitrarily prescribed complex attenuation constant and an arbitrary complex terminating impedance. Then the wave may be described in terms of the voltage and

current measured along the length of the line.[2] The voltage and current are given by the following pair of equations:

$$\begin{aligned} \mathbf{V} &= \mathbf{A}_0 e^{\gamma l} + \mathbf{B}_0 e^{-\gamma l}, \\ \mathbf{I}\mathbf{Z}_0 &= \mathbf{A}_0 e^{\gamma l} - \mathbf{B}_0 e^{-\gamma l}, \end{aligned} \tag{1}$$

where l = the line length measured from the termination, $\mathbf{V}$ = the voltage, $\mathbf{I}$ = the current along the line, $\mathbf{Z}_0$ = the complex characteristic impedance of the line, $\mathbf{A}_0$ and $\mathbf{B}_0$ are two complex constants, $\gamma = \alpha + j\beta$ = complex propagation constant, α = (real) attenuation constant, and β = (real) phase constant.

We know that the solution of (1), i.e., the voltage and the current propagated in the stationary state along the line, are harmonic functions in space and time. These we may represent in two distinct ways. If x is the argument of a harmonic function we may put

$$\cos x = \Re e(e^{jx}), \quad \sin x = -\Re e(je^{jx}).$$

The diagram of these equations is a vector rotating counterclockwise in the complex plane. The physical

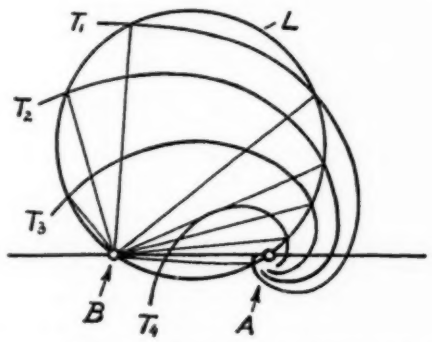

FIG. 5. The position of the locus circle with respect to the whole family of spirals.

quantity is represented by the projection of the vector on to one of the axes. Alternatively we may put

$$\cos x = \frac{e^{jx} + e^{-jx}}{2}, \quad \sin x = \frac{e^{jx} - e^{-jx}}{2j}.$$

In this case the diagram consists of two vectors rotating in opposite directions in the complex plane, but now the physical quantity is represented by the resultant of two vectors. We shall show that the latter representation is much to be preferred for the solution of Eq. (1) because, though one may expect the necessity for four rotating vectors for the representation of voltage and current, it will actually turn out that one pair coalesces into a single vector and that the other pair becomes a pair of equal and opposite vectors. This leads to a remarkable simplification in the graphical representation.

We eliminate in (1) one of the constants ($\mathbf{B}_0$) by

[2] This procedure is originally due to Kirchoff; for its limitations see, e.g., M. Abraham-Becker, *Classical Electricity and Magnetism* (Blackie and Son, Ltd., London, 1937), p. 215 ff.

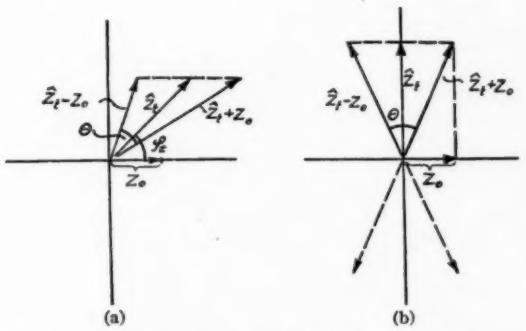

FIG. 6. Graphical representation of the reflection coefficient at the termination of a transmission line.

noting that at the termination (i.e., at $l=0$)

$$\begin{aligned} \mathbf{V}_t &= \mathbf{A}_0 + \mathbf{B}_0, \\ \mathbf{I}_t\mathbf{Z}_0 &= \mathbf{A}_0 - \mathbf{B}_0. \end{aligned} \tag{2}$$

Addition and subtraction of this pair yields

$$\begin{aligned} \mathbf{V}_t + \mathbf{I}_t\mathbf{Z}_0 &= 2\mathbf{A}_0, \\ \mathbf{V}_t - \mathbf{I}_t\mathbf{Z}_0 &= 2\mathbf{B}_0, \end{aligned} \tag{3}$$

and by division we obtain

$$\begin{aligned} \mathbf{B}_0/\mathbf{A}_0 &= (\mathbf{V}_t - \mathbf{I}_t\mathbf{Z}_0)/(\mathbf{V}_t + \mathbf{I}_t\mathbf{Z}_0) \\ &= (\mathbf{V}_t/\mathbf{I}_t - \mathbf{Z}_0)/(\mathbf{V}_t/\mathbf{I}_t + \mathbf{Z}_0) \\ &= (\mathbf{Z}_t - \mathbf{Z}_0)/(\mathbf{Z}_t + \mathbf{Z}_0) = \mathbf{r}, \end{aligned} \tag{4}$$

or

$$\mathbf{B}_0 = \mathbf{A}_0\mathbf{r}, \tag{5}$$

where

$\mathbf{Z}_t$ = complex terminal impedance and
$\mathbf{r}$ = complex reflection coefficient at the termination of the line.

If $\mathbf{r}$ has the phase angle θ we can also express it in the form $\mathbf{r} = re^{j\theta}$, and this or the terminating impedance together with the constants of the line will in general be the given data (see footnote for relation of Fig. 6 to the foregoing).*

This result shows that *at the termination* voltage and current may be represented by the sum and difference of two vectors, $\mathbf{A}_0$ and $\mathbf{B}_0$, according to Eq. (2), which are derivable from the reflection coefficient of the termination. We shall now show that the voltage and the current *at an arbitrary point* along the line are also represented by the sum and difference of 2 vectors. We

* It is useful to represent the relation between the reflection coefficient and its phase angle (θ), and the terminal impedance and its phase angle (φ_t), at least for the important case when Z_0 is purely resistive, in an auxiliary diagram [Fig. 6(a), (b)]. If we (initially) exclude negative resistances, $\mathbf{Z}_t$ can lie only in the first and fourth quadrant, i.e., θ is positive for an inductive load, θ is negative for a capacitive load, $\theta=0$ if Z_t is purely resistive and $Z_t > Z_0$, $\theta=\pi$ it Z_t is purely resistive and $Z_t < Z_0$.

Further we have $|\mathbf{r}|=1$, if $\mathbf{Z}_t$ is purely inductive or purely capacitive, i.e., purely imaginary. In this case Fig. 6(b) shows that θ jumps discontinuously from the value $+\pi$ to $-\pi$ while $\mathbf{Z}_t$ passes through zero. Finally, if $\mathbf{Z}_t$ is an arbitrary impedance and we exclude negative resistances we must always have $|\mathbf{r}| \leqq 1$.

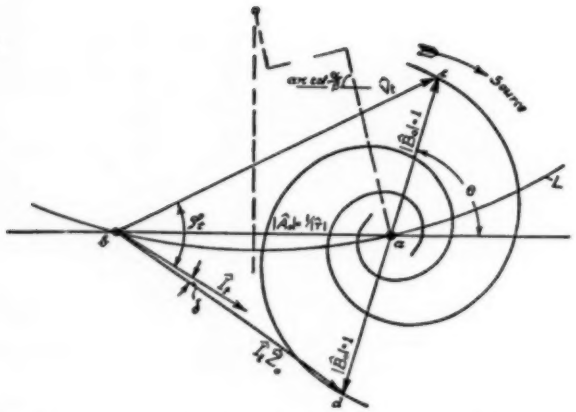

FIG. 7. Vector representation of voltage, current, and phase angle along a general transmission line.

write Eq. (1) by analogy to Eq. (2) in the form

$$\begin{aligned} \mathbf{V}&=\mathbf{A}+\mathbf{B}, \\ \mathbf{I}\mathbf{Z}_0&=\mathbf{A}-\mathbf{B}, \end{aligned} \tag{6}$$

which necessitates

$$\begin{aligned} \mathbf{A}&=\mathbf{A}_0 e^{\gamma l}, \\ \mathbf{B}&=\mathbf{B}_0 e^{-\gamma l}, \end{aligned} \tag{7}$$

and we have analoguously to Eqs. (3) and (4)

$$\begin{aligned} \mathbf{V}+\mathbf{I}\mathbf{Z}_0&=2\mathbf{A}, \\ \mathbf{V}-\mathbf{I}\mathbf{Z}_0&=2\mathbf{B}, \end{aligned} \tag{8}$$

and

$$\begin{aligned} \mathbf{B}/\mathbf{A}&=(\mathbf{V}-\mathbf{I}\mathbf{Z}_0)/(\mathbf{V}+\mathbf{I}\mathbf{Z}_0)=(\mathbf{V}/\mathbf{I}-\mathbf{Z}_0)/(\mathbf{V}/\mathbf{I}+\mathbf{Z}_0) \\ &=(\mathbf{Z}_i-\mathbf{Z}_0)/(\mathbf{Z}_i+\mathbf{Z}_0)=\mathbf{r}_i, \end{aligned} \tag{9}$$

or

$$\mathbf{B}=\mathbf{A}\mathbf{r}_i.$$

Here $\mathbf{Z}_i$ is the input impedance and $\mathbf{r}_i$ is the reflection coefficient at a distance l from the termination.

We now proceed to demonstrate a simple relation between all these vectors in the complex plane.

Using Eq. (5) we rewrite Eq. (1) as

$$\begin{vmatrix} \mathbf{V} \\ \mathbf{I}\mathbf{Z}_0 \end{vmatrix} = \mathbf{A}_0(e^{\gamma l}\pm\mathbf{r}e^{-\gamma l})=(\mathbf{A}_0 e^{j\beta l}|\mathbf{r}|)[e^{\alpha l}] \times\{1/|\mathbf{r}|\pm e^{-2\alpha l}e^{j(-2\beta l+\theta)}\} \tag{10}$$

and consider the bracketed factors on the right of Eq. (10) in turn: the first term in round brackets contains only the phase constant and is common to both voltage and current. It specifies the scale and a common rotation of voltage and current vectors in the complex plane. Therefore it is unimportant for the operation of the line and will not be considered further. But the second factor in square brackets is essential because it is real and contains the line length as variable. However, we shall temporarily set this term aside and take care of it in a manner shown below. The third term in double brackets, $\rho=\{1/r\pm e^{-2\alpha l}e^{j(-2\beta l+\theta)}\}$, is the equation of a symmetrical pair of equiangular spirals in the complex plane with their asymptotic point at a distance $1/r$ from the origin. Choosing $|\mathbf{B}_0|$ as the unit of length in the complex plane we obtain the representation shown in Fig. 7.

On the real axis we lay off the distance $ab=1/r$, and from a the two vectors $+|\mathbf{B}_0|=+1$ and $-|\mathbf{B}_0|=-1$ at an angle θ, the phase angle of the reflection coefficient of the termination. The vectors $\mathbf{V}_l$ and $\mathbf{I}_l\mathbf{Z}_0$ are then given according to Eq. (2) by the distances bc and bd, respectively, i.e., at the termination ($l=0$) we can read off the voltage directly. However, for an arbitrary line, $\mathbf{Z}_0$ has a phase angle. If this phase angle δ is given, as we assume, we can immediately construct the current vector $\mathbf{I}_l$ by turning $\mathbf{I}_l\mathbf{Z}_0$ through δ^0, as shown in Fig. 7, and calculating its vector length by the usual rules of complex multiplication. (The angle δ is for a high-frequency transmission line of the order of one degree and usually negative. For a telephone line or for an artificial line it can of course have any value.) It is important to note that for any other distance l along the line, voltage and current are still given by the same vectors bc and bd, provided the arrow heads c and d of these vectors are advanced along the pair of equiangular spirals defined by Eq. (10) by rotating the radius vector $\pm\mathbf{B}$ through the angle $2\beta l$ clockwise in the direction towards the source. Proceeding thus from the initial position ($l=0$) to increasing values of l, the voltage and current vectors bc and bd oscillate about b in the manner shown in the figure. Thereby the actual current vector $\mathbf{I}$ moves as if it were rigidly connected to $\mathbf{I}\mathbf{Z}_0$; this does not detract from the usefulness of the diagram in any way.

However, since we have neglected the factor $[e^{\alpha l}]$ in Eq. (10) we find that all voltages and currents taken from the diagram are too small by this factor. The diagram supplies the *ratios* of the actual voltages to the *voltages of a matched line* that has the same constants and the same length rather than the actual voltages themselves. This applies also to the currents. This may actually be an advantage, as we shall see below. (In the following, these "reduced" voltages and currents are designated by a star). It is a simple matter, however, to construct an auxiliary scale or rule in order to read off absolute values of voltages and currents directly. Such a "neper" or "decibel" rule is shown in Fig. 8. There is no zero point on this rule. Any point of the scale may be selected as a "zero neper" or "zero decibel" point. (See examples below.) The rule may also be used to draw the equiangular spirals, though in many practical applications it may not even be necessary to draw the spirals. For high-frequency transmission lines Fig. 7 represents a gross exaggeration of the attenuation since for these

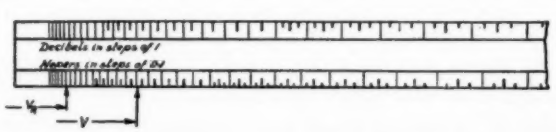

FIG. 8. A "neper" and "decibel" rule.

lines the coefficient of attenuation α is of the order of 10^{-4} nepers/cm.

3. GRAPHICAL DETERMINATION OF VOLTAGE CURRENT AND PHASE DISTRIBUTION

The diagram Fig. 7 together with the scale Fig. 8 are an exact and exhaustive graphical representation of the line Eq. (10) and therefore determine the wave pattern completely. The following relations can be directly derived by inspection:

(a) As long as we are interested only in impedances the attenuation factor $[e^{\alpha l}]$ does not appear in the result because it occurs in both the numerator and the denominator of the impedance. Thus the line impedance at any point l of the line is

$$\mathbf{Z}_i=\mathbf{V}_i/\mathbf{I}_i=\left|\frac{bc}{bd}\cdot\mathbf{Z}_0\right|\underline{\varphi_i^0}, \tag{11}$$

provided distances are measured in the same units (e.g., inches or centimeters). φ_i is here the angle between bc and bd diminished (or increased) by δ, i.e., the angle between $\mathbf{V}_i$ and $\mathbf{I}_i$ measured in degrees. φ_i is to be taken as positive or negative depending on whether the current vector lags or leads the voltage vector, respectively.

(b) Since we also have

$$\mathbf{Z}_i/\mathbf{Z}_0=|bc/bd|\,\underline{\varphi_i^0-\delta^0}, \tag{12}$$

we see that the distance bc, for any fixed position of the diagram, represents the input impedance of the line correctly in magnitude and phase to the same scale to which the distance bd represents the characteristic impedance $|\mathbf{Z}_0|$. In other words by considering bd to be the real axis we may look upon the whole diagram also as a diagram of impedance operators instead of voltage and current vectors. This is important when lumped impedances are placed across or in series with the line. These may then be added graphically to the line impedance and thus the voltage or current distribution obtained for the whole system. A similar consideration shows that the vector diagram may also be looked upon as a diagram of admittance operators.

(c) We further recognize immediately a well-known theorem of line theory: when the line length l becomes very large the points c and d approach the asymptotic point indefinitely. In the limit we have

$$|\mathbf{Z}_i|=|\mathbf{Z}_0| \qquad \varphi_i=\delta$$

or

$$\mathbf{Z}_i=\mathbf{Z}_0, \tag{13}$$

i.e., for a line of sufficient length the input impedance is *always* equal to the characteristic impedance, irrespective of the nature of the load (and of the line constants).

(d) We now formulate the question which is our main interest in this note: When the absolute value of the magnitude of the voltage or current vector is plotted versus the line length l, *where do the maxima and minima occur?* If the line were loss-free, we know (see paragraph (e) below) that maxima and minima would follow each other at distances equal to one half of the free-space wavelength. For an arbitrary line no such simple relation exists but the question is completely answered by the theorem of section (1). The maxima and minima occur where the spirals intersect the circle L, in Fig. 7, whose center is constructed in the manner shown in section (1) and where k (in arc cot k) is now α/β, the ratio of the attenuation constant to the phase constant of the line (see Fig. 7). This follows on puttlng $2\beta l=\chi$ and $\theta=0$ in Eq. (10), i.e., by considering the spiral $e^{k\chi}$ with the polar angle χ starting at the axis $\theta=0$. Then $2\alpha l=(\alpha/\beta)\chi$ or $k=\alpha/\beta$. If one tries to determine the maxima and minima analytically one finds that this is by no means a simple task and does not yield a particularly simple result. It is quite remarkable therefore that such a simple geometrical solution exists.

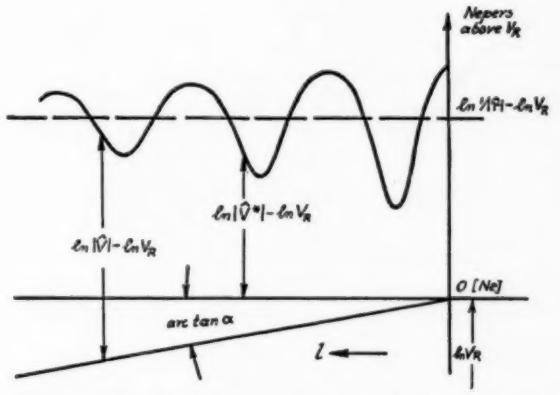

FIG. 9. Logarithmic plot of the voltage distribution in an oblique system of coordinates.

As an example we proceed to plot the voltage distribution along an arbitrary line using the "neper rule" of Fig. 8. We first select a suitable standard or reference voltage V_R. The ratio of the actual line voltage $|\mathbf{V}|$ to the reference voltage is then

$$|\mathbf{V}|/V_R=|\mathbf{V}^*|e^{\alpha l}/V_R. \tag{14}$$

Taking the logarithm of Eq. (14) we obtain

$$\ln(|\mathbf{V}|/V_R)=\ln(|\mathbf{V}^*|/V_R)+\alpha l$$
$$=\ln|V^*|-\ln V_R+\alpha l. \tag{15}$$

This leads immediately to the voltage diagram Fig. 9. We start by taking the natural logarithms of successive values of bc as we proceed from the termination towards the generator, i.e., as we rotate the radius vector $\pm|\mathbf{B}_0|$ in Fig. 7 clockwise. These we plot *versus* the line length as abscissa as shown. The value $\ln(V_R/V_R)=0$ is therefore the origin of the coordinate system. Since we are using natural logarithms we may designate this point as "zero nepers with respect to the reference voltage V_R." There is another reason why the use of natural logarithms is to be preferred for this purpose. In this work it

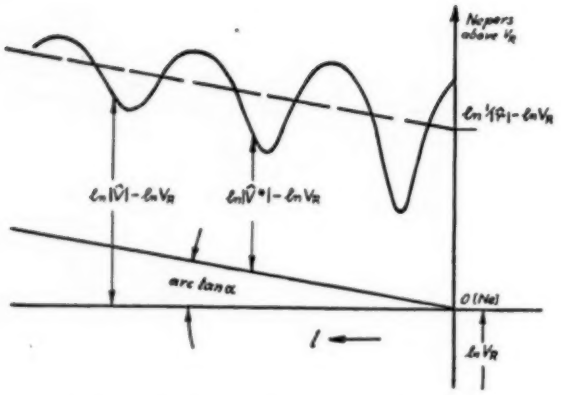

FIG. 10. Logarithmic plot of the voltage distribution in a rectangular system of coordinates.

is customary to tabulate the attenuation constant in nepers/cm or micronepers/cm. However, we may of course use common logarithms (or logarithms to any base for that matter) if desired. Further we obtain from Eq. (10) the asymptote for the voltage curve as the horizontal straight line with the ordinate $\ln(r^{-1}V_R^{-1})$. Finally we draw a straight line at an angle arc tan α to the l axis through 0 and we obtain now the absolute values of the voltages as the vertical distances in logarithmic measure between the points of the curve and of the oblique line.† This procedure also illustrates the use of the rule of Fig. 8. Instead of taking logarithms of the voltages we may select any point on the rule as "zero neper" point, corresponding to an arbitrary reference voltage V_R, and then measure all distances in Fig. 7 in nepers from this reference point. In a similar manner we could plot the current distribution.

We can avoid the somewhat cumbersome oblique system of coordinates simply by drawing the straight line at an angle arc tan α to the l axis *upwards* to the left as shown in Fig. 10. In this case the logarithms of the voltages taken from Fig. 7 are layed out vertically from this line as shown. Finally we mention that the choice of the reference voltage V_R is entirely arbitrary. The same holds for the reference point on the rule.

(e) When the line is loss-free, i.e., when $\alpha \to 0$ the two equiangular spirals in Fig. 7 degenerate into a circle of radius $|\mathbf{B}_0| = 1$ and we are left with a well-known circle

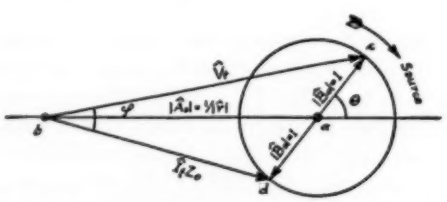

FIG. 11. The circle diagram of a transmission line as a limiting case of the spiral diagram.

† If the line voltage is plotted versus the *line angle* instead of the *line length* it follows from Eq. (10) that the oblique line must be drawn at an angle $\alpha/2\beta$.

diagram which was first treated by Green[3] and has since been often mentioned in the literature.[4,5] This diagram is shown in Fig. 11. From it all the properties of loss-free lines may be derived and it may be put to many other uses which are far too numerous to be dealt with here. We only mention that Professor V. A. Bailey of this School has used a mechanical model of a variant of this diagram for lecture demonstrations for many years. It is also of interest that Bloch[4] has shown that the well-known "Smith chart"[6] as well as the "Kennelly chart"[7] may be produced from Fig. 11 by a transformation by reciprocal radii.

4. GRAPHICAL SOLUTION OF INTERFERENCE OF WAVES IN AN ATTENUATING MEDIUM

In this section we shall solve graphically the following problem: two monochromatic beams of light originating from the same source are directed (e.g., by a system of mirrors) in such a way that they propagate in exactly opposite directions through an attenuating medium. What is the standing wave pattern along the path of the beams through the medium? In transmission line language the configuration would be described by stating that we have two generators of the same frequency feeding a lossy line from both ends.

In preparation for the solution of this problem we consider again Fig. 7. We have so far only ascertained that the vectors represent the voltage and current along the line if we start with an initial configuration given by the angle θ of the reflection coefficient at the termination and turn the vector $\pm\mathbf{B}_0$ in a *clockwise* sense. It is obvious to ask the meaning of a rotation of $\pm\mathbf{B}_0$ in an *anticlockwise* sense past the initial position. To answer this question we note that the line length l then becomes negative so that we obtain instead of Eq. (10)

$$\left|\frac{\mathbf{V}}{\mathbf{I}Z_0}\right| = (\mathbf{A}_0 e^{-i\beta l|\mathbf{r}|})[e^{-\alpha l}]\{1/|\mathbf{r}| \pm e^{+2\alpha l} e^{j(+2\beta l+\theta)}\}, \quad (16)$$

where $\mathbf{V}$ and $\mathbf{I}$ now hold for negative line-lengths l. We interpret Eq. (16) thus: By rotating $\pm\mathbf{B}_0$ anticlockwise as described up to a final position where $+\mathbf{B}_0$ forms an angle θ' with the real axis we find *a new section of line, which, together with the new terminating impedance* (θ'), *can replace the original terminating impedance*, i.e., without changing the standing wave pattern on the original line. We further note that in the range of negative length the "reduced" voltages and currents taken from the

[3] E. Green, Exp. Wireless and Wireless Engr. (now Wireless Engr.) **5**, 304 (1928).

[4] A. Bloch, Wireless Engr. **21**, 161 (1944).

[5] G. W. O. Howe, Wireless Engr. **20**, 215 (1943); See also Abraham-Becker, reference 2, p. 209, and the discussion following a paper by W. Jackson and L. G. H. Huxley read to the Institution of Electrical Engineers, London [J. Inst. Elec. Engrs. (London) **91** Pt. III, 105 (1944)].

[6] P. H. Smith, Electronics **12**, 29 (1939); **17**, 130 (1944).

[7] A. E. Kennelly, *Chart Atlas of Complex Hyperbolic and Circular Functions* (Harvard University Press, Cambridge, 1924), Chart No. IX.

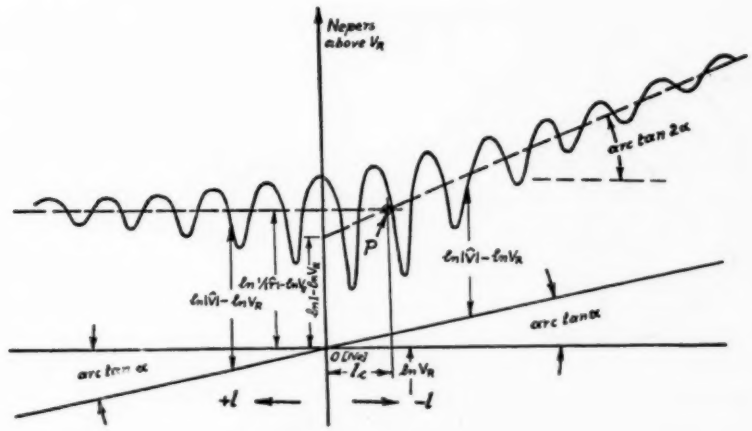

FIG. 12. Standing waves in an attenuating medium (oblique coordinates).

diagram are now *too large* by the factor $e^{\alpha l}$. Finally we see from Fig. 7 that now there exists a critical line coordinate l_c beyond which the *resistive component* of the load impedance becomes negative. This state is reached as soon as the equiangular spirals transgress the circle described with radius $1/|\mathbf{r}|$ about the asymptotic point from the inside.

If we admit of negative resistances, i.e., if we imagine that there exists in the new terminating impedance a generator of the same frequency as the generator feeding the original line then we may rotate the vector $\mathbf{B}_0$ in Fig. 7 anti-clockwise as far as we please. Lastly the properties of the system of spirals discussed in section 1 now reveal a hidden, and at first sight unexpected, symmetry in Fig. 7: The maxima and minima of the "reduced" voltages and currents must still be located on the locus circle L. This means that there must exist a *last maximum* and a *last minimum* because the radius of L is a constant which depends only on (α/β). Therefore the oscillating character of the voltage and current plots must also vanish at the "negative side" of the line.

We now replot Fig. 9 for this negative side. Here we have instead of Eq. (14)

$$|\mathbf{V}|/V_R=(|\mathbf{V}^*|/V_R)e^{-\alpha l}, \tag{17}$$

and, taking the logarithm of Eq. (17),

$$\ln(|\mathbf{V}|/V_R)=\ln(|\mathbf{V}^*|/V_R)-\alpha l. \tag{18}$$

It is easy to construct the asymptote to the voltage curve. From Eq. (16) above we see that for increasing negative l

$$\lim_{l\to\infty}(|\mathbf{V}^*|/V_R)=\lim_{l\to\infty}(e^{2\alpha l}/V_R) \tag{19}$$

because the term $1/|\mathbf{r}|$ in the last bracket on the right-hand side of Eq. (16) finally becomes insignificant compared to $e^{2\alpha l}$. Therefore the equation of the asymptote in the logarithmic plot becomes

$$\ln(A^*/V_R)=\ln(e^{2\alpha l}/V_R)=2\alpha l-\ln V_R, \tag{20}$$

where A^* is now the ordinate of the running point of the asymptote. For the abscissa $l=0$ we have

$$\ln(A^*/V_R)\Big|_{l=0}=\ln 1-\ln V_R, \tag{21}$$

and the diagram takes the form shown in Fig. 12. We can straighten it again into a rectangular system, whereupon we obtain the form shown in Fig. 13.‡ This then is the behaviour of a line fed by two synchronous gener-

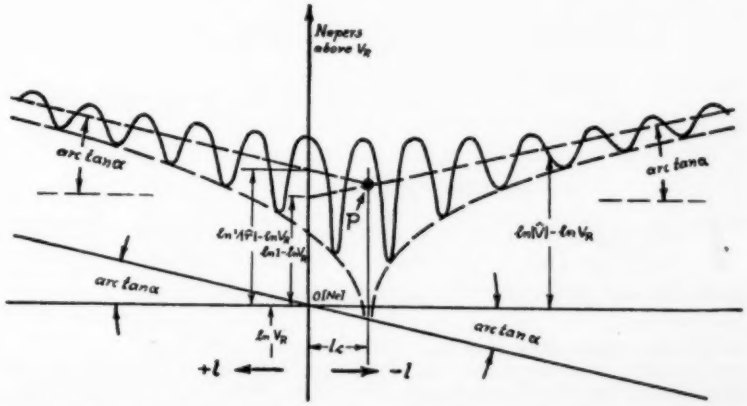

FIG. 13. Standing waves in an attenuating medium (rectangular coordinates).

‡ If the abscissas in Figs. 12 and 13 are line angles instead of line lengths, the angles arc tan α and arc tan2 α become arc tan$(\alpha/2\beta)$ and arc tan(α/β), respectively. This follows from Eq. (10) or (16) in the same way, as shown in Secs. 2 and 3.

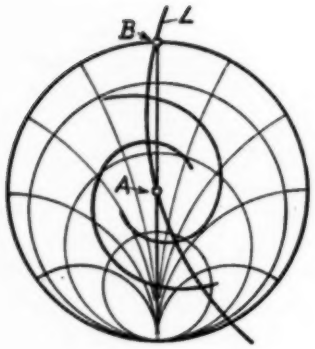

FIG. 14. The locus circle in the "Smith Chart."

ators at each end or the wave (interference) pattern of two beams of light travelling in opposite directions under the conditions set out at the beginning of this section. We note that we have a standing wave pattern in the middle but, with a sufficiently long line, a purely exponential rise of voltage towards each end.

Finally we immediately read off the following properties of the arrangement from the diagram:

(a) The asymptotes to the positive and negative branches of the voltage curve do not intersect the ordinate for $l=0$ (the $\ln|\mathbf{V}^*|$ axis) in the same point but intersect each other at the negative side at the point P.

(b) By constructing this point P we obtain automatically the critical coordinate l_e, i.e., at the left of P we have a flow of wave energy from left to right and at the right of P from right to left. The point P, and not $l=0$, is the actual point of symmetry of the whole system.

(c) It is possible that at the point P the absolute value of the voltage or of the current, but not of both, may become equal to zero *in spite of* the attenuation of the line. The envelope of the voltage curve possesses at l_e in the logarithmic plot a sharp edge (a pole) going to $-\infty$.

5. THE LOCATION OF THE LOCUS CIRCLE IN THE SMITH CHART

From the foregoing it is clear that the theorem of section 1 also enables one to locate the maxima and minima of voltage and current with the Smith Chart. This is indicated schematically in Fig. 14. Here the locus circle L is shown together with the two guiding spirals for the voltage and current vectors.

The writer is indebted to Professor V. A. Bailey, Professor of Experimental Physics in this School, who first drew his attention to problems of this type. Thanks are also due Mr. F. H. Hibberd of New England University College for help in the preparation of the manuscript.

JOURNAL OF APPLIED PHYSICS VOLUME 25, NUMBER 1 JANUARY, 1954

Effect of Gas Slip on Unsteady Flow of Gas Through Porous Media

J. S. ARONOFSKY
Magnolia Petroleum Company, Field Research Laboratories, Dallas, Texas
(Received May 20, 1953)

A numerical method is presented for describing either the one-dimensional or radial transient flow of gases through a porous medium in which the initial and terminal pressures and/or rates are specified. The purpose of this investigation was to evaluate the effect on transient gas flow of a pressure-sensitive gas permeability resulting from gas-slip effects. The gas-slip permeability or apparent permeability is assumed to vary as a linear function with the reciprocal pressure. The computations were carried out by means of punch card machines.

The results demonstrate that under certain conditions, the transient flow system is greatly influenced by gas-slip permeability. However, the results also indicate that the effect of gas slip on transient flow behavior is negligible for pressure conditions usually associated with gas or petroleum reservoirs, and would be of most importance in the conduct and analysis of gas flow experiments in the laboratory. A specific laboratory application of the calculations is a possible transient method for the determination of porosity and/or gas-slip corrected permeability.

INTRODUCTION

THIS paper describes the third part of a series of investigations in the study of transient flow of gases through porous media. The first[1] and second[2] parts of this general investigation involved certain idealized assumptions for both the flowing fluid and the porous medium. These assumptions are:

1. The continuity equation is valid.
2. A velocity potential exists. (Darcy's law.)
3. An average permeability and porosity can be associated with a homogeneous porous medium, and they are not dependent upon properties of a particular fluid.
4. The gas viscosity remains constant.

[1] J. S. Aronofsky and R. Jenkins, "Unsteady flow of gas through porous media, one-dimensional case," Proc. First U. S. Natl. Cong. Appl. Mech., Am. Soc. Mech. Engins. New York (1952).

[2] R. Jenkins and J. Aronofsky, "Unsteady flow of gases through porous media: Part II—radial case," Trans. Am. Soc. Mech. Engrs. 20, No. 2, 210 (1953).

5. The gas contracts and expands as an ideal gas under constant-temperature conditions.

6. Gravitational forces are neglected.

Of all the assumptions listed above, only the first is considered to be fundamental and valid under a wide range of conditions. The other five assumptions require examination in greater detail to determine, quantitatively, the relative importance that each of these five can have on the calculated solutions of the problem of gas flow through porous media under transient conditions.

In this paper, a part of the third assumption (which deals with constancy of gas permeability) is examined and numerical solutions are described in detail which consider the permeability "constant" to be some function of the gas pressure. A mathematical method has been developed for determining the nature of transient gas flow when gas slip is taken into consideration. The method consists of substituting a finite difference equation for the differential equation describing the flow process, and solving this finite difference equation by means of an IBM electronic calculator. In order to evaluate the effects of gas slip on the flow system, curves are presented for a particular problem representing transient flow of gas in a long, slender core of porous material. The results definitely indicate that, under certain conditions, the pressures and flow-rate distributions are very much influenced by gas slip.

These calculations show promise of permitting the determination of gas-slip permeability and/or porosity under transient conditions. The steady-state flow experiment has been used for many years to evaluate quantitatively the effects of gas slip, but it has some severe practical limitations for large, massive cores of very low permeability.

The same methods used in this paper to evaluate gas-slip effects in a long core of a porous medium can be applied directly to radial flow systems.

FLOW EQUATIONS

The continuity equation for single phase flow of any fluid through a porous medium may be expressed as[3] *

$$\nabla\cdot(\rho\bar{v})=-\phi\frac{\partial\rho}{\partial t}. \tag{1}$$

In the viscous-flow region Darcy's Law is valid and, when gravity forces are neglected, can be expressed in the form of a velocity potential

$$\bar{v}=-\frac{k}{\mu}\nabla P. \tag{2}$$

Substituting Eq. (2) into Eq. (1) gives

$$\nabla\cdot\left(\frac{\rho k}{\mu}\nabla P\right)=\phi\frac{\partial\rho}{\partial t}. \tag{3}$$

[3] M. Muskat, *Flow of Homogeneous Fluids Through Porous Media* (J. Edwards, Inc., Ann Arbor, Michigan, 1946).

* List of symbols given at end of paper.

If the ideal gas law is expressed by

$$\rho=\frac{\rho_s}{P_s}P, \tag{4}$$

and if the fluid viscosity is assumed to remain constant, then Eq. (3) becomes

$$\nabla\cdot(kP\nabla P)=\phi\mu\frac{\partial P}{\partial t}; \tag{5}$$

where the permeability, k, is assumed pressure-dependent. The relationship between permeability and pressure under steady-state conditions is discussed below.

STEADY-STATE PERMEABILITY

There is a considerable amount of data recorded in the literature which suggests that the apparent gas permeability is not constant.[4–6] The experimental procedure for determining the apparent gas permeability under steady-state conditions is described by Muskat.[4]

The apparent gas permeability can be calculated from a single set of observations in the laboratory for a specified pressure differential and associated flow rate (steady state). Careful experiments[5] have shown that even under viscous flow conditions the apparent permeability for gas flow is not a constant but is a function, also, of the mean flowing gas pressure ($\bar{P}$) in the core sample under steady-state flow conditions and of the type of gas being employed. To evaluate the effect, it is necessary to employ a gas of constant composition and make several independent determinations of apparent gas permeability at different mean pressures ($\bar{P}$). With such data available it is possible to plot an experimental curve of apparent permeability (k_a), versus $1/\bar{P}$, as suggested by Klinkenberg,[5] and extrapolate this curve to infinite average pressure ($1/\bar{P}=0$) to obtain a value of permeability dependent only on the porous matrix.

This phenomenon has been explained in terms of molecular slippage of the gas at the solid grain surfaces, and generally satisfies an equation of the form

$$k_a=b+m/\bar{P}. \tag{6}$$

where b and m are constants and represent the intercept and slope, respectively, of a straight line in a plot of k_a versus $1/\bar{P}$. This type of equation for molecular slippage was developed in the year 1875 for gas flow through capillary tubes of circular cross section.[7]

[4] M. Muskat, *Physical Principles of Oil Production* (McGraw-Hill Book Company, Inc., New York, 1949).

[5] L. J. Klinkenberg, "The permeability of porous media to liquids and gases," *Drilling and Production Practice* (American Petroleum Institute, 1941).

[6] H. Adzumi, Bull. Chem. Soc. Japan **12**, 304 (1937).

[7] A. Kundt and E. Warburg, "Ueber Reibung und Waermeleitung Verduennter Gase," Poggendorf Ann. Physik **155**, 337, 525 (1875).

Of particular importance is the observation that the constant b, which is the limiting value of k_a at infinite mean pressure, $\bar{P}$, for gases, is found to be equal, within experimental error, to the permeability as measured with liquids.[5] This quantity, b, which represents a property of the rock formation should be independent of the particular fluid used to evaluate the permeability, and is therefore called the true or slip-corrected permeability. The quantity m is dependent upon properties of both rock formation and gas (mean free path). A proper understanding of what natural laws control values of the quantities b and m is still lacking; however, it is not the purpose of this investigation to delve more deeply into this subject. A more recent paper[6] indicates that important studies are being carried out on gas-slip problems.

UNSTEADY-STATE CONDITIONS

In evaluating the transient flow problem, the following additional assumptions are made to permit evaluation of the effects of gas slip in the unsteady-state picture represented by Eq. (5). For each infinitesimal volume element let us assume that:

1. The permeability term in Eq. (5) is an apparent permeability k_a and is functionally related to the average flowing gas pressure by Eq. (6).

2. Equation (6), although developed and experimentally verified under steady-state conditions, is also valid under transient conditions.

After utilizing the above conditions, Eq. (5) will reduce to

$$\nabla\cdot\left[\left(P+\frac{m}{b}\right)\nabla P\right]=\frac{\phi\mu}{b}\frac{\partial P}{\partial t}. \tag{7}$$

Equation (7) is therefore the basic differential equation that must be solved in order to understand or predict what effect gas slip will have on a given flow system. Equation (7) can be further simplified by introducing the new variable

$$W=P+(m/b). \tag{8}$$

Substituting Eq. (8) into Eq. (7)

$$\nabla\cdot(W\nabla W)=\frac{\phi\mu}{b}\frac{\partial W}{\partial t}. \tag{9}$$

The problem is therefore resolved to finding solutions for Eq. (9) which is still a nonlinear partial differential equation. The purpose of introducing the new variable W (termed the equivalent pressure) is to put the equation in a form analogous to the differential equation used in the previous papers[1,2] when gas slip was neglected. Some particular solutions have already been determined for Eq. (9) by means of punch card machines and such solutions also can be used as solutions to Eq. (7), except that the boundary conditions must be properly modified. The actual numerical solutions given in this paper were carried out in the P system rather than the W system, but either system could be used.

FIG. 1. Schematic section of finite core of porous material.

[6] Heid, McMahon, Nielsen, and Yuster, "Study of permeability of rocks to homogeneous fluids," *Drilling and Production Practice* (American Petroleum Institute, 1950).

NUMERICAL SOLUTIONS

The numerical method used in this paper consists of reducing the differential equation to a difference equation and then solving the difference equation by means of a digital computing machine. The one-dimensional form of Eq. (9) was studied in detail in reference 1 and the following form of difference equation was developed.

$$\left(\frac{W}{W_m}\right)_{x,\ t+\Delta t}=\frac{1}{4}\left[\left(\frac{W}{W_m}\right)^2_{x+\Delta x,\ t}+\left(\frac{W}{W_m}\right)^2_{x-\Delta x,\ t}-2\left(\frac{W}{W_m}\right)^2_{x,\ t}\right]+\left(\frac{W}{W_m}\right)_{x,\ t} \tag{10}$$

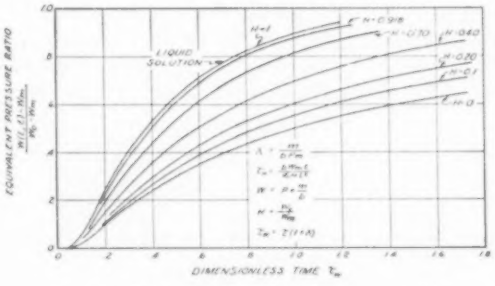

FIG. 2. History of equivalent pressure ratio at closed end of linear tube of porous material.

where

$$\frac{1}{2}\frac{\Delta t W_m b}{(\Delta x)^2\phi\mu}=\frac{1}{4}. \tag{11}$$

Depending upon the circumstances of the problem, it is sometimes desirable to compute directly in the P system instead of the W system. The difference equation in the P system becomes

$$\left(\frac{P}{P_m}\right)_{x,\ t+\Delta t}=\frac{1}{4(1+\lambda)}\{(P/P_m)^2_{x+\Delta x,\ t}+(P/P_m)^2_{x-\Delta x,\ t}-2(P/P_m)^2_{x,\ t}+2\lambda[(P/P_m)_{x+\Delta x,\ t}+(P/P_m)_{x-\Delta x,\ t}-2(P/P_m)_{x,\ t}]\}+(P/P_m)_{x,\ t}, \tag{12}$$

where

$$\frac{1}{2}\frac{\Delta t P_m b}{(\Delta x)^2\phi\mu}=\frac{1}{4(1+\lambda)}. \tag{13}$$

The difference equation can be solved with ease for a given set of initial and boundary conditions, although the numerical computations are tedious and lengthy. All the computations of Eq. (12) that are recorded in this paper were performed on IBM electronic punch card machines.

FINITE TUBE—ONE END CLOSED

Consider a finite tube of porous medium charged with a gas pressure, P_m, (equivalent pressure W_m) as illustrated in Fig. 1. Pressure at one end of the tube, $(x=0)$, is suddenly lowered to a constant value P_0 (equivalent pressure W_0); the other end of the tube is sealed off so that no flow occurs across the plane $x=L$. The problem

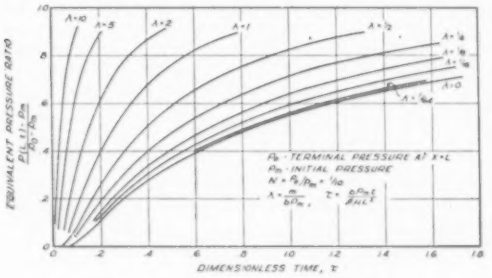

FIG. 3. Dimensionless pressure draw-down curves at closed end of tube of porous material.

is to determine the pressure distribution throughout the tube and the flow rate for any instant of time and for any values of m and b. The above initial and boundary conditions were chosen because these conditions can be duplicated in laboratory experiments with comparative ease (a rate-measuring device is not needed).

For the purposes of computation the long core was divided into nine equal segments and the flowing pressure distributions were computed at the ten pressure stations indicated in Figure 1.

It is of considerable interest from an experimental viewpoint to determine the pressure declines at the sealed end of the tube $(x=L)$. Such a plot is given in Fig. 2 where the equivalent pressure ratio

$$\frac{W(L,t)-W_m}{W_0-W_m}$$

is plotted as a function of τ_w, where τ_w is a dimensionless time parameter. A family of curves is shown for various values of $H=W_0/W_m\leq 1$. The spread of the curves can be taken as an indication of the non-linearity of the basic differential Eq. (9), since different curves are shown for different values of H. As was stated in the previous publication,[1] the gas solution must approach the liquid solution in the limit as $H\to 1$. This condition, which is indicated in Fig. 2 for $H\to 1$, was obtained by an analytical solution of the classical diffusion equation.

The curves of Fig. 2 are quite general in the sense that they are valid for a large range of values for both pressure conditions $(N=P_0/P_m)$ and types of gases as characterized by the dimensionless parameter λ. This can be illustrated in the following manner.

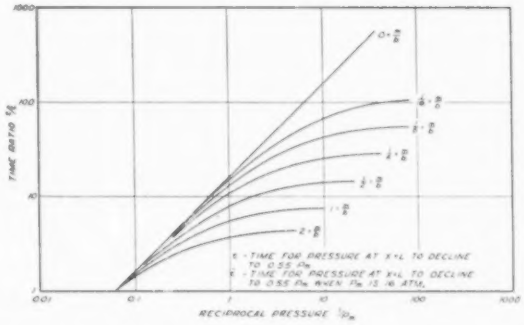

FIG. 4. Time ratio versus reciprocal pressure for gas flow in tube of porous material.

Consider the physical system where the terminal pressure (P_0) at $x=0$ is maintained at 1/10 of the initial pressure P_m. Therefore

$$N=P_0/P_m=1/10, \tag{14}$$

$$\lambda=(N-H)/(H-1), \tag{15}$$

$$\tau=\tau_w/(1+\lambda), \tag{16}$$

where τ represents the dimensionless time parameter in the P system. Also

$$\frac{W(L,t)-W_m}{W_0-W_m}=\frac{P(L,t)-P_m}{P_0-P_m}. \tag{17}$$

Replotting Fig. 2 in terms of $[P(L,t)-P_m]/[P_0-P_m]$ and τ gives the results shown in Fig. 3 where a family of curves is given for different values of λ. These plots are valid for a large range of both m/b and P_m for the specific pressure ratio $N=1/10$. Different families of curves are obtainable for other values of N simply by reevaluation of λ in Eq. (15). The curves of Fig. 3 demonstrate that the pressure distribution at any time is very much influenced by the dimensionless parameter λ which involves m, b, and P_m. Experiments designed to test this conclusion are described in another paragraph of this paper.

It is desirable to re-plot the information in Fig. 3 in a manner that will show how the parameter m/b will influence values of $P(L,t)$ for different time values. Such a plot is shown in Fig. 4 where t represents the time required for $P(L,t)$ to decline to 55 percent of its original value $[P(L,t)=0.55\,P_m]$. The curves are all based on the quantity $\bar{t}$, which represents the time for $P(L,t)$ to decline from a P_m value of 16 atmos. Figure 4 then is a plot of $t/\bar{t}$ versus $1/P_m$, and displays a family of curves for different values of m/b. Such a plot permits an evaluation of m/b from experimental data since it is possible to superimpose experimental points on Fig. 4 and select an m/b curve that best fits the experimental data. This topic is discussed further in a following paragraph.

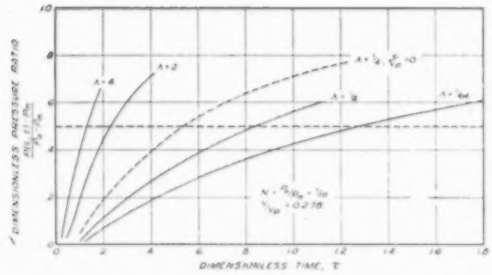

FIG. 5. Dimensionless pressure draw-down curves at $x=L$ for dead volume to pore volume ratio of 0.278—gas flow in tube of porous material.

FINITE TUBE—SEALED-IN DEAD VOLUME

Consider the previously described initial and boundary conditions of Fig. 1 with the additional stipulation that a dead volume, V, is trapped or sealed in at the closed end ($x=L$) of the long core. Such a situation (sealed-in dead volume) would occur in the laboratory when some pressure-measuring device is used to record the pressure at $x=L$. The use of any practical pressure-measuring device will necessarily introduce some trapped gas into the flow system so it is important to investigate what influence such a dead volume can have on the flow system as a whole. (Further analysis shows that variation in V can be used to experimentally evaluate b and ϕ.)

For purposes of comparison, the same problem described in Fig. 1 was recalculated for various values of dead volume. The inclusion of a trapped gas volume at $x=L$ necessitates a re-evaluation of the boundary condition and will give

$$\frac{\partial P}{\partial t}=-\frac{A}{V\mu}(bP+m)\frac{\partial P}{\partial x} \tag{18}$$

for $x=L$.[9] It is a simple matter to rewrite Eq. (18) in the difference form and then compute numerical solutions by means of the punch card machines. It was found that the type curves of Fig. 3 are greatly influenced by the inclusion of a trapped gas volume at $x=L$. For instance, the curves of Fig. 5 illustrate the effect on the pressure at $x=L$ of a trapped dead volume equal to 0.278 times the pore volume ($V=0.278\,V_p$). A comparison of Fig. 5 with Fig. 3 shows that corresponding curves of equal λ on Fig. 5 are shifted to the right on the τ scale as compared in Fig. 3. (The curve for $\lambda=\frac{1}{4}$, $V/V_p=0$, originally from Fig. 3 has been redrawn in Fig. 5 to facilitate this comparison.)

Another point of interest is that the type plot of Fig. 4 is *not* sensitive to different size dead volumes. As an example, the information available in Fig. 5 ($V/V_p=0.278$) was recalculated and compared with the plot of Fig. 4 which was previously determined from Fig. 3 ($V/V_p=0$). The newly calculated values from Fig. 5 were in good agreement on Fig. 4 with the corresponding values calculated from Fig. 3. This demonstrates that the curves of Fig. 4 are insensitive to dead volumes. (It is of course necessary in calculating $t/\bar{t}$ for a given value of $1/P_m$ that both t and $\bar{t}$ be determined for the same V/V_p ratio.) Similar numerical calculations were carried out for dead-volume-to-pore-volume ratios (V/V_p) equal to 0, 0.0555, 0.278, 0.611, 1.272, 2.61, 5.37, and 13.49, and in all cases the type plot of Fig. 4 was insensitive to V/V_p.

It is desirable to correlate the pressure decline history at $x=L$ to demonstrate what influence V/V_p will have on pressure declines for various values of λ. Figure 6 is a plot of the dimensionless time τ for the pressure at $x=L$ to decline to 0.55 P_m as a function of V/V_p for various λ values. An important characteristic of the curves of Fig. 6 is that they are approximately straight-line plots that can be represented by a slope and intercept for any value of λ. The open circular points are actual calculations from the punch-card machines. The curves are useful for experimental determination of ϕ and b; this is discussed in the next section.

PROPOSED EXPERIMENTS

A series of experiments is proposed as a means of testing the punch card results. The basic experiment described by Fig. 1 can be conducted in the following manner to allow suitable variation of the physical coefficients m, b, P_m, and the ratios N and V/V_p.

1. The coefficients m and b can be held constant by conducting the experiment described in Fig. 1 for a specified core with a specified gas and a fixed dead-volume ratio V/V_p. Then P_m is varied by starting a series of experiments at different initial pressures for the fixed value of $N=1/10$.

2. The coefficients b and P_m can be held constant in another series of experiments by using one porous core and always starting at the same initial pressure for a fixed dead-volume ratio and a specified pressure ratio N. Then the slope m can be varied by using different gases with different mean free paths.

3. The coefficients b and m can be varied in a series of experiments (where P_m, N, and V/V_p are held con-

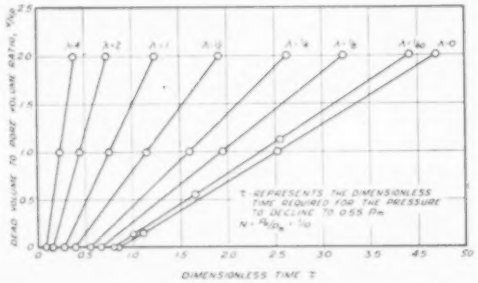

FIG. 6. Dead volume ratio versus dimensionless time—gas flow in tube of porous material.

[9] A system of transient gas flow through porous media with a sealed-in dead volume is reminiscent of a heat-conduction system where the edge of a slab is in contact with a well-stirred fluid. H. Carslaw, and J. Jaegar, *Conduction of Heat in Solids* (Oxford Clarendon Press, 1947) p. 106.

stant) by using different porous cores with different pore geometry.

4. It is possible to vary the dead-volume ratio V/V_p while all the other coefficients are held constant. This is done easily by changing V for a fixed V_p.

5. Similarly, it is possible to vary the ratio N while all the other coefficients are held constant.

It is clear then that experimental procedures are available to verify the numerical solutions of Fig. 3, provided the experimental results can be interpreted in terms of the dimensionless parameters λ, τ, and V/V_p. This can be done since it is possible to evaluate m, b, and ϕ from the experimental data by proper use of the curves of Figs. 3, 4, and 6. The following procedure is suggested as one possible way of evaluating m, b, and ϕ.

The proposed Experiment (1) is performed where the initial pressure, P_m, takes on several values (say 16, 4, and 2 atmospheres), and the time is recorded when $P(L, t)=0.55\ P_m$. The experimental points from these tests are plotted on Fig. 4, and an m/b curve is selected that best fits the experimental data. The ratio m/b is thus determined. (The selection of m/b can be done more accurately by making proper cross-plots of Fig. 4.)

The proposed experiment corresponding to (4) above is performed where the volume ratio V/V_p takes on at least two different values for known values of m/b, P_m, and therefore λ, and the time is recorded for $P(L, t)=0.55\ P_m$. From the straight-line plots of Fig. 6 it is possible now to evaluate b and ϕ. A straight-line curve of Fig. 6 is characterized by two constants; namely, the *slope* and *intercept*. If proposed Experiment (4) is carried out for two different dead volumes, V_1 and V_2, then b and ϕ could be evaluated directly from the following equations

$$b=\frac{\text{slope}\,\mu L^2}{P_m(AL)}\left(\frac{V_1-V_2}{t_1-t_2}\right), \tag{19}$$

$$\phi=\frac{\text{slope}\,(t_2V_1-t_1V_2)}{\text{intercept}\,(AL)(t_1-t_2)}, \tag{20}$$

where t_1 and t_2 represent the time required for the pressure at $x=L$ to decline to $0.55\ P_m$, for the cases, respectively, involving the dead volumes V_1 and V_2; the slope-intercept values are obtained from extrapolation or cross plotting of Fig. 6. The coefficient m can now be calculated directly, since both m/b and b are already evaluated.

ACKNOWLEDGMENT

Acknowledgment is made to the management of the Magnolia Petroleum Company for permission to publish the results of this investigation. The author wishes to acknowledge the assistance of O. D. Ferris in connection with the punch card calculations.

NOMENCLATURE

- A cross-sectional area of core, cm^3.
- b permeability in darcys (which is the limiting value of k_a at infinite gas pressure).
- H an equivalent pressure ratio W_0/W_m.
- k permeability, darcys.
- k_a apparent permeability, darcys.
- L length of core, cm.
- m a constant which represents the slope of a plot of k_a versus $1/P$. The units of m are darcy atmospheres.
- N a pressure ratio P_0/P_m.
- P gas pressure, atmospheres absolute.
- P_s pressure in atmospheres absolute at standard conditions.
- $\bar{P}$ mean pressure, atmospheres absolute.
- P_m maximum pressure in flow system, atmospheres absolute.
- P_0 terminal pressure at $x=0$, atmospheres absolute.
- t time in seconds.
- V sealed-in dead volume, cm^3.
- V_p pore volume, cm^3.
- $\bar{v}$ macroscopic fluid velocity, cm/sec.
- W equivalent pressure, atmospheres absolute.
- W_m largest value of W in flow system $[P_m(1+\lambda)]$.
- W_0 terminal equivalent pressure at $x=0$, atmospheres absolute.
- $(W/W_m)_{x,\,t}$ equivalent pressure at distance x and time t.
- $(W/W_m)_{x,\,t+\Delta t}$ equivalent pressure at distance x and time $(t+\Delta t)$.
- $(W/W_m)_{x+\Delta x,\,t}$ equivalent pressure at distance $(x+\Delta x)$ and time t.
- $(W/W_m)_{x-\Delta x,\,t}$ equivalent pressure at distance $(x-\Delta x)$ and time t.
- x distance from boundary of porous medium at which pressure is applied, cm.
- λ a dimensionless parameter (equal to m/bP_m).
- μ viscosity, centipoises.
- ρ mass density, gm/cm^3.
- ρ_s mass density at standard conditions gm/cm^3.
- τ a dimensionless time parameter $(bP_mt/\phi\mu L^2)$.
- τ_w a dimensionless parameter (equal to $\tau(1+\lambda)$).
- ϕ porosity, fraction equal to V_p/AL.

JOURNAL OF APPLIED PHYSICS VOLUME 25, NUMBER 1 JANUARY, 1954

Cylindrical Shock Waves Produced by Instantaneous Energy Release*

SHAO-CHI LIN
Graduate School of Aeronautical Engineering, Cornell University, Ithaca, New York
(Received May 20, 1953)

Taylor's analysis of the intense spherical explosion has been extended to the cylindrical case. It is found that the radius R of a strong cylindrical shock wave produced by a sudden release of energy E per unit length grows with time t according to the equation $R=S(\gamma)(E/\rho_0)^{1/4}t^{1/2}$, where ρ_0 is the atmospheric density and $S(\gamma)$ is a calculated function of the specific heat ratio γ. For $\gamma=1.4$, $S(\gamma)$ is found to be approximately unity. For this case, the pressure p_1 behind the shock wave decays with radius R according to the relation $p_1=0.216E/R^2$. Applying the results of this analysis to the case of hypersonic flight, it can be shown that the shock envelope behind a meteor or a high-speed missile is approximately a paraboloid given by $R=(D/\rho_0)^{1/4}(x/V)^{1/2}$ where D and V denote the total drag and the velocity of the missile, respectively, and x is the distance behind the missile.

INTRODUCTION

IN the light of recent interest in strong cylindrical shock waves and their connection with the luminous trials of meteors,[1] Taylor's analysis of an intense spherical explosion[2] is being extended to the cylindrical case. An ideal problem is considered in which a finite amount of energy per unit length, in an infinitely concentrated form, is suddenly released along a straight line of infinite extent in the atmosphere. The pressure, density, and velocity distribution behind an intense cylindrical shock wave thus produced are then calculated according to a set of similarity assumptions which is consistent with the fluid-dynamic equations and the strong shock conditions. As a simplification, the uniform atmosphere is assumed to consist of perfect gases with constant heat capacities. Furthermore, heat transfer (conduction, radiation, etc.) is knowingly neglected, and the flow behind the shock wave is assumed to be particle-isentropic.

On account of the imposed strong shock conditions, the results of this analysis cease to be accurate when the shock strength decays to such an extent that the pressure behind the shock front is no longer much greater than the atmospheric pressure. Also, because of the constant specific-heat assumption, these results cannot be expected to be accurate on the other extreme of shock strength (i.e., very strong shock waves) where dissociation and other high-temperature effects become appreciable. On the other hand, Taylor observed that the agreement between theory and experiment for the very intense spherical explosion was surprisingly good (see Part II of reference 2). Therefore, these results would probably predict the decay of very strong cylindrical shock waves with comparable degree of accuracy. A further discussion on this point will be given later.

It should be pointed out that this analysis is not only applicable to the strictly one-dimensional situation (where only one space variable, namely the radius, is involved; the explosion of a long thin wire is an example of this situation), but also to certain axially symmetrical hypersonic flow problems,[3] such as the shock envelope behind a fast meteor, or missile. An application of this type will be illustrated later in the Discussion Section.

To facilitate reference to and comparison with Taylor's paper, Taylor's symbols will be used to denote their cylindrical counterparts in the present analysis.

FLUID-DYNAMIC EQUATIONS AND SIMILARITY ASSUMPTIONS

The equations governing the flow behind a cylindrical shock wave are as follows:

Equation of Motion,

$$\frac{\partial u}{\partial t}+u\frac{\partial u}{\partial r}=-\frac{1}{\rho}\frac{\partial p}{\partial r}; \tag{1}$$

Equation of Continuity,

$$\frac{\partial \rho}{\partial t}+u\frac{\partial \rho}{\partial r}+\rho\left(\frac{\partial u}{\partial r}+\frac{u}{r}\right)=0, \tag{2}$$

where u, p, and ρ are velocity, pressure, and density of the flow at radius r and time t.

In addition to the above two basic equations, we may assume that the flow behind the shock wave is particle-isentropic. As a further simplification, we assume that air is a perfect gas with constant specific heats. Thus we have a third equation defining the thermodynamic process of the flow,

$$\left(\frac{\partial}{\partial t}+u\frac{\partial}{\partial r}\right)\left(\frac{p}{\rho^\gamma}\right)=0, \tag{3}$$

where γ is the ratio of the specific heats.

We now introduce the similarity assumptions for the cylindrical flow in a manner similar to that of Taylor for the spherical case:

* This work was partially supported by the U. S. Office of Naval Research.

[1] F. L. Whipple and A. Kantrowitz, "Theoretical and observed radii of meteor trials" (to be published).

[2] G. I. Taylor, Proc. Roy. Soc. (London) **A201**, 159 (1950).

[3] W. D. Hayes, Quart. Appl. Math. **V**, 105 (1947).

Pressure,

$$p/p_0=f_1(\eta)/R^2; \tag{4}$$

Density,

$$\rho/\rho_0=\psi(\eta); \tag{5}$$

Flow velocity,

$$u=\phi_1(\eta)/R, \tag{6}$$

where R is the radius of the cylindrical shock wave, p_0 and ρ_0 are the pressure and density of the undisturbed atmosphere ahead of the shock wave, $\eta\equiv r/R$ is a nondimensional radial variable, and f_1, ψ, ϕ_1 are functions of η only. Substituting Eqs. (4), (5), and (6) into Eqs. (1)–(3), we obtain

$$(\phi_1+\eta\phi_1')\frac{1}{R^2}\frac{dR}{dt}-\frac{\phi_1\phi_1'}{R^3}=\frac{p_0}{\rho_0}\frac{f_1'}{\psi R^3}; \tag{7}$$

$$\frac{\eta\psi'}{R}\frac{dR}{dt}-\frac{\phi_1\psi'}{R^2}-\left(\phi_1'+\frac{\phi_1}{\eta}\right)\frac{\psi}{R^2}=0; \tag{8}$$

$$\left(\gamma\eta f_1\frac{\psi'}{\psi}-\eta f_1'-2f_1\right)\frac{1}{R^3}\frac{dR}{dt}+\frac{\phi_1 f_1'}{R^4}-\frac{\gamma f_1\phi_1\psi'}{\psi R^4}=0, \tag{9}$$

where $f_1'\equiv df_1/d\eta$, etc. These three equations may be reduced to the standard "variable-separation" form,

$$R\frac{dR}{dt}=\left(\phi_1\phi_1'+\frac{p_0}{\rho_0}\frac{f_1'}{\psi}\right)(\phi_1+\eta\phi_1')^{-1}; \tag{7a}$$

$$R\frac{dR}{dt}=\frac{\phi_1}{\eta}+\left(\phi_1'+\frac{\phi_1}{\eta}\right)\frac{\psi}{\eta\psi'}; \tag{8a}$$

$$R\frac{dR}{dt}=\left(\frac{\gamma f_1\phi_1\psi'}{\psi}-\phi_1 f_1'\right)\left(\gamma\eta f_1\frac{\psi'}{\psi}-\eta f_1'-2f_1\right)^{-1}, \tag{9a}$$

which can be satisfied if, and only if,

$$R\frac{dR}{dt}=A, \tag{10}$$

$$\phi_1\phi_1'+\frac{p_0}{\rho_0}\frac{f_1'}{\psi}=A(\phi_1+\eta\phi_1'), \tag{11}$$

$$\phi_1+\left(\phi_1'+\frac{\phi_1}{\eta}\right)\frac{\psi}{\psi'}=A\eta, \tag{12}$$

$$\gamma f_1\phi_1\frac{\psi'}{\psi}-\phi_1 f_1'=A\left(\gamma\eta f_1\frac{\psi'}{\psi}-\eta f_1'-2f_1\right), \tag{13}$$

where A is a common constant having the dimension of length $\times$ velocity.

We may non-dimensionalize the functions f_1 and ϕ_1 by writing,

$$f_1(\eta)\equiv A^2 f(\eta)/a^2 \tag{14}$$

and

$$\phi_1(\eta)\equiv A\phi(\eta), \tag{15}$$

where $a\equiv(\gamma p_0/\rho_0)^{\frac{1}{2}}$ is the speed of sound of the undisturbed atmosphere.

Substituting Eqs. (14) and (15) into Eqs. (11), (12), and (13) yields

$$(\eta-\phi)\phi'+\phi=\frac{f'}{\gamma\psi}; \tag{11a}$$

$$(\eta-\phi)\frac{\psi'}{\psi}=\phi'+\frac{\phi}{\eta}; \tag{12a}$$

$$(\eta-\phi)\gamma f\frac{\psi'}{\psi}=(\eta-\phi)f'+2f. \tag{13a}$$

Solving these three equations simultaneously for f', ϕ', and ψ', we obtain:

$$f'=\frac{2\eta(\eta-\phi)+\gamma\phi^2}{f-(\eta-\phi)^2\psi}\frac{\psi f}{\eta}; \tag{16}$$

$$\phi'=\frac{f'-\gamma\psi\phi}{\gamma\psi(\eta-\phi)}; \tag{17}$$

$$\psi'=\frac{(\eta\phi'+\phi)\psi}{(\eta-\phi)\eta}, \tag{18}$$

which can be used to calculate the non-dimensional functions f, ϕ, and ψ by numerical integration when the boundary values of f, ϕ, and ψ are known.

BOUNDARY CONDITIONS AT THE SHOCK WAVE

When the shock wave remains sufficiently strong, and assuming that air is a perfect gas with constant specific heats, the pressure p_1, density ρ_1, and flow velocity u_1, immediately behind the shock wave approach their asymptotic values,

$$\frac{p_1}{p_0}=\frac{2\gamma}{\gamma+1}\frac{U^2}{a^2}, \tag{19}$$

$$\frac{\rho_1}{\rho_0}=\frac{\gamma+1}{\gamma-1}, \tag{20}$$

$$\frac{u_1}{U}=\frac{2}{\gamma+1}, \tag{21}$$

where $U\equiv dR/dt$ is the radial velocity of the shock wave. Hence, according to Eqs. (4), (5), (6), (10), (14), (15), (19), (20), and (21), the boundary values of f, ψ, and ϕ at the shock wave are approximately given by

$$f(1)\approx 2\gamma/(\gamma+1), \tag{19a}$$

$$\psi(1)\approx(\gamma+1)/(\gamma-1), \tag{20a}$$

$$\phi(1)\approx 2/(\gamma+1). \tag{21a}$$

TABLE I. Numerical solution for $\gamma=1.4$. [Note that $\eta=r/R$, $f=(a^2/U^2)(p/p_0)$, $\psi=\rho/\rho_0$, and $\phi=u/U$.]

η	f	ψ	ϕ
1.000	1.1667	6.000	0.8333
0.995	1.1210	5.575	0.8257
0.990	1.0788	5.190	0.8182
0.985	1.0398	4.840	0.8107
0.980	1.0036	4.521	0.8033
0.97	0.9365	3.940	0.7888
0.96	0.8789	3.456	0.7747
0.95	0.8291	3.050	0.7610
0.94	0.7858	2.706	0.7477
0.93	0.7481	2.412	0.7348
0.92	0.7150	2.160	0.7223
0.91	0.6859	1.941	0.7101
0.90	0.6602	1.750	0.6983
0.88	0.6146	1.416	0.6753
0.86	0.5790	1.159	0.6536
0.84	0.5509	0.958	0.6331
0.82	0.5285	0.798	0.6135
0.80	0.5105	0.668	0.5949
0.78	0.4959	0.561	0.5770
0.76	0.4841	0.473	0.5598
0.74	0.4745	0.399	0.5431
0.70	0.4588	0.274	0.5107
0.65	0.4462	0.165	0.4721
0.60	0.4392	0.097	0.4352
0.55	0.4354	0.055	0.3989
0.50	0.4335	0.029	0.3627
0.40	0.4317	0.000	0.2901
0.30	0.4317	0.000	0.2176
0.20	0.4317	0.000	0.1451
0.10	0.4317	0.000	0.0725
0.00	0.4317	0.000	0.0000

NUMERICAL SOLUTION FOR $\gamma=1.4$

Numerical solution has been worked out for $\gamma=1.4$ (perfect diatomic gas). For this value of γ, the boundary values of f, ψ, and ϕ at $\eta=1$ are 7/6, 6, and 5/6, respectively, according to Eqs. (19a), (20a), and (21a). Values of f, ψ, and ϕ for $\eta<1$ were then calculated step by step according to Eqs. (16), (17), and (18). Because of the very steep slopes experienced in Taylor's calculations for the f and ψ curves near $\eta=1$, smaller steps were taken at the early stages of the present calculation to replace his iteration method. The numerical results are given in Table I and are shown in the curves of Fig. 1. Comparison of the present results with those of Taylor shows that the distribution functions f, ψ, and ϕ for the cylindrical and the spherical shock waves are very much alike.

ENERGY AND DECAY LAWS FOR THE CYLINDRICAL SHOCK WAVE

The total energy of the disturbance per unit length of the cylindrical shock wave is given by

$$E=2\pi\int_0^R \rho\left(C_v T+\frac{1}{2}u^2\right)r\,dr;$$

$$=2\pi\int_0^R \left(\frac{p}{\gamma-1}+\frac{1}{2}\rho u^2\right)r\,dr, \quad (22)$$

where C_v is the constant-volume specific heat of the gas; or, in terms of the non-dimensional distribution functions,

$$E=2\pi\rho_0 A^2\int_0^1\left[\frac{1}{\gamma(\gamma-1)}f+\frac{1}{2}\psi\phi^2\right]\eta\,d\eta, \quad (23)$$

which shows that the total energy of the disturbance is time-independent. For $\gamma=1.4$, the integral in Eq. (23) can be readily integrated by using the numerical values of f, ψ, and ϕ given in Table I. If we do this, we obtain

$$E=3.85\rho_0 A^2. \quad (24)$$

By integrating Eq. (10), and by using Eq. (24), we obtain a relation between the radius R of the shock wave, and the time t after a finite amount of energy E per unit length is suddenly released in the atmosphere of density ρ_0 to initiate the shock wave,

$$R=(2At)^{1/2}=1.009(E/\rho_0)^{1/4}t^{1/2}. \quad (25)$$

From either Eq. (10) or Eq. (25), we obtain the decay law for the radial velocity of the shock wave,

$$U=A/R=dR/dt=0.505(E/\rho_0)^{1/4}t^{-1/2}. \quad (26)$$

According to Eqs. (4), (10), (14), and (26), the pressure p is given by

$$p=p_0\frac{U^2}{a^2}f(\eta)=0.182(\rho_0 E)^{\frac{1}{2}}t^{-1}f(\eta). \quad (27)$$

Thus, the pressure immediately behind the shock wave p_1 decays with time according to the law,

$$p_1=0.212(\rho_0 E)^{1/2}t^{-1}, \quad (28)$$

since Eq. (19a) gives $f(1)=7/6$ when $\gamma=1.4$.

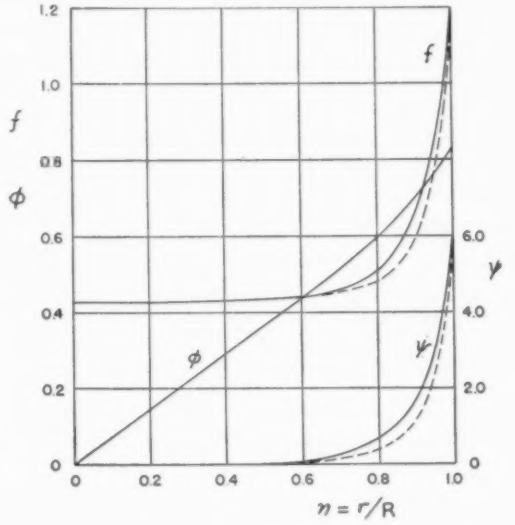

FIG. 1. Numerical solution for $\gamma=1.4$. Solid curves are plotted according to values given in Table I. Dotted curves are the corresponding distribution functions for the spherical shock wave, taken from reference 1 for comparison.

It is interesting to see that, by combining Eq. (28) with Eq. (25), we obtain a simple relation between p_1 and R which is independent of the atmospheric density ρ_0:

$$p=0.216E/R^2. \tag{29}$$

From the perfect gas law, the temperature T is given by

$$T/T_0=p\rho_0/p_0\rho, \tag{30}$$

where T_0 is the temperature of the undisturbed atmosphere. Making use of Eqs. (5) and (27), we obtain

$$\frac{T}{T_0}=0.182\frac{(\rho_0E)^{1/2}}{p_0t}\frac{f(\eta)}{\psi(\eta)}. \tag{31}$$

DISCUSSION

The simple results from this analysis may be used to estimate the propagation and decay of the disturbance left behind a cylindrical shock wave. Such a shock wave may be produced by the explosion of a long thin wire, or by a long intense electrical discharge in air such as the thunderbolt, or by any other mechanism in which a large amount of energy is suddenly released (that is, in a time short compared with the time interval during which the growth of the shock wave is studied) along a straight path in a gaseous atmosphere.

As pointed out in the introductory section, this analysis can also be applied to certain axially symmetrical hypersonic flow problems[3] where the axial flow component may be neglected and hence the radial flow may be considered as locally one-dimensional, (i.e., only one space variable involved). As an example, when a meteor, or a hypersonic missile, is shooting through the atmosphere at great speed, the shock envelope at distances sufficiently far behind the flying object can be considered as locally one-dimensional. Thus, if we know the energy transferred to the atmosphere per unit path length E (which, incidentally is the same as the total aerodynamic drag of the missile) at a distance x behind the flying object, then the radius R of the shock envelope at this station will be given by Eq. (25) where t is interpreted as the time elapsed after the passage of the object. If, for instance, the object is flying at constant velocity V, then $t=x/V$, and hence according to Eq. (25), the shock envelope is a paraboloid given by (for $x\gg$dimension of the meteor),

$$R=1.009(E/\rho_0)^{1/4}(x/V)^{1/2}.$$

As mentioned before, the results of this type of analysis cease to be accurate after the shock strength has decayed to the point where the pressure ratio across the shock wave is no longer large (say, about 10) compared with unity. This is simply due to the fact that for weak shock waves, the density ratio across the shock front will not be a constant so that the boundary values for the functions f, ψ, and ϕ at the shock front cannot be approximated by (19a), (20a), and (21a). Consequently, the similarity assumptions (4), (5), and (6) cannot be satisfied.

Taylor[2] has pointed out that the constant specific heat assumption is definitely not realistic for air at high temperature due to the effects of increased vibrational heat capacity, dissociation, ionization, radiation, etc.; however he found that his theoretical prediction of the radial growth of the spherical shock wave with time agreed surprisingly well with experiment (observation of the first nuclear explosion in New Mexico). Taylor thought that the good agreement between theory and experiment was probably due to the neutralizing effects of radiation and other accompaniments of high temperature, so that the whole system behaved as though γ has an effective value of 1.4. If this is true, then it can be expected that the results from the present analysis would give a reasonably good prediction of the radius growth of the cylindrical shock wave with time. Also, because the pressure immediately behind the shock wave is approximately equal to ρ_0U^2 and is quite insensitive to variations of specific heats of the gas, it is expected that the present results will be quite good for predicting the pressure behind the cylindrical shock wave. However, on account of the unrealistic constant specific heat assumption, it appears doubtful that the theory would predict other quantities, especially density, and temperature distributions, with comparable degree of accuracy.

ACKNOWLEDGMENT

The author is indebted to Professor A. R. Kantrowitz, for suggesting this problem, and for his advice. He also wishes to thank Professor F. L. Whipple, as well as Professor Kantrowitz, for his encouragement to submit this work for publication.

Thermal Diffusivity of Metals at High Temperatures*

P. H. SIDLES AND G. C. DANIELSON
Institute for Atomic Research, Iowa State College, Ames, Iowa

(Received May 27, 1953)

A modified Ångström method for measuring thermal diffusivity and hence thermal conductivity of metals has been developed. Like previously reported dynamic methods, this method uses a heat source, whose temperature varies sinusoidally with time, located at one end of an effectively infinite rod. Unlike these methods, only one period of the heat pulse is required to eliminate the unknown coefficient determining the heat lost by radiation since both velocity and amplitude decrement of the heat pulse are measured. In addition to providing greater reliability at high temperatures by using only one period, the new method is faster in taking data and simpler in computation. The thermoelectric potentials from two thermojunctions are amplified and plotted on a Brown electronic recorder in order to obtain a permanent record of all necessary data for computing the thermal diffusivity. Results for copper, nickel, and thorium over the temperature range 0–500°C are given.

INTRODUCTION

TWO of the more important characteristics of metals and alloys in high temperature applications are thermal conductivity and thermal diffusivity, properties which usually depend upon temperature, composition, and past history of the material. In comparing the methods which have been used to measure these quantities, a dynamic method first used by Ångström[1] and later by King[2] and Starr,[3] offers the following advantages:

1. Good thermal contacts between the sample and the heat source and between the sample and the heat sink are not important factors in evaluating the reliability of the measurements.
2. Insulating or guarding the sample to prevent heat losses is not necessary.
3. The thermal diffusivity is determined at a fixed temperature rather than as an average value over a large temperature range.
4. Sample dimensions and shape are such that only a small amount of material is required and no difficult fabrication problems are encountered.

Unfortunately, dynamic methods do not measure thermal conductivity. Instead, they measure thermal diffusivity (k) which is related to the thermal conductivity (K) by the relation

$$K=kc\rho, \tag{1}$$

where c is the specific heat and ρ is the density. Since K and k are the fundamental thermal properties for steady-state and for nonsteady-state problems, respectively, it is possible to measure these quantities independently. Equation (1) can then be used to calculate the specific heat. This investigation is concerned primarily with the measurement of the least known of these two fundamental thermal properties, namely, thermal diffusivity.

THEORY

Under steady-state conditions the theory of heat conduction is based upon the following hypothesis suggested by experiment.

$$Q=KAt(T_2-T_1)/d. \tag{2}$$

In this equation Q is the quantity of heat which flows in time t through a plate of homogeneous material of area A and uniform thickness d when a temperature difference (T_2-T_1) is maintained between its two faces. The constant of proportionality (K) is called the thermal conductivity of the material. Since K is a slowly varying function of temperature, Eq. (2) may be applied to obtain an average value of K over the temperature range (T_2-T_1).

Under nonsteady-state conditions, however, Eq. (2) is not very useful. Instead of being concerned with quantities of heat, the nonsteady-state problem is concerned with temperature as a function of position and time. The fundamental equation for the temperature (θ) of a body which, in addition to conducting heat, is radiating heat to its surroundings is

$$k\Delta\theta=(\partial\theta/\partial t)+\mu\theta, \tag{3}$$

where k is the thermal diffusivity, Δ is the Laplacian operator, t is the time, and μ is the radiation constant.

This investigation is concerned with the determination of the thermal diffusivity of a semi-infinite, thin, radiating rod. The temperature at any position x and time t in a rod, thin enough so that radial temperature gradients are unimportant, may be found by solving the one dimensional partial differential equation

$$k(\partial^2\theta/\partial x^2)=(\partial\theta/\partial t)+\mu\theta. \tag{4}$$

If a heat source, whose temperature varies periodically with time, is located at one end of this semi-infinite rod, the boundary conditions will be:

$$\begin{aligned}&\theta \text{ is periodic} && \text{at } x=0,\\ &\theta=0 && \text{at } x=\infty.\end{aligned} \tag{5}$$

* Work was performed in the Ames Laboratory of the U. S. Atomic Energy Commission. Abstract of this paper appeared in Phys. Rev. 85, 710 (1952).

[1] A. J. Ångström, Ann. Physik Leipzig 114, 513 (1861); Phil. Mag. 25, 130 (1863); 26, 161 (1863).
[2] R. W. King, Phys. Rev. 6, 437 (1915).
[3] C. Starr, Rev. Sci. Instr. 8, 61 (1937).

The temperature at any position x will be periodic in time with the same period ($T=2\pi/n\omega$) as the temperature at $x=0$ and can therefore be expressed by the Fourier sum

$$\theta(x,t)=\sum_{n=0}^{\infty}P_n(p)\cos n\omega t+Q_n(x)\sin n\omega t. \tag{6}$$

The unknown coefficients $P_n(x)$ and $Q_n(x)$ are determined by the ordinary differential equations,

$$\begin{aligned} k(d^2P_n/dx^2)-\mu P_n&=n\omega Q_n,\\ k(d^2Q_n/dx^2)-\mu Q_n&=-n\omega P_n, \end{aligned} \tag{7}$$

obtained by substituting (6) in (4) and equating coefficients of $\sin n\omega t$ and $\cos n\omega t$. Solving these equations[4] for P_n and Q_n and applying the boundary conditions from (5) the results[5] are

$$\begin{aligned} P_n(x)&=A_n\exp(-\alpha_n x)\cos(\beta_n x-\epsilon_n),\\ Q_n(x)&=A_n\exp(-\alpha_n x)\sin(\beta_n x-\epsilon_n), \end{aligned} \tag{8}$$

where A_n and ϵ_n are arbitrary constants and

$$\begin{aligned} \alpha_n&=\{(\tfrac{1}{2}k)[(\mu^2+n^2\omega^2)^{\frac{1}{2}}+\mu]\}^{\frac{1}{2}},\\ \beta_n&=\{(\tfrac{1}{2}k)[(\mu^2+n^2\omega^2)^{\frac{1}{2}}-\mu]\}^{\frac{1}{2}}. \end{aligned} \tag{9}$$

Substituting for P_n and Q_n in (6) the general solution is therefore

$$\theta(x,t)=\sum_{n=0}^{\infty}A_n\exp(-\alpha_n x)\cos(n\omega t-\beta_n x+\epsilon_n). \tag{10}$$

In this experimental investigation an additional restriction imposed is that the temperature at $x=0$ shall be not only periodic but also sinusoidal in time; that is,

$$\theta(0,t)=A_0+A_1\cos(\omega t+\epsilon_1). \tag{11}$$

The general solution given in (10) then reduces to two terms:

$$\begin{aligned} \theta(x,t)=&A_0\exp(-\alpha_0 x)\\ &+A_1\exp(-\alpha_1 x)\cos(\omega t-\beta_1 x+\epsilon_1). \end{aligned} \tag{12}$$

These temperature oscillations will be propagated along the rod with a velocity

$$v=\frac{\omega}{\beta_1}=\frac{2\pi}{T}\left[\frac{2k}{(\mu^2+4\pi^2/T^2)^{\frac{1}{2}}+\mu}\right]^{\frac{1}{2}}. \tag{13}$$

The amplitude decrement will be

$$q=\exp(-\alpha_1 x_1)/\exp(-\alpha_1 x_2)=\exp\alpha_1(x_2-x_1)=\exp(\alpha_1 L).$$

Hence,

$$\ln q=\alpha_1 L=L\left[\frac{(\mu^2+4\pi^2/T^2)^{\frac{1}{2}}-\mu}{2k}\right]^{\frac{1}{2}} \tag{14}$$

where L is the distance between any two points (x_1 and x_2) on the rod.

METHODS OF MEASUREMENT

A. Velocity Method

Following King,[2] if measurements are made of the velocities (v_1 and v_2) of the temperature oscillations between two points along the rod for two different periods (T_1 and T_2) of the sinusoidal boundary condition, these two substitutions in (13) can be used to eliminate the radiation constant (μ). Solving the two simultaneous equations for the thermal diffusivity (k) gives the result:

$$k=\frac{T_1T_2v_1v_2}{4\pi}\left[\frac{v_1^2-v_2^2}{T_2^2v_2^2-T_1^2v_1^2}\right]^{\frac{1}{2}}. \tag{15}$$

B. Amplitude Method

Similarly following Starr,[3] if measurements are made of the amplitude decrements q_1 and q_2 corresponding to two different periods T_1 and T_2 of the sinusoidal boundary condition, these two substitutions in (14) can be used to eliminate the radiation constant (μ). Solving these two simultaneous equations for the thermal diffusivity (k) gives the result:

$$k=\frac{\pi L^2}{T_1\ln q_1\ln q_2}\left[\frac{a^2-b^2}{b^2-1}\right], \tag{16}$$

where $a=T_1/T_2$ and $b=\ln q_1/\ln q_2$.

C. Modified Ångström Method[1,6]

Both of the foregoing methods require that measurements be made over a considerable period of time. After the necessary data for period T_1 has been taken, the period of the sinusoidal boundary condition must be changed and the sample allowed to reach an equilibrium condition for the new period T_2 before the remaining data can be taken. During the time required to reach a second equilibrium and take a second set of data, errors may enter into the experiment because of surface reactions altering the radiation constant or to annealing altering the thermal diffusivity. Such factors become increasingly important at high temperatures.

A modification of the original method used by Ångström reduces the possibility of errors arising from the variation of experimental conditions with time and reduces the time required for making measurements. Instead of measuring either the amplitude decrement or the velocity for two periods of the sinusoidal boundary condition, both the amplitude decrement and the velocity are measured for a single period. From (14) and (13):

$$\alpha_1=\ln q/L,\quad \beta_1=\omega/v. \tag{17}$$

[4] H. S. Carslaw and J. C. Jaeger, *Conduction of Heat in Solids* (Oxford University Press, London, 1947), p. 116.

[5] The solutions for P_n and Q_n may be easily checked by substituting P_n and Q_n from (8) into (7) and noticing from (9) that $\alpha_n^2-\beta_n^2=\mu/k$ and $\alpha_n\beta_n=n\omega/2k$.

[6] T. Preston, *Theory of Heat* (Macmillan Company, Ltd., London, 1929), fourth edition, Art. 309, p. 627.

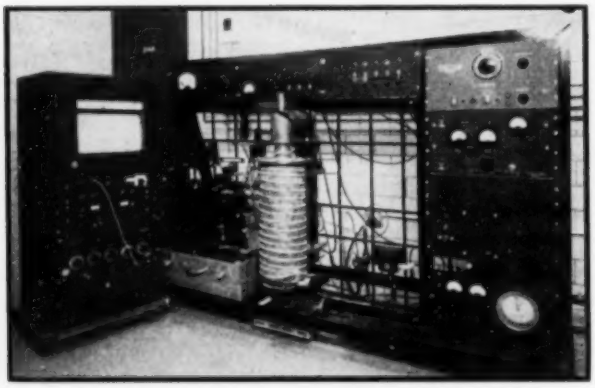

FIG. 1. Photograph of apparatus for measuring the thermal diffusivity of metals.

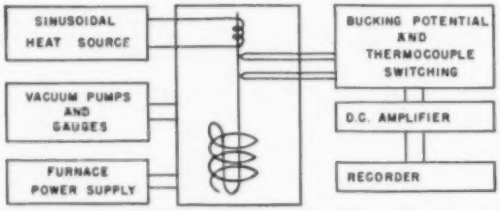

FIG. 2. Block diagram of apparatus for measuring thermal diffusivity.

Hence,

$$\alpha_1\beta_1=\omega \ln q/Lv; \tag{18}$$

but from (9)

$$\alpha_1\beta_1=\omega/2k. \tag{19}$$

Therefore, the thermal diffusivity is

$$k=Lv/2 \ln q. \tag{20}$$

It is apparent that this expression for k is not only simpler in form but also has the advantage that it does not explicitly contain the period of the sinusoidal boundary condition. The smaller number of quantities which must be measured contributes to the greater reliability and simplification of this method.

APPARATUS

A block diagram of the apparatus is shown in Fig. 2. Samples were approximately $\frac{1}{8}$ inch in diameter and at least 50 cm in length. These dimensions adequately fulfill the requirement for a thin, semi-infinite rod. Two butt-welded AWG-28 chromel-alumel thermocouples were peened into holes drilled along a diameter of the sample with a No. 79 drill. It was thus possible to locate the thermocouple junction at the center of the rod. The thermocouple separation (L) was selected so that the time required for a heat pulse to travel between the two thermocouples could be conveniently measured. A distance of several centimeters separated the heat source, whose temperature varied sinusoidally with time, and the nearest thermocouple; thus, any irregularity in the cross-sectional distribution of the heat

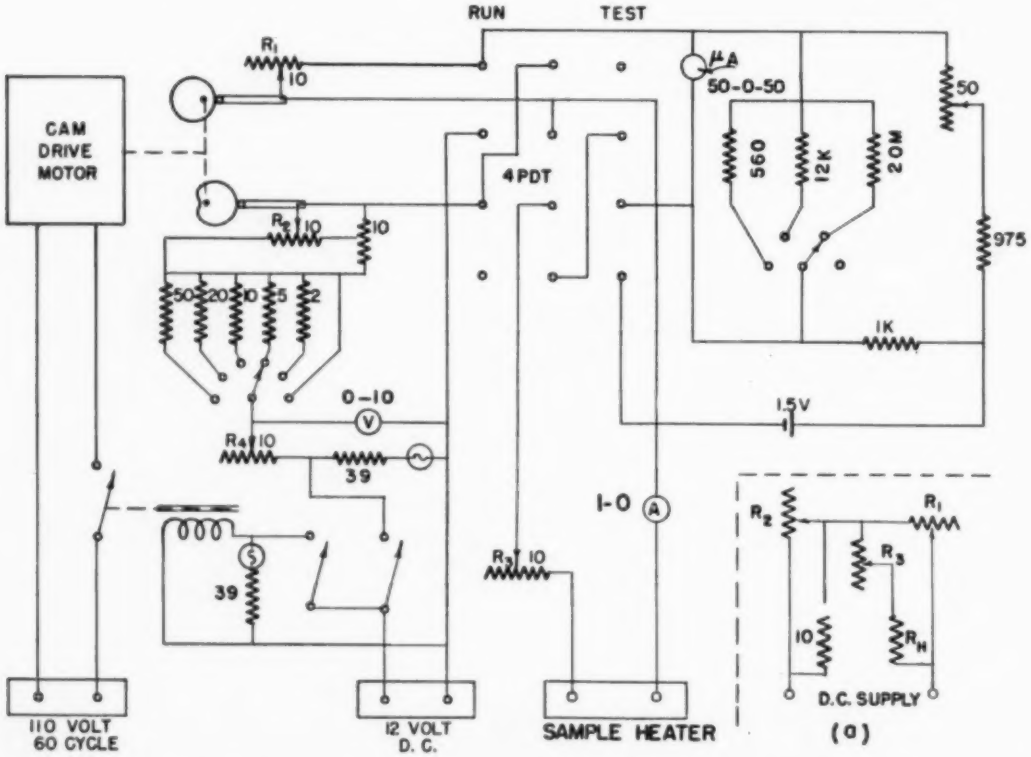

FIG. 3. Schematic diagram of generator for sinusoidal boundary condition. Figure 3(a) is a simplified diagram of the generator.

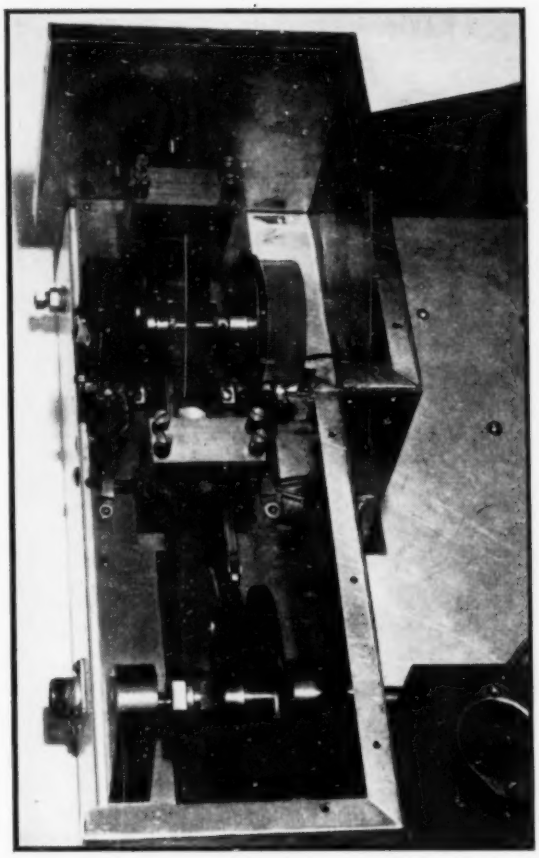

FIG. 4. Photograph of cam-driven mechanism for generating sinusoidal boundary condition.

pulse would be smoothed out before it reached the first thermocouple. The remainder of the sample was coiled into a helix as shown in Fig. 2 so that it could be conveniently accommodated in a small vacuum furnace.

The generator shown in Fig. 3 supplied a periodically varying current to the sample heater shown in Fig. 5. Figure 3(a) shows only the basic elements of the generator. The following discussion will show that this generator-heater combination provided the sinusoidal temperature at the $x=0$ end of the sample as required by Eq. (11).

In Figs. 3 and 3(a), the resistances r_1 and r_2 are 10 ohm, 10-watt General Radio type 214A potentiometers. As shown in Fig. 3, these resistances were varied by cams which were driven at $\frac{1}{2}$ rpm by a synchronous motor. The current through the sample heater r_h will depend upon the relative resistances of r_1 and r_3+r_h, and will vary as r_1 varies. Since this r_1, r_3, r_h combination will not be a constant load on the dc supply, any series resistance for reducing the average power input to the sample heater will alter the waveform of the current supplied to r_h. Under these conditions a different cam would be required for each power input. To permit a range of power inputs without changing cams the potentiometer r_2 and the parallel 10 ohm resistance were provided. The cam driving r_2 was cut so that the entire resistance combination in Fig. 3(a) would be a constant 10-ohm load on the dc supply. Since r_h will vary slightly with different heaters and will also change with the ambient temperature, a compensating resistance r_3 was provided. The sample heaters used had resistances slightly less than 10 ohms and r_3 was adjusted so that $r_3+r_h=10$ ohms. Under these conditions,

$$[10r_2/(10+r_2)]+[10r_1/(10+r_1)]=10. \qquad (21)$$

Since a constant current I_0 flowed through the resistance combination, the current I_h through the sample heater r_h was

$$I_h=I_0r_1/(r_1+10). \qquad (22)$$

It will be shown later that, if I_h varies as $|\sin\phi/2|$, the required boundary condition will be satisfied.

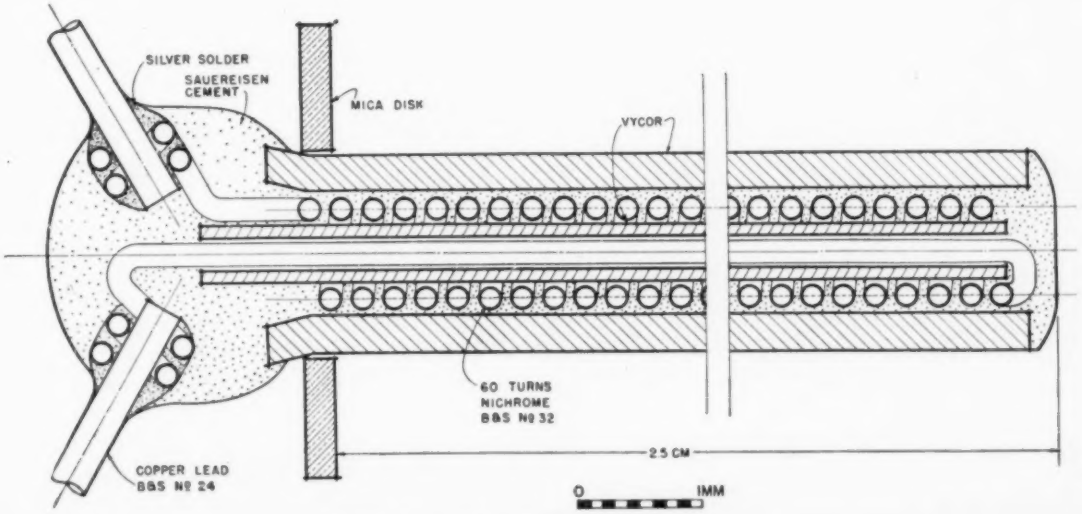

FIG. 5. Detail diagram of sample heater.

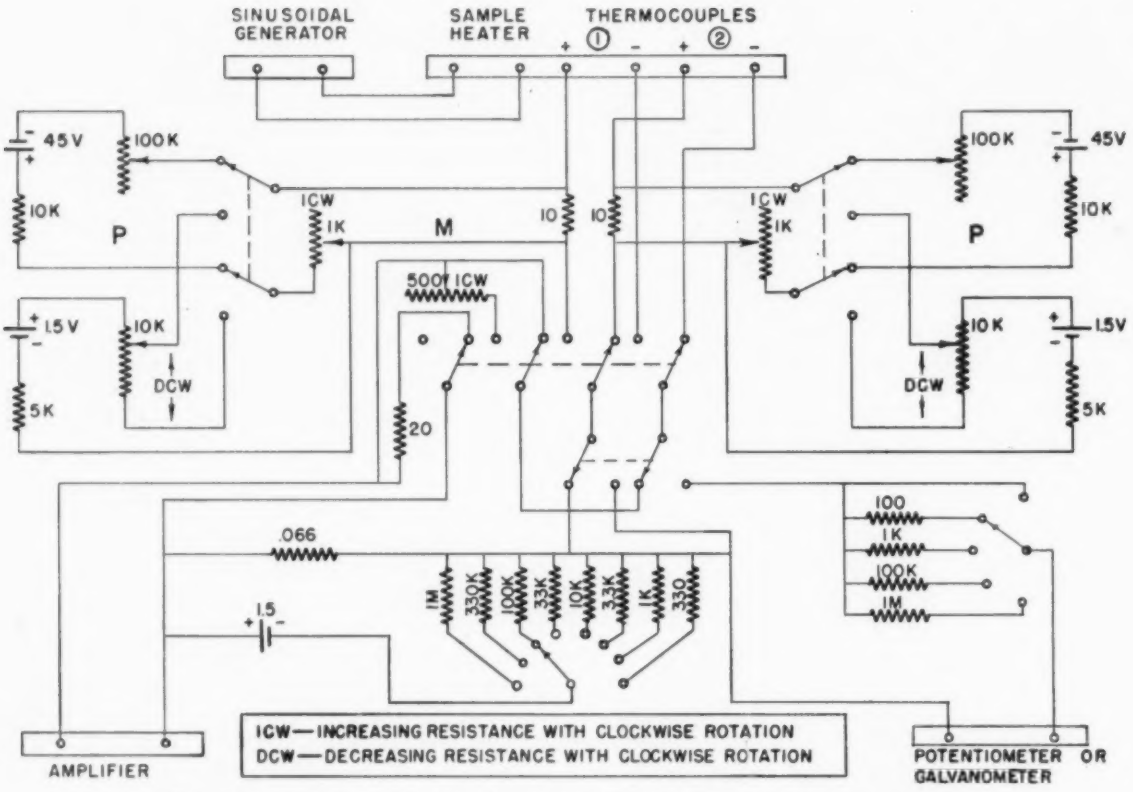

FIG. 6. Schematic diagram of bucking-potential and thermocouple-switching apparatus.

Therefore,

$$I_h = I_0 r_1/(r_1+10) = A\,|\sin\phi/2|, \qquad (23)$$

where A is an arbitrary amplitude. However, since $r_h+r_2=r_1(\max)=10$, A is determined to be $I_0/2$. Substituting this value for A and solving (23) for r_1:

$$r_1 = \frac{10\,|\sin\phi/2|}{2-|\sin\phi/2|}. \qquad (24)$$

Knowing r_1, r_2 is determined from (21). The shapes of the cams were then determined by calculating r_1 and r_2 for different values of ϕ, manually positioning the potentiometer sliders to the calculated value and measuring the required radii.

The heat produced in the sample heater is given by

$$I_h^2 R = \frac{I_0^2 R}{4}\,|\sin\phi/2|^2 = \frac{I_0^2 R}{4}\left[\frac{1-\cos\phi}{2}\right]$$

$$= A_0 + A_1\cos\omega t. \qquad (25)$$

The temperature of the sample adjacent to the heater is directly proportional to the heat produced in the heater if the temperature difference between the sample and the heater is small. Thus, the boundary condition requirement of Eq. (11) is satisfied.

The resistances selected by SW_2 were provided so that the voltage supplied to the resistance combination shown in Fig. 2(a) could be conveniently changed. Thus, the average power supplied to the sample heater r_h could be easily varied. Resistance r_4 and voltmeter V were provided to permit compensation for changes in battery voltage. Twelve volt storage batteries provided dc power and r_4 was adjusted so that the meter indicated 10 volts. The Wheatstone bridge and the RUN-TEST switch shown in Fig. 2 were provided to permit rapid adjustment of r_3 so that $r_3+r_h=r_1(\max)$.

Constructional details of the sample heater are shown in Fig. 5. This heater fitted loosely in a hole bored axially into the $x=0$ end of the sample with a No. 50 drill. With this type of heater the solid angle subtended by the sample is nearly 4π, and almost all of the energy supplied to the heater is transferred to the sample by radiation. A representative power input to the sample heater was $\frac{1}{2}$ watt. This was sufficient input power to cause a temperature variation of the order of 1°C at a point in the sample 3.5 cm from the heater. No significant distortion of the heat wave due to the finite length of the heater was observed.

The heat pulses generated at $x=0$ were measured at two points x_1 and x_2 by thermocouples embedded in the sample. The output voltages of these two thermocouples were fed into the circuit shown in Fig. 6. The purpose of this circuit was to provide means for selecting which thermocouple output would be fed to the amplifier and to oppose the thermocouple outputs with dc

potentials which corresponded roughly to the ambient temperature at which the measurements were made. When this bucking potential was applied, only the sinusoidal component of the thermocouple output remained to be amplified and recorded. This bucking potential also provided a convenient means of positioning the thermocouple outputs on the recorder chart. With no bucking potential applied, the outputs of the thermocouples could be switched to a potentiometer and the ambient temperature of the sample measured.

Since the amplitude of the thermocouple nearest the sample heater was considerably larger than that of the farther thermocouple, a means was provided for attenuating the output of the nearest thermocouple so that the outputs of both thermocouples could be recorded using the same amplifier gain setting. This simplified the calibration procedure in that only one amplifier gain setting had to be calibrated. Calibration signals provided by the circuit shown in Fig. 6 were used for calibration purposes.

A Liston-Folb Model 10-dc amplifier and a high-speed variable range, variable suppression Brown electronic strip-chart recorder were used to make a record of the data necessary for calculating the thermal diffusivity of the sample. The Liston-Folb amplifier had a maximum gain of 80 db and a frequency response sufficient to follow a one cycle per second signal. The Brown recorder had a full-scale pen-travel time of 2 seconds which was more than ample for it to follow the signals used in this investigation. Since the output voltage of the Liston-Folb amplifier was quite large, a voltage divider was required between the amplifier and the recorder.

A cross section of the furnace used for maintaining the ambient temperature of the sample is shown in Fig. 7. The temperature of this furnace was controlled either manually using Powerstat variable transformers or automatically using a MacDonald Model 18 thyratron temperature controller. The furnace was evacuated to a pressure of 10^{-4} mm Hg. Water cooling was used throughout, the cold water going first to the small chamber shown in the upper left quadrant of Fig. 7 which functioned as a constant temperature reference junction for the thermocouples. Four copper radiation shields were used to prevent excessive heat loss.

EXPERIMENTAL PROCEDURE

After the sample had been installed in the furnace, the furnace evacuated and temperature equilibrium reached; the following calibration was carried out for each thermocouple to determine the sensitivity (microvolts/millimeter) of the amplifier-recorder system. The ratio dial (M in Fig. 6) and the amplifier gain were turned to the dial settings for which calibration was required. The output of one of the thermocouples was switched to the amplifier input and the positioning controls (P in Fig. 6) for that thermocouple used to position the recorder pen near the lower end of the recorder chart. Using the calibrating equipment shown in Fig. 6, a known calibrating potential was then inserted in the thermocouple circuit. This caused an upscale pen deflection. The calibrating potential was then removed, returning the recorder pen to its original position. An identical procedure was followed for the second thermocouple. When all necessary calibration data had been obtained the chart was removed from the recorder and the pen displacements accurately measured. Dividing each calibration voltage by the pen displacement resulting from that voltage gave the sensitivity of the amplifier-recorder system for the

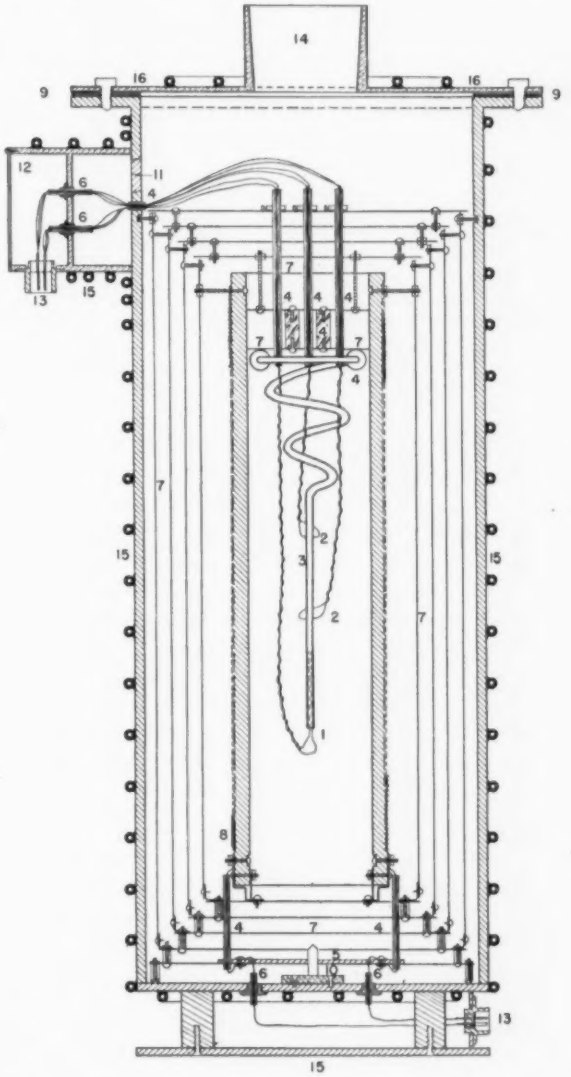

FIG. 7. Cross-section diagram of furnace. 1. Sample heater 2. Thermocouples, 3. Sample. 4. Ceramic insulators. 5. Teflon insulator. 6. Stupakoff vacuum seals. 7. Copper or stainless steel radiation shields. 8. Alundum core wound with molybdenum wire. 9. Neoprene gasket, 10. Brass centering pin. 11. Plug. 12. Water-cooled chamber for thermocouple reference junctions. 13. Amphenol connectors. 14. Tapered connection to vacuum pumps. 15. Copper cooling coils on steel furnace wall. 16. Water-cooled brass lid.

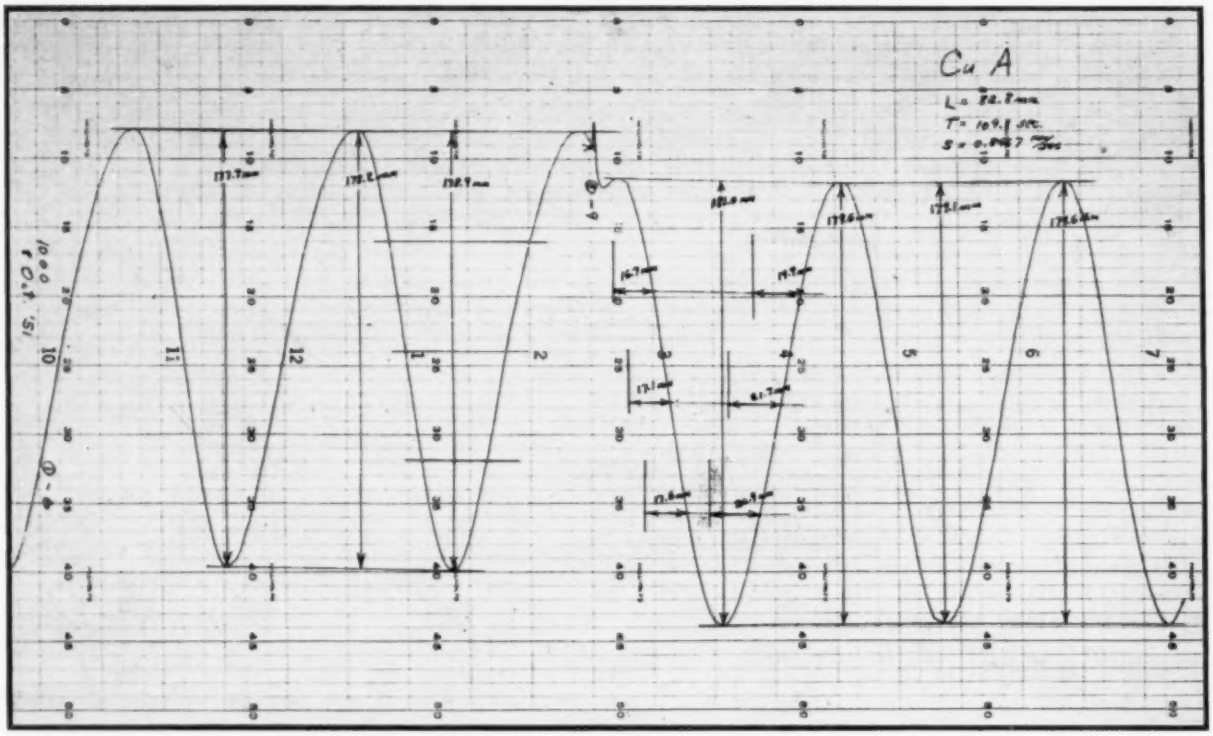

FIG. 8. Typical record illustrating the form in which data is obtained and the manner in which measurements are made to obtain values of q and m for substitution in Eq. 26.

conditions under which the calibration had been performed.

After the system had been calibrated the sinusoidal boundary condition was applied and the sample allowed to reach equilibrium. The outputs of both thermocouples were then positioned on the recorder chart and the output of the thermocouple nearest the sinusoidal heater was recorded for several cycles. Immediately after either a maximum or a minimum was recorded, the output of the other thermocouple was switched to the amplifier input and several cycles of its output were recorded. A typical record is shown in Fig. 8. The amplitudes were measured and the average amplitude for each thermocouple was calculated. The calibration data previously obtained was used to convert these distance amplitudes to voltage amplitudes. The ratio of the voltage amplitudes for the two thermocouples is the amplitude decrement q.

The velocity v of the temperature pulse as it passed between the two thermocouples was found in the following manner. The one-quarter, half, and three-quarter points were geometrically determined on the chart for the nearest cycle on each side of the point at which the thermocouples were switched. The six points thus determined for the output of the thermocouple nearest the sinusoidal heater were then advanced along the chart a distance corresponding to one cycle. The distance m along the chart separating each of these points from the corresponding point in the output of the farthest thermocouple, together with the chart speed (s) and the thermocouple separation (L), determines the velocity (v).

Since $v=Ls/m$ the expression for the thermal diffusivity as given in Eq. (20) can be written

$$k=\frac{Lv}{2\ln q}=\frac{L^2S}{2m\ln q}. \tag{26}$$

If reliable specific heat and density data are available for the metal being measured and for the temperature at which the measurements were made, Eq. (1) can be used to calculate the thermal conductivity.

RESULTS

This experimental procedure was used to determine the thermal diffusivities of copper, nickel, and thorium in the temperature range from approximately 30°C to 500°C.

The thermal diffusivity of high-purity copper is shown in Fig. 9.[7–9] The most prominent impurity was Ag which comprised less than 0.05 percent of the sample. No detectable Fe, Ca, or Cr and only trace amounts of Si and Pb were present.

[7] C. J. Smithells, *Metals Reference Book* (Interscience Publishers, New York, 1949), p. 456.

[8] Bronson, Chisholm, and Dockerty, Can. J. Research **8**, 282 (1933).

[9] T. Lyman, ed. *Metals Handbook* (The American Society for Metals, Cleveland, 1948), p. 24.

Values of thermal diffusivity calculated using Eq. (1) and reliable thermal conductivity, specific heat, and density data for high-purity copper are also shown in Fig. 9. The measured and calculated thermal diffusivities agree to within about 4 percent. This indicates that the dynamic method can be used to give reliable results. King[2] and Sager[10] also have measured the thermal diffusivity of copper. In general, King's results in the temperature range from 76°C to 362°C are 10 percent lower than the results of this investigation and Sager's results in the temperature range from 95°C to 497°C are 10 percent higher.

The nickel sample which was measured was not of high purity. Chemical analysis showed 97.92 percent nickel. Spectrographic analysis indicated that the major impurities were Mn and Si. Trace quantities of Co, Fe, and Mg were also present. A comparison of the thermal diffusivity of this 97.92 percent Ni at 25°C with thermal diffusivity results by other observers for nickel of various purities is shown in Fig. 10.[11–16] Included in this plot are also some values calculated from reliable thermal conductivity, specific heat, and density data. Figure 10 shows that the measured thermal diffusivity of 97.92 percent Ni is in good agreement with results of other observers. The thermal diffusivity of 97.92 percent Ni in the temperature range from 44°C to 503°C is shown in Fig. 11. An abrupt change in slope is observed at 312°C indicating that this is the Curie point. The Curie point for pure nickel is 353°C. It has been shown[17] that, with the exception of iron and cobalt, addition of impurities to pure nickel causes a shift in the Curie point to lower temperatures. For example, about 1 percent silicon impurity depresses the Curie point from 353°C to about 285°C. The observed Curie point at 312°C is at least consistent with the type and amount of impurity in the 97.92 percent Ni sample. A comparison was made of the observed plot of thermal diffusivity and a similar plot obtained by calculating thermal diffusivities from reliable thermal conductivity, specific heat and density data for high purity nickel. This comparison showed that the two curves had the same general shape but that the measured values were consistently smaller than the calculated values for the same temperature and that the Curie point was shifted as indicated above. This is the behavior that would be expected of an impure sample.

The thermal diffusivity of 99.85 percent thorium is shown in Fig. 12. This plot of thermal diffusivity against temperature is the result of a considerable number of measurements at various temperatures made on six

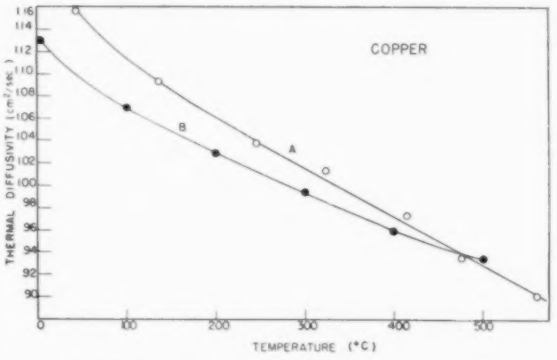

FIG. 9. A. Measured values of the thermal diffusivity of copper. B. Thermal diffusivity of copper calculated from thermal conductivity (reference 7), specific heat (reference 8), and density (reference 9) data.

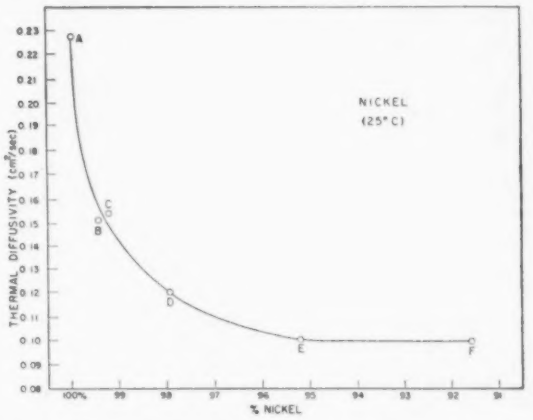

FIG. 10. Thermal diffusivity of nickel *vs* nickel purity. A. Calculated for 99.95 percent nickel using Eq. (1) with $K=0.22$ cal/sec cm °C (reference 11), $c=0.108$ cal/g °C (reference 14), and $\rho=8.902$ g/cm³ (reference 12); B. Calculated for commercial "A" nickel with $K=0.145$ cal/sec cm °C (reference 11), $c=0.108$ cal/g °C (reference 14), and $\rho=8.885$ g/cm³ (reference 12); C. Experimental (reference 15); D. Experimental (reference 16); E. Calculated for commercial "D" nickel with $K=0.115$ cal/sec g °C (reference 11), $c=0.13$ cal/g °C (reference 13), and $\rho=8.78$ g/cm³ (reference 12); F. Experimental (reference 15).

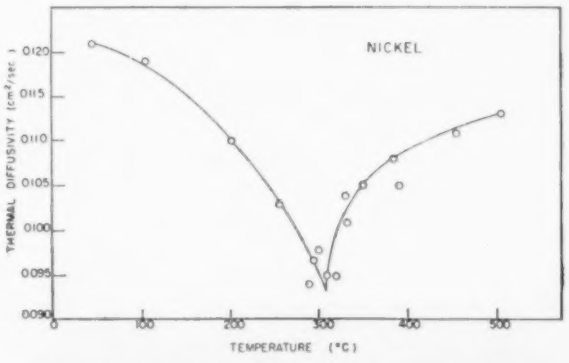

FIG. 11. Thermal diffusivity of 97.9 percent nickel.

[10] G. F. Sager, Rensselaer Polytech. Inst. Bull., Eng. and Sci. Ser. No. 27 (1930).
[11] T. Lyman, editor *Metals Handbook* (The American Society for Metals, Cleveland, Ohio, 1948), p. 26.
[12] Reference 11, p. 25.
[13] Reference 11, p. 1047.
[14] J. S. Marsh, *The Alloys of Iron and Nickel* (McGraw-Hill Book Company, Inc., New York, 1938), Vol. I, pp. 126–130.
[15] R. H. Frazier, Phys. Rev. **39**, 515 (1932).
[16] This investigation.
[17] E. M. Wise and R. H. Schaefer, Metals and Alloys **16**, 426 (1942).

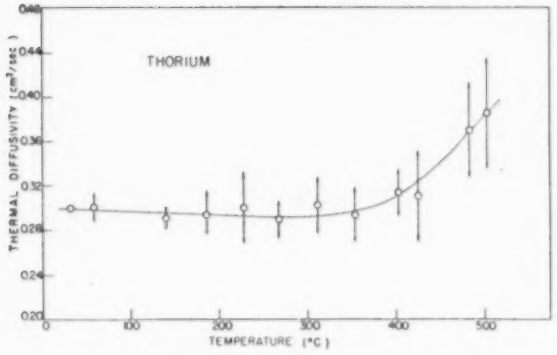

FIG. 12. Thermal diffusivity of 99.85 percent thorium.

different samples of high purity thorium. As shown in Fig. 12 the thermal diffusivity of thorium is nearly constant in the temperature range from 20°C to 400°C. Above 400°C the thermal diffusivity of thorium appears to increase with increasing temperature.

The specific heat of thorium has been found by Griffel and Skochdopole[18] to be 0.1179 joule/g °C at 300°K and by C. F. Miller[19] to be 0.1188 joule/g °C in the temperature range 0–200°C. These results are in good agreement. The density of thorium was found to be 11.557 g/cm³. Using this density value and Griffel and Skochdopole's specific heat values at 300°K, the thermal conductivity of thorium at room temperature has been calculated to be 0.409 watt/cm °C. Since the specific heat[19] of thorium in the temperature range 0–200°C is very nearly the same as the room temperature value and since the thermal diffusivity of thorium is essentially constant in the temperature range from room temperature to 400°C, it is concluded that the thermal conductivity of thorium will be essentially constant from room temperature up to at least 200°C.

DISCUSSION

The range of thermal diffusivities of metals extends from approximately 1.7 cm²/sec for the case of silver to about 0.03 cm²/sec for the case of mercury. Measurements in the thermal diffusivity range from 1.2 to 0.09 cm²/sec have been made using the method of measurement developed during this investigation. There was no indication while using this method that it would not be useful over the entire thermal diffusivity range for metals. There was also no indication that the temperature range over which the method would be useful could not be extended to both higher and lower temperatures than those used in this investigation.

It should be noted, however, that the ambient temperature at which the thermal diffusivity measurement is being made must be held to a tolerance which is of the same order as the amplitude of the heat pulse at the thermocouple farthest from the sample heater. In this investigation this amplitude was about $\frac{1}{4}$°C; thus, this requirement was a stringent one and could limit the extension of this method to much higher temperatures due to difficulty in controlling the ambient temperature to a sufficiently close tolerance. It should be further noted, however, that this ambient temperature requirement need be met only during the time required to take the necessary data. At least two possibilities might be suggested in order to overcome this stability requirement. The furnace for maintaining ambient temperature could be built with a large heat capacity so that it could not change temperature at a rapid rate or the time required to take the necessary data could be reduced so that a slow rate of ambient temperature change would not affect the thermal diffusivity measurement.

In practice it was found that the current supplied to the sample heater could vary considerably from a sinusoidal variation without seriously affecting the measured values of diffusivity. As an extreme case a square wave was supplied to the sample heater with the resulting value for diffusivity differing by only 7.44 percent from that obtained using a sinusoidal variation. A Fourier analysis of the square wave results gave essentially the same diffusivity as was obtained using the sinusoidal boundary condition.

ACKNOWLEDGMENTS

The authors wish to express appriciation to the machine shop personnel of the Ames Laboratory of the U. S. Atomic Energy Commission for their assistance in constructing equipment used in this investigation, to Q. Halbeisen for helping with the measurements and to Dr. J. M. Keller for several valuable discussions of the problem.

[18] Private communication.
[19] Private communication.

Brightness Waves and Transitory Phenomena in the Quenching of Luminescence by Alternating Electric Fields

G. DESTRIAU*
Laboratoire de Luminescence, Faculté des Sciences de Paris, France
(Received May 7, 1953)

Zinc or cadmium sulfide phosphors, especially phosphors having short persistence, are less sensitive to ultra-violet light or to x-rays when they are submitted to the action of an alternating electric field. With a half-wave x-ray generator and an alternating field of frequency equal to the frequency of the potential applied to the x-ray generator (50 cps), and in phase with it, the brightness waves (a curve giving the variation in the instantaneous brightness as a function of time in the interval of a period) are greatly modified. A sharp secondary maximum appears when the field passes through zero in each cycle; the amplitude of this maximum varies quickly during the cycles which immediately follow the application of the field.

If the light is filtered, the shape of the brightness wave varies according to the spectral region which is observed.

INTRODUCTION

IT has already been shown that zinc or cadmium sulfide phosphors are less sensitive to ultraviolet light or x-rays when they are submitted to electric fields, and especially to alternating electric fields.[1–3] For some of these sulfides the phenomenon is masked when the field is first applied by a superimposed momentary enhanced emission (Gudden and Pohl effect). Sulfides having short persistence usually show a negligible Gudden and Pohl effect, or do not show it at all; in general, however, those sulfides used in the preparation of radioscopic screens are very sensitive to the quenching effect and they were therefore chosen as the material to be used in the study of this phenomenon.

This quenching effect may be represented schematically by Fig. 1. The variation of the average brightness under the action of x-rays with no applied field is represented by curve *OA*. If now an alternating potential is applied to the cell, there is an abrupt drop *AB*; then, with the field maintained, the average brightness progressively increases, following *BC* to reach the state represented by the plateau *CD*. When the field is removed there is, in general, a slight drop *DE*; the brightness then follows *EF* until it reaches the same value as was obtained at *A* before the field was applied. If the field is applied before the x-rays and maintained during the irradiation, the average brightness follows the curve designated *OHCDI*.

The writer has studied, in collaboration with Mattler,[4] various features of this quenching; but these studies, made by means of a barrier-layer type of photoelectric cell, represent an average brightness and illustrate principally the "permanent" quenching effect (plateau *CD*). However, before this permanent state can be established, the application of the alternating electric field is immediately followed by a transitory period (represented by *BC*) during the course of which complex and exceedingly fleeting phenomena occur.

In the present work, it is first proposed to study primarily this transitory period which immediately follows the application of the field and, furthermore, to correlate the phenomenon with each half-cycle of the field.

EXPERIMENTAL ARRANGEMENT

The experimental arrangement includes an electron photomultiplier in conjunction with an oscilloscope. The sensitive materials are excited by means of a beam of x-rays. In order to follow the transitory perturbations which immediately follow the application of the field, the screen of the oscilloscope is photographed with 16-mm movie film. The speed of the camera is adjusted to suit the sweep speed of the oscilloscope.

After development the film is projected so as to reproduce the appearance of the phenomena. With these

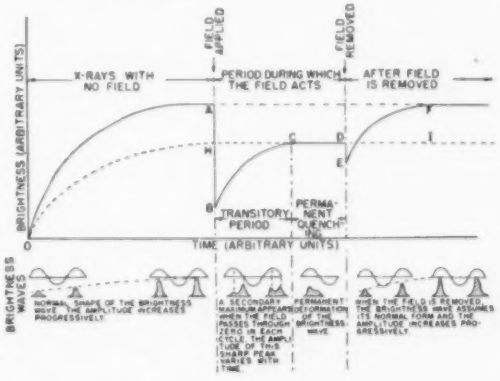

FIG. 1. Variation in time of the average brightness stimulated by a beam of x-rays. Curve *OA* and dotted line *AF* when no electric field is applied. Curve *OHCDI* when the electric field is applied before the x-rays and maintained during the irradiation. Curve *OA*, drop *AB*, curve *BCD*, drop *DE*, curve *EF* when the electric field is applied at *A* and removed at *D*. The corresponding shapes of the brightness waves are shown schematically under every period.

* Consultant, Westinghouse Electric Corporation, Lamp Division, Bloomfield, New Jersey.

[1] G. Destriau, J. Phys. **4**, 32 (1943).

[2] F. Matossi and S. Nudelman, Phys. Rev. **89**, 660 (1953).

[3] T. Miller, J. Appl. Phys. **23**, 1289 (1952), has described experiments on the quenching of the luminescence of sulfide phosphors (excited by ultraviolet light) by the application of an electric field of radio-frequency.

[4] G. Destriau and J. Mattler, J. Phys. **9**, 258 (1948); **11**, 529 (1950); J. Mattler, Compt. rend. **230**, 76 (1950).

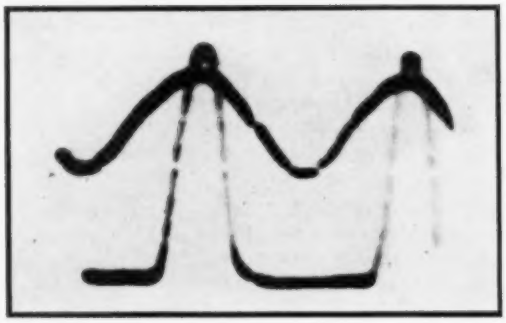

FIG. 2. Simultaneous recording of the voltage (upper curve) applied to a half-wave x-ray generator and of the brightness wave (lower curve) stimulated by the x-rays.

enlarged images some of the phases in the evolution of the phenomena taking place at various times may be easily picked out by means of the frame number of the image and the speed of the camera.

The electrophotoluminescent cells were made up in the usual manner and consist of a solid dielectric condenser incorporating the sensitive material, with one of the electrodes being formed by an aluminum deposit and the other transparent electrode consisting of a conducting glass.

BRIGHTNESS WAVES AND THEIR DEFORMATION BY THE FIELD IN THE PERMANENT STATE

With a half-wave x-ray generator, a single brightness wave appears upon the two half-waves showing the variation of the alternating potential (Fig. 2). When the phosphor is irradiated with x-rays and then subjected to the action of the field, the transitory period *BC* which is discussed below immediately follows; then after several seconds under the action of the alternating field (plateau *CD*) the brightness waves take on a permanent form which is quite different from their initial appearance shown in Fig. 2. Furthermore, the shape varies according to the spectral region observed. For example, by having the total light fall upon the electron multiplier, the pattern shown by Fig. 3 is obtained; by filtering the light by means of green and red filters, respectively, the waves of Figs. 4 and 5, which differ slightly, are obtained.

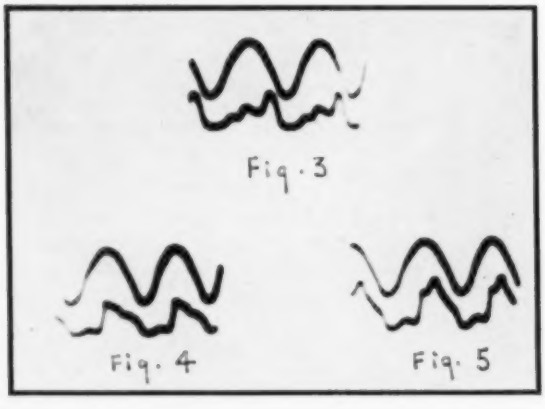

FIGS. 3 TO 5. Simultaneous recording of the electric field (upper curves) and of the brightness waves (lower curves) when the plateau *CD* of Fig. 1 is reached. (Sample No. 2 of Levy-West.) Fig. 3. No filter. Fig. 4. Green filter. Fig. 5. Red filter.

DEFORMATION OF BRIGHTNESS WAVES DURING THE TRANSITORY PERIOD

The application of the electric field is immediately followed by marked complex perturbations which are modified by time. Figures 6 to 15 illustrate various phases of these transformations. The emission during this period is, moreover, dependent upon the previously applied field; thus by having the field act many times in succession at very short time intervals, the maximum of the sharp peak at the right can be exaggerated.

These rapid deformations also show differences for various spectral regions, different curves being obtained by passing the light through colored filters. Figures which do not show quantitatively significant results have not been included. Furthermore, since the theory of the occurrence of these deformations is still very uncertain in the opinion of the writer, it is deemed prudent to restrict the discussion to the purely experimental field.

With removal of the alternating field, the brightness waves instantly resume their regular form, but the amplitude of the maximum appears reduced (Fig. 16). This amplitude progressively increases to its normal value in a few seconds (Fig. 17). All these transformations are represented schematically on the same Fig. 1, where the different shapes of the brightness waves are represented under each region.

INTERPRETATION OF THE SECOND SHARP PEAK OF THE TRANSITORY PERIOD WHICH IMMEDIATELY FOLLOWS THE APPLICATION OF THE FIELD

It has been seen that immediately upon the application of a sinusoidal electric field of the same frequency as, and in phase with, the voltage applied to an x-ray tube functioning as a half-wave source, the brightness wave undergoes a series of fleeting perturbations which may be summarized as follows:

1. Immediately upon the application of the field, the principle maximum is reduced and a very sharp secondary maximum appears. The amplitude of this secondary maximum first increases, then decreases. This secondary maximum is produced at the moment when the voltage passes through zero and therefore lags the principal maximum, which is in phase with the voltage, by a quarter of a cycle (see Figs. 6, 7, and 11–13).

2. The trough of the brightness wave, situated between the two maxima, widens gradually. The amplitude of the secondary maximum slowly decreases while the amplitude of the principle maximum gradually increases again slightly.

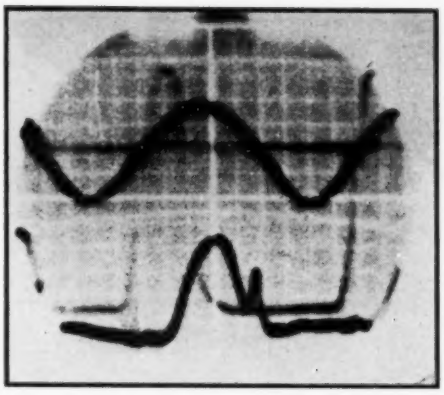

FIG. 6.

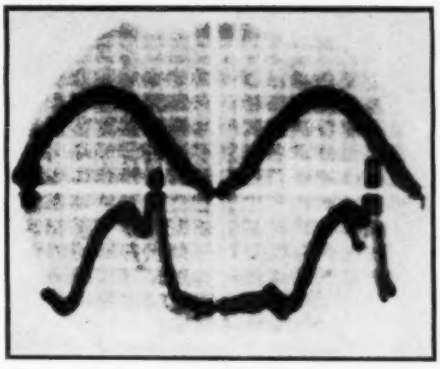

FIG. 7.

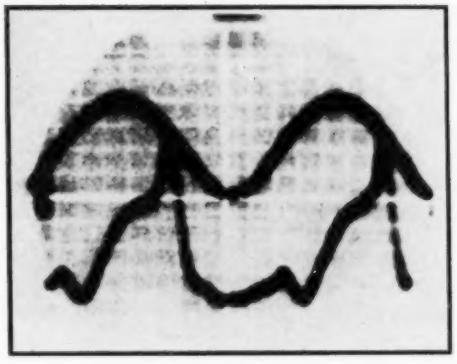

FIG. 8.

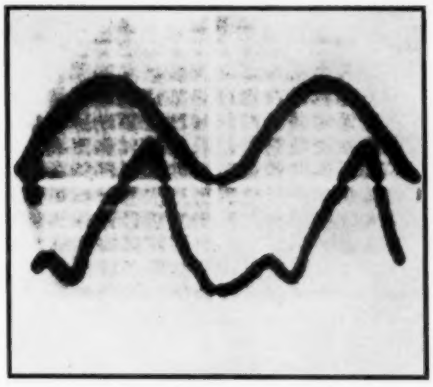

FIG. 9.

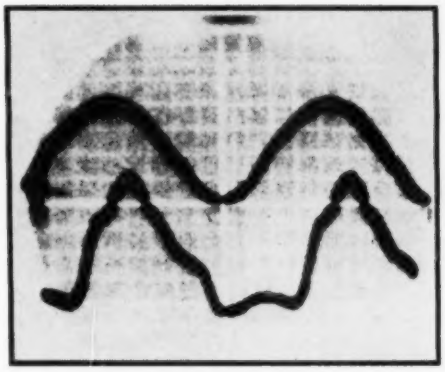

FIG. 10.

FIGS. 6 TO 10. Fleeting perturbations of the brightness waves immediately after the field is applied (sample No. 1). Fig. 6. At application of field. Fig. 7. 0.06 to 0.08 sec after application of field. Fig. 8. 0.18 to 0.20 sec after application of field. Fig. 9. 0.90 to 0.92 sec after application of field. Fig. 10. 4.56 to 4.58 sec after application of field.

It appears that the fleeting deformations of the brightness waves during the first transitory period are characterized, first of all, by the appearance of a second maximum of variable amplitude which lags the normal maximum by a quarter of a cycle. This observation suggests that the quenching effect might be due to the action of the electric field on the electrons responsible for the luminescence of the sulfide, an effect which is analogous to that which produces emission by pure electroluminescence in other substances. These temporarily displaced electrons return to their original position as soon as the field falls to zero and produce the emission which is expressed as the secondary sharp maximum.

An explanation is required, however, of why this maximum has a variable amplitude and why it almost disappears. It is quite certain that the perturbations caused by the field are not instantaneous. Of the electrons momentarily displaced when the field is a maximum, only a certain number return to their original levels when the field falls to zero; the others, which have been more effectively displaced, have a smaller probability of return and these are progressively displaced still further with each successive half-cycle.

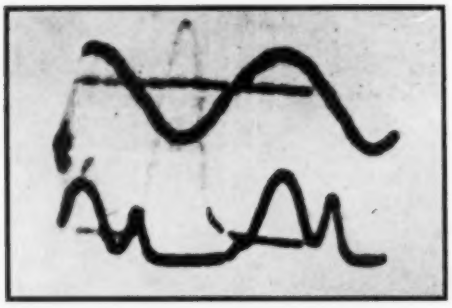

FIG. 11.

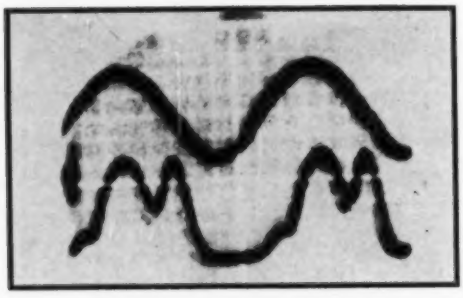

FIG. 12.

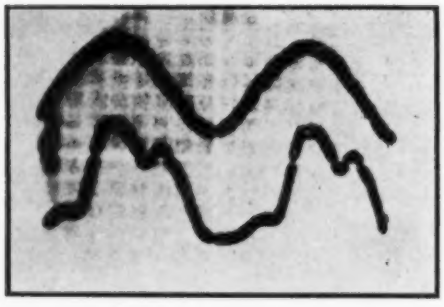

FIG. 13.

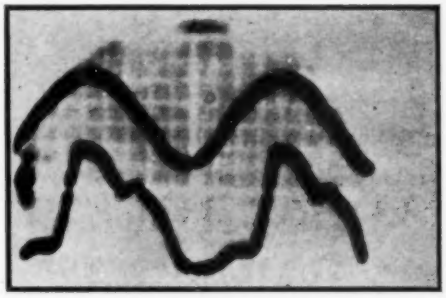

FIG. 14.

FIG. 15.

FIGS. 11 TO 15. Fleeting perturbations of the brightness waves immediately after the field is applied (sample No. 2). Fig. 11. At application of field. Fig. 12. 0.18 to 0.20 sec after application of field. Fig. 13. 0.90 to 0.92 sec after application of field. Fig. 14. 1.86 to 1.88 sec after application of field. Fig. 15. 3.78 to 3.80 sec after application of field.

There is thus gradually established, under the action of the varying field, a statistical distribution of the electrons so that those which have been displaced too far cannot return until a certain time—which may be even greater than a second—has passed. In this distribution, even when the permanent region has been reached, there are always a small number of electrons which remain in the neighborhood of their respective centers and have a tendency to return each time the field falls to zero. Thus, there is a residual deformation of the brightness wave even during the permanent state.

When the field is completely removed, all the electrons gradually return to their original levels and the brightness wave resumes its normal form, its amplitude gradually increasing as the electrons return.

This effect of the alternating electric field substantiates a previous study,[5] in the course of which it was shown that under the action of an alternating electric field alone, a semi-permanent modification is produced in the electronic structure of the crystal. This also explains why the brightness waves immediately exhibit their permanent deformations at the beginning of x-ray irradiation when the electric field has been applied for some time before irradiation and is maintained during irradiation.

EFFECT OF A CONSTANT FIELD

The action of a constant electric field causes no deformation of the brightness waves, the amplitude of the maximum being simply reduced and then rapidly regaining its original form after a few seconds. Upon removal of the field, exactly the same phenomenon is observed (Fig. 18). This behavior is readily explained. The crystal is slightly conductive, especially in the neighborhood of the luminescent centers, so that by applying an external field E_0 at zero time, the field E acting in the interior of the crystal at time t is given by

[5] G. Destriau, Compt. rend. **230**, 1061 (1950).

the exponentially decreasing relation

$$E = E_0 e^{-(4\pi/K\rho)t},$$

of "time-constant" $\theta = K\rho/4\pi$, where K is the dielectric constant and ρ the resistivity of the crystal.[6]

The inner field is cancelled when the electric charges have finally taken the distribution which corresponds to electrostatic equilibrium. When the external field is removed, the opposing field produced by the displaced charges acts alone and the intensity of the field in the interior of the crystal starts from the same value E_0 and decreases, following the same exponential relation. Thus, it is quite correct to find again the same behavior when the external field is removed.

FIG. 16.

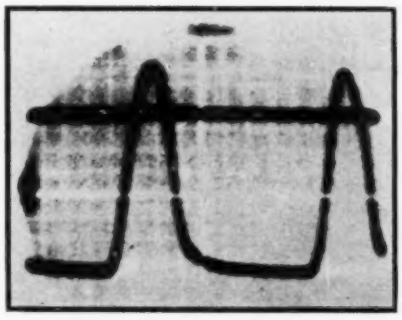

FIG. 17.

FIGS. 16 AND 17. When the field is removed the brightness wave immediately assumes its usual form (Fig. 16) and the amplitude of the maximum then increases progressively until its normal value (Fig. 17).

[6] G. Destriau, J. chim. phys. 34, 462 (1937).

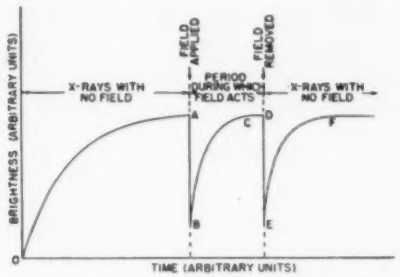

FIG. 18. Action of a constant electric field upon the brightness of a phosphor excited by x-rays.

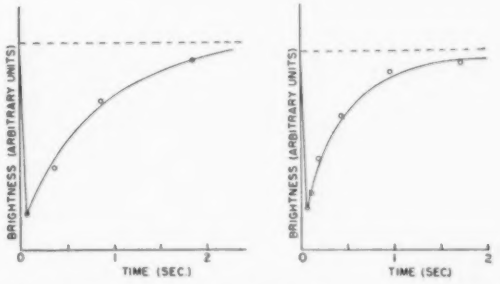

FIG. 19. Variation in brightness when a constant electric field is applied (on the left) and when it is removed (on the right).

The curve which gives the brightness as a function of time (Fig. 19) shows that the time constant θ is here of the order of 0.3 to 0.6 second; that is to say, resistivities ρ of the order of 10^{12} ohm-cm in the neighborhood of the luminescent centers.

CONCLUSIONS

In the quenching effect produced upon luminescent materials by alternating electric fields, the brightness waves are greatly modified by the appearance of a sharp maximum when, in each cycle, the field passes through zero. The amplitude of this maximum varies quickly during the cycles which immediately follow the application of the field.

The behavior is different according to the spectral region observed.

A constant electric field does not produce any disturbance in the shape of the brightness waves. In this case only the amplitude is changed.

Direct Determination of the Flow Curves of Non-Newtonian Fluids. III. Standardized Treatment of Viscometric Data

IRVIN M. KRIEGER AND SAMUEL H. MARON
Department of Chemistry and Chemical Engineering, Case Institute of Technology, Cleveland, Ohio
(Received May 28, 1953)

A scheme is proposed for systematizing the handling of viscometric data through use of the variables apparent fluidity ϕ_a and shearing stress F. The rate of shear $g(F)$ is obtained from the relation: $g(F)/F = \phi_a[1+\Delta(F)]$. Methods are presented for obtaining the correction term $\Delta(F)$ from capillary and concentric-cylinder viscometric data. Use of the proposed scheme is illustrated.

INTRODUCTION

PRECEDING papers[1,2] in this series described methods for obtaining rate-of-shear *vs* shearing-stress curves of non-Newtonian fluids from capillary and concentric cylinder viscometer data, without the prior assumption of a flow equation. It has since been found possible to systematize these methods through the use of the apparent fluidity ϕ_a, which is simply the reciprocal of the apparent viscosity. With the aid of this quantity the rate of shear $g(F)$ can be related to the shearing stress F by an equation of the general form

$$g(F)/F=\phi_a[1+\Delta(F)], \tag{1}$$

where $\Delta(F)$ is a correction term specific for the instrument used and the fluid investigated. For Newtonian fluids $\Delta(F)$ is zero, while for non-Newtonian fluids $\Delta(F)$ may be determined by the methods indicated below.

CAPILLARY VISCOMETER

Symbols:

R = capillary radius,
L = capillary length,
P = pressure drop across capillary due to viscous resistance,
Q = volume rate of flow through capillary,
$F_w = RP/2L$ = shearing stress at capillary wall,
$\phi_a = 8LQ/\pi R^4P$ = apparent fluidity,
$g(F_w)$ = rate of shear at capillary wall.

In the first paper of this series Krieger and Maron rearranged the equation of Saal and Koens[3] to give

$$\frac{g(F_w)}{F_w}=\phi_a+\frac{1}{4}\frac{d\phi_a}{d\ln F_w}. \tag{2}$$

Factoring ϕ_a from the right side of Eq. (2), we get

$$\frac{g(F_w)}{F_w}=\phi_a\left(1+\frac{1}{4}\frac{d\log\phi_a}{d\log F_w}\right), \tag{3}$$

which is identical with Eq. (1) on setting

$$\frac{1}{4}\frac{d\log\phi_a}{d\log F_w}=\Delta(F). \tag{4}$$

The correction term $\Delta(F)$ can thus be obtained from the slope of a plot of $\log\phi_a$ *vs* $\log F_w$. For Newtonian fluids this slope will be zero. It is a well-known empirical fact that for many non-Newtonian fluids the slope may be constant over wide ranges of shearing stress.

CONCENTRIC CYLINDER VISCOMETER

Symbols:

R_1 = radius of inner cylinder (bob),
R_2 = radius of outer cylinder (cup),
$s = R_2/R_1$ = radius ratio,
L = length of inner cylinder,
Ω = angular velocity of cup relative to bob,
M = torque on cylinders due to viscous resistance,
$F_1 = M/(2\pi R_1^2L)$ = shearing stress at bob,
$F_2 = M/(2\pi R_2^2L)$ = shearing stress at cup,
$g(F_1)$ = rate of shear at bob,
$\phi_s = 4\pi R_1^2R_2^2L\Omega/M(R_2^2-R_1^2) = 2\Omega/(F_1(1-1/s^2))$
= apparent fluidity.*

1. Double-Bob Method

By considering the radius ratio s as a variable, Krieger and Maron were able to obtain an exact solution for the rate of shear in the concentric cylinder viscometer, namely,

$$g(F_1)=s\left(\frac{\partial\Omega}{\partial s}\right)_{F_2}. \tag{5}$$

From the definitions of ϕ_s, F_2, and s,

$$\Omega=\tfrac{1}{2}F_2\phi_s(s^2-1), \tag{6}$$

and hence

$$\left(\frac{\partial\Omega}{\partial s}\right)_{F_2}=sF_2\phi_s+\tfrac{1}{2}F_2(s^2-1)\left(\frac{\partial\phi_s}{\partial s}\right)_{F_2} \tag{7}$$

[1] I. M. Krieger and S. H. Maron, J. Appl. Phys. **23**, 147, 1412 (1952).
[2] I. M. Krieger and H. Elrod, J. Appl. Phys. **24**, 134 (1953).
[3] R. N. I. Saal and P. Koens, J. Inst. Petroleum Technol. **19**, 176 (1933).

* Whereas apparent fluidity shearing stress curves are superposable for all capillary instruments, for concentric cylinder viscometers the apparent fluidity depends on the radius ratio s. Accordingly, the symbol ϕ_s is employed here instead of ϕ_a.

Substituting (7) in Eq. (5) and recalling that $F_1=s^2F_2$,

$$\frac{g(F_1)}{F_1}=\phi_s+\frac{s^2-1}{2s}\left(\frac{\partial\phi_s}{\partial s}\right)_{F_2}. \tag{8}$$

Factoring ϕ_s and noting that $2sds/(s^2-1)=d\ln(s^2-1)$,

$$\frac{g(F_1)}{F_1}=\phi_s\left\{1+\left(\frac{\partial\log\phi_s}{\partial\log(s^2-1)}\right)_{F_2}\right\}. \tag{9}$$

Equation (9) is equivalent to Eq. (1) on setting

$$\left(\frac{\partial\log\phi_s}{\partial\log(s^2-1)}\right)_{F_2}=\Delta(F). \tag{10}$$

A convenient and reasonably accurate method for evaluating $\Delta(F)$ would be to employ a single cup and two bobs of the same length but different radii, giving two radius ratios s_a and s_b. The restriction of constant F_2 is thus equivalent to constant torque. If ϕ_a and ϕ_b are the apparent fluidities obtained with bobs a and b respectively at the same torque, then

$$\Delta(F)=\left(\frac{\log\phi_b/\phi_a}{\log(s_b^2-1)/(s_a^2-1)}\right)_M. \tag{11}$$

The error involved in this approximation has been discussed previously.[1]

2. Single-Bob Method

Using Euler and Maclaurin's method, Krieger and Elrod obtained the following asymptotic solution for $g(F_1)$, which converges rapidly for $s^2-1\ll1$:

$$g(F_1)=\frac{\Omega}{\ln s}\left(1+m\ln s+\tfrac{1}{3}(m\ln s)^2+\frac{(\ln s)^2}{s}\frac{dm}{d\ln F_1}+\cdots\right). \tag{12}$$

Here $m=d\log\Omega/d\log F_1$, and s is constant. From the definition of ϕ_s,

$$m=1+\frac{d\log\phi_s}{d\log F_1}. \tag{13}$$

Substituting for Ω and m in Eq. (12) and rearranging,

$$\frac{g(F_1)}{F_1}=\phi_s\left\{\frac{s^2-1}{s^2}\left(\frac{1}{2\ln s}+\frac{1}{2}+\frac{\ln s}{6}\right)+\frac{s^2-1}{2s^2}(1+\tfrac{2}{3}\ln s)\frac{d\log\phi_s}{d\log F_1}+\frac{s^2-1}{6s^2}\ln s\left[\left(\frac{d\log\phi_s}{d\log F_1}\right)^2+\frac{d^2\log\phi_s}{d(\log F_1)^2}\right]+\cdots\right\}. \tag{14}$$

For a Newtonian fluid of viscosity η, $\phi_s=1/\eta$ and $d\log\phi_s/d\log F_1=0$. Hence the term

$$\alpha(s)=\frac{s^2-1}{s^2}\left(\frac{1}{2\ln s}+\frac{1}{2}+\frac{\ln s}{6}\right) \tag{15}$$

must be unity. That $\alpha(s)$ may be taken as unity can readily be demonstrated by expanding $\alpha(s)$ in powers of s^2-1, obtaining thus

$$\alpha(s)=1+\frac{(s^2-1)^4}{720}-\frac{(s^2-1)^5}{1440}+\cdots. \tag{16}$$

Since s rarely exceeds 1.2 in practical viscometers, $\alpha(s)=1$ with negligible error. Letting now

$$k_1=\frac{s^2-1}{2s^2}(1+\tfrac{2}{3}\ln s), \tag{17}$$

$$k_2=\frac{s^2-1}{6s^2}\ln s, \tag{18}$$

and neglecting derivatives of $d\log\phi_s/d\log F_1$, Eq. (14) becomes

$$\frac{g(F_1)}{F_1}=\phi_s\left[1+k_1\frac{d\log\phi_s}{d\log F_1}+k_2\left(\frac{d\log\phi_s}{d\log F_1}\right)^2\right]. \tag{19}$$

Equation (19) is equivalent to Eq. (1) with

$$\Delta(F)=k_1\frac{d\log\phi_s}{d\log F_1}+k_2\left(\frac{d\log\phi_s}{d\log F_1}\right)^2. \tag{20}$$

The constants k_1 and k_2 are instrumental constants of order $\frac{1}{2}(s^2-1)$ and $1/12(s^2-1)^2$, respectively, while $d\log\phi_s/d\log F_1$ is the slope of a graph of $\log\phi_s$ *vs* $\log F_1$. As with the capillary viscometer, this slope is zero for Newtonian fluids and may be constant for many non-Newtonian fluids.

Since the radius ratio s may vary from unity to infinity, it is of interest to examine briefly the behavior of Δ at these limits. When $s=1$, we have the parallel plane viscometer. For this case, k_1 and k_2 vanish, and hence $\Delta=0$. The behavior at $s=\infty$ can not be inferred from Eq. (20), because the asymptotic series on which the solution is based diverges in this limit. For this situation, however, a simple solution for the rate of

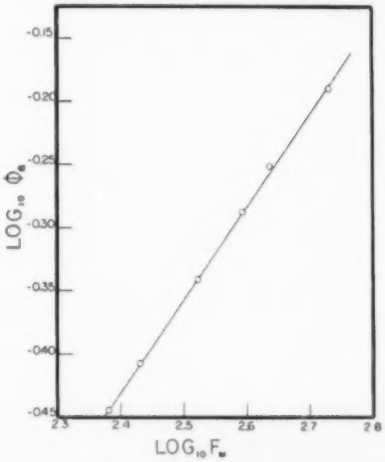

FIG. 1. Plot of $\log\phi_a$ *vs* $\log F_m$ for 62.2 percent solids latex in capillary viscometer at 30°C.

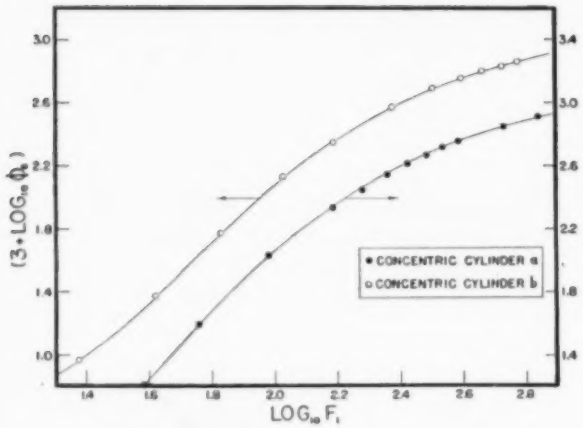

FIG. 2. Plot of $\log\phi_a$ *vs* $\log F_1$ for 62.2-percent solids latex in two concentric cylinder viscometers at 30°C.

shear was described in the first paper,[1] namely,

$$g(F_1)=2d\Omega/d\ \ln F_1=2F_1d\Omega/dF_1. \tag{21}$$

Integration of Eq. (21) for a Newtonian fluid gives for the viscosity $\eta=F_1/2\Omega$, and hence we may define the apparent fluidity as

$$\phi_a=2\Omega/F_1. \tag{22}$$

Using this definition in Eq. (21), we obtain

$$2d\Omega/dF_1=F_1d\phi_a/dF_1+\phi_a, \tag{23}$$

and hence

$$g(F_1)/F_1=\phi_a(1+d\ \log\phi_a/d\ \log F_1). \tag{24}$$

In this limit, therefore,

$$\Delta=d\ \log\phi_a/d\ \log F_1, \tag{25}$$

and thus Δ ranges from 0 to $d\ \log\phi_a/d\ \log F_1$ as s varies from 1 to ∞.

ILLUSTRATION OF METHODS

To illustrate the application of the proposed treatment of viscometric data, the same non-Newtonian fluid was studied at 30°C in three different viscometers. Two concentric cylinder instruments of different radius ratio and a capillary viscometer were used to investigate

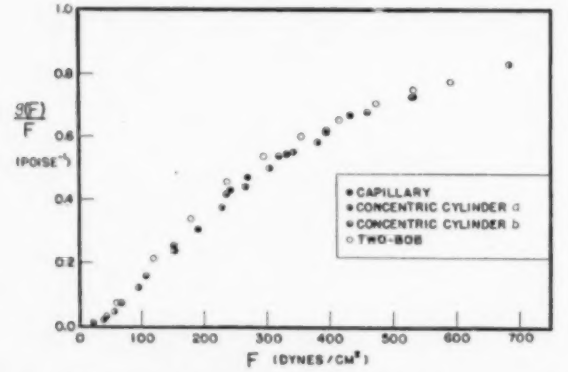

FIG. 3. Composite plot of $g(F)/F$ *vs* F for 62.2-percent solids latex at 30°C.

the flow behavior of a GR-S latex containing 62.2 percent solids by weight.

Table I gives the dimensions of the capillary tube and the pressure *vs* rate-of-flow data obtained, together with the steps in the calculation of the rate of shear–shearing stress ratio. Values of the correction term in the fifth column of this table were obtained from the slope in Fig. 1. As is the case with many non-Newtonian fluids, this graph of $\log\phi_a$ *vs* $\log F_m$ is linear, and hence $\Delta(F)$ is constant.

Table II gives torque angular velocity data obtained on the same latex with two concentric cylinder instruments of different clearance. The necessary dimensions are given in the table, as are the steps in the computation of the rate of shear–shearing stress ratio. The shearing stress F_2 at the cup is computed in the fourth column for subsequent use in the two-bob method. Values of $d\ \log\phi_a/d\ \log F_1$ given in the sixth column were obtained by graphical measurement of slopes of Fig. 2 at the experimental points.

Because angular velocities were not determined at exactly the same torque values in the two instruments,

TABLE I. Capillary viscometer. Data and calculations for 62.2 percent solids latex at 30°C. ($R=0.01856$ cm, $L=15.215$ cm.)

$P\times10^{-5}$ (dynes/cm^2)	$Q\times10^3$ (cm^3/sec)	F_m (dynes/cm^2)	ϕ_a (poise^{-1})	$\frac{\Delta(F)}{}=\frac{1}{3}\frac{d\ \log\phi_a}{d\ \log F_m}$ (from Fig. 1)	$g(F_m)/F_m$ Eq. (1) (poise^{-1})
3.954	0.436	241.2	0.360	0.185	0.427
4.423	0.530	269.8	0.392	0.185	0.465
5.461	0.762	333.1	0.456	0.185	0.540
6.439	1.016	392.8	0.516	0.185	0.611
7.105	1.220	433.4	0.561	0.185	0.665
8.807	1.742	537.2	0.647	0.185	0.747

values of ϕ_a in the two viscometers were interpolated so that apparent fluidities could be compared at the same F_2 values for the application of the two-bob method. These interpolated data are shown in Table III. From these data, $\Delta(F)$ and the rate of shear–shearing stress ratio were calculated by means of Eqs. (11) and (1). In using Eq. (1),

$$\phi_a=\tfrac{1}{2}(\phi_b+\phi_a), \tag{26}$$

while F corresponds to

$$F=s_m{}^2F_2, \tag{27}$$

where

$$s_m=\tfrac{1}{2}(s_a+s_b).$$

The four different determinations of the rate of shear–shearing stress ratio made on the same latex at 30°C are plotted *versus* shearing stress in Fig. 3. It should be noted that this mode of presentation is considerably more sensitive than the conventional plot of rate-of-shear *vs* shearing stress. Agreement among the results is excellent except for the two-bob method values in the intermediate F range. These deviations demonstrate an inherent weakness in the two-bob method. In

TABLE II. Concentric cylinder viscometer. Data and calculations for 62.2 percent solids GR-S latex at 30°C.

Ω (rad/sec)	$M\times10^{-4}$ (dynes/cm²)	F_1 (dynes/cm²)	F_2 (dynes/cm²)	ϕ_a (poise⁻¹)	$d\log\phi_a/d\log F_1$ (from Fig. 2)	$\Delta(F)$ Eq. (20)	$g(F)/F$ Eq. (1) (poise⁻¹)
(Viscometer a: $R_{1a}=2.357$ cm, $R_{2a}=2.508$ cm, $L_a=7.33$ cm, $k_1=0.0608$, $k_2=0.00121$)							
0.0367	0.974	38.1	33.6	0.0165	2.20	0.140	0.0188
0.131	1.46	57.1	50.4	0.0392	2.09	0.133	0.0444
0.602	2.44	95.1	84.0	0.108	1.72	0.108	0.120
1.94	3.90	152	134	0.218	1.32	0.082	0.236
3.12	4.87	190	168	0.280	1.20	0.075	0.301
4.66	5.84	228	202	0.350	1.05	0.065	0.372
6.41	6.82	266	235	0.412	0.970	0.060	0.437
8.33	7.79	304	269	0.468	0.915	0.057	0.495
10.45	8.76	343	303	0.522	0.845	0.052	0.550
12.51	9.74	381	336	0.563	0.762	0.047	0.590
21.7	13.63	533	471	0.698	0.576	0.035	0.723
32.2	17.52	685	605	0.805	0.507	0.031	0.830
(Viscometer b: $R_{1b}=2.253$ cm, $R_{2b}=2.508$ cm, $L_b=7.45$ cm, $k_1=0.1035$, $k_2=0.00345$)							
0.0217	0.569	24.0	19.3	0.0094	1.42	0.154	0.0108
0.0969	1.008	41.9	33.8	0.0239	1.90	0.209	0.0289
0.391	1.293	67.7	54.6	0.0598	1.83	0.201	0.0718
1.384	2.54	107	86.3	0.134	1.61	0.176	0.157
3.26	3.59	151	122	0.223	1.34	0.145	0.256
8.48	5.61	236	190	0.372	1.00	0.107	0.412
15.16	7.58	319	257	0.492	0.757	0.080	0.532
22.0	9.40	395	319	0.575	0.659	0.070	0.615
28.1	10.90	459	370	0.633	0.600	0.063	0.674
35.2	12.61	531	428	0.687	0.547	0.058	0.727
41.7	14.11	594	479	0.727	0.508	0.054	0.766

TABLE III. Two-bob method. Calculations for 62.2 percent solids latex at 30°C.

F_2 (dynes/cm²)	ϕ_b (interpolated)	ϕ_a (interpolated)	$\phi_s=\frac{1}{2}(\phi_b+\phi_a)$ (poise⁻¹)	$\Delta(F)$ Eq. (11)	$g(F)/F$ Eq. (1) (poise⁻¹)	$F=s_m{}^2F_2$ (dynes/cm²)
50	0.055	0.039	0.047	0.579	0.074	59.3
100	0.169	0.138	0.154	0.342	0.206	118.5
150	0.288	0.247	0.268	0.264	0.339	177.8
200	0.393	0.344	0.369	0.224	0.452	237
250	0.480	0.437	0.459	0.158	0.532	296
300	0.553	0.515	0.534	0.122	0.599	356
350	0.614	0.580	0.597	0.090	0.651	415
400	0.664	0.633	0.649	0.081	0.702	474
450	0.708	0.680	0.694	0.068	0.741	533
500	0.746	0.723	0.735	0.053	0.774	593

computing $\Delta(F)$ by this method, small differences must be taken between two large numbers, and hence experimental errors are greatly magnified. For this reason, as well as for greater convenience, the use of the single-bob method employing Eq. (19) is to be preferred for obtaining the rate of shear in concentric cylinder viscometers.

CONCLUSIONS

Methods previously proposed for obtaining rate of shear *vs* shearing stress curves have been unified by the use of the apparent-fluidity function. In the proposed scheme the raw viscometric data are converted to apparent fluidity and shearing-stress values, from which the rate of shear-shearing stress ratio can be obtained by the formula

$$\frac{g(F)}{F}=\phi_a[1+\Delta(F)].$$

$\Delta(F)$ is zero for Newtonian fluids and is easily evaluated for non-Newtonian ones. The procedures involved are simple and accurate, and no prior knowledge of the flow behavior is required. They are applicable to both capillary and concentric cylinder viscometers over the entire region of laminar flow. The authors believe that the treatment presented in this paper merits adoption as a standard technique for handling viscometric data on non-Newtonian fluids.

ACKNOWLEDGMENT

The work discussed herein was performed as a part of the research project sponsored by the Reconstruction Finance Corporation, Office of Synthetic Rubber, in connection with the government Synthetic Rubber Program.

The authors also wish to thank Messrs. S. M. Fok and A. W. Sisko of this laboratory for obtaining the experimental data used in illustrating the proposed method.

JOURNAL OF APPLIED PHYSICS VOLUME 25, NUMBER 1 JANUARY, 1954

On the Detection of Sure Signals in Noise

R. C. DAVIS*
U. S. Naval Ordnance Test Station, Pasadena, California
(Received June 5, 1953)

The purpose of this paper is to attempt to present known results on detection in simplified form and to relate these to new results found by the author. For a signal of known form and nonrandom in nature (sure signal) upon which a background noise is linearly superimposed, several criteria for an optimum pre-detection filter are compared. The background noise may be of very general nature and restricted merely to possessing a continuous covariance function and need not, in general, possess even a frequency spectrum. Specifically, it is shown that, when the input noise to a pre-detection filter is Gaussian (with no restrictions concerning its possible spectrum), the filter which maximizes—for a fixed "false alarm" probability—the probability of detecting the signal when it is present is identical with the linear filter which maximizes the output signal-to-noise ratio. For a Gaussian noise input an explicit expression is obtained for the probability of detection. The stability of the optimum filter is discussed in some detail and some restrictions on the form of the input signal necessary for stability are given. The techniques used throughout limit one, in general, to the practical case of finite memory filters. Finally it is shown how an optimum signal shape of given energy content and duration can be chosen.

INTRODUCTION

DURING the past decade a considerable amount of study on the detection in noise of sure signals (i.e., nonrandom signals of known mathematical form) has resulted in an equally considerable volume of literature on the subject. Recently the author presented at an Institute of Radio Engineers convention[1] some statistical techniques—developed by mathematical statisticians during the past two decades—which are useful in solving certain problems arising in the study of detection. The techniques are such that all results are obtained in the time domain and are of such generality that it is not necessary to assume that input noise even possesses a frequency spectrum. It was shown (see reference 1, pp. 5–6), however, that if the noise input is stationary of the second order† (the first two moments of the noise independent of time), explicit solutions to certain problems in detection can be obtained under the same assumptions usually made in obtaining optimum filters by the technique developed by N. Wiener, i.e., assuming that the noise possesses a spectral density which is a rational function of frequency. In more general cases one must, except for isolated exceptions, obtain approximate solutions to the linear integral equation which arises in attempting to expand the noise input into a series the terms of which are pairwise uncorrelated. It is worth noting here that the majority of problems arising in the theory of linear filters in which the answers cannot be obtained explicitly can be approximated by solving a finite system of linear algebraic equations, the number of equations being determined by the required accuracy of the approximation and the speed of convergence of the solution of the finite system to the rigorous system which is in general an infinite one.

Some of the results are not new and are so indicated, but the treatment of the exact conditions under which the predetection filter which maximizes the probability of detection coincides with the linear filter which maximizes the output signal-to-noise ratio, is believed to be new. Moreover, the theory which yields the optimum pulse shape, for fixed pulse energy, is believed to be new. In order to carry out the computations to determine optimum pulse shape, however, one must resort to some computing technique for solving systems of linear algebraic equations.

The discussion is limited to finite memory filters for the simple reason that, in general, the expansion which we use of the noise into uncorrelated components is not convergent (in a sense defined later) over an interval of time of infinite extent. In special cases the expansion is, of course, valid over an infinite interval. It is realized that in most practical cases one actually prefers, in view of the finite duration of the signal, a finite memory filter, but since infinite memory filters are easier to construct at the present stage of the art of filter design, one may prefer to approximate the desired finite memory filter by one with infinite memory.

II. THE FILTER WHICH MAXIMIZES THE PROBABILITY OF DETECTION

We denote by $S_1(\tau)$ the input signal to a predetection filter F and by $N_1(\tau)$ the input noise. The filter is to have a finite memory of duration T. We denote by $EN_1(\tau)$ the expected value (ensemble average) of $N_1(\tau)$ and by $r(u,v)=EN_1(u)N_1(v)$ the covariance function of the noise. We make the following assumptions concerning the probability distribution of $N_1(\tau)$: (1) $N_1(\tau)$ is Gaussian, (2) $EN_1(\tau)\equiv 0$, (3) $r(u,v)$ is a

* Presently research physicist at Hughes Aircraft Company, Culver City, California.

† A. Khintchine introduced the expression "stationary of the second order." Later other authors introduced other terms. J. L. Doob introduced the term "stationary in the wide sense," and H. B. Mann the term "quasi-stationary." Although Khintchine's term is the most descriptive, we use the term "quasi-stationary" because of its succinctness.

[1] R. C. Davis, "New techniques and results in the mathematical analysis of random noise," presented at West Coast Institute of Radio Engineers Convention, August, 1952.

symmetric, continuous function of the pair (u, v) in the closed square $0 \leqslant u \leqslant T$, $0 \leqslant v \leqslant T$. Moreover in the closed square, $r(u, v)$ is a positive definite function with respect to the function space $L[0, T]$.

We denote by $L[0, T]$—in future we denote this simply by L—the space of real valued functions which are Lebesgue integrable over an interval of length T corresponding to the memory of the filter F. The covariance function is defined to be positive definite in $L[t_0-\tau, t_0]$ if, for every $f(u) \epsilon L$,

$$\int_{t_0-T}^{t_0}\int_{t_0-T}^{t_0} r(u, v) f(u) f(v) du dv \geq 0,$$

with equality if and only if $f(u) \equiv 0$ in $[t_0-\tau, t_0]$. The assumptions concerning the nature of the known input signal $S_1(\tau)$ will be given later. We note that assumption 3 holds for all noise inputs of interest except for idealized white noise, for which $r(u, v)$ is discontinuous along the line $u=v$. $r(u, v)$ is continuous, for example, in the case of band-limited noise possessing a flat spectrum. We consider the following problem: During the time interval $t-T \leqslant \tau \leqslant t$ we observe an input process $X_1(\tau)$. If noise alone is present, $X_1(\tau) \equiv N_1(\tau)$ and, if signal plus noise are present, $X_1(\tau) \equiv N_1(\tau)+S_1(\tau)$. We do not specify the instant at which the signal originated and are interested only in its values during the interval $t-T \leqslant \tau \leqslant t$. Consider the class of functionals $G[X_1(\tau)$; $t-T \leqslant \tau \leqslant t]$ and a number g such that, if $X_1(\tau)=N_1(\tau)$ during the interval of length T, the probability of the event $G[X_1(\tau)] \geqslant g$ is equal to a preassigned number $\epsilon (0<\epsilon<1)$. Out of this class of functionals we seek a functional $G_0[X_1(\tau)]$ with the property that, if $X_1(\tau) = N_1(\tau)+S_1(\tau)$ during the sampling interval of length T, then

$$\text{Pr. } \{G_0[X_1(\tau)] \geqslant g\} \geqslant \text{Pr. } \{G_i[X_1(\tau)] \geqslant g\}$$

where $G_i[X_1(\tau)]$ represents any functional in the class $G[X_1(\tau)]$.

Before determining $G_0[X_1(\tau)]$, we expand the noise input $N_1(\tau)$ in a series given originally by K. Karhunen (described by the author, reference 1, p. 4), namely,

$$N_1(\tau)=\sum_{i=1}^{\infty} \frac{\varphi_i(\tau; t)}{[\lambda_i(t)]^{\frac{1}{2}}} z_i(t), \tag{1}$$

for $t-T \leqslant \tau \leqslant t$, in which the $z_i(t)$ are random variables all with mean values zero and pairwise mutually uncorrelated; i.e.,

$$\left.\begin{aligned} Ez_i(t)&=0 \\ Ez_i(t)z_j(t)&=\delta_{ij} \end{aligned}\right\} \quad \begin{aligned} i&=1, 2, \cdots \\ j&=1, 2, \cdots, \end{aligned}$$

and in which $\{\varphi_i(\tau; t)\}$ and $\{\lambda_i(t)\}$ are the eigenfunctions and eigenvalues respectively of the integral equation

$$\varphi(u)=\lambda \int_{t-T}^{t} r(u, v)\varphi(v) dv. \tag{2}$$

It is obvious from the above integral equation that in general the eigenfunctions and eigenvalues depend parametrically upon the time instant t, the end of the sampling interval. In the particular case in which the noise input $N_1(t)$ is quasi-stationary in character, i.e., $r(s, t)=r(|s-t|)$, it is clear that

$$\left.\begin{aligned} \varphi(\tau; t)&=\varphi(\tau) \\ \lambda_i(t)&=\lambda_i \end{aligned}\right\} \quad \text{for all } t.$$

In the future, for the sake of simplicity in notation, we will omit the parameter t in writing the eigenfunctions and eigenvalues, remembering that these quantities change continuously as t varies unless the noise is quasi-stationary. In assumption 3 we have assumed that $r(s, t)$ is a positive definite function with respect to L. It is then easy to show that the system of eigenfunctions $\{\varphi_i(u)\}$ of Eq. (2), when normalized so that

$$\int_{t-T}^{t} [\varphi_i(u)]^2 du=1,$$

forms a complete orthornormal set of functions in L_2, the space of quadratically Lebesgue integrable functions defined over the interval $[t-T, t]$. [Since over a finite interval $L \supset L_2$, we are assured that $r(s, t)$ is positive definite with respect to L_2. Later we will require the condition to be satisfied in L.]

Returning now to consideration of the input signal $S_1(\tau)$ it is clear that

$$\int_{t-T}^{t} [S_1(\tau)]^2 d\tau < \infty \tag{3}$$

and, hence, $S_1(\tau) \epsilon L_2$. Later we will see that other restrictions must be placed upon $S_1(\tau)$. We define the sequence $\{a_i(t)\}$ as

$$a_i(t)=\int_{t-T}^{t} S_1(\tau)\varphi_i(\tau) d\tau. \tag{4}$$

Denoting, for convenience, by ω the realization of $X_1(\tau)$ during the interval $[t-T, t]$, we describe ω in terms of the infinite sequence $y_1, y_2 \cdots$ (termed "observable coordinates" by U. Grenander[2]), where

$$y_i(t)=\int_{t-T}^{t} X_1(\tau)\varphi_i(\tau) d\tau. \tag{5}$$

It we denote by $g_0^{(n)}(\omega)$ and $g_1^{(n)}(\omega)$ the probability density functions‡ of the first n observable coordinates $y_1, y_2, \cdots, y_n$ for the cases $X_1(\tau)=N_1(\tau)$ and $X_1(\tau) = N_1(\tau)+S_1(\tau)$, respectively, we have (since the y_i are

[2] Ulf Grenander, Arkiv Mat. 1 (1950).

‡ Recently [J. Appl. Phys. 24, 844 (1953)] G. W. Preston obtained by direct methods the probability density of a realization of a stationary Gaussian continuous process. As a matter of fact, however, his form can be obtained more easily by the use of Karhunen's expansion than by the use of direct methods.

Gaussian and mutually independent)

$$g_0^{(n)}(\omega)=\frac{(\lambda_1\lambda_2\cdots\lambda_n)^{\frac{1}{2}}}{(2\pi)^{n/2}}\exp\{-\tfrac{1}{2}\sum_{i=1}^{n}\lambda_i y_i^2\},$$

$$g_1^{(n)}(\omega)=\frac{(\lambda_1\lambda_2\cdots\lambda_n)^{\frac{1}{2}}}{(2\pi)^{n/2}}\exp\{-\tfrac{1}{2}\sum_{i=1}^{n}\lambda_i[y_i-a_i(t)]^2\}.$$

Hence,

$$\frac{g_1^{(n)}(\omega)}{g_0^{(n)}(\omega)}=\exp\{\sum_{i=1}^{n}[\lambda_i y_i a_i(t)-\tfrac{1}{2}\lambda_i[a_i(t)]^2]\}. \quad (6)$$

In line with our original problem of seeking a functional $G_0[X_1(\tau);t-T\leqslant\tau\leqslant t]$, which maximizes $\Pr.\{G_0[X_1(\tau)]\geqslant g\}$ when $X_1(\tau)=N_1(\tau)+S_1(\tau)$, subject to the restraint $\Pr.\{G_0[X_1(\tau)]\geqslant g\}=\epsilon$ when $X_1(\tau)=N_1(\tau)$, Neyman and Pearson have shown[3] that the functional $G_0[X_1(\tau)]$ is given by the expression

$$\lim_{n\to\infty}\frac{g_1^{(n)}(\omega)}{g_0^{(n)}(\omega)}.$$

Hence from Eq. (6) and the monotoneness of the function e^x, we see that the test criterion for detection is given by

$$\sum_{i=1}^{\infty}[\lambda_i a_i(t)y_i-\tfrac{1}{2}\lambda_i[a_i(t)]^2]\geq g. \quad (7)$$

We must distinguish now between two cases.

Case I

$$\sum_{i=1}^{\infty}\lambda_i[a_i(t)]^2<\infty.$$

In this case we can replace (7) by the inequality

$$\sum_{i=1}^{\infty}\lambda_i a_i(t)y_i\geq g. \quad (8)$$

It is not difficult to show (by the use of a variant of a theorem of Kolmogoroff on the almost certain convergence of a series of mutually independent random variables) that

$$\sum_{i=1}^{n}\lambda_i a_i(t)y_i\to\Omega,$$

almost certainly as $n\to\infty$, in which Ω is a Gaussian random variable, the distribution of which depends on which of the two processes under consideration was sampled. Hence the functional which maximizes the probability of detection is the random variable Ω. First we will determine the appropriate value of g'. Since we wish to hold the probability of accepting noise alone as a signal at some small predetermined value ϵ, we have

$$\Pr.\{\Omega\geqslant g'\,|X_1(\tau)=N_1(\tau)\}=\epsilon.$$

[3] J. Neyman, J. Roy. Statistical Soc. **105**, 292 (1942).

For the sake of simplicity, we define

$$\Omega=\Omega_0, \quad \text{when } X_1(\tau)=N_1(\tau)$$
$$\Omega=\Omega_1, \quad \text{when } X_1(\tau)=N_1(\tau)+S_1(\tau)$$

Clearly,

$$E\Omega_0=0, \quad \text{and} \quad E\Omega_0^2=\sum_{i=1}^{\infty}\lambda_i[a_i(t)]^2=\sigma_0^2,$$

Since Ω_0 is Gaussian,

$$\Pr.\{\Omega_0\geq g'\}=\epsilon=\frac{1}{(2\pi)^{\frac{1}{2}}}\int_{g'/\sigma_0}^{\infty}\exp(-t^2/2)dt,$$

so that $g'=\sigma_0\psi(\epsilon)$, with

$$\psi(\epsilon)=\sqrt{2}\,\mathrm{erf}^{-1}(\pi\epsilon/2).$$

Hence the criterion used for detection becomes

$$\Omega\gtrless\sigma_0\psi(\epsilon). \quad (9)$$

Hence, when inequality (9) holds, we say that detection occurs. In order to determine the probability of detection, we require the first two moments of the distribution of Ω_1. Clearly,

$$E\Omega_1=\sum_{i=1}^{\infty}\lambda_i[a_i(t)]^2=\sigma_0^2,$$
$$E[\Omega_1-E\Omega_1]^2=\sigma_0^2.$$

Hence the probability of detection is given by

$$\Pr.\{\Omega_1\geq\sigma_0\psi(\epsilon)\}=\frac{1}{(2\pi)^{\frac{1}{2}}}\int_{\psi(\epsilon)-\sigma_0}^{\infty}\exp(-t^2/2)dt$$
$$=\frac{2}{\pi}\,\mathrm{erf}[\psi(\epsilon)-\sigma_0]. \quad (10)$$

The probability of detection is a function of the two parameters σ_0 and ϵ. The choice of ϵ is determined by the importance attached to the avoidance of detecting a false signal. The nature of the parameter σ_0 is easy to investigate. The power delivered in the input signal during the time interval $[t-T, t]$ is proportional to

$$P_{S1}=\frac{1}{T}\int_{t-T}^{t}[S_1(\tau)]^2d\tau=\frac{1}{T}\sum_{i=1}^{\infty}[a_i(t)]^2.$$

The expected value of the input noise power delivered during the same interval is proportional to

$$P_{N1}=\frac{1}{T}\int_{t-T}^{t}E[N_1(\tau)]^2d\tau=\frac{1}{T}\sum_{i=1}^{\infty}\frac{1}{\lambda_i}.$$

If we denote by P_{Si} the input signal power associated with the eigenfunction $\varphi_i(\tau)$ and the corresponding input noise power by P_{Ni}, then clearly

$$P_{Si}=\frac{[a_i(t)]^2}{T}, \quad \text{and} \quad P_{Ni}=\frac{1}{T\lambda_i}.$$

Hence σ_0^2 is given by

$$\sigma_0^2=\sum_{i=1}^{\infty} P_{Si}/P_{Ni}, \tag{11}$$

and, hence, the probability of detection is a function (for given ϵ) of the sum of the input signal-to-noise ratios associated with all of the eigenfunctions of the noise. We note also that for the optimum filter

$$S_0(t)=E[N_0(t)]^2=\sum_{i=1}^{\infty}\lambda_i[a_i(t)]^2, \tag{12}$$

a relation which has been obtained by other authors when using another criterion for optimization which we will discuss later.

Case II

$$\sum_{i=1}^{\infty}\lambda_i[a_i(t)]^2=\infty.$$

By glancing at Eq. (10) we see that this case yields a detection probability of unity regardless of the value of ϵ. If it were possible to achieve this utopia, it would be desirable. We shall show later, however, that this situation can be achieved only by the use of an unstable filter. Moreover, the impracticality of attempting this is insured by Eq. (12) in which we note that the mean-square noise output is infinite also, and there appears to be no physical system which can distinguish among orders of infinity in the output.

Up to the present we have shown that the functional $G_0[X_1(\tau);\ t-T\leqslant\tau\leqslant t]$, which maximizes the probability of detection, is the linear functional Ω of (8), in which y_i is defined in (5). In order to show the connection, if any, between Ω and the output of a linear filter of the conventional variety, we are tempted to do the following manipulations:

$$\Omega=\sum_{i=1}^{\infty}\lambda_i a_i(t)\int_{t-T}^{t}X_1(\tau)\varphi_i(\tau)d\tau$$

$$=\int_{t-T}^{t}X_1(\tau)d\tau\sum_{i=1}^{\infty}\lambda_i a_i(t)\varphi_i(\tau),$$

and define a function

$$W(\tau;t)=\sum_{i=1}^{\infty}\lambda_i a_i(t)\varphi_i(\tau), \tag{13}$$

so that we can write

$$\Omega=\int_{t-T}^{t}W(\tau;t)X_1(\tau)d\tau. \tag{14}$$

If the above steps could be justified, the optimum filter would be linear with the weight function given by (13). The following condition is sufficient to justify the above steps:

If the integral equation

$$\int_{t-T}^{t}r(u,v)W(v;t)dv=S_1(u), \tag{15}$$

for $t-T_0\leqslant u\leqslant t$ has—for $S_1(u)\epsilon L_2$—a solution $W(v,t)\epsilon L$ and, if the infinite series on the right hand of (13) *is in L, then the unique solution of* (15) *in L is*

$$W(v;t)=\sum_{i=1}^{\infty}\lambda_i a_i(t)\varphi_i(v). \tag{16}$$

Proof

The proof is carried largely by noting that, since $r(u,v)$ is positive-definite in L, the set of eigenfunctions of (2) is complete in L. We write

$$\int_{t-T}^{t}W(v;t)dv\sum_{i=1}^{\infty}\frac{\varphi_i(u)\varphi_i(v)}{\lambda_i}=S_1(u).$$

Since $r(u,v)$ is continuous, symmetric, and positive-definite, we know from Mercer's theorem that the above series for $r(u,v)$ converges absolutely and uniformly in the square $t-T\leqslant u\leqslant t;\ t-T\leqslant v\leqslant t$. We may, therefore, interchange the order of summation and integration and obtain

$$\sum_{i=1}^{\infty}\frac{w_i(t)}{\lambda_i}\varphi_i(u)=S_1(u),$$

where

$$w_i(t)=\int_{t-T}^{t}W(v;t)\varphi_i(v)dv.$$

Multiplying both sides of the above expression by $\varphi_j(u)$ and integrating over the interval $[t-T,t]$, we obtain $w_i(t)=\lambda_i a_i(t)$. Hence, $W(v,t)$ given by (16) is a solution of (15). Moreover, it is the only solution in L, this following immediately from the completeness in L of the set of eigenfunctions $\{\varphi_i(u)\}$.

The immediate conclusion is that if the above condition is satisfied, the linear filter whose output is given by (14) is the unique stable filter which maximizes the property of detection.

We close the discussion of this criterion of optimum by noting the obvious fact that if we desire to maximize the probability of detection at every instant of time, then the optimum filter is time-varying. If we are interested merely in meeting this condition at a single instant t_0, we have

$$W(v;t_0)=\sum_{i=1}^{\infty}\lambda_i a_i(t_0)\varphi_i(v). \tag{16}$$

If the noise input is quasi-stationary, the integral Eq. (15) reduces to a simpler form. First since $W(v;t_0)=W(t_0-v)$, we have

$$\int_{t_0-T}^{t_0}r(u-v)W(t_0-v)dv=S_1(u),\quad t_0-T\leq u\leq t_0.$$

Making the substitutions $s=t_0-v$, $t=t_0-u$, we obtain

$$\int_0^T r(s-t)W(s)ds=S_1(t_0-t), \quad 0\leq t\leq T. \quad (17)$$

The integral Eq. (17) for $W(s)$ was obtained by Zadeh and Ragazzini[4] for the weight function of the linear filter which maximizes the output signal-to-noise ratio. We shall now consider this alternative criterion for an optimum.

III. MAXIMIZATION OF THE OUTPUT SIGNAL-TO-NOISE RATIO

If we drop the assumption that the input noise $N_1(\tau)$ is Gaussian and assume that all one knows is the covariance function of $N_1(\tau)$, we must resort to another definition of optimum predetection filter. Before we proceed to this, however, we wish to note a result found by Khintchine[5] which apparently is unknown to the majority of authors working in the applications of noise theory. The result is that, given any continuous covariance function whatsoever, there exists a Gaussian process which has the prescribed covariance function. As a result it follows that, if no information is available on the probability distribution function of $N_1(\tau)$ which warrants the rejection of the assumption that it is Gaussian, there is no logical reason not to assume that the input noise is Gaussian with the given covariance function.

A criterion for an optimum predetection filter which was used by North[6] for a white noise background is the maximization of the output signal-to-noise ratio. Dwork[7] extended this analysis to handle a noise input with arbitrary spectral density. The difficulty with the Dwork filter is that for non-white noise it might not in general be physically realizable. Recently Zadeh and Ragazzini[4] were able to overcome this difficulty and extend the whole theory to finite memory filters.

The results of this section are not new and merely generalize the results of Zadeh and Ragazzini for finite memory filters. The methods of proof used are different, however, and are possibly more readily understood by an engineer with the average background in mathematics. We wish to compare the linear filter which maximizes the output signal-to-noise ratio with the filter (which turned out to be linear) which maximizes the probability of detection when the noise input is Gaussian. Moreover, we shall need some of the results when discussing optimum signal shapes.

Denoting by $X_0(\tau)$ and $X_1(\tau)$ the output and input, respectively, of a filter F_0, we have

$$X_0(t_0)=\int_{t_0-T}^{t_0} W_0(\tau;t_0)X_1(\tau)d\tau,$$

in which the weight function $W_0(\tau;t_0)$ is to be determined so as to maximize

$$\rho=\frac{[S_0(t_0)]^2}{E[N_0(t_0)]^2}, \quad (18)$$

where, of course,

$$S_0(t_0)=\int_{t_0-T}^{t_0} W_0(\tau;t)S_1(\tau)d\tau,$$

and

$$N_0(t_0)=\int_{t_0-T}^{t_0} W_0(\tau;t)N_1(\tau)d\tau.$$

Clearly,

$$E[N_0(t_0)]^2 = \int_{t_0-T}^{t_0}\int_{t_0-T}^{t_0} W_0(\tau_1;t_0)W_0(\tau_2;t_0)r(\tau_1,\tau_2)d\tau_1 d\tau_2.$$

From the Schwarz' inequality, we obtain

$$\left\{\int_{t_0-T}^{t_0} W_0(u;t_0)S_1(u)du\right\}^2 \leq \int_{t_0-T}^{t_0} W_0(u;t_0)du \int_{t_0-T}^{t_0} W_0(v;t_0)r(u,v)dv \times \int_{t_0-T}^{t_0} \frac{[S_1(u)]^2 W_0(u;t_0)du}{\int_{t_0-T}^{t_0} W_0(v;t_0)r(u,v)dv}.$$

Hence,

$$\rho\leq\int_{t_0-T}^{t_0} \frac{[S_1(u)]^2 W_0(u;t_0)du}{\int_{t_0-T}^{t_0} W_0(v;t_0)r(u,v)dv}, \quad (19)$$

with equality if and only if

$$\int_{t_0-T}^{t_0} r(u,v)W_0(v;t_0)dv=KS_1(u), \quad (20)$$

for $t_0-T\leqslant u\leqslant t_0$, where K is a constant. Since Eq. (20) is identical with Eq. (15) except for the arbitrary gain factor K, we conclude that, if the linear filter which maximizes ρ is stable, it is identical with the filter which in the presence of Gaussian input noise—with the same covariance function $r(s,t)$—maximizes the probability of detection. From (19) and (20) we conclude that

$$\rho_{max}=\int_{t_0-T}^{t_0} W_0(u;t_0)S_1(u)du=S_0(t_0)=E[N_0(t_0)]^2, \quad (21)$$

[4] L. Zadeh and J. Ragazzini, Proc. Inst. Radio Engrs. 42 1223–1231 (1952).
[5] A. Khintchine, "Korrelationstheorie der stationären stochastischen Prozesse," Math. Ann. (1934).
[6] D. North, "Analysis of the factors which determine signal/noise discrimination in radar," Report PTG-GC, RCA Laboratories, June, 1943.
[7] B. Dwork, Proc. Inst. Radio Engrs. 38, 771–774 (1950).

a result obtained for quasi-stationary noise input by Zadeh and Ragazzini (see reference 4, p. 1229). Moreover, if $W_0(u; t_0)\epsilon L$, we have

$$\rho_{\max}=\sum_{i=1}^{\infty}\lambda_i[a_i(t_0)]^2. \tag{22}$$

Hence, if the filter F_0 is stable, its efficiency is determined by the same function which, for a given ϵ, determined the probability of detection.

IV. THE STABILITY OF THE OPTIMUM PREDETECTION FILTER

The weight function of the optimum linear predetection filter satisfies the integral Eq. (15). By definition the filter is stable if $W(v; t_0)\epsilon L$, i.e.,

$$\int_{t_0-T}^{t_0}|W(v; t_0)|dv<\infty.$$

We remark that there is no general theory for the solution in L of Eq. (15). We will be satisfied with giving a few restrictions on the covariance function of the noise $r(u, v)$ and the input signal $S_1(v)$, which are necessary in order that the optimum filter be stable. These conditions are in no way sufficient. In the first place the assumption (3) that $r(u, v)$ is continuous in the pair (u, v) in the closed square $t_0-T\leqslant u\leqslant t_0$, $t_0-T\leqslant v\leqslant t_0$ restricts the input signal $S_1(u)$ to be continuous if the filter is to be stable. This follows from the fact that Eq. (15) for $W(v; t_0)\epsilon L$ defines a completely continuous linear operator on L to a subset of the space of continuous functions (see reference 8, p. 97).

Another necessary condition is derivable from the practical consideration that any input signal $S_1(u)$ must be bounded in absolute value. Hence $S_1(u)\epsilon L_\infty$, the function space conjugate to L. Since by assumption 3 it follows that the eigenfunctions $\{\varphi_i(u)\}$ associated with the kernel $r(u, v)$ are complete in L and hence also in L_∞, we have

$$\int_{t_0-T}^{t_0}W(\tau; t_0)S_1(\tau)d\tau=\sum_{i=1}^{\infty}\lambda_i[a_i(t_0)]^2<\infty. \tag{23}$$

This constitutes a proof of an earlier assertion that the divergence of the series

$$\sum_{i=1}^{\infty}\lambda_i[a_i(t_0)]^2$$

implies the instability of the optimum filter. We note the obvious fact that the convergence of the series in no manner implies the stability§ of the optimum filter.

A sufficient condition that (16) is a solution in L of Eq. (15) can be obtained from a result on orthogonal expansions given in the book by Kacmarz and Steinhaus.[9] They give a necessary and sufficient condition (p. 217) that a given expansion in a set of orthogonal functions lies in the space L. If this condition is satisfied by the expansion given in Eq. (16), then clearly (16) is a solution of the integral Eq. (15) and is moreover unique in L, since the orthonormal set of eigenfunctions is complete in L. The condition given by Kacmarz and Steinhaus is, however, so complicated as to be useless as a practical tool.

From a practical point of view it should be sufficient to restrict ourselves to input signals $S_1(\tau)$ which, for a given input noise covariance function, yield filters with weight functions always in L_2. In this case it follows from a result attributed to Picard[10] that the necessary and sufficient condition that, for an input signal $S_1(\tau)$ ϵL_2 Eq. (16) yield a solution in L_2 of the integral Eq. (15), is

$$\sum_{i=1}^{\infty}\lambda_i^2[a_i(t_0)]^2<\infty. \tag{24}$$

If we restrict ourselves to weight functions in L_2, condition (24) gives the whole story regarding the existence of an optimum filter. It is clear of course that a stable filter (with weight function in L) can exist even when condition (24) is not satisfied.

V. CONSIDERATIONS ON OPTIMUM SIGNAL SHAPE FOR DETECTION

It appears to the author that the presence of a number of practical considerations concerning signal shape may limit the usefulness of a theoretical approach to the determination of optimum signal shape for a prescribed signal energy. Even if a practical theory could be evolved, it seems necessary to use appropriate computing facilities to arrive at specific conclusions on optimum signal shape. The theory developed previously does shed some light on the problem and for this reason it is considered worth while to make a few remarks on the matter.

Referring to Eq. (21) we see that, subject to certain practical restrictions, it is desirable to choose an input signal $S_1(\tau)$ so as to maximize

$$\int_{t_0-T}^{t_0}W_0(\tau; t_0)S_1(\tau)d\tau.$$

If the filter is stable, this reduces to the simple criterion

$$\sum_{i=1}^{\infty}\lambda_i[a_i(t_0)]^2=\text{maximum}. \tag{25}$$

One obvious restriction on the signal is that of a pre-

[8] S. Banach, "Theorie des opérations linéaires," Monografje Matematyczne, Warsawa, 1932.

§ A referee has pointed out the inadequacy of the criterion for the stability of a filter that its weight function be in L. He points out as an example that the weight function of the optimum filter for detecting a square wave in Markoffian noise is not in L. The result follows immediately from Banach's theorem.

[9] S. Kacmarz and H. Steinhaus, *Theorie der Orthogonalreihen*, Second Edition (Chelsea Publishing Company, New York, 1951).

[10] E. Picard, Rend. circ. mat. Palermo 29, 79–97 (1910).

scribed energy content, this being expressed by

$$\int_{T_0} [S_1(\tau)]^2 d\tau = P_{S_1},$$

in which T_0 is the time of duration of the signal. In what follows we shall assume that this duration is equal to T, the duration of memory of the optimum linear filter. This is not a restriction necessitated by the techniques but results in a considerable simplification of the mathematics. In this case, if we take t_0 as the instant corresponding to the "trailing edge" of the incoming signal, then the energy restriction becomes simply

$$\sum_{i=1}^{\infty} [a_i(t_0)]^2 = P_{S_1}. \tag{26}$$

Before proceeding to generalities we note an obvious result for the case in which the input noise is idealized white noise. Since in this case the λ_i are all equal, we note the obvious fact that the value of the expression in (25) is independent of the form of $S_1(\tau)$, so that the only parameter of interest is the ratio of the total energy in the input signal to the total input noise energy during the time interval $[t_0-T, t_0]$.

We note that, in reality, (25) should be written in slightly different form. It is well known from the theory of linear integral equations (see reference 11, p. 84) that, under assumption 3 on the covariance function $r(u, v)$, the sequence $\{\lambda_i\}$ of eigenvalues is never decreasing and each λ_i has finite multiplicity. That is, to each λ_i correspond a finite number n_i of orthogonal functions $\varphi_i^1(v)$, $\varphi_i^2(v)$, $\cdots$, $\varphi_i^{n_i}(v)$, so that (25) becomes

$$\sum_{i=1}^{\infty} \lambda_i \{[a_i^1(t_0)]^2 + [a_i^2(t_0)]^2 + \cdots + [a_i^{n_i}(t_0)]^2\} = \text{maximum}. \tag{25a}$$

Clearly the maximization of (25a) subject to (26) is achieved by choosing the largest index (i) which is feasible. Let us denote this value by j. Then the optimum signal shape is merely

$$S_1(\tau) = \sum_{k=1}^{n_j} a_j^k(t_0)\varphi_j^k(\tau),$$

with no restriction on the individual a_j^k other than one giving the available input signal energy

$$\sum_{k=1}^{n_j} [a_j^k(t_0)]^2 = P_{S_1}.$$

Let us consider now the effect of adding another restriction on the input signal; namely, that a percentage α of its spectral energy must be confined within the finite range of frequencies $\omega_1 \leqslant \omega \leqslant \omega_2$. If the optimum filter is to be stable, $\alpha < 1$. This follows from the facts that for stability the input signal $S_1(\tau)$ must be continuous, and any continuous time function having finite duration T cannot be band limited. (This fact is established readily by appeal to the theory of integral functions of a complex variable, as has been noted by J. Chalk.[12]) Considering the Fourier transform of $S_1(\tau)$,

$$G(\omega) = \int_{-\infty}^{\infty} S_1(\tau) e^{-i\omega\tau} d\tau = \int_{t_0-T}^{t_0} \sum_{i=1}^{\infty} \sum_{j=1}^{n_i} a_i^j(t_0)\varphi_i^j(\tau) e^{-i\omega\tau} d\tau$$

$$\sum_{i=1}^{\infty} \sum_{j=1}^{n_i} a_i^j(t_0) g_i^j(\omega),$$

in which $g_i^j(\omega)$ is the Fourier transform of the eigenfunction $\varphi_i^j(\tau)$. Denoting by $\bar{G}(\omega)$ the complex conjugate of $G(\omega)$, we have

$$\int_{\omega_1}^{\omega_2} G(\omega)\bar{G}(\omega) d\omega = \sum_{i,k}^{\infty} \sum_{j,l}^{n_i, n_k} \beta_{ijkl} a_i^j(t_0) a_k^l(t_0) = \alpha, \tag{27}$$

where

$$\beta_{ijkl} = \int_{\omega_1}^{\omega_2} g_i^j(\omega)\bar{g}_k^l(\omega) d\omega.$$

Hence we wish to maximize (25a) subject to the two restrictions given in (26) and (27). Introducing Lagrangian multipliers, μ_1 and μ_2, we determine $a_i^j(t_0)$, μ_1, and μ_2 such as to maximize Ω, where Ω is given by

$$\Omega = \sum_{i=1}^{\infty} \sum_{j=1}^{n_i} \lambda_i [a_i^j(t_0)]^2 + \mu_1 \{\sum_{i,k}^{\infty} \sum_{j,l}^{n_i, n_k} \beta_{ijkl} a_i^j(t_0) a_k^l(t_0) - \alpha\} + \mu_2 \{\sum_{i=1}^{\infty} \sum_{j=1}^{n_i} [a_i^j(t_0)]^2 - P_{S_1}\}.$$

Without going through the formality of writing down the equations obtained, it is clear that one obtains an infinite system of linear equations for the Fourier coefficients, $a_i^j(t_0)$, of the desired signal $S_1(\tau)$. From the practical viewpoint the solution is impossible to obtain, but an adequate approximation by a reasonably small system may be obtainable in the case in which to each eigenvalue there corresponds a single eigenfunction. In any case the existence of a solution of the infinite system and the speed of convergence of any finite approximation require careful study before any feasible approximation technique can be evolved.

[11] G. Hamel *Integralgleichungen* (Springer-Verlag, Berlin, 1949).

[12] J. Chalk, Proc. Inst. Elec. Engrs. **92** (1950).

The Effect of Inelastic Collisions on the Slowing-Down Length of Neutrons in a Hydrogenous Mixture

HOWARD C. VOLKIN
Lewis Flight Propulsion Laboratory, National Advisory Committee for Aeronautics, Cleveland, Ohio
(Received June 8, 1953)

An expression for the slowing-down length of neutrons in a hydrogenous mixture in which inelastic collisions occur is derived from the rigorous transport equation under the assumptions that (1) the masses of the nonhydrogen nuclei are infinite and (2) the inelastic scattering is of the type in which only discrete well-defined energy levels of the target nucleus are involved. The result is applied to an iron-water mixture.

INTRODUCTION

A QUANTITY used in the problem of the slowing down of neutrons in a given material is the so-called slowing-down length, L_s, which is defined as follows: if a monoenergetic point source continuously emits neutrons of energy E_0 in an infinite medium composed of the material in question, then the slowing-down length is given by $L_s^2(u)=(\frac{1}{6})\langle r^2(u)\rangle_{Av}$, where the logarithmic energy variable, u, is defined by $u\equiv\log(E_0/E)$, E being the neutron kinetic energy; $r(u)$ is the distance of a neutron with energy corresponding to u, the average being taken over all neutrons of this energy in the stationary spatial distribution of slowed-down neutrons. This paper is concerned with the determination of the slowing-down length for the case of hydrogenous mixtures in which inelastic scattering occurs. The nonhydrogen nuclei are considered to be infinitely heavy and the inelastically scattered neutrons are assumed to lose energy only in discrete amounts corresponding to a well-defined level structure of the product nucleus at the energies involved.

The problem of determining the slowing-down length in isotropic media from the transport equation can, in general, be reduced to the solution of the following system of integral equations[1]

$$\varphi_{00}(u)=\int_0^u du'\,\varphi_{00}(u')F_0(u,u')+\delta(u), \tag{1a}$$

$$\varphi_{11}(u)=\frac{l(u)}{3}\varphi_{00}(u)+\int_0^u du'\,\varphi_{11}(u')F_1(u,u'), \tag{1b}$$

$$\varphi_{02}(u)=2l(u)\varphi_{11}(u)+\int_0^u du'\,\varphi_{02}(u')F_0(u,u'), \tag{1c}$$

in which $l(u)$ is the total mean free path and $F_j(u,u')$ is the jth Legendre moment of the scattering function $F(\mu_0;u,u')$ for the medium. The source term is $\delta(u)$, the Dirac δ function, defined by $\delta(u)=0$, $u\neq 0$ and $\int_a^b\delta(u)F(u)du=F(0)$, $b>0$, $a\leqslant 0$. The slowing-down length is given by

$$2L_s^2(u)=\varphi_{02}(u)/\varphi_{00}(u). \tag{2}$$

[1] R. E. Marshak, Revs. Modern Phys. **19**, 185 (1947). (The notation here follows closely that of Marshak.)

The scattering function $F(\mu_0;u,u')$ may be defined as follows: If a neutron before a collision has velocity direction and magnitude specified by $\underline{\Omega}'$, u', then the probability that after a collision the values of these parameters lie in the elements $d\Omega$ about $\underline{\Omega}$ and du about u is $F(\mu_0;u,u')d\Omega du$, where $\mu_0=\underline{\Omega}\cdot\underline{\Omega}'$ (the μ_0 dependence is valid for isotropic media). The scattering function is normalized so that $\int d\Omega\int du F(\mu_0;u,u')$ for any $\underline{\Omega}'$, u' is equal to the probability that a collision at energy corresponding to u' is a scattering collision of any kind. Also it follows that $F(\mu_0;u,u')\equiv 0$ when $u'>u$ if only slowing-down collisions are considered. The $F_j(u,u')$ in Eqs. (1) are given by

$$F_j(u,u')=\int d\Omega_0 P_j(\mu_0)F(\mu_0;u,u'), \tag{3}$$

where $P_j(\mu_0)$ is the jth Legendre polynomial

SCATTERING FUNCTION

An expression for the scattering function $F(\mu_0;u,u')$ in hydrogenous media will now be obtained by considering the contributions from the various scattering processes occurring in the medium. The relative scattering function $f(\mu_0;u-u')$ for elastic collisions with hydrogen nuclei in which spherically symmetric scattering in the center of mass system (s wave scattering) occurs is given by[2]

$$f(\mu_0;u-u')=(1/2\pi)e^{-(u-u')}\delta[\mu_0-e^{-(u-u')/2}]. \tag{4}$$

It will be assumed that the nucleus of the non-hydrogen element has infinite mass and discrete, well-defined energy levels between the ground state and the source energy E_0. In an inelastic collision which leaves the nucleus in the nth state with excitation energy W_n, the incident neutron energy E' and the neutron energy after collision E are related by

$$E'=E+W_n$$

or in terms of the logarithmic energy variable

$$u'=w_n(u)\equiv-\log[\exp(-u)+\exp(-a_n)], \tag{5}$$

where $a_n=\log E_0/W_n$. The function $w_n(u)$ gives the incident logarithmic energy of a neutron whose energy

[2] See reference 1, Eq. (7).

after an inelastic collision involving the energy level W_n corresponds to u; it is defined for $u \geqslant b_n \equiv \log[E_0/(E_0-W_n)]$, vanishing at the initial point, which corresponds to a collision of a source energy neutron, and increasing asymptotically to the value a_n, which corresponds to a collision of a neutron at the threshold energy W_n. The relative scattering function for inelastic collisions in which the product nucleus is left in the nth excited level is given by

$$f_n(\mu_0; u, u') = [\sigma_n(\mu_0, u')/\sigma_{n0}(u')] \times \delta[w_n(u)-u'](dw_n/du), \quad u \geqslant b_n, \quad (6)$$

$$f_n(\mu_0; u, u') = 0, \quad u < b_n,$$

where $\sigma_n(\mu_0, u')$ and $\sigma_{n0}(u')$ are the differential and total cross sections respectively for inelastic collisions involving the nth level. The factor (dw_n/du) is the required normalization factor,[3] for if $F(x)$ is monotonic and $F(a)=0$, then

$$\delta[F(x)]\,|dF/dx| = \delta(x-a). \quad (7)$$

Letting $w_0(u)=u$ and $W_0=0$, the $n=0$ equation of (6) gives the scattering function for elastic collisions with the nonhydrogen nucleus.

Let $l(u)$ be the total mean free path in the mixture. If the mean free paths for elastic collisions with hydrogen and nonhydrogen nuclei are $l_H(u)$ and $l_0(u)$, respectively, and for inelastic collisions involving the nth energy level, W_n, $l_n(u)$, then the probabilities that a given collision is one of these types are $c(u)=l/l_H$, $c_0(u)=l/l_0$ and $c_n(u)=l/l_n$ respectively. When $u>a_n$, that is, for energies below the threshold for excitation of the nth level, $c_n(u)\equiv 0$, $n>1$. If only the aforementioned kinds of collisions occur, then $1/l \equiv 1/l_H + \sum_{n=0} 1/l_n$ and we have $c(u)+\sum_{n=0} c_n(u) \equiv 1$.

The complete scattering function may now be written

$$F(\mu_0; u, u') = c(u')f(\mu_0; u-u') + \sum_{n=0} c_n(u')f_n(\mu_0; u, u'). \quad (8)$$

Substituting Eq. (8) into Eq. (3) gives

$$F_0(u, u') = c(u')e^{-(u-u')} + \sum_{n=0} c_n(u')f_{n0}(u, u'), \quad (9a)$$

$$F_1(u, u') = c(u')e^{-(1)(u-u')} + \sum_{n=0} c_n(u')f_{n1}(u, u'), \quad (9b)$$

with

$$f_{n0}(u, u') = \delta[w_n(u)-u']dw_n/du, \quad u \geqslant b_n,$$

$$f_{n0}(u, u') = 0, \quad u < b_n,$$

$$f_{n1}(u, u') = [\sigma_{n1}(u')/\sigma_{n0}(u')]\delta[w_n(u)-u']dw_n/du, \quad u \geqslant b_n,$$

$$f_{n1}(u, u') = 0, \quad u < b_n,$$

$$\sigma_{nj}(u') = \int d\Omega_0 P_j(\mu_0)\sigma_n(\mu_0, u').$$

The extension of Eq. (8) to the case of hydrogenous mixtures containing more than one kind of nonhydrogen nucleus follows easily.

DETERMINATION OF THE SLOWING-DOWN LENGTH

For a given source energy E_0 there will be a definite number of excited energy levels, say N, in which the product nucleus may be left after an inelastic collision. These are the energy levels satisfying $W_n \leqslant E_0$, $n=1, 2, \cdots, N$. Because of the δ-function source in Eq. (1a) there will be δ-function singularities in the solutions of Eqs. (1) at points corresponding to combinations of successive inelastic collisions from the source. These points may be designated by

$$b_\alpha \equiv \log\left[E_0/(E_0-\sum_{j=1}^{N} n_j W_j)\right], \quad (10)$$

where n_j is a positive integer or zero and α represents the set $(n_1, \cdots, n_N)$. The constant b_α is the logarithmic energy which a neutron would have after undergoing directly from the source only inelastic collisions, n_1 of which involved W_1, n_2 of which involved W_2, etc.

The total mumber of these "b points" is limited by the fact that a δ-function singularity occurring below the threshold of the first excited level is not propagated to still lower energies by further inelastic collisions. In case a different set of integers $\alpha'=(n_1', \cdots, n_N')$ which involves at least one level W_k (i.e. $n_k' \neq 0$) not in the set $\alpha=(n_1, \cdots, n_N)$ (i.e. $n_k=0$) gives the same point in Eq. (10), such a point will be called a "double" point. More generally if there are q such sets, for any two of which there exists at least one level which is involved in one but in not the other such a point will be called an "q-tuple" point. The singularities in the solutions of Eqs. (1) are made explicit by taking

$$\varphi_{rs} = \chi_{rs} + \textstyle\sum_{\alpha'} K_{rs}(\alpha')\delta(u-b_{\alpha'}) \quad (11)$$

in which the K's are constants and the summation is extended over all distinct b points, including the origin $(n_1'=\cdots=n_N'=0)$. Of course χ_{rs}, the part of the solutionr emaining after the δ functions have been separated out, will be finite but not necessarily continuous at the b points.

The b points divide the u range into intervals. The solution of Eqs. (1) in any such interval may be determined rigorously provided the solution in all the preceding intervals is known. Hence by proceeding from interval to interval the solution for any value of u may be found.

Consider the interval formed by consecutive points b_α, $\alpha=(n_1, \cdots, n_N)$, and b_β, $\beta=(\bar{n}_1, \cdots, \bar{n}_N)$. Since

[3] The factor arises from the fact that the inelastic collisions involving W_n which scatter neutrons into the interval du occur in the interval $(dw_n/du)du$. For numerical computations it is convenient to use the logarithmic energy variable, however, and so it has been retained here.

b_n is the minimum value of u which a neutron may have after an inelastic collision involving W_n, and if $M \leqslant N$ is the largest value of m for which $b_m \leqslant b_\alpha$, then in the set α, $n_j=0$ for $j>M$. Also $f_n(\mu_0; u, u')=0$ when $n>M$ for values of u in the interval, and the summations in Eqs. (9) extend effectively from $n=0$ to $n=M$. From the solution in the previous intervals, all of the K's preceding $K_{rs}(\alpha)$ are known in Eq. (11). To evaluate the $K_{rs}(\alpha)$ we substitute Eq. (11) into Eqs. (1) and equate coefficients of $\delta(u-b_\alpha)$. If we make use of Eq. (7) and of the relationship $w_k(b_\alpha)=b_{\alpha,k}$, $n_k>0$, where the set (α, k) differs from α only in the kth integer, which has the value n_k-1, we obtain

$$K_{00}(\alpha)=[1-c_0(b_\alpha)]^{-1}\sum_k K_{00}(\alpha, k)c_k(b_{\alpha,k}); \quad (12a)$$

$$K_{11}(\alpha)=[1-g_0(b_\alpha)]^{-1} \times[\tfrac{1}{3}l(b_\alpha)K_{00}(\alpha)+\sum_k K_{11}(\alpha, k)g_k(b_{\alpha,k})]; \quad (12b)$$

$$K_{02}(\alpha)=[1-c_0(b_\alpha)]^{-1} \times[2l(b_\alpha)K_{11}(\alpha)+\sum_k K_{02}(\alpha, k)c_k(b_{\alpha,k})], \quad (12c)$$

where

$$g_n(u)=[c_n(u)\sigma_{n1}(u)/\sigma_{n0}(u)]$$

and the summations in Eqs. (12) extend over the suffixes k for which $n_k>0$ in the set α. Equations (12) are complete unless b_α is a q-tuple point, in which case q additional expressions would appear in each. In Eqs. (12) the next set of K's are given in terms of the known preceding ones. For $b_\alpha<u<b_\beta$ Eqs. (1) may now be written as

$$[1-c_0(u)]\chi_{00}(u)=B_{00}e^{-u} +\int_0^u du'\chi_{00}(u')c(u')e^{-(u-u')}+F_{00}(u); \quad (13a)$$

$$[1-g_0(u)]\chi_{11}(u)=B_{11}e^{-3u/2}+\tfrac{1}{3}l(u)\chi_{00}(u) +\int_0^u du'\chi_{11}(u')c(u')e^{-3(u-u')/2}+F_{11}; \quad (13b)$$

$$[1-c_0(u)]\chi_{02}(u)=B_{02}e^{-u}+2l(u)\chi_{11}(u) +\int_0^u du'\chi_{02}(u')c(u')e^{-(u-u')}+F_{02}(u), \quad (13c)$$

where

$$F_{rs}(u)=\sum_{n=1}^{M}\chi_{rs}(w_n)c_n(w_n)(dw_n/du), \quad rs=00, 02, \quad (14a)$$

$$F_{11}=\sum_{n=1}^{M}\chi_{11}(w_n)g_n(w_n)(dw_n/du), \quad (14b)$$

and

$$B_{rs}=\sum K_{rs}(\alpha')c(b_{\alpha'})\exp(b_{\alpha'}), \quad (15a)$$

$$B_{11}=\sum K_{11}(\alpha')c(b_{\alpha'})\exp(\tfrac{3}{2}b_{\alpha'}), \quad (15b)$$

the summations in Eqs. (15) extending over all b points up to and including b_α. The integral Eqs. (13) for the χ's may be solved by first differentiating them, and then solving the corresponding set of first-order differential equations obtained thereby. This gives

$$\left.\begin{aligned}
\chi_{00}(u)&=[1-c_0(u)]^{-1}\{C_{00}\exp[-E(u)]+F_{00}(u) \\
&\qquad +\exp[-E(u)]\int_{b_\alpha}^u c(u')[1-c_0(u')]^{-1}F_{00}(u')\exp[E(u')]du'\}, \\
\chi_{11}(u)&=[1-g_0(u)]^{-1}\{C_{11}\exp[-G(u)]+\tfrac{1}{3}l(u)\chi_{00}(u)+F_{11}(u) \\
&\qquad +\exp[-G(u)]\int_{b_\alpha}^u c(u')[1-g_0(u')]^{-1}[\tfrac{1}{3}l(u')\chi_{00}(u')+F_{11}(u')]\exp[G(u')]du'\}, \\
\chi_{02}(u)&=[1-c_0(u)]^{-1}\{C_{02}\exp[-E(u)]+2l(u)\chi_{11}(u)+F_{02}(u) \\
&\qquad +\exp[-E(u)]\int_{b_\alpha}^u c(u')[1-c_0(u')]^{-1}[2l(u')\chi_{11}(u')+F_{02}(u')]\exp[E(u')]du'\}
\end{aligned}\right\} \quad (16)$$

where

$$\left.\begin{aligned}
E(u)&=\int_{b_\alpha}^u\left[1-\frac{c(u')}{1-c_0(u')}\right]du', \\
G(u)&=\int_{b_\alpha}^u\left[\tfrac{3}{2}-\frac{c(u')}{1-g_0(u')}\right]du',
\end{aligned}\right\} \quad (17)$$

and

$$C_{00}=[1-c_0(b_\alpha)]\chi_{00}(b_\alpha+)-F_{00}(b_\alpha+), \quad (18a)$$

$$C_{11}=[1-g_0(b_\alpha)]\chi_{11}(b_\alpha+)-\tfrac{1}{3}l(b_\alpha)\chi_{00}(b_\alpha+)-F_{11}(b_\alpha+), \quad (18b)$$

$$C_{02}=[1-c_0(b_\alpha)]\chi_{02}(b_\alpha+)-2l(b_\alpha)\chi_{11}(b_\alpha+)-F_{02}(b_\alpha+). \quad (18c)$$

TABLE I. Slowing-down length at various energies below the source energy.

E(Mev)	L_s Including inelastic scattering	L_s Neglecting inelastic scattering
2.0	4.93	5.58
1.5	4.91	5.58
1.0	5.11	5.52
0.50	5.34	5.64
0.25	5.40	5.68
0.10	5.37	5.74
11×10^{-3}	5.50	5.86
1.2×10^{-3}	5.61	5.96
100×10^{-6}	5.74	6.08
1.44×10^{-6}	5.93	6.26
0.025×10^{-6}	6.02	6.35

The limit from the right side is taken because of the discontinuities in the χ's at the b points. The C's may be evaluated in terms of quantities which are known from the solution in the preceding intervals by referring back to the integral Eqs. (13). Using the expressions obtained by taking the right-hand limit at b_α of Eq. (13) and the left-hand limit at b_α of the corresponding equation for the preceding interval, we obtain

$$C_{00}=[1-c_0(b_\alpha)]\chi_{00}(b_\alpha-)-F_{00}(b_\alpha-)+K_{00}(\alpha)c(b_\alpha). \quad (19a)$$

Similarly from the other integral equations, we get

$$C_{11}=[1-g_0(b_\alpha)]\chi_{11}(b_\alpha-)-\tfrac{1}{3}l(b_\alpha)\chi_{00}(b_\alpha-)-F_{11}(b_\alpha-)+K_{11}(\alpha)c(b_\alpha); \quad (19b)$$

$$C_{02}=[1-c_0(b_\alpha)]\chi_{02}(b_\alpha-)-2l(b_\alpha)\chi_{11}(b_\alpha-)-F_{02}(b_\alpha-)+K_{02}(\alpha)c(b_\alpha). \quad (19c)$$

Equations (12), (16), and (19) furnish the desired solution for the given interval in terms of the solution in the preceding intervals.

IRON-WATER MIXTURE

The slowing-down length for a mixture of iron-water in 1:1 volume ratio was computed from Eqs. (16) for a source energy of 2.25 Mev. According to the level structure of the Fe^{56} nucleus determined by Elliot and Deutsch,[4] two energy levels, $E_1=0.85$ Mev and $E_2=2.1$ Mev, will be involved in the inelastic scattering for this source energy. The angular distribution for the inelastic scattering was assumed to be spherically symmetric. The inelastic scattering cross sections were calculated by means of the expressions deduced by Feld[5] on the basis of a simplified theory in which the emission of the neutron from the compound nucleus with orbital angular momentum other than zero is neglected. This appears to be satisfactory for neutron energies such as those involved here, which are small enough to excite only a few levels of the product nucleus. The cross section for formation of the compound nucleus was taken to be 1.5 barns, which is the value used by Feld.

The cross section for elastic collisions with Fe was obtained from the theoretical transport cross section given by Feshbach.[6] The transport cross section is an average cross section for elastic and inelastic scattering, weighted so as to suppress the coutribution from the small angle elastic scattering, which is relatively unimportant in the transport process. The elastic scattering was assumed to be spherically symmetrical with the cross section so obtained. The value of the nuclear radius R in Feshbach's results was chosen so as to make πR^2 equal to 1.5 barns in order to be consistent with the value used in the inelastic cross section expressions. For the other elements in the mixture, experimental values of the cross sections were used.

The slowing-down length was found to be 5.93 cm at the In resonance energy (1.44 ev) and 6.02 cm at thermal energy (0.025 ev). The corresponding slowing-down lengths computed by neglecting the inelastic collisions[7] (i.e. attributing the total Fe cross section to elastic scattering) are 6.26 cm and 6.35 cm, respectively, which amounts to a 5.5 percent difference in each case. The calculated slowing-down length for pure water is about 5.6 cm for In resonance neutrons. In Table I the slowing-down lengths for various energies below the source energy of 2.25 Mev are given as computed from Eqs. (16) and from the expression which neglects all but elastic scattering. It is seen that the inelastic scattering is particularly influential at the high-energy end where the hydrogen cross section has its smallest magnitude.

For a water to iron volume ratio of 1.3:1 and a Ra$-\alpha-$Be source, Munn and Pontecorvo[8] give as the measured slowing-down length at resonance the value 7.3 $\pm$0.3 cm. The larger percentage of water would be expected to decrease the slowing-down length somewhat, but the higher source energies (the average energy of the Ra$-\alpha-$Be neutron energy spectrum is about 5 Mev) would tend to increase the slowing-down length compared to the case used in the computation.

ACKNOWLEDGMENT

Thanks are due Mr. L. Soffer who assisted in the numerical work.

[4] L. G. Elliot and M. Deutsch, Phys. Rev. **64**, 321 (1943).
[5] B. T. Feld, Phys. Rev. **75**, 1115 (1949).
[6] H. Feshbach, U. S. Atomic Energy Commission publication, AECD-2904.
[7] See reference 1, Eq. (108).
[8] A. M. Munn and B. Pontecorvo, Can. J. Research **A25**, 157 (1947).

JOURNAL OF APPLIED PHYSICS VOLUME 25, NUMBER 1 JANUARY, 1954

Preparation of Aerosols for Electron Microscopy

ERNEST H. KALMUS
University of California, Los Alamos Scientific Laboratory, Los Alamos, New Mexico
(Received June 1, 1953)

A technique is described whereby fall-out particles from dust clouds, commonly called aerosols, may be prepared for observation with the electron microscope. Specimens are collected by means of various types of precipitators on molecular filters which are made from cellulose esters. During the process of dissolving this material in acetone, the particles adhering to the filter are transferred to the Formvar-coated specimen screens of the electron microscope. Losses are negligible, residual filter background is eliminated, and particles are clearly visible for measuring.

I. INTRODUCTION

THE sampling of aerosols, as practiced in this and many other laboratories,[1] generally involves the use of thermal or electrostatic precipitators, cascade impactors, and other devices. In some of these instruments, filter paper serves as the collecting substrate from which fall-out particles may be transferred for microscopic examination; or, if desired, statistical counts and measurements may be made directly on air-borne dust particles adhering to the filter surface. Experience has shown that complete elimination of the filter background is not only desirable and advantageous but becomes important whenever very small particles (less than 0.1 micron) are to be studied. As a result of the inherent roughness of the highly permeable filter material, such small particles, e.g., transparent crystallites, are difficult to detect on its surface and do not resolve sufficiently for microscopy, be it optical photomicrography or electronmicrography. Attempts have been made, therefore, to produce a filter material which, in addition to having optimum collecting capacity, could be dissolved chemically after collection, thus freeing surface and embedded particles without leaving any residue or background. Such media, known as molecular or membrane filters were first developed experimentally by A. Goetz *et al.*,[2] and are now commercially available.[3] Several laboratories working in the field of industrial hygiene have already availed themselves of this new opportunity.

II. PREVIOUS TRANSFER ATTEMPTS

Numerous aerosols are being routinely electronmicrographed in this laboratory for statistical evaluation. First attempts to transfer such samples from the collecting filter to a Formvar-covered specimen screen by mechanical means as well as by electrostatic condenser discharge failed, because many crystallites were so deeply embedded as to resist all efforts to dislodge them. These experiments included application of the rolling-pin, rubber roller, and the familiar "squeegee" technique. Equally ineffective was the attempt to remove a sufficient number of particles from the filter surface by way of electric shocks from high-voltage dc or ac power supplies, with the filter-screen combination sandwiched between two highly charged condenser plates. The large electrostatic fields thus produced did not, however, materially increase the yield as expected, mainly because deeper embedded particulates remained unaffected. It was finally decided to dissolve the filter chemically, and it is the application of this technique which may be of interest to other workers in this field.

III. DISSOLUTION OF THE FILTER

Based on the reported solubility of the filter medium in acetone, the method facilitates rapid and effective specimen transfer with negligible losses; also, because of background elimination, particles are visualized in sharp contour for easy measurement. Accordingly, Formvar films were prepared with ethylene dichloride as solvent (0.5 percent to 1.0 percent, depending on particle size), and cast on water in the usual way. Copper specimen screens[4] were then covered with the formvar membrane and desiccated overnight in vacuo.

A simple setup for reflux washing consists of one or more petri dishes (6 cm in diameter), containing supports for mounting the specimen screens. Such supporting "bridges" are easily made from rectangular strips of No. 100 stainless steel wire mesh, bent sharply to an inverted "U" (Figs. 1(a,d)), their length fitting the diameter of the petri dish;[5] sidewalls should not exceed $\frac{3}{16}$ of an inch in height, while the upper flat surface is one quarter of an inch wide. The bridges are covered lengthwise with paper strips, cut from Whatman filters, of slightly smaller width than that of the bridge so that fluid movement along the edges can be observed under a low-power preparation microscope (Fig. 1(b)). One of these strips is placed on top of each bridge with its projecting ends drawn tight and bent downwards so as to touch the floor of the petri dish (Fig. 1(d)). Since filterpaper and bridge exhibit great resiliency, it

[1] M. W. First and L. Silverman, Arch. Ind. Hyg. and Occupational Med. **7**, 1 (1953).
[2] Kerckhoff Laboratories of Biology, California Institute of Technology, Pasadena, California.
[3] Manfactured by Lovell Chemical Company, Watertown, Massachusetts and A. G. Chemical Company, Pasadena, California.
[4] C. E. Challice and C. D. Sutton, Brit. J. App. Phys. **3**, 384 (1952).
[5] M. S. Jaffe, J. App. Phys. **19**, 1187 (1948).

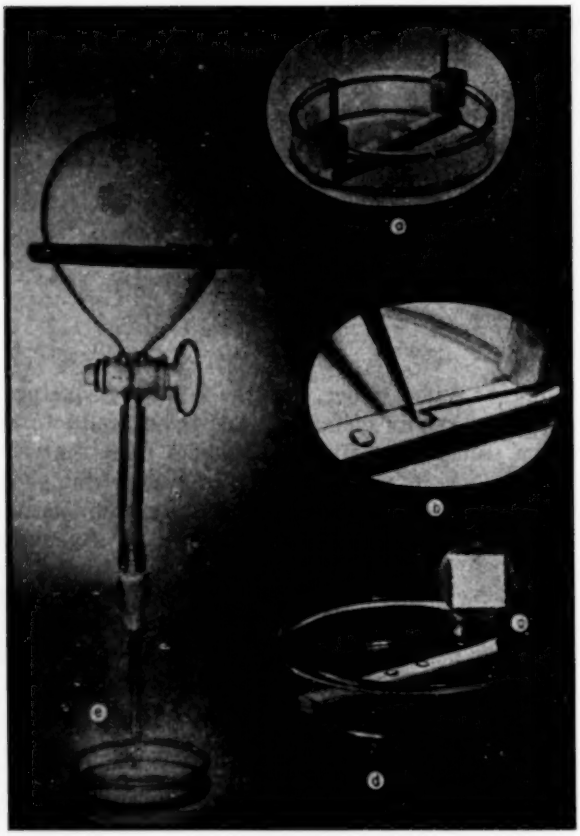

FIG. 1.

is necessary to hold the filterstrip down at both ends during "loading" with small weights or suitable clamps. Little brass blocks with handles, slotted to fit over the sidewalls of the dish, are satisfactory (Fig. 1(a)). Several Formvar-coated specimen screens, film-side up, are then spaced evenly along the filterstrip, and covered with square pieces of the molecular filter, collecting-side down. These squares are cut somewhat smaller than the area of an "inscribed" square over the screen diameter, in order to prevent the loss of particles along edges and screen periphery during dissolution of the filter medium (Fig. 1(c)). The filter pieces are transferred to the screens with watchmaker tweezers (No. 5) and a dissecting needle, both of which constantly touch screen and filter to neutralize the high electrostatic surface charge of the filter material (Fig. 1(b)). After loading one or more petri dishes with the screen-filter combination, a few drops of acetone are applied to each end of the filterpaper "wick" with a medicine dropper; these are rapidly absorbed and drawn up to the top of the bridge, thus starting dissolution (Fig. 1(d)). The weights may then be removed and the dish is further filled with acetone to approximately one-half the height of the bridge. In this way, the screen-filter combination is bathed constantly in a liquid film, surrounded by a saturated acetone atmosphere, without contacting the solvent.[6] Four to five changes of acetone during eight hours will eliminate any filter residue. A permanent source for repeated washings may be provided, such as the separatory funnel in Fig. 1(e). It is important, while changing the solvent, that the screens remain undisturbed; therefore, the liquid should be pipetted off and renewed slowly. During washing and between all steps, dishes are covered from dust and the process of dissolution is followed under the preparation microscope. After washing is completed, the screens are transferred to filterpaper, allowed to dry overnight under vacuum, and sterilized with ultraviolet light.[7] These irradiated Formvar screens appeared to be more resistant to electron bombardment, probably as a result of enhanced

FIG. 2. Aerosol particles after transfer.

polymerization. They are then ready to be examined and photographed in the electron microscope under low to medium intensity only, with just enough image brightness to allow for sharp focusing. This precaution will minimize carbonization and thermal "drift." Prior to examination, metallic shadowing may be applied whenever necessary for better visualization of particle shape.

IV. CONCLUSIONS

It is evident from the electron micrograph in Fig. 2 that, by this technique, the transfer of large numbers of particles from any given aerosol sample which is

[6] I. W. Fischbein, J. App. Phys. **21**, 1199 (1950).

[7] GE miniature mercury vapor lamp, 4w, 0.35a, 10 to 12v, 1849–2537A; 300 Ohm, 50w resistor. Exposure 15 minutes at 2 inches distance.

insoluble in acetone may be achieved. The additional advantage of avoiding initial replication of the filter-background thus makes it essentially a one-step operation which is easily adaptable to special requirements.

The writer gratefully appreciates the helpful criticism and suggestions received during the course of his work from J. W. Dutli, Dr. C. R. Emigh and L. R. Megill of the Radiographic Research Group. Thanks are due also to E. C. Hyatt and H. F. Schulte from the laboratory's Industrial Hygiene Group for their continued interest and cooperation.

JOURNAL OF APPLIED PHYSICS VOLUME 25, NUMBER 1 JANUARY, 1954

Velocity Attenuation of Explosive-Produced Air Shocks

JACOB SAVITT AND R. H. F. STRESAU
U. S. Naval Ordnance Laboratory, White Oak, Maryland
(Received May 22, 1953)

A method for measuring the velocities of explosive-produced air shocks using an electrical ionization probing system is described. The results of such measurements indicate that under varying conditions of confinement of explosive and air shock, that the reciprocal of the air-shock velocity varies linearly with the distance to the charge surface.

INTRODUCTION

IT is the purpose of this report to present the results of some recent measurements of the attenuation of explosive-produced air shocks. Figure 1 shows the arrangement of explosive charge and the probe for measurements made on unconfined air shocks. The explosive was loaded into cylindrical holes, 0.2 inch in diameter and 0.5 inch long, axially centered in brass cylinders 1.0 inch long and 1.0 inch in diameter under a pressure of 10 000 psi. A special electrical primer con-

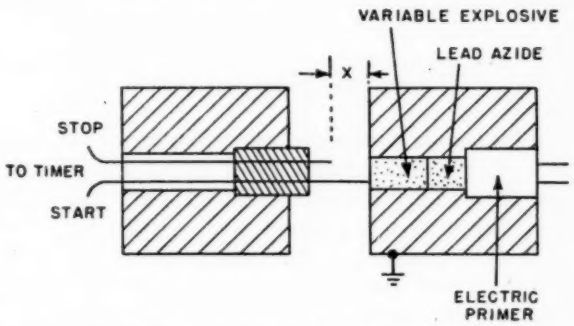

FIG. 1. Explosive system and probe for measurement of unconfined shocks.

taining about 20 mg of lead azide was used as shown in Fig. 1 to begin the reaction.

When the ionized detonation front reached the explosive air interface, the high-potential start probe was grounded to the explosive containing cylinder starting the timer[1] whose basic circuit is shown schematically in Fig. 2.

THE THERMOCOUPLE TIMER

V_1 and V_2 are thyratrons. Triggering V_1 starts a nearly constant current flowing through the heater of the vacuum thermocouple. When V_2 is triggered this part of the circuit is shunted and the current flowing through the thermocouple heater is suddenly reduced to a negligible quantity. The condenser C_3 has a discharge time through the thermocouple circuit which is long compared with the times to be measured. Thus the energy $\int i^2 R dt$ absorbed by the heater is nearly proportional to the time during which the current is flowing through it so that the temperature rise of the heater is proportional to the time. Since the output voltage of the thermocouple is proportional to its temperature, it is clear that the peak output voltage is proportional to the time in which we are interested. In most of the measurements the thermocouple output was amplified and recorded on an Esterline-Angus recording milliammeter. For some of the output measurements a peak holding voltmeter circuit was used.

THE CONDENSER TIMER

The interval timer recently developed by H. W. Anderson and J. V. Atanasoff was used to measure a few of the shorter time intervals. In this timer a constant current pulse is used to charge a condenser. Consequently, the voltage developed across the con-

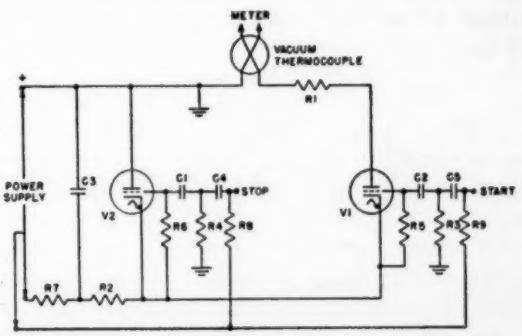

FIG. 2. Basic thermocouple timer circuit.

[1] R. H. Stresau, Phys. Rev. 76, 880(A) (1949).

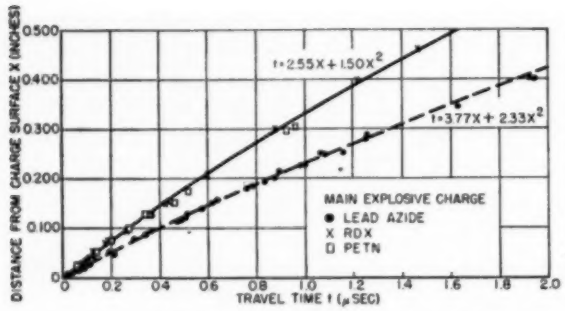

FIG. 3. Travel times for unconfined air shocks.

denser is proportional to the time during which the current is flowing. An electrometer type circuit is used to measure the voltage. Such circuits are capable of measuring very small voltages while drawing only extremely small currents. This latter feature permits the use of very small condensers so that very small charging currents give measurable voltages in times of the order of a small fraction of a microsecond.

UNCONFINED AIR SHOCKS

When the shock produced in the air has traveled the distance x, from the charge surface to the stop probe shown in Fig. 1, V_2 is triggered and a time measurement is obtained. The travel distance for which measurements of travel times were obtained were varied from about 0.010 to about 0.500 inch from the explosive-air interface to the stop probe. These distances were measured with an accuracy of 0.001 inch. The thermocouple timer is capable of measuring times with an accuracy of 0.01 microsecond. The condenser timer can better this by at least an order of magnitude.

Figure 3 is a presentation of the results of time-distance measurements of the type described above. These measurements clearly distinguish between the shocks produced by the high explosives RDX and PETN and those produced by the primary explosive lead azide. No significant difference in shock velocities is observed between RDX and PETN. Initially it appears for these high explosives that the shock velocity is of the order of 10 km/sec while for lead azide the initial shock velocity is 6.7 km/sec. These velocities decrease to about 7.7 km/sec and 4.2 km/sec respectively for $x=\frac{1}{2}$ inch.

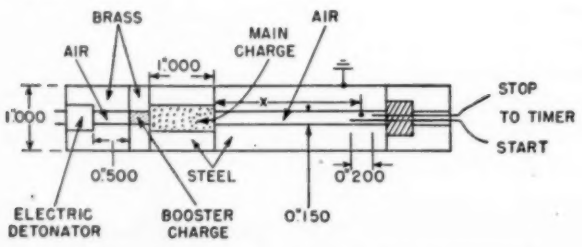

FIG. 4. Explosive system and probe for measurement of confined air shocks.

AN EMPIRICAL CORRELATION

It has been consistently observed for all of the data to be presented in this report that a good empirical fit is obtained when it is assumed that

$$1/U=1/U_0+Kx, \tag{1}$$

where U is the observed air shock velocity at a distance x from the charge surface, K is a constant and U_0 is the value of U for $x=0$. Integration of (1) from $t=0$ to $t=t$ yields

$$t=x/U_0+Kx^2/2, \tag{2}$$

where t is the time measured from the instant of the initial appearance of the air shock at the charge surface. As shown in Fig. 3 Eq. (2) fits the data very well.

CONFINED AIR SHOCKS

Figure 4 illustrates the experimental arrangement used for the measurement of explosive-produced air shocks propagating in heavy-walled steel tubes having an internal diameter of 0.150 inch. The air shocks were produced by detonating one-inch long columns of high explosive of varying diameters loaded into steel cylinders one inch in external diameter. The high explosive was detonated as shown by a booster charge of dextrinated lead azide $\frac{1}{4}$ inch long and 0.150 inch in diameter which in turn was initiated by a special electric detonator containing 50 mg of dextrinated lead azide. All of the explosive charges were loaded into their respective cylindrical cavities in increments of height equal to or less than the cavity diameter and pressed with a snug-fitting ram under a pressure of 4000 psi.

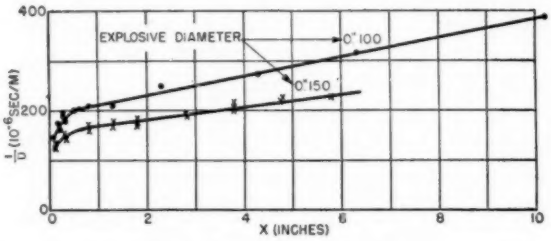

FIG. 5. One-dimensional attenuation of RDX-produced air shocks in steel tubes of 0.150 inch diameter.

The air shock was detected by probes like those used in the measurement of the unconfined air shocks except that the distance between the start and stop points was kept fixed at 0.200 inch. The variation of the one dimensional air shock velocity with distance in the confined tube was obtained by varying the distance x, from the charge surface to the center of the start-stop probe system by varying the tube length and measuring the travel time of the shock over the distance of 0.200 inch centered at the distance x from the charge surface.

In Fig. 5 reciprocal velocities obtained by the procedure outlined above using RDX main charges are shown as functions of x. Equation (1) is clearly a good fit of the data for distances greater than one inch. Note that this is true for all of the explosive diameters

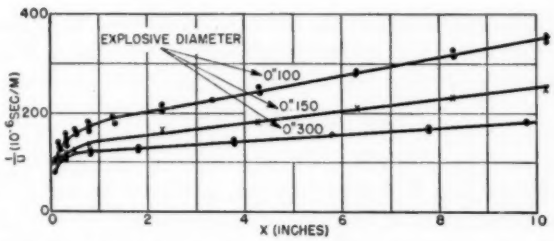

FIG. 6. One-dimensional attenuation of TNT-produced air shocks in steel tubes of 0.150 inch diameter.

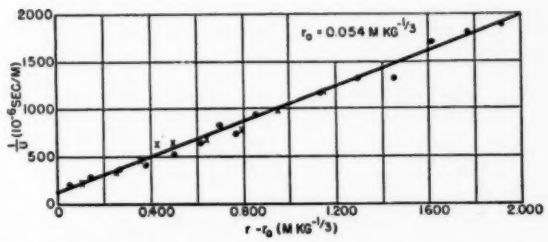

FIG. 7. Three-dimensional attenuation of spherical air shocks produced by spheres of TNT (Weibull's measurements).

used and that the air shock velocity is greater for larger explosive diameters at every distance where it was observed. The same general behavior is observed for TNT as shown in Fig. 6.

SPHERICAL AIR SHOCKS

It was also observed that $1/U$ is a linear function of distance from the surface of a spherical charge of TNT. This is shown in Fig. 7, which is taken from the measurement reported by W. Weibull.[2]

CONCLUSIONS

It can be concluded then, that it is possible to make measurements of explosive-produced air shock velocities very near to, and as far away as ten inches from small highly confined charges using ionization probing systems to detect the arrival of the air shocks. It has been observed that, for distances of less than $\frac{1}{2}$ inch from the charge surface of highly confined cylindrical charges, the reciprocal shock velocity increases linearly with distance from the end of the charge when the shock is unconfined. For shocks confined in tubes the same velocity attenuation law is observed to hold for distances greater than one inch from the charge end. For a spherical 1-kg TNT charge, Weibull's data shows this same linear variation in reciprocal shock velocity with distance from the charge surface. Why this linear relationship between the reciprocal air shock velocity and the distance from the charge surface should hold for all three of these systems is not clear.

[2] W. Weibull, Ballistic Research Laboratories Report No. X-127. Translation by L. N. Enequist from Tidskr. Kustartilleriet **1**, (1947).

JOURNAL OF APPLIED PHYSICS VOLUME 25, NUMBER 1 JANUARY, 1954

A Method of Measuring Magnetostriction

A. W. COCHARDT
Westinghouse Research Laboratories, East Pittsburgh, Pennsylvania
(Received June 10, 1953)

Torsion tests are made on wires of various ferromagnetic materials. It is found that the relationship between shear stress and shear strain is different for magnetized and unmagnetized wires. The difference is explained in terms of wall movement and rotation of ferromagnetic domains, and magnetostriction values are derived from it. This method of determining magnetostriction has several advantages. It is simpler to carry out than most other methods, its accuracy is 4×10^{-7}, and it can be used at elevated temperatures. Its main limitation is that saturation magnetostriction values are not obtainable for alloys which have a large crystal anisotropy energy.

INTRODUCTION

ALL experimental methods of determining magnetostriction, which have been developed so far, are based on magnetic measurements.[1] A sample is placed in a magnetic field which aligns the ferromagnetic domains in the material and changes the dimensions of the sample. This change in dimensions is then measured using either mechanical or optical levers or, more recently, using electrical resistance strain gages.

Becker and Kornetzki have shown some 20 years ago that an applied mechanical stress aligns the ferromagnetic domains in a similar way as a magnetic field does.[2] In addition to the "mechanical" strain, a "magnetostrictive" strain is generally observed when a stress-strain diagram is recorded on a ferromagnetic material. This is illustrated in Fig. 1. If an Fe–14 percent Al alloy is placed in a strong magnetic field and is subjected to a tensile test, it is found that the stress *vs* strain data lie on a straight line up to about 8000 psi, the stress level at which plastic flow begins. But the relationship between stress and strain is different if the alloy is not magnetized. In this case more strain is observed due to the orientation of the domains

[1] R. M. Bozorth, *Ferromagnetism* (McGraw-Hill Book Company, Inc., New York, 1951), p. 628.

[2] R. Becker and M. Kornetzki, Z. Physik. **88**, 634 (1934).

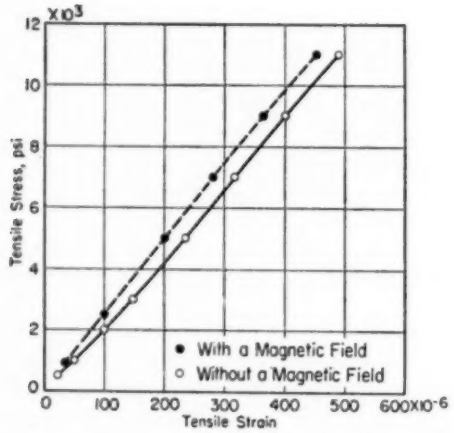

FIG. 1. Tensile stress *vs* tensile strain of Fe–14 percent Al with and without a magnetic field as derived from torsion tests.

under the influence of the applied stress. It is evident from Fig. 1 that in this particular alloy all domains are aligned at a stress of about 5000 psi because the two curves are parallel from there on. The difference in strain between the two curves is hereafter called "magnetostriction" since it is equal in magnitude to the strain that is observed when the domains are oriented in a magnetic field. The magnetostriction is denoted by the symbol λ and is defined as the fractional change in length of the material in the direction in which the ferromagnetic domains align. From these considerations it is apparent that stress-strain measurements should often represent a convenient way of determining magnetostriction. But no attempts have been made, so far as the author is aware, to quantitatively measure magnetostriction using stress rather than a magnetic field.

Small differences in strain are difficult to measure in tension. The described method uses, therefore, a shear stress to orient the domains instead of a tensile stress. In this way measurements are simpler to carry out than with other methods since no elaborate apparatus is required. The experimental arrangement consists simply of a suspended wire which is twisted in torsion. From the angle of twist and the torque, the magnetostriction is more accurately determined than with most of the magnetic methods. The preparation of the samples is simpler since a wire is easier to prepare than a flat strip or a bar. Another advantage is that magnetostriction can be measured at higher temperatures. This is often desirable but is not attainable using the most common magnetic methods. Finally, the procedure can be conveniently used for the study of vibration effects caused by magnetostriction, such as the damping phenomenon in steam turbine and compressor blades[3] and the noise problem of transformers.[4]

One of the limitations of the method is that it does not yield the sign of the magnetostriction, but only its absolute magnitude. Furthermore, the saturation magnetostriction is measurable only if the required stress is lower than the torsional strength of the material.

[3] A. W. Cochardt, Trans. Am. Soc. Mech. Engrs. **75**, 196 (1953).
[4] H. Fahnoe, Trans. Am. Inst. Elec. Engrs. **60**, 277 (1941).

EXPERIMENTAL METHOD

The experimental arrangement is schematically shown in Fig. 2. A wire is firmly clamped between two steel pin vises P. The upper-pin vise is rigidly mounted while the bottom-pin vise is fastened by means of a rigid coupling C to a brass bar which can rotate freely. A galvanometer coil G consisting of a copper frame and about 1000 turns of copper wire is clamped to the bar and is placed in the field of a large alnico magnet. A copper bar is soldered to the bottom end of the galvanometer coil and is immersed in mercury. V is a vane attached to the copper bar in order to damp the system overcritically. This is obtained by floating silicone fluid of the proper viscosity on the mercury. A fine copper wire F is fastened to the brass bar and is connected to the one pole of a dc voltage source consisting of 20 storage batteries, while the copper cylinder Z is connected to the other pole. The test wire is inside a solenoid S and can be subjected to a magnetic field of about 800 oersteds.

If a current flows through the galvanometer coil, the test wire is twisted. The angle of twist θ is measured from the deflection of a light beam, reflected by the mirror M, according to the relation

$$\theta = \tfrac{1}{2} \operatorname{arctg} \frac{a}{D}, \tag{1}$$

where a is the deflection and D the distance between mirror and scale. The torque necessary to twist the

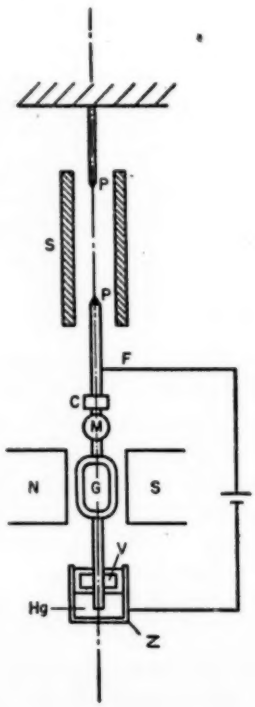

FIG. 2. Schematic diagram of experimental arrangement.

wire is given directly by the current and the angle of twist once the torque is calibrated in terms of the current. This was done by removing the coupling C (Fig. 2) and connecting a torsion balance between pin vise and brass bar. The balance used for the calibration has been described by Becker and Kornetzki[2] for a horizontal arrangement. As expected, it was found that linearity between torque M and current I exists within the range of torque applied during the measurements; the constant K in the relation

$$M = KI\cos\theta \tag{2}$$

was determined in this manner. The error of measurement is mainly given by the distance between mirror and scale since the current is determined more accurately than the deflection. The distance between mirror and scale is either 200 or 450 cm, and the error of the torque-angle of twist measurements is estimated to be 0.2 percent.

PREPARATION OF THE WIRE

Measurements were made using wires whose compositions and dimensions are listed in Table I. The carbon concentration of the Puron wire was 0.006 percent. Alloys 1, 3, 4, and 7 were vacuum-melted, while the others were melted in air. The alloys were first forged and then swaged, except wires 5 and 6 which were centerless ground.

Before making the measurements, the wires were heat treated two times in order to reduce the amount of preferred orientation. The final heat-treatment for all wires was at 900°C for 2 hr in a hydrogen atmosphere with subsequent cooling at a rate of 120°C/hr. X-ray photographs were taken on wire No. 5 for determining the degree of preferred orientation using a Debye-Scherrer camera. The reflection pattern of the unetched surface indicated a slight preferred orientation while the pattern of the etched surface failed to show this.

RESULTS AND INTERPRETATION OF MEASUREMENTS

In order to simplify the procedure, measurements were made in a stress range in which plastic flow could be neglected. The plastic strain was always below 0.25×10^{-6}. Figure 3 illustrates the torque angle of twist curve recorded on wire No. 5. The dashed curve represents the curve postulated by Hooke's law and is obtained either by drawing a tangent at the measured curve (solid line) at the lowest measured value of angle of twist or, more accurately, by measuring θ as a function of M in a strong magnetic field. In the latter case, no additional magnetostrictive strain can occur since all domains remain in the direction of the applied magnetic field; in other words, the M-θ curve must be a straight line in the absence of plastic flow.

TABLE I. Compositions and dimensions of wires.

Alloy No.	% Fe	% Ni	% Co	% Al	% Cr	Length in.	Diam in.	$\frac{1}{4}K_1/\lambda_s$ 1000 psi
1	99.99	...	...	...	...	12.0	0.051	250
2	...	99.99	...	...	...	12.0	0.051	12
3	85	15	...	...	...	12.0	0.051	20
4	72	28	...	...	...	12.0	0.051	4
5	60	...	40	...	...	11.5	0.0595	7
6	86	...	...	14	...	12.0	0.0525	2
7	87	...	...	...	13	8.5	0.0595	80

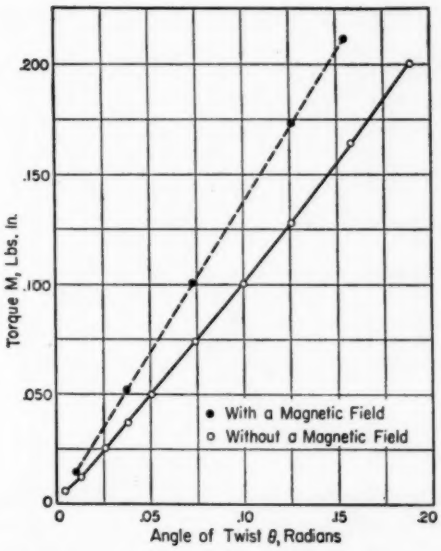

FIG. 3. Torque *vs* angle of twist for Fe–40 percent Co.

The next step of the procedure consists in transforming the M-θ curve into a shear-stress shear-strain curve of the material. This is easily done using the equation

$$\gamma = \theta d/2l \tag{3}$$

for the shear strain and the equation

$$\tau = \frac{4}{\pi d^3}\left(3M + \theta\frac{dM}{d\theta}\right) \tag{4}$$

for the shear stress, where l is the length and d the diameter of the wire. These two relations, which follow from the theory of plasticity,[5] are frequently used for the determination of stress-strain diagrams beyond the yield point. Since the change of slope of the M-θ curve in Fig. 2 is only slight, and even more slight for the M-θ curves of the other materials (Table I), not much accuracy is lost due to this transformation. Figure 4 shows the two $\tau-\gamma$ curves obtained in this fashion on the Fe–40 percent Co alloy. The difference of the abscissa values between the solid and the dashed curve represents the magnetostrictive shear strain; it is evident that this strain is about 30 percent of the total strain at 1000 psi and about 20 percent at 5000 psi.

Since a magnetostrictive shear strain, denoted hereafter by γ_m, is not a common quantity, a final transformation will be made in order to express γ_m in terms of the magnetostriction λ. Instead of using the

[5] A. Nadai, *Theory of Flow and Fracture of Solids* (McGraw-Hill Book Company, Inc., New York, 1950), second edition, Vol. 1, p. 349.

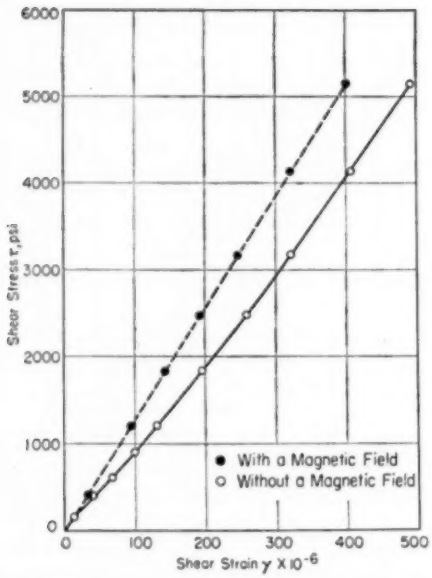

FIG. 4. Shear stress *vs* shear strain for Fe–40 percent Co.

indirect method of determining the $\tau-\gamma$ curve of the Fe–40 percent Co alloy, this curve could have been measured directly by twisting a hollow thin-walled cylinder.[6] A surface element of such a cylinder is schematically shown in Fig. 5. If the cylinder is twisted in pure torsion so that the torque vector is directed upwards (Fig. 5), the mechanical tension strain lies in the x direction and is equal in magnitude to the mechanical compression strain (y direction). Both strains are on a helix line at an angle of 45° to the axis. It is now known[7] that ferromagnetic domains align in direction of the tensile or compression strain depending upon whether λ, determined in a magnetic field, is positive or negative. This means that, for example, in an Fe–40 percent Co cylinder having positive magnetostriction the domains become oriented in the x direction. The total strain in this direction is then

$$\epsilon_x=\epsilon+\lambda,$$

where ϵ is the mechanical strain. Analogously, the strains in the other principal directions are

$$\epsilon_y=-\epsilon-\tfrac{1}{2}\lambda$$
$$\epsilon_z=-\tfrac{1}{2}\lambda,$$

provided the volume magnetostriction is small compared to λ, as is generally the case.[8] From the principal strains the measured shear strain γ is determined according to the expression[9]

$$\gamma^2/4=a_x^2a_y^2(\epsilon_x-\epsilon_y)^2+a_y^2a_z^2(\epsilon_y-\epsilon_z)^2+a_z^2a_x^2(\epsilon_z-\epsilon_x)^2$$

if the values $a_x=1/\sqrt{2}$, $a_y=1/\sqrt{2}$, and $a_z=0$ of the direction cosines are substituted. In this manner the magnetostriction λ is finally obtained as

$$\lambda=\tfrac{2}{3}\gamma_m. \qquad (5)$$

It can be shown on the basis of the same considerations that the same magnetostrictive shear strain is obtained for a material with an equal negative magnetostriction. Consequently, the procedure does not give any information on the sign of the magnetostrictive value.

From Eq. (5) the absolute magnitude of the magnetostriction can be determined by measuring the magnetostrictive shear strain (Fig. 4). This was done for the Fe–40 percent Co alloy as well as for all the other materials listed in Table I. The results are shown in Fig. 6 where λ is plotted against stress. The shear stress τ is hereby replaced by the tension stress σ according to the Mises criterion[10] $\sigma=\sqrt{3}\tau$. This relation holds quite well for various anelastic phenomena,[11] and it is assumed that it is applicable also in this particular case.

Before discussing the results of the measurements, something must be said about the accuracy of the method. It is evident from Fig. 2 that the postulated condition of pure torsion is not fulfilled. In addition to the stresses resulting from the applied torque, there are tensile stresses of the order of 100 psi in the material due to the weight hanging on the wire. It follows from elementary considerations that the observed shear stress τ is not the maximum shear stress of the material at very small stresses. Consequently, the Mises criterion, which is related to the maximum shear stress, is not applicable in this stress range; in other words, the magnetostriction values in Fig. 6 should be higher at stresses of the order of a few hundred psi. However, at

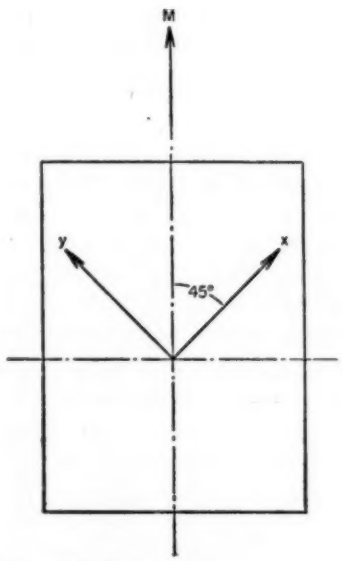

FIG. 5. Surface element of thin-walled cylinder.

[6] S. Timoshenko, *Strength of Materials* (D. Van Nostrand Company, Inc., New York, 1941), second edition, part 2, p. 384.
[7] Reference 1, p. 610.
[8] R. Becker and W. Döring, *Ferromagnetismus* (Julius Springer Verlag, Berlin, 1939), p. 291.
[9] Reference 5, p. 115.
[10] Reference 5, p. 211.
[11] G. I. Taylor and H. Quinney, Trans. Roy. Soc. (London) **A230**, 323 (1931).

larger stresses the x and y directions (Fig. 5) virtually become principal directions, and the recorded values become more accurate. The error of measurement is estimated to be about 3 percent at stresses higher than 1000 psi.

In general, the data in Fig. 6 agree very well with magnetostriction values reported in the literature. Saturation magnetostriction was virtually obtained for the Fe–40 percent Co and the Fe–14 percent alloys, but not for some of the other materials. This is explainable because the stress required to align the domains in cubic metals must be larger than

$$\sigma > \frac{2K_1}{3\lambda_s}, \qquad (6)$$

where K_1 is the anisotropy constant and λ the saturation magnetostriction.[12] The last column in Table I gives the values of this stress for the seven materials, if reported values[13,14] of K_1 and λ_s are substituted in inequality (6). Evidently, the applied stress was not large enough for wires 1, 2, 3, and 7 to satisfy inequality (6), but for the Fe–40 percent Co and for the Fe–14 percent Al the stress was apparently sufficient. This is seen also from a comparison between the measured values of λ_s on these two materials and the reported ones. For Fe–40 percent Co for example, λ was observed as 62×10^{-6} at 9200 psi while the reported value[15] of λ_s is 65×10^{-6}.

The saturation magnetostriction could have been measured also for the other materials, except Puron, if larger stresses would have been applied. This is apparent from Table I. The required stress for the orientation of the domains is smaller than the yield stress of these materials. But the error of measurement would have been increased since the M-θ curve, taken in the magnetic field, no longer would have been a straight line.

The high value of λ for Fe–13 percent Cr (Fig. 6) is due to the high value of magnetostriction in the easy direction. This was already reported by Snoek.[16] The measured values for pure nickel are as expected. For this material the saturation magnetostriction of 40×10^{-6} should occur at a stress higher than 12 000 psi, and this is consistent with the measured value of 17.5 at 3500 psi. The data taken on Puron are slightly higher then those measured on not quite so pure iron at the point of the Villari reversal,[17] but they are still lower than the theoretical value of the magnetostriction in the easy direction.[18] The only values which do not agree with reported ones are those taken on Fe–15 percent Ni. Although the stress was not large enough to rotate the domains, it was sufficient to move the domains in the easy directions. Thus the easy direction magnetostriction, reported[16] to be about 30×10^{-6}, should have been measured, but the observed value was only 4×10^{-6} at 4000 psi. A study of the microstructure of this alloy revealed that its major component is austenite at room temperature. It therefore seems doubtful that the reported value is correct.

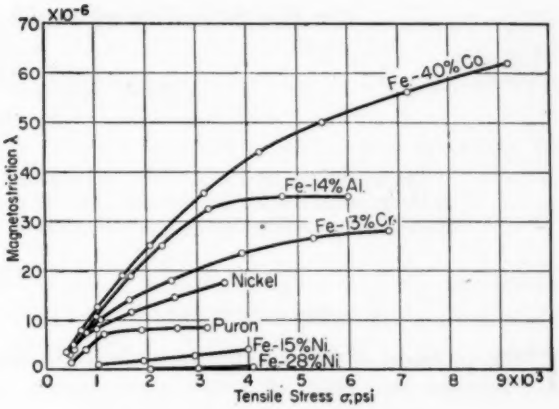

FIG. 6. Magnetostriction *vs* stress.

All in all, it can be safely concluded that the data in Fig. 6 are consistent with our concept of domain wall movement and domain rotation.

SUMMARY

An experimental arrangement is described by which the angle of twist of a test wire is recorded as a function of the external torque. The deviation of this curve from a straight line, or the difference between the curves taken within and without a magnetic field, is due to the alignment of ferromagnetic domains in direction of one of the principal strains. In order to interpret these data in terms of what is commonly understood under magnetostriction, two transformations are made. First, the shear-stress *vs* shear-strain curve of the material is determined from the data. This then leads to the magnetostrictive shear strain of the particular alloy as a function of stress or strain. The second step of the procedure consists in expressing this magnetostrictive shear strain in terms of magnetostriction. that is in terms of the fractional change in length. This is obtained by making use of the relation between shear and principal strains. The method is illustrated using seven different materials. It is found that the measured magnetostriction values are in agreement with values which were obtained using magnetic methods.

ACKNOWLEDGMENT

The author wishes to express his great appreciation to Dr. C. Zener, Associate Director of the Westinghouse Research Laboratories, for many stimulating discussions. Thanks are also due Mr. Albert G. Hartwick for his assistance in taking the measurements.

[12] Reference 1, p. 636.
[13] Reference 1, pp. 570, 655–680.
[14] J. L. Snoek, *New Developments in Ferromagnetic Materials* (Elsevier Publishing Company, Inc., Amsterdam, 1947), p. 16.
[15] S. R. Williams, Rev. Sci. Instr. **3**, 675 (1932).
[16] Reference 14, p. 15.
[17] M. Kornetzki, Z. Physik. **87**, 560 (1933).
[18] Reference 8, p. 288.

On the Stability of Fluid Flows with Spherical Symmetry

M. S. PLESSET*
California Institute of Technology, Pasadena, California
(Received June 15, 1953)

The conditions for the stability or instability of the interface between two immiscible incompressible fluids in radial motion are deduced. The stability conditions derived by Taylor for the interface of two fluids in plane motion do not apply to spherical flows without significant modifications.

I. INTRODUCTION

THE problem of the stability of a plane interface between two fluids of different densities in accelerated motion has been solved by Taylor,[1] who showed that the interface is stable or unstable according as the acceleration is directed from the heavier to the lighter fluid, or conversely. The corresponding problem for a spherical interface has been discussed recently by Binnie,[2] whose analysis, however, appears to be in error as he has omitted some terms of the same order as those considered in his paper. The problem will be reconsidered here. It may be stated as follows: A fluid of density ρ_1 is contained within a sphere of radius R; a fluid of density ρ_2 occupies the region exterior to this sphere. The fluids will be assumed to be immiscible, incompressible, and nonviscous. If it is assumed that the initial and boundary conditions have spherical symmetry, then the equation of motion for the interface radius R as a function of time is readily determined. The question of present concern is the stability of this spherical interface. The answer to this question has application to the pulsations of underwater explosion bubbles and to the growth or collapse of cavitation bubbles.

The discussion of the stability problem given here will be limited to disturbances of the spherical interface of small amplitude. While the stability question is thereby answered, the results cannot be applied to the determination of the rate of development of interface distortions of significant amplitude.

II. SOLUTION OF THE STABILITY PROBLEM

The origin of a spherical coordinate system is taken at the center of the spherical interface $R(t)$. When the interface is strictly spherical, the velocity potential is

$$\varphi=(R^2\dot{R})/r, \tag{1}$$

where the radial velocity at the point r in the fluid is $-\partial\varphi/\partial r$. This potential, of course, implies a source or sink at the origin according as $\dot{R}$ is positive or negative. The stability of the spherical interface will be established by considering whether a distortion of the interface of small amplitude grows or diminishes. Consider, therefore, a distortion of the interface from R to r_s, where

$$r_s=R+aY_n. \tag{2}$$

Y_n is a spherical harmonic of degree n, and a is a function of time such that

$$|a(t)|\ll R(t).$$

The stability analysis given here will be limited to the first order in a. To this order, the fluid particle velocity at the interface in the radial direction is given by

$$u=\dot{R}+\dot{a}Y_n. \tag{3}$$

Across the interface the normal component of the fluid velocity must be continuous. The difference between the normal component of the fluid velocity at the interface and the radial velocity u of Eq. (3) is of second order in a so that the boundary condition is satisfied by the requirement of continuity of u across the interface.

If one chooses a potential which corresponds to a disturbance which decreases away from the interface in both the inward and outward directions, then one has in place of Eq. (1) the potential

$$\varphi=\varphi_1=[(R^2\dot{R})/r]+b_1r^nY_n, \qquad r<R;$$
$$\varphi=\varphi_2=[(R^2\dot{R})/r]+b_2[Y_n/(r^{n+1})] \quad r>R.$$

The quantities b_1 and b_2 are determined by the requirement that

$$-\left(\frac{\partial\varphi_1}{\partial r}\right)_{r_s}=-\left(\frac{\partial\varphi_2}{\partial r}\right)_{r_s}=\dot{R}+\dot{a}Y_n,$$

with the result that

$$\varphi_1=\frac{R^2\dot{R}}{r}-\frac{r^n}{nR^{n-1}}Y_n\left[\dot{a}+2a\frac{\dot{R}}{R}\right] \tag{4}$$

and

$$\varphi_2=\frac{R^2\dot{R}}{r}+\frac{R^{n+2}}{(n+1)r^{n+1}}Y_n\left[\dot{a}+2a\frac{\dot{R}}{R}\right], \tag{5}$$

to the first order.

* Consultant to Rand Corporation.

[1] G. I. Taylor, Proc. Roy. Soc. (London) **A201**, 192 (1950).

[2] A. M. Binnie, Proc. Camb. Phil. Soc. **49**, 151 (1953). In the evaluation of the velocity potentials, Binnie has applied the boundary condition of continuity of the radial velocity across the interface to the unperturbed instead of to the perturbed interface. Consequently, an important term is missing from his Eqs. (2) and (3) for the velocity potentials which is of the same order as that retained. In addition, his equation of motion (5) does not include the term $u\partial u/\partial r$ and a term is missing from his evaluation of $\partial u/\partial t$. Finally, the perturbation in the flow is not given by a simple exponential because of the time variation in the unperturbed interface.

One now uses the Bernoulli integral to evaluate the pressure on either side of the interface surface. Thus, if p_1 is the pressure at the interface in region 1 and p_2 is the pressure at the interface in region 2, one has

$$p_1=P_1(t)+\rho_1\left[\left(\frac{\partial\varphi_1}{\partial t}\right)_{r_s}-\tfrac{1}{2}(\text{grad}\varphi_1)^2_{r_s}\right], \quad (6)$$

$$p_2=P_2(t)+\rho_2\left[\left(\frac{\partial\varphi_2}{\partial t}\right)_{r_s}-\tfrac{1}{2}(\text{grad}\varphi_2)^2_{r_s}\right]. \quad (7)$$

$P_1(t)$ and $P_2(t)$ are the constants of the spatial integration of the equation of motion which lead to the Bernoulli integral; $P_2(t)$ has the further significance of being the pressure at infinity. The quantities entering in Eqs. (6) and (7) are readily found in the first order to be

$$\left(\frac{\partial\varphi_1}{\partial t}\right)_{r_s}=\frac{1}{R}\frac{d}{dt}(R^2\dot{R})-\frac{aY_n}{R^2}\frac{d}{dt}(R^2\dot{R})$$
$$-\frac{\ddot{a}}{n}RY_n+\frac{(n-3)}{n}\dot{a}\dot{R}Y_n$$
$$-\frac{2a}{n}(d^2R/dt^2)Y_n+2a\frac{\dot{R}^2}{R}Y_n; \quad (8)$$

$$\left(\frac{\partial\varphi_2}{\partial t}\right)_{r_s}=\frac{1}{R}\frac{d}{dt}(R^2\dot{R})-\frac{aY_n}{R^2}\frac{d}{dt}(R^2\dot{R})$$
$$+\frac{\ddot{a}}{n+1}RY_n+\frac{(n+4)}{(n+1)}\dot{a}\dot{R}Y_n$$
$$+\frac{2a}{n+1}(d^2R/dt^2)Y_n+2a\frac{\dot{R}^2}{R}Y_n; \quad (9)$$

$$(\text{grad}\varphi_1)^2_{r_s}\approx(\text{grad}\varphi_2)^2_{r_s}\approx u^2\approx\dot{R}^2+2\dot{a}\dot{R}Y_n. \quad (10)$$

It may be noted that while the components of velocity perpendicular to the radial velocity are of first order, their contributions to $(\text{grad}\varphi)^2_{r_s}$ are of second order and are therefore to be neglected.

The pressures at the interface are connected by the relation

$$p_2=p_1-\sigma(1/R'+1/R''),$$

where R' and R'' are the principle radii of curvature of the interface and σ is the surface tension. To the first order one has[3]

$$\frac{1}{R'}+\frac{1}{R''}=\frac{2}{R}+\frac{(n-1)(n+2)}{R^2}aY_n,$$

so that

$$p_2=p_1-\frac{2\sigma}{R}-\frac{(n-1)(n+2)}{R^2}\sigma aY_n. \quad (11)$$

The terms in this relation between p_2 and p_1 which are independent of Y_n give the equation of motion for the unperturbed interface:

$$R(d^2R/dt^2)+(3/2)\dot{R}^2=(P_1-P_2-2\sigma/R)/(\rho_2-\rho_1). \quad (12)$$

The terms proportional to Y_n in Eq. (11) give the differential equation for a from which stability conditions may be deduced:

$$\ddot{a}+[(3\dot{R})/R]\dot{a}-Aa=0, \quad (13)$$

where

$$A=\frac{[n(n-1)\rho_2-(n+1)(n+2)\rho_1](d^2R/dt^2)-(n-1)n(n+1)(n+2)\sigma/R^2}{R[n\rho_2+(n+1)\rho_1]}. \quad (14)$$

III. DISCUSSION OF THE STABILITY CONDITIONS

The stability of a small-amplitude distortion of a spherical interface is determined by the differential Eq. (13). The nature of the solutions $a(t)$ of this equation follows from the variation of R with time, such variation to be consistent with Eq. (12). It is convenient to make the substitution

$$a=\alpha\exp\left[-\frac{3}{2}\int_{t_0}^{t}\frac{\dot{R}(t')}{R(t')}dt'\right]=\left(\frac{R_0}{R}\right)^{\frac{3}{2}}\alpha, \quad (15)$$

where R_0 is the value of R at some fixed time t_0. Equation (13) then becomes

$$\ddot{\alpha}-G(t)\alpha=0, \quad (16)$$

with

$$G(t)=-\frac{3}{2}\frac{d}{dt}\left(\frac{\dot{R}}{R}\right)+\frac{9}{4}\left(\frac{\dot{R}}{R}\right)^2+A$$
$$=-\frac{3}{4}\frac{\dot{R}^2}{R^2}+\frac{(d^2R/dt^2)}{R}\left[\frac{3}{2}+\frac{n(n-1)\rho_2-(n+1)(n+2)\rho_1}{n\rho_2+(n+1)\rho_1}\right]$$
$$-\frac{(n-1)n(n+1)(n+2)\sigma/R^2}{R[n\rho_2+(n+1)\rho_1]}. \quad (17)$$

It should be noted that the factor $(R_0/R)^{\frac{3}{2}}$ in Eq. (15) is always a stabilizing factor when R is increasing and destabilizing when R is decreasing. Aside from this

[3] H. Lamb, *Hydrodynamics* (Cambridge University Press, Cambridge, 1932), sixth edition, Sec. 275.

factor, the stability of the deformation is determined by the function $G(t)$ occurring in the differential Eq. (16). As is well known for differential equations of this form,[4] both solutions cannot be bounded for $t>t_0$ when $G(t)>0$; thus one concludes that the deformation is unstable when $G(t)$ is positive. Conversely, the deformation is stable when $G(t)$ is negative.[5]

While the general criterion for instability has been obtained, the complexity of the function G makes simple physical interpretations somewhat obscure so that some special cases may be considered with advantage.

Case 1. $\sigma=0$; $\rho_2 \gg \rho_1$

The function $G(t)$ simplifies to

$$G(t)=-\frac{3}{4}\frac{\dot{R}^2}{R^2}+\frac{(d^2R/dt^2)}{R}\left[n+\frac{1}{2}\right]. \tag{18}$$

G is certainly positive for $(d^2R/dt^2)\geq 0$ so that one has instability. The surface tension factor which has been neglected is always stabilizing and its effect increases more rapidly with increasing n and decreasing R than the destabilizing terms. As always, the factor $(R_0/R)^3$ is to be included in an over-all stability determination. It may be remarked that the instability found for $(d^2R/dt^2)>0$ is similar to the instability determined by Taylor for the plane case; there is, however, a possibility for instability in the spherical problem even when $(d^2R/dt^2)<0$. This possibility is evident from Eq. (18). A form of this equation which is useful when ρ_1 is small is obtained by using Eq. (12) which gives for Eq. (18)

$$G(t)=\frac{P_1-P_2}{2\rho R^2}+\frac{n(d^2R/dt^2)}{R}\approx\frac{p_1-P_2}{2\rho R^2}+n\frac{(d^2R/dt^2)}{R}, \tag{19}$$

where p_1 is the pressure at the interface in region 1 and P_2 is the pressure at infinity. It is evident that $G(t)>0$ for $(d^2R/dt^2)<0$ when

$$(p_1-P_2)/\rho>2nR\,|\,(d^2R/dt^2)\,|, \tag{20}$$

where $\rho=\rho_2$. This instability will occur more readily when p_1 is large compared with P_2 and when the values of n are not too great. This type of instability may be the explanation of the deformations on expansion of underwater explosion bubbles[6] and the deformations of pulsating air bubbles.[7]

It may be noted that the above instability conditions apply as well to the case where n is large and where ρ_2 merely exceeds ρ_1.

Case 2. $\sigma=0$; $\rho_1 \gg \rho_2$

The function $G(t)$ becomes, in this case,

$$G(t)=-\frac{3}{4}\frac{\dot{R}^2}{R^2}-\frac{(d^2R/dt^2)}{R}\left(n+\frac{1}{2}\right). \tag{21}$$

When $(d^2R/dt^2)\leq 0$, $G(t)>0$ so that one has instability. This instability is of the type found by Taylor for the plane case. The effect of the factor $(R_0/R)^3$ should be kept in mind as well as the obvious stabilizing effect of surface tension. In addition to this Taylor type of instability, there is the possibility of instability for $(d^2R/dt^2)>0$, as is evident from Eq. (21). The condition for this instability may be expressed by the relation

$$R(d^2R/dt^2)<\frac{(3/2)\dot{R}^2}{2n+1},$$

or

$$(d^2R/dt^2)>\frac{P_1-P_2}{2(n+1)\rho_1 R}. \tag{22}$$

[4] See, for example, R. Bellman, ONR Report (NAVEXOS P-596), January, 1949.

[5] By stability (or instability) is meant here that there is no exponential increase (or decrease) in the amplitude of the disturbance. There may still be an algebraic increase or decrease in the amplitude such as is shown in Eq. (15).

[6] R. H. Cole, *Underwater Explosions* (Princeton University Press, Princeton, New Jersey, 1948), illustration facing p. 247.

[7] A. T. Ellis, thesis, California Institute of Technology (1953); ONR Report No. 21-12, Hydrodynamics Laboratory, California Institute of Technology.

JOURNAL OF APPLIED PHYSICS VOLUME 25, NUMBER 1 JANUARY, 1954

Some Problems in the Diffusion of Minority Carriers in a Semiconductor

S. VISVANATHAN AND J. F. BATTEY
Sylvania Electric Products, Inc., Electronics Division, Ipswich, Massachusetts
(Received June 17, 1953)

The exact solutions to the problems of the diffusion of minority carriers involved in the measurement of surface-recombination velocity in a semiconductor with a sample geometry bounded by two infinite planes are presented. The reduction of the exact solutions to simple forms used in the analysis of experimental data is shown.

INTRODUCTION

THE electrical properties of a semiconductor depend on the attenuation of injected carriers as they move through the semiconductor. The loss in the total number of added carriers is the result of the recombination on the surface and in the volume of the semiconductor. The recombination in the bulk is characterized by a bulk lifetime and the recombination on the surface is described by assuming the recombination rate on the surface to be proportional to the added minority carrier concentration on the surface. The constant of proportionality is called the surface-recombination velocity.

The surface-recombination velocity is conveniently measured in a sample bounded by two infinite planes.[1] The solutions to the diffusion equation for this geometry are presented for a point and a line source of injected carriers, and the limits of validity of simple asymptotic expressions are explored. The bulk lifetime must be known for the measurement of surface-recombination velocity. The method of measurement considered here is the diffusion of injected carriers away from a point source on the surface of a semi-infinite semiconductor. It is shown that the error made in neglecting surface recombination in the bulk-lifetime measurements, made to fulfill the need of the preceding problem, is not serious in the case of germanium, if the surface of the semi-infinite sample is etched to yield a low surface-recombination velocity.

These problems are cast in a form similar to heat-conduction problems where the solutions are well known for a variety of sources and boundary conditions.

GENERAL THEORY

The continuity equation for low concentrations of added holes in an n-type semiconductor is given by

$$\partial p/\partial t = -(p/\tau_p) + D_p \nabla^2 p, \tag{1}$$

where p is the added hole density; D_p, their diffusion coefficient; and τ_p, their lifetime. With the following substitutions:

$$X = x/L_p, \quad Y = y/L_p, \quad Z = z/L_p, \quad \text{and} \quad T = t/\tau_p,$$

Eq. (1) becomes

$$\partial p/\partial T = -p + \nabla^2 p,$$

where L_p is the diffusion length. Setting $p = e^{-T}\psi$ the equation for ψ is

$$\partial \psi/\partial T = \nabla^2 \psi. \tag{2}$$

The boundary conditions on the surface of the semiconductor are obtained by equating the diffusion current flowing into the surface to the recombination rate on the surface, that is,

$$D_p(\partial p/\partial n) = -sp,$$

where n is the outward normal to the surface, and s is the surface-recombination velocity. In the reduced form

$$\partial p/\partial N = -s(L_p/D_p)p \equiv -\lambda p. \tag{3}$$

It will be noticed that Eq. (2) is formally the same as the heat-conduction equation with the boundary condition (3) the same as the surface-radiation condition in heat conduction.[2] Thus, the standard methods of heat conduction[3] can be adapted to our problems.

SAMPLE BOUNDED BY TWO INFINITE PLANES

Previously,[1] an approximate solution for the case of a point source was indicated. Here we shall obtain an exact solution and discuss the question of decay of the higher modes. We have to solve (2) with the boundary condition (3) on $Z=0$ and $Z=a$, with a point source at $x=x'$, $y=y'$, $z=z'$ or a line source at $x=x'$, $z=z'$.

The solution to (3) for the point source is given as

$$\psi = \psi_1(X, X'; T)\psi_2(Y, Y'; T)\psi_3(Z, Z'; T),$$

where ψ_1, ψ_2, ψ_3 are the solutions of the following differential equations:

$$\frac{\partial^2 \psi_1}{\partial X^2} = \frac{\partial \psi_1}{\partial T}, \quad \text{for } T>0, \quad -\infty < X < \infty,$$

$$\frac{\partial^2 \psi_2}{\partial Y^2} = \frac{\partial \psi_2}{\partial T}, \quad \text{for } T>0, \quad -\infty < Y < \infty,$$

$$\frac{\partial^2 \psi_3}{\partial Z^2} = \frac{\partial \psi_3}{\partial T}, \quad \text{for } T>0, \quad 0 < Z < a,$$

[1] J. F. Battey and Maynard Dawson, "Measurements of Surface Recombination Velocity in Germanium" (to be published).

[2] This similarity has been pointed out by W. Van Roosbroeck in an unpublished memorandum from the Bell Telephone Laboratories.

[3] H. S. Carslaw and J. C. Jaeger, *Conduction of Heat in Solids* (Clarendon Press, Oxford, 1948).

with the boundary conditions $\psi \to 0$ as $X, Y \to \infty$ or $-\infty$ and

$$\partial\psi_3/\partial Z = \lambda\psi_3, \quad \text{on} \quad Z=0,$$
$$\partial\psi_3/\partial Z = -\lambda\psi_3, \quad \text{on} \quad Z=a,$$

together with a point source at X', Y', Z'.

The solutions ψ_1 and ψ_2 are well known to be

$$\psi_1 = \frac{1}{2(\pi T)^{\frac{1}{2}}} \exp -(X-X')^2/4T,$$

$$\psi_2 = \frac{1}{2(\pi T)^{\frac{1}{2}}} \exp -(Y-Y')^2/4T.$$

ψ_1 (or ψ_2) represents an instantaneous point source in the sense that as $T \to 0$, $\psi_1 \to 0$ for all $X \neq X'$. However, when ψ_1 (or ψ_2) is integrated over all space, the integral has unit value independent of T. ψ_3 is obtained by setting

$$\psi_3 = u + v,$$

where

$$u = \frac{\exp -[(Z-Z')^2/4T]}{2(\pi T)^{\frac{1}{2}}}$$

represents the point source, and v satisfies

$$\frac{\partial v}{\partial T} = \frac{\partial^2 v}{\partial Z^2}, \quad \text{for } T>0,$$

$$v = 0, \quad \text{for } T=0.$$

The solution for ψ_3 is obtained by the standard Laplace transform method and is

$$\psi_3 = \sum_{n=1}^{\infty} 2 \exp -(\alpha_n^2 T) \times \frac{(\alpha_n \cos\alpha_n Z + \lambda \sin\alpha_n Z)(\alpha_n \cos\alpha_n Z' + \lambda \sin\alpha_n Z')}{[a(\alpha_n^2+\lambda^2)+2\lambda]}.$$

The α_n's are given as the roots of the transcendental equation

$$\tan\alpha a = \frac{2\alpha\lambda}{(\alpha^2-\lambda^2)}. \tag{4}$$

Thus,

$$\psi = \psi_1\psi_2\psi_3 = \frac{\exp -[(X-X')^2+(Y-Y')^2]/4T}{4\pi T} \times \sum_{n=1}^{\infty} 2 \exp -(\alpha_n^2 T) \times \frac{(\alpha_n \cos\alpha_n Z + \lambda \sin\alpha_n Z)(\alpha_n \cos\alpha_n Z' + \lambda \sin\alpha_n Z')}{[a(\alpha_n^2+\lambda^2)+2\lambda]}.$$

The steady-state solution for p, obtained by integrating the time-dependent solution with respect to T from zero to infinity, is

$$p(X, Y, Z; X', Y', Z') = \int_0^{\infty} e^{-T}\psi dT = \sum_{n=1}^{\infty} \frac{K_0[(\alpha_n^2+1)^{\frac{1}{2}}R]}{\pi} \times \frac{(\alpha_n \cos\alpha_n Z + \lambda \sin\alpha_n Z)(\alpha_n \cos\alpha_n Z' + \lambda \sin\alpha_n Z')}{[a(\alpha_n^2+\lambda^2)+2\lambda]},$$

where $R^2 = (X-X')^2+(Y-Y')^2$ and K_0 is a modified Bessel function of order zero.

The hole concentration on the surface of the semiconductor when the source is also on the surface is

$$p(X, Y, 0; X', Y', 0) = \sum_{n=1}^{\infty} \frac{K_0[(\alpha_n^2+1)^{\frac{1}{2}}R]}{\pi} \times \frac{\alpha_n^2}{[a(\alpha_n^2+\lambda^2)+2\lambda]}. \tag{5}$$

If the point source is replaced by a line source of infinite extent at $X=X'$ and $Z=Z'$, the steady-state solution obtained by the procedure illustrated above is

$$p(X, Z; X', Z') = \sum_{n=1}^{\infty} \frac{\exp -(\alpha_n^2+1)^{\frac{1}{2}}(X-X')}{(\alpha_n^2+1)^{\frac{1}{2}}} \cdot \frac{(\alpha_n \cos\alpha_n Z + \lambda \sin\alpha_n Z)(\alpha_n \cos\alpha_n Z' + \lambda \sin\alpha_n Z')}{[a(\alpha_n^2+\lambda^2)+2\lambda]},$$

whence

$$p(X, 0; 0, 0) = \sum_{n=1}^{\infty} \frac{\exp -(\alpha_n^2+1)^{\frac{1}{2}}X}{(\alpha_n^2+1)^{\frac{1}{2}}} \cdot \frac{\alpha_n^2}{[a(\alpha_n^2+\lambda^2)+2\lambda]}. \tag{6}$$

Returning to (5), the expression for the modified Bessel function can be approximated by its asymptotic form for R greater than unity, that is, after one diffusion length. Equation (5) then becomes

$$p \simeq \sum_{n=1}^{\infty} \frac{1}{(2\pi)^{\frac{1}{2}}} \frac{1}{(\alpha_n^2+1)^{\frac{1}{4}}} \times \frac{\alpha_n^2}{[a(\alpha_n^2+\lambda^2)+2\lambda]} \frac{\exp -(\alpha_n^2+1)^{\frac{1}{2}}R}{R^{\frac{1}{2}}}. \tag{5a}$$

It can be shown that for values of $R>1$, all terms except the first one in the summation can be neglected. This result can be expeditiously obtained by factoring the

transcendental Eq. (4) into the equations

$$\frac{\alpha a}{2}\tan\frac{\alpha a}{2}=\frac{\lambda a}{2},$$

$$\frac{\alpha a}{2}\cot\frac{\alpha a}{2}=-\frac{\lambda a}{2},$$

and noting that only positive values of the angle $\alpha a/2$ need be considered in (5a).

For small values of $\lambda a/2=(sb)/(2D_p)$, where b is the sample thickness in nonreduced notation, the first root of the tangent equation may be approximated by $(\lambda a/2)^{\frac{1}{2}}$, and subsequent one by multiples of π; the roots of the cotangent equations may be approximated by odd multiples of $\pi/2$. For $\lambda<1$ and $n\pi/a>1$, the summation of the terms other than the first can then be approximated by an integral

$$\frac{1}{(2\pi)^{\frac{1}{2}}a}\int_1^\infty \frac{1}{(n\pi R/a)^{\frac{1}{2}}}\exp(-n\pi R/a)dn,$$

which is negligible compared to the first term at $R=1$ and relatively smaller for larger values of R. In the case of the line source (6) the corresponding integral,

$$\int_1^\infty \frac{1}{a(n\pi/a)}\exp(-n\pi X/a)dn,$$

is even more favorable to the first-term approximation of the summation at one diffusion length.

Thus for a point source on the surface of a sample thin compared to a diffusion length, and values of $r>L_p$ (where $r=L_pR$), if $\log pr^{\frac{1}{2}}$ is plotted against r, the slope of the resulting straight line is

$$\left(\frac{\alpha_0^2}{L_p^2}+\frac{1}{L_p^2}\right)^{\frac{1}{2}}\simeq-\left(\frac{2s}{bD_p}+\frac{1}{L_p^2}\right)^{\frac{1}{2}}.$$

The equality holds good for $sb/2D_p\ll1$, which can be easily achieved for almost any surface treatment in the case of germanium. It is in this approximation which we have shown that only the first term in the summation need be considered at one diffusion length and beyond. For the line source, $\log p$ itself can be plotted against r and the same slope obtained. Again the first-term approximation is valid under the same conditions.

In order to analyze experimental data for surface-recombination velocity using the preceding expressions, it is necessary to know the diffusion length or bulk lifetime. This can be obtained by measuring the distribution of injected-carriers diffusing away from a point or line source[4] on the surface of a semi-infinite semiconductor. For the sake of brevity only the point source will be considered here.

[4] L. B. Valdes, Proc. Inst. Radio Engrs. **40**, 1420 (1952).

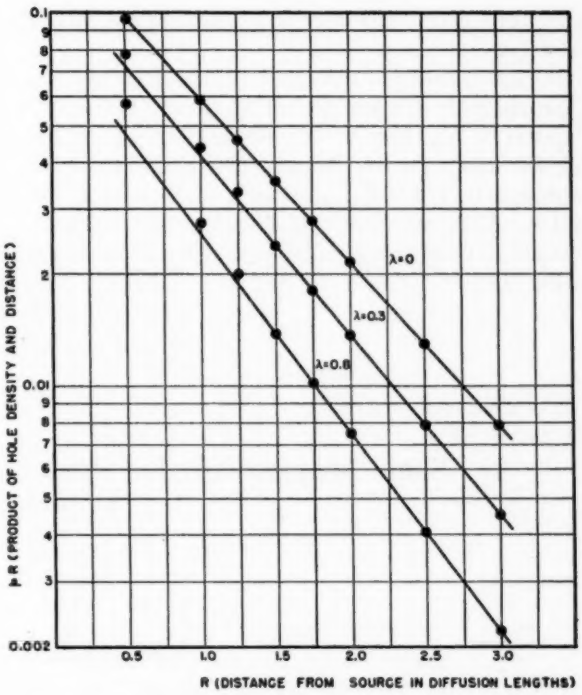

FIG. 1. The plotted points show the hole density p, computed as a function of distance R from a point source on the surface of a semi-infinite n-type semiconductor. The hole density is computed at the semiconductor surface, and the parameter λ is proportional to the surface-recombination velocity $\lambda=S(\tau_p/D_p)^{\frac{1}{2}}$.

The time-dependent solution, for the semi-infinite semiconductor ($Z>0$) with surface recombination on $Z=0$, is given by[5]

$$\psi(X,Y,Z;X',Y',Z';T)$$

$$=\frac{1}{8(\pi T)^{\frac{1}{2}}}\exp-[(X-X')^2+(Y-Y')^2]/4T$$

$$\times\left\{\exp[-(Z-Z')^2/4T]+\exp[-(Z+Z')^2/4T]\right.$$

$$\left.-2\lambda\int_0^\infty \exp[-\lambda\xi-(Z+Z'+\xi)^2/4T]d\xi\right\}.$$

The steady-state solution is*

$$p(R,0;0,0,0)=\frac{1}{2\pi}\left\{\frac{e^{-R}}{R}-\lambda\right.$$

$$\left.\times\int_0^\infty \frac{\exp[-\lambda\xi-(R^2+\xi^2)^{\frac{1}{2}}]}{(R^2+\xi^2)^{\frac{1}{2}}}d\xi\right\}.$$

The integral cannot be evaluated analytically. It has been evaluated numerically as a function of R for several values of λ representative of germanium treated

[5] See reference 3, page 308.

* The same expression is obtained in reference 2.

with an etch yielding low surface-recombination velocity.

If $\log pr$ is then plotted against r, it so happens that an approximately straight line is obtained. For $\lambda=0$, the slope is $1/L_p$. For $\lambda=0.3$ (corresponding to $s=200$ cm/sec and $\tau_p=100$ microseconds) the slope is approximately $1/0.90L_p$, and for $\lambda=0.8$ ($s=200$ cm/sec and $\tau_p=1000$ microseconds) the slope is approximately $1/0.82L_p$. This somewhat surprising result is illustrated in Fig. 1.

Thus, for the determination of surface-recombination velocity in the case of the semiconductor bounded by two infinite planes, if $1/L_p^2$ is small compared to $2s/bD_p$, the error made in adopting the slope of the preceding plot as $1/L_p$ is not serious. This procedure seems more reasonable when one considers the degree of reproducibility of surface-recombination velocities obtained from a specified surface treatment and the inhomogeneity of a given crystal with respect to bulk lifetime.

JOURNAL OF APPLIED PHYSICS VOLUME 25, NUMBER 1 JANUARY, 1954

Some Magnetostriction Relations in Materials Possessing Preferred Domain Orientations

GEORGE T. RADO
Naval Research Laboratory, Washington 25, D. C.
(Received June 19, 1953)

Simple relations between certain magnetostrictive strains are derived for polycrystalline ferromagnetic materials possessing a preferred axis in the distribution of domain orientations. Good agreement with experimental results is obtained.

I. INTRODUCTION

TO obtain certain desirable properties in ferromagnetic materials it is sometimes necessary to establish a preferred axis in the distribution of domain orientations. Such properties include a high remanence in magnetically hard materials used for permanent magnets, and a rectangular hysteresis loop in magnetically soft materials used for special transformer cores. The treatments employed to establish a preferred axis include subjecting the material to an external stress, annealing it in a magnetic field, and orienting its crystallites.

In a given material, an analysis of magnetostriction measurements is one possible method for obtaining information on the distribution of domain orientations. Since a survey of the literature shows that this method has not been exploited adequately, it seems worth while to offer a simple but precise formulation of the magnetostriction equation needed for such an analysis. This formulation elaborates on established concepts but leads to magnetostriction relations which do not seem to have been pointed out previously. They provide good correlations of various experimental results and permit useful inferences regarding some aspects of the distribution of domain orientations.

II. MAGNETOSTRICTION RELATIONS

A. Assumptions

An experimentally observed magnetostrictive change in volume or in length results from a combination of three mechanisms: the "spontaneous magnetostriction," the "forced magnetostriction," and the "form effect."[1] The physical origin of these mechanisms is the dependence of anisotropy, exchange, and magnetostatic energy, respectively, on the state of strain in the material. On a fractional basis, the changes in length due to the forced magnetostriction and the form effect, as well as the three types of volume changes, are usually small and will be neglected here. The fractional change in length due to the spontaneous magnetostriction is the only kind of magnetostriction considered in this paper. Such a change in length will be referred to as a "magnetostrictive strain." It will be assumed that the magnetostrictive strains are isotropic in the sense of being independent of the orientations of the domains with respect to crystallographic directions. This simplifying assumption proves to be a reasonably good approximation for polycrystalline materials in which the preferred axis is established by means of a stress or by annealing in a magnetic field, but it cannot be expected to hold for materials in which the preferred axis is established by means of crystallite alignment. Finally, only those magnetostrictive strains will be considered in which the rearrangement of the domain orientations (which causes the change in anisotropy energy and thus the change in the spontaneous distortion of the lattice) proceeds from some arbitrary initial distribution to some *saturated* final distribution.

For a quantitative discussion, introduce the unit

[1] For a review of magnetostriction, see R. Becker and W. Döring *Ferromagnetismus* (Verlag Julius Springer, Berlin, 1939), R. M. Bozorth, *Ferromagnetism* (D. Van Nostrand Company, Inc., New York, 1951); E. W. Lee, Science Prog. 41, 58 (1953).

vectors $\mathbf{u}_{sat}$ and $\mathbf{u}_{str}$ parallel to the direction of final saturation and to the direction of strain measurement, respectively. Let the angle between these two vectors be ψ_s, and their orientations relative to the rectangular coordinate system x, y, z be arbitrary (see Fig. 1). Suppose, temporarily, that the initial distribution of domain orientations is that of magnetic saturation along $\mathbf{u}_{str}$. If the material is subsequently saturated along $\mathbf{u}_{sat}$, then a certain magnetostrictive strain, λ^*, appears along $\mathbf{u}_{str}$. Since λ^* must vanish when $\psi_s=0$, and since λ^* cannot change when ψ_s is replaced by $\psi_s+\pi$ (because the anisotropy energy does not change upon a 180° reversal of the magnetization vector), it is reasonable to expand λ^* in a series of even powers of $\sin\psi_s$. Keeping only the lowest-order term that gives a dependence on ψ_s, one obtains

$$\lambda^*=-C\sin^2\psi_s, \tag{1}$$

where C, which may be positive or negative, is a (temperature dependent) constant of the material; C may depend on the atomic arrangement but not on the domain structure.

B. Arbitrary Distribution

Now suppose that the initial distribution of domain orientations is that described by the arbitrary function $f(\theta, \phi)$. If the material is subsequently saturated along $\mathbf{u}_{sat}$, then a certain magnetostrictive strain, λ, appears along $\mathbf{u}_{str}$. Application of the superposition principle to Eq. (1) gives

$$\lambda=C\int_\phi\int_\theta \sin^2\psi f(\theta,\phi)d\theta d\phi-C\sin^2\psi_s. \tag{2}$$

Here $f(\theta, \phi)d\theta d\phi$ is the volume fraction of material possessing domains oriented (within the solid angle $\sin\theta d\theta d\phi$) parallel to the direction $\mathbf{u}_{\theta,\phi}$, and ψ is the angle between $\mathbf{u}_{\theta,\phi}$ and $\mathbf{u}_{str}$. The coordinate system x, y, z defining θ and ϕ (see Fig. 1) is still oriented in some arbitrary manner relative to $\mathbf{u}_{sat}$ and $\mathbf{u}_{str}$, and the integrations over ϕ and θ extend from zero to 2π and from zero to π, respectively. Since, by definition, $f(\theta, \phi)$ satisfies

$$\int_\phi\int_\theta f(\theta,\phi)d\theta d\phi=1, \tag{3}$$

Eq. (2) becomes

$$\lambda=C\left[\cos^2\psi_s-\int_\phi\int_\theta \cos^2\psi f(\theta,\phi)d\theta d\phi\right]. \tag{4}$$

This general equation has two properties which do not depend on the nature of $f(\theta, \phi)$.

First, it is seen that for any given direction of $\mathbf{u}_{str}$ the difference of the magnetostrictive strains characterized by any two ψ_s values, called ψ_s' and ψ_s'', is given by $C(\cos^2\psi_s'-\cos^2\psi_s'')$, independent of $f(\theta, \phi)$. In particular, consider $\psi_s'=0$ and $\psi_s''=\pi/2$, and define the corresponding magnetostrictive strains, $\lambda_{l\xi}$ and $\lambda_{t\xi}$, to be the longitudinal and transversal magnetostrictive strain, respectively; the subscript ξ denotes the (arbitrary) direction of $\mathbf{u}_{str}$. Equation (4) then gives

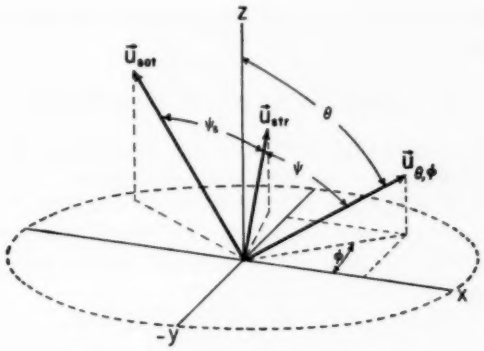

FIG. 1. Coordinates used in the text.

$$\lambda_{l\xi}=C\left[1-\int_\phi\int_\theta \cos^2\psi f(\theta,\phi)d\theta d\phi\right] \tag{5}$$

and

$$\lambda_{t\xi}=-C\int_\phi\int_\theta \cos^2\psi f(\theta,\phi)d\theta d\phi, \tag{6}$$

so that

$$C=\lambda_{l\xi}-\lambda_{t\xi}, \tag{7}$$

is independent of $f(\theta, \phi)$.

Second, it is easily shown that the magnetostrictive change in volume vanishes in the approximation used. Consider three mutually orthogonal directions ($k=1$, 2, 3) of $\mathbf{u}_{str}$ and let them form the angles $\psi_s^{(k)}$ with $\mathbf{u}_{sat}$ and the angles $\psi^{(k)}$ with $\mathbf{u}_{\theta,\phi}$. Since the relations

$$\sum_{k=1}^{3}\cos^2\psi_s^{(k)}=\sum_{k=1}^{3}\cos^2\psi^{(k)}=1,$$

as well as Eq. (3), are always valid, it follows from Eq. (4) that the sum of the three orthogonal strains is given by

$$C\left[\sum_{k=1}^{3}\cos^2\psi_s^{(k)}-\sum_{k=1}^{3}\int_\phi\int_\theta \cos^2\psi^{(k)}f(\theta,\phi)d\theta d\phi\right]=0, \tag{8}$$

showing explicitly that the change in volume vanishes in accord with the original assumption.

In this connection, it may be pointed out explicitly that Eq. (4) is in accord with two other assumptions also. Since it does not contain any reference to the shape of the sample, Eq. (4) neglects any change in length due to the form effect, and since it presumes a constant magnitude of the spontaneous magnetization during the process of magnetizing the sample, Eq. (4) neglects any change in length due to the forced magnetostriction. As stated above in an equivalent way, Eq. (4) is concerned solely with the change in length due to changes in

the orientations of the spontaneous magnetization vectors.

C. Axially Symmetrical Distribution

If the initial distribution of domain orientations in a macroscopically homogeneous polycrystal contains a preferred axis, then the distribution must be symmetrical about this axis. Consequently, $f(\theta, \phi)$ may be written as $F(\theta)$ by identifying, without loss of generality, the z axis with the preferred axis.

Let the subscripts p and n refer, respectively, to parallel and normal orientation of $\mathbf{u}_{st}$ relative to the z axis, and note that p corresponds to $\cos\psi = \cos\theta$ whereas n corresponds to $\cos\psi = \sin\theta\cos\phi$. If one uses the abbreviation

$$D = 2\pi \int_\theta \cos^2\theta F(\theta) d\theta, \tag{9}$$

and notes that Eq. (3) leads to

$$\int_\theta F(\theta) d\theta = 1/2\pi, \tag{10}$$

one obtains from Eq. (5)

$$\lambda_{lp}{}^a = C(1-D) \tag{11a}$$

and

$$\lambda_{ln}{}^a = (C/2)(1+D), \tag{11b}$$

and from Eq. (6)

$$\lambda_{tp}{}^a = -CD \tag{11c}$$

and

$$\lambda_{tn}{}^a = -(C/2)(1-D), \tag{11d}$$

where the superscript a refers to an axially symmetrical distribution.

The quantity D, which will be called the "alignment index," is a convenient measure of the alignment of the domains parallel (or anti-parallel) to the preferred axis. Thus D has the value unity for complete alignment, $\frac{1}{3}$ for an isotropic distribution $[F(\theta) = (1/4\pi)\sin\theta]$, and zero for 90° orientation of all the domains relative to the preferred axis. It should be noted that D depends on the domain structure whereas C does not. However, the value of D in Eq. (9), together with the validity of Eq. (10), obviously does not determine $F(\theta)$ uniquely.

To obtain relations independent of the nature of $F(\theta)$, the quantity D must be eliminated from Eqs. (11). After substituting Eq. (11c) into Eqs. (11a), (11b), and (11d), these equations may be combined appropriately to give

$$C = \lambda_{lp}{}^a - \lambda_{tp}{}^a, \tag{12}$$

$$C = \lambda_{ln}{}^a - \lambda_{tn}{}^a, \tag{13}$$

and

$$\lambda_{lp}{}^a + 2\lambda_{tn}{}^a = 0. \tag{14}$$

These particular versions of Eqs. (11) are stated here because they show that Eqs. (12) and (13), being applications of Eq. (7), are valid even if the distribution marked "a" is not axially symmetrical, whereas Eq. (14) is valid only if this distribution actually is axially symmetrical. It follows that for a condition of axial symmetry one can use either Eq. (14) or any combination of Eq. (14) with Eqs. (12) and (13). The two examples

$$\lambda_{ln}{}^a + \lambda_{tn}{}^a + \lambda_{tp}{}^a = 0 \tag{15}$$

and

$$2\lambda_{ln}{}^a + \lambda_{lp}{}^a = 2C \tag{16}$$

of such a combination are stated explicitly because Eq. (15), together with Eq. (14), confirms the expected vanishing of volume magnetostriction [see Eq. (8)] for the case of an axially symmetrical distribution, and Eq. (16) is pertinent to the analysis of certain experimental data (see Sec. IIIB).

D. Isotropic Distribution

If the initial distribution of domain orientations is isotropic, then $f(\theta, \phi)$ is given by $(1/4\pi)\sin\theta$, and $\cos\psi$ may be identified with $\cos\theta$ without loss of generality. Thus Eq. (4) becomes

$$\lambda^i = C[\cos^2\psi_s - (\tfrac{1}{3})], \tag{17}$$

where the superscript i refers to an isotropic distribution. From Eq. (17) one obtains

$$C = (\tfrac{3}{2})\lambda_{l\xi}{}^i \tag{18}$$

and

$$C = -3\lambda_{t\xi}{}^i, \tag{19}$$

where the subscripts $l\xi$ and $t\xi$ have the same meaning as before.

It may be noted that the quantity $\lambda_{l\xi}{}^i$ is usually referred to, somewhat ambiguously, as the saturation magnetostriction (or magnetostriction coefficient), and denoted by the symbol λ_s. Furthermore, Eqs. (17) and (18) give

$$\lambda^i = (\tfrac{3}{2})\lambda_{l\xi}{}^i[\cos^2\psi_s - (\tfrac{1}{3})], \tag{20}$$

which represents (except for the symbols) the familiar magnetostriction equation.[1] Since it is well known that in general the initial distribution is not isotropic, the use of Eq. (4) supplemented by Eq. (7) is preferable to the use of Eq. (20).

The equations

$$C = \lambda_{l\xi}{}^i - \lambda_{t\xi}{}^i \tag{21}$$

and

$$\lambda_{l\xi}{}^i = -2\lambda_{t\xi}{}^i, \tag{22}$$

which follow from Eqs. (18) and (19), are stated here because Eq. (21), being an application of Eq. (7), is valid even if the distribution marked "i" is not isotropic, whereas Eq. (22) [as well as Eq. (18) and Eq. (19)] is valid only if this distribution actually is isotropic. Equation (22), of course, confirms the expected vanishing of the volume magnetostriction [see Eq. (8)] for the case of an isotropic distribution.

III. ANALYSIS OF EXPERIMENTAL RESULTS

A. Method

Suppose that for a given material there are available experimental data on the quantities $\lambda_{l\xi}{}^i$ and $\lambda_{t\xi}{}^i$ for the "untreated" state, and on any three of the quantities $\lambda_{lp}{}^a$, $\lambda_{ln}{}^a$, $\lambda_{tp}{}^a$, and $\lambda_{tn}{}^a$ for the "treated" state, the term "treated" referring to the possibility that an axially symmetrical distribution of domain orientations may have been established. If the basic assumptions of Sec. IIA are found to be valid, as determined by the applicability of Eqs. (7) and (8) to the experimental results, then a systematic analysis of the data should include the following steps: (a) Calculate a value of C by means of Eq. (21) as well as by means of Eq. (12) or Eq. (13). If these two C values agree, the *intrinsic* magnetostrictive properties (which may be affected, for example, by the atomic ordering)[2] have not changed as a result of the treatment; if the two C values do not agree, these properties have changed. (b) In either case, use Eq. (22) to determine whether the initial distribution of domain orientations is isotropic in the untreated state, and Eq. (14) [or any combination of this equation with Eqs. (12) and (13)] to determine whether that distribution is axially symmetrical in the treated state. (c) If there is axial symmetry in the treated state, calculate the alignment index D by means of one of the Eqs. (11).

B. Applications

Only two papers[3,4] seem to contain sufficient data for the analysis planned above. One[3] of these involves aligned crystallites (columnar crystals) so that the assumption of isotropic magnetostriction, and hence the present analysis is not applicable. The other[4] involves annealing in a magnetic field so that the present analysis may be applicable. If one uses the data of Hoselitz and McCaig[4] given in Table I, one obtains $C=28$ [from Eq. (21)] for the untreated state, and $C=29$ [from Eq. (12)] or $C=30$ [from Eq. (13)] for the treated state, so that if any change took place due to the treatment, it could have taken place in the domain orientations only. Since Eq. (22) is not fulfilled, and Eq. (16) is approximately fulfilled (within the estimated fractional error of the measurements), the distribution in the untreated state was not isotropic, whereas that in the treated state was roughly axially symmetrical. [The use of Eq. (16) is preferable to the use of Eq. (14) because $\lambda_{tn}{}^a$, being approximately zero in this case, probably involves a relatively large fractional error.] Finally it is found from Eqs. (11a), (11b), or (11c) that D is about 0.9 so that the alignment of the domains is fairly complete.

Hoselitz and McCaig[4] analyzed their data quite differently. They *assumed* that "in the sample which has been cooled in a magnetic field the domains in each crystal are magnetized along the cube edge which is in nearest alignment with the direction in which the field was applied during cooling." They also assumed that certain specific types of domain changes occur during magnetization and thus derived two relations which may be written as

$$\lambda_{ln}{}^a=\lambda_{l\xi}{}^i-\lambda_{t\xi}{}^i+\lambda_{tn}{}^a$$

and

$$\lambda_{tp}{}^a=\lambda_{t\xi}{}^i-\lambda_{l\xi}{}^i+\lambda_{lp}{}^a,$$

if the notation of the present paper is used. Noting that their data satisfy these relations, they concluded that their "hypothesis about domain magnetization explains the changes in magnetostriction due to heat treatment in a magnetic field."

It should be pointed out, however, that these relations do not, in fact, involve any assumptions with regard to the initial distribution of domain orientations or the nature of the domain changes during magnetization. As shown by the derivations of the present paper, the relations of Hoselitz and McCaig merely assume that the C values (that is, the *intrinsic* magnetostrictive properties) are unaffected by the treatment used to establish the preferred orientation. Consequently, the agreement between their relation and their data cannot be regarded as evidence for their hypothesis. It seems unlikely, in fact, that any relation based on isotropic magnetostriction can be used for deciding whether the domains are oriented along the cube edge nearest to the annealing field.

Most of the relevant papers[5–8] contain data on $\lambda_{lp}{}^a$, $\lambda_{ln}{}^a$, and $\lambda_{l\xi}{}^i$ only. Thus, the method of analysis given in Sec. IIIA is not applicable in these cases, and hence a correlation of the experimental results requires additional assumptions. In the following, it will be assumed that the initial distribution of domain orientations is isotropic in the untreated state of the sample and axially symmetrical in the treated state, and that the C values in the two states are equal. Equations (16) and (18) may then be combined to give

$$2\lambda_{ln}{}^a+\lambda_{lp}{}^a=3\lambda_{l\xi}{}^i, \tag{23}$$

which may be compared with the experimental data of

TABLE I. Measured magnetostrictive strains (in units of 10^{-6}) in Alcomax II.

$\lambda_{l\xi}{}^i$	$\lambda_{t\xi}{}^i$	$\lambda_{lp}{}^a$	$\lambda_{ln}{}^a$	$\lambda_{tp}{}^a$	$\lambda_{tn}{}^a$
20	−8	3	30	−26	0

The data were taken from the paper of Hoselitz and McCaig, reference 4 and expressed in the terminology used in the present paper.

[2] J. E. Goldman and R. Smoluchowski, Phys. Rev. **75**, 140 (1949).
[3] M. McCaig, Proc. Phys. Soc. (London) **B62**, 652 (1949).
[4] K. Hoselitz and M. McCaig, Proc. Phys. Soc. (London) **B62**, 163 (1949).
[5] H. Kirchner, Ann Physik **V27**, 49 (1936).
[6] E. A. Nesbitt, J. Appl. Phys. **21**, 879 (1950).
[7] Williams, Bozorth, and Christensen, Phys. Rev. **59**, 1005 (1941).
[8] H. E. Stauss and G. Sandoz, J. Metals **4**, 1342 (1952).

TABLE II. Comparison of measured $\lambda_{l\xi}{}^i$ with calculated $\lambda_{l\xi}{}^i$.

Material	Treatment*	$\lambda_{ln}{}^a \times 10^6$ meas.	$\lambda_{lp}{}^a \times 10^6$ meas.	D calc.	$\lambda_{l\xi}{}^i \times 10^6$ meas.	$\lambda_{l\xi}{}^i \times 10^6$ calc.
Nickel†	12	−60	≈0	≈1	−40	−40
Nickel†	6	−57	− 7	0.89	−40	−40
Nickel†	2	−47	−27	0.55	−40	−40
50% Ni–50% Fe†	6	30	11	0.70	22	24
50% Ni–50% Fe†	2	26	15	0.55	22	22
Alnico V‡	AIMF	38	2.5	0.94	26	26
68 Permalloy§	AIMF	22.4	2.3	0.90	18	16
87% Fe–13% Al‖	AIMF	45	26	0.55	39	39
69% Co–31% Fe‖	AIMF	107	37	0.71	87	84

* The numbers in this column denote the tension or compression, in Kg/mm², used to establish the preferred axis; the letters AIMF denote that annealing in a magnetic field was used to establish the preferred axis. For further details the original papers should be consulted.
† Reference 5. Arbitrarily selected points were taken from Figs. 8, 14, 21, and 22 of this paper.
‡ Reference 6.
§ Reference 7.
‖ Reference 8.

Table II. It is seen that for all samples of the six materials listed, good or excellent agreement exists between the calculated value of $\lambda_{l\xi}{}^i$, deduced from Eq. (23) and the measured value of $\lambda_{l\xi}{}^i$. Consequently, the additional assumptions introduced above are well fulfilled in most of these particular samples even though the values of D, calculated from $\lambda_{lp}{}^a$ and $\lambda_{ln}{}^a$ by using Eqs. (11a) and (11b), do vary over a considerable range.

It should be noted in this connection that if the domains are completely aligned along the preferred axis, then Eq. (11a) shows that $\lambda_{lp}{}^a$ is zero. In this special case Eq. (23) gives

$$\lambda_{ln}{}^a = (\tfrac{3}{2})\lambda_{l\xi}{}^i,$$

a relation first obtained theoretically by Becker and Kersten[9] and verified experimentally by Kirchner[5] (see Table II, line 1). But if the domains are not completely aligned along the preferred axis, then $\lambda_{lp}{}^a$ is not zero, and a correlation of the experimental data requires Eq. (23) or the other equations of the present paper.

[9] R. Becker and M. Kersten, Z. Physik **64**, 660 (1930). See also reference 1.

JOURNAL OF APPLIED PHYSICS VOLUME 25, NUMBER 1 JANUARY, 1954

Field Emission Current-Density Distribution*

W. P. DYKE, J. K. TROLAN, W. W. DOLAN, AND F. J. GRUNDHAUSER
Physics Department, Linfield College, McMinnville, Oregon

(Received June 8, 1953)

A quantitative measurement of the current-density distribution over the surface of monocrystalline tungsten field emitters is obtained by densitometric analysis of calibrated photographic negatives of emission patterns observed with a modified Mueller projection tube. Analysis of distributions thus obtained permits an improved evaluation of average field current density and a confirmation of the surface distribution of electric field previously derived; an earlier comparison of experiment with field emission theory is thus strengthened. Current-density ratios for various crystal faces of the emitter confirm recent values of the work function for those faces. Emission patterns were viewed on an aluminum backed phosphor, the advantages and fabrication of which are discussed. Relative light output from such phosphors is presented for excitation by field currents at various values of the applied potential for both steady state and microsecond operation.

INTRODUCTION

A NUMBER of field emission experiments require for their interpretation a quantitative knowledge of the distribution of current density J over the surface of the emitter. Qualitative descriptions of the distribution from monocrystalline cathodes of various materials, as well as from coated cathodes, were obtained earlier by several workers[1–6] from the distinctive electron emission patterns made visible on the fluorescent screen of a Mueller-type projection tube.[1] A pattern from clean tungsten, a common emitter material, reveals a marked variation in J which is related to crystallographic direction.

Quantitative knowledge of that distribution is needed for a more accurate comparison between experiment and the wave mechanical theory,[7]

$$J = 1.54\times10^{-6}(F^2/\phi)\exp(-6.83\times10^7\phi^{\frac{3}{2}}f(y)/F), \quad (1)$$

where ϕ is the work function in ev, J is in amp/cm², F is in volts/cm and $f(y)$ is Nordheim's[8,9] elliptic function of the variable $y = 3.79\times10^{-4}F^{\frac{1}{2}}/\phi$, when

* This work was sponsored by the U. S. Office of Naval Research and by the U. S. Air Force, the latter funds through the Microwave Laboratory of the University of California.

[1] E. W. Mueller, Z. Physik. **106**, 541 (1937).
[2] M. Benjamin and R. O. Jenkins, Proc. Roy. Soc. (London) **A176**, 264 (1940).
[3] J. A. Becker, Bell System Tech. J. **30**, 907 (1951).
[4] R. H. Haefer, Z. Physik. **116**, 604 (1940).
[5] R. Gomer, J. Chem. Phys. **21**, 293 (1953).
[6] H. W. Schleicher, Z. Naturforsch. **7a**, 471 (1952).

[7] A. Sommerfeld and H. Bethe, *Handbuch der Physik* (Verlag. Julius Springer, Berlin, Germany, 1933), Vol. XXIV, No. 2, p. 441.
[8] L. W. Nordheim, Proc. Roy. Soc. (London) **121**, 626 (1928).
[9] Burgess, Kroemer, and Houston, Phys. Rev. **90**, 515 (1953).

presently accepted values of the physical constants are used. A non-uniform distribution of J over the surface of the hemispherical tungsten monocrystal is expected from Eq. (1) and the known surface distributions of the electric field[10] and work function.[11]

Comparisons between experiment[4,12,13] and Eq. (1), in which the cathode field was known have used an average experimental current density $\bar{J}$ obtained from the ratio of the measured current to the total emitting area. The emitting area was estimated from the emission pattern[4] or calculated on the assumption that the theory was correct[12] using an average value of ϕ and the known distribution of electric field at the cathode.[10] One purpose of the present paper is to determine a more accurate value of $\bar{J}$ obtained from an experimental measurement of the distribution of current density over the hemispherical monocrystalline tungsten emitter surface. It will be shown that the values of $\bar{J}$ thus obtained are sufficiently close to those formerly used[12] that the previously established validity of the theory is not impaired.

A second purpose of the present work is to test experimentally the validity of the field distribution reported earlier for the present type cathode.

A third purpose is to test further the published values of the work functions at various crystallographic directions for clean tungsten. Values of the work function of the (110) crystal face reported by several workers[14–17] have not been in agreement.

In order to accomplish the preceding aims, a method was developed by which the current-density distribution could be obtained from experimental data recorded photographically during single microsecond intervals of operation. It was thus possible to detect changes in the distribution occurring on a pulse-to-pulse basis as required in several experiments[12,13,18] concerning field emission at large current densities. Use of an aluminum-backed phosphor screen avoided difficulties believed present in earlier work.[15,16] The method has been used in this laboratory for some time[19] but has not been reported in detail previously.

A prerequisite to the foregoing is knowledge of the relative light output per unit incident electron current at various voltages for aluminum-backed phosphors of the present type. The phosphor response for both direct current and pulse operation is presented.

[10] Dyke, Trolan, Dolan and Barnes, J. Appl. Phys. **24**, 570 (1953).
[11] M. H. Nichols, Phys. Rev. **57**, 297 (1940).
[12] W. P. Dyke and J. K. Trolan, Phys. Rev. **89**, 799 (1953).
[13] Barbour, Dolan, Trolan, Martin, and Dyke, Phys. Rev. **91**, 45 (1953).
[14] E. W. Mueller, Z. Physik. **120**, 270 (1943).
[15] M. K. Wilkinson, J. Appl. Phys. **24**, 1203 (1953).
[16] W. B. Nottingham, Abstracts of Field Emission Seminar, Linfield College, 1952.
[17] G. F. Smith, Abstracts of Field Emission Seminar, Linfield College, 1952.
[18] Dyke, Trolan, Martin, and Barbour, Phys. Rev. **91**, 1043 (1953).
[19] W. P. Dyke and J. K. Trolan, Phys. Rev. **85**, 391 (1952).

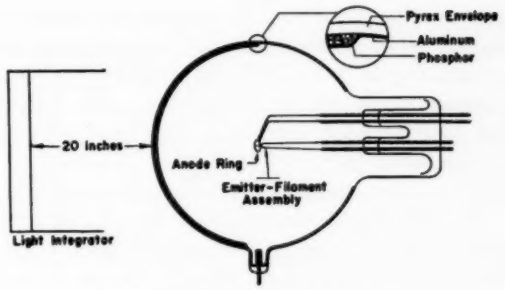

FIG. 1. Experimental tube.

EXPERIMENTAL METHOD

For a number of reasons it was advantageous to obtain the current-density distribution from a densitometric analysis[20] of the calibrated photographic negatives which recorded the emission pattern as viewed on the phosphor screen of the modified Mueller-type projection tube shown in Fig. 1. One advantage provided by the visible emission pattern was knowledge that the cathode surface was clean. Two advantages were provided by the photographic method: (1) a permanent record of the light distribution from the entire phosphor, and (2) the ability to obtain exposures during single microsecond intervals of operation, thus permitting analysis of pulse-to-pulse variations in the distributions recorded during high current-density operation.

Two problems were recognized during preliminary experiments with uncoated phosphor screens. First, the accumulation of "sticking charges" on the insulating phosphor[21] caused stray electric fields at the cathode resulting in uncertainties in the calculated field.[10] Second, scattered light and excitation of the phosphor from sources other than primary field electrons, such as secondary electrons, soft x-rays, and negative ions, caused a background illumination at the phosphor which was large compared with that produced by primary field electrons in the area of the pattern related to the (110) crystal direction. With uncoated phosphors, maximum light-intensity ratios measured on the phosphor were about 100/1, and this value is less than that found with improved techniques, as will be noted.

Both of the foregoing difficulties were adequately minimized for the present purpose by use of a thin aluminum film in contact with the phosphor on its cathode side, as shown in the experimental tube in Fig. 1. Electrons from the emitter passed through the aluminum film anode and excited the phosphor. Use of the anode ring will be described later. Methods for fabricating the cathode and obtaining its geometry from electron micrographs have been discussed.[10] Extension of the aluminum film over most of the inner glass surface of the Pyrex envelope prevented "sticking

[20] C. B. Neblette, *Photography*, (D. Van Nostrand Company, Inc., New York, 1927).
[21] W. B. Nottingham, J. Appl. Phys. **10**, 73 (1939).

charges" on these surfaces, a precaution which earlier was found to be necessary.[12] Methods for evacuating the experimental tube and determining its residual gas pressure have been described along with techniques for the simultaneous recording of current, voltage,[12] and the emission pattern.[13,18]

Emission patterns in these studies were photographed with a Speed Graphic camera, size four by five inches, equipped with a coated 7-inch Aero Ektar $f/2.5$ lens or with an $f/3.5$ Eastman Kodak Model 35 camera equipped with a Portra 2 lens. The densitometer first used was the Kodak Color Densitometer Model 1. The field of view of this instrument was small compared with the significant areas on four-by-five inch negatives. This requirement was not fulfilled when 35-mm negatives were used; also the time required for reading and recording was long, hence an automatic photoelectric recording densitometer was designed and built here, as reported in another paper.[22] With this instrument it was possible to record the variation of density along any straight line across the negative as an oscillographic record. These recorded densities were then transformed[20] at convenient intervals to exposure.

While the fabrication of metal-backed phosphors is achieved commercially,[23] a few brief comments on the present method may be useful. Luminescent screens having an area density of 1 mg/cm^2, were made of zinc silicate (Zn_2SiO_4: Mn 3 percent Sylvania No. 2281), and were deposited on the inner surface of the spherical Pyrex experimental tubes by the lacquer flow method with good uniformity and reproducibility. The lacquer stock solution consisted of 40-gm phosphor mixed with 50-cc amyl acetate and 25-cc Varniton 21B label varnish. The lacquer was removed after the deposit by an air-bake at 500°C.

Evaporation of the aluminum directly onto the phosphor screen[24] was tried here but found inadequate for the present purpose since deposits thin enough to transmit electrons were not sufficiently continuous to provide both high opacity to light and high electrical conductivity.

The aluminum film was evaporated in vacuum (10^{-4} mm Hg) onto a thin nitrocellulose membrane which was stretched across the phosphor crystals[23] between them and the cathode. This membrane was subsequently removed by baking in air at a temperature of 340°C. The thickness of the aluminum film in several experimental tubes varied from 1000A to 1500A. Epstein and Pensak[25] have investigated the electron absorbing characteristics of such films of various thicknesses. Eighty percent of the power in an incident electron beam is transmitted by a film 1000A thick at 10 kv; at 5 kv, 40 percent of the incident power is transmitted by the same film. A 2000A film transmits 50 percent of the power at 10 kv and 10 percent at 5 kv.

The aluminum film had a sufficiently low electrical resistance that emission currents (during vacuum arc) as large as 100 amperes[18] were drawn without serious potential drop in the film. It provided an anode of known potential required for electric field calculations[10] and its opacity to the several sources of stray excitation mentioned above increased its useful contrast permitting measured ratios of current density exceeding 10^3.

Halation was minimized by reducing the optical contact of the phosphor with the glass by use of relatively large phosphor crystals.[26,27] Internal reflection of light at the glass-air surface was effectively minimized by coating that surface with Glydag,[28] a colloidal suspension of graphite in glycerine, having an index of refraction equal to that of Pyrex. Small uncoated areas were left at crystallographic directions under observation. These precautions were required to minimize background light at areas on the emission pattern such as those corresponding to the (110) crystal faces of the emitter.

PHOSPHOR RESPONSE

The present work requires assurance that the phosphor screen response is known. In fact a linear response is preferred, that is, that light output per unit area from the phosphor, as measured by photographic exposure, is proportional to incident electron current density for the range of current densities found in a single emission pattern.

Nottingham, in an earlier paper,[21] established the linear relationship for an uncoated phosphor, where anode voltage V entered the equation in the form

$$L/I = kV^n, \tag{2}$$

where L is light output of the phosphor, I the incident electron current, and n a constant depending on the phosphor. Gomer noted the linearity of the response of another type of metal-backed phosphor;[24] however, no reference regarding the linearity of the present type phosphor was found either for direct current or pulse operation.

The response of the present type of phosphor screens for direct current operation was obtained with the experimental tube shown in Fig. 1, in which the anode ring concentric with the emitter tip was added to permit independent variation of field current and screen potential. Light intensities were recorded by a photographic emulsion whose density-exposure relationship was obtained as part of the experiment. When several exposures were required during a run, they were all recorded on parts of the same piece of film together with a grey scale, itself exposed from the phosphor

[22] G. Barnes, J. Opt. Soc. Am. (to be published).
[23] E. R. Ewald, Electronics **23**, 76–79 (1950).
[24] R. Gomer, J. Chem. Phys. **21**, 73 (1953).
[25] Epstein and Pensak, RCA Rev. **7**, 5 (1946).
[26] H. W. Leverenz, *An Introduction to Luminescence of Solids* (John Wiley and Sons, Inc., New York, 1950).
[27] R. R. Law, Proc. Inst. Radio Engrs. **27**, 511 (1939).
[28] Suggested during a conversation with E. W. Mueller.

light at the highest level of intensity used in the run. All exposures were made at a constant value of time, and uniform development of the film was insured by careful agitation in a constant temperature bath. Light intensities were reproducible and known within 5 percent by this method.

It was observed here that prolonged baking at high temperature (400–500°C), required during the evacuation of the experimental tube, caused changes in screen response contributed by changes in phosphor efficiency[26] and a decrease in thickness of the aluminum coating. It was therefore desirable to determine the phosphor response and obtain the current-density distribution from the field cathode without subjecting the screen to a bake-out process between those measurements. This requirement suggested use of the field cathode as electron source for both measurements.

It was convenient to relate average light output from the phosphor to incident current at constant voltage (Fig. 2) or to constant incident current at various voltages (Fig. 3). The non-uniformity of the current-density distribution incident at the phosphor provides no difficulty below the level at which phosphor saturation occurs, and that level was higher than required for the present determination of current-density distributions.

A photographic emulsion placed about 20 inches from the tube face served to integrate the light from the phosphor by recording a uniformly exposed, "defocused" image of the screen.

Coincident with each exposure thus obtained with the light integrator, a focused negative of the emission pattern was recorded by use of an auxiliary camera. The latter negative was also calibrated by use of a grey scale. The focused pattern was used for both the analysis of the current-density distribution and the determination of a correction for the change in the area of the pattern caused by the electron lens effect of the anode ring. A maximum area change of 25 percent was observed.

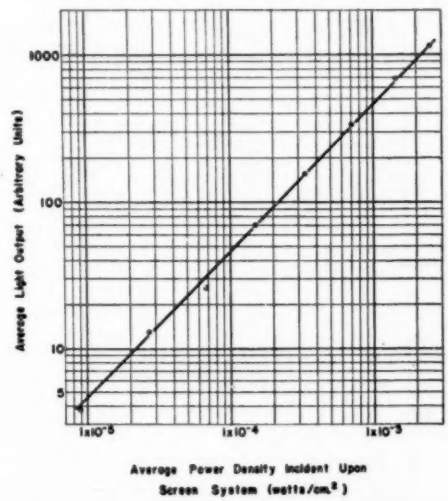

FIG. 2. Graph of average light output *vs* average incident power per cm² in electron beam at aluminum-backed phosphor screen of experimental tube, for direct current operation with constant screen potential 5 kv.

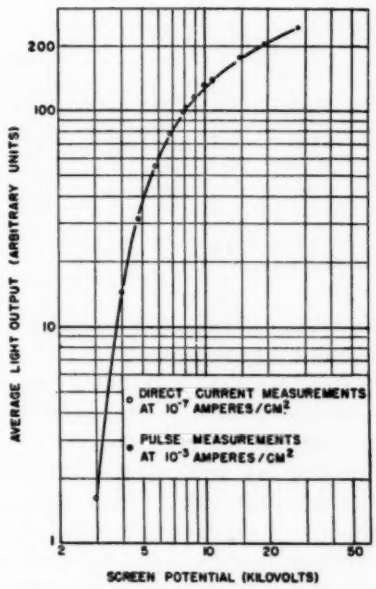

FIG. 3. Graph of average light output *vs* screen potential at constant current, for direct current and pulsed operation of experimental tube with indicated average incident current densities at the phosphor.

Figure 2 represents the data taken from this tube with the screen at 5 kv. The curve indicates direct proportionality between the average light output from the total area and the average power per unit area incident upon the screen system for values below 2.5×10^{-3} watt/cm². No saturation of the phosphor is observed in Fig. 2. Emission pattern photographs used in the analysis presented in the next section were taken at a level well below phosphor saturation.

Relative light output from the same phosphor at a constant incident current density is shown in Fig. 3, which combines direct current operation at voltages $3<V<11$ kv and individual two microsecond pulse operation at voltages $8<V<28$ kv. Respective average current densities at the phosphor were 10^{-7} amps/cm² for direct currents and 10^{-3} amp/cm² for pulse operation. Since the light output was recorded in arbitrary units in each case, the two curves were matched by multiplying the ordinates of the pulse data by a constant. The phosphor response shown in Fig. 3 is not well described by Eq. (2), two contributing factors being recognized. Light output was reduced at low voltages by the absorption of electrons in the aluminum film and at high voltages by increased penetration of electrons through the phosphor.[25] Decreased phosphor efficiency because of heating at the higher power levels may have been a contributing factor.[26]

Relative light output at constant voltage (10 kv) for a typical range of microsecond field currents was

FIG. 4. Graph of average light output *vs* field emission current for experimental tube of reference 13, for microsecond operation at constant screen potential 10 kv.

obtained for a similar aluminum-backed phosphor used in the experimental tube shown in Fig. 2 of reference 13. The methods were identical with those reported above except that various values of field current for constant voltage were obtained by use of various coatings of barium-on-tungsten, an equivalent method to use of the anode ring described above. The response of that phosphor, which is approximately linear, is shown in Fig. 4. The voltage chosen was typical of those used with that experimental tube during pulse operation in reference 13.

PATTERN ANALYSIS

Experience indicated that density readings from the emission pattern negative along certain radial lines relative to the (110) crystal direction were most useful for analysis of the current-density distribution. It is known that the (110) crystal direction of the hemispherical, single-crystal tungsten emitter nearly always coincides with the emitter axis. Hence detail from that face indicated by a dark rectangle corresponding to low current density appears near the center of the pattern, with the (211), (100), and other readily identifiable faces appearing in a familiar arrangement of light and dark areas.[1] Figure 6 contains a photograph of a typical (positive) pattern from clean tungsten, with the principal crystal faces identified. The lettered radial lines are those along which densities were recorded. They pass through the dark "holes" or bisect the angles between them; they cover the areas of maximum and minimum exposure and are oriented the same way for all tungsten patterns. It should be remembered that the actual readings were made on a photographic negative so that the "holes" appeared as the least dense areas. When additional density readings were made at intermediate angles, the results confirmed that the twelve azimuths of the figure were typical, gradations between them showing no unexpected density fluctuations of significant magnitude.

To transform exposure E to current density J, the entire visible pattern to be analyzed was mapped in a manner somewhat similar to Wilkinson's[15] but differing in details and depending on densitometer readings rather than on visual estimates. The area was divided into subregions A_1, A_2, etc., over each of which the calculated exposures (and hence current densities) were fairly uniform. The total measured current I was then equated to the sum of the products J_iA_i as follows:

$$I=\sum J_iA_i=\sum cE_iA_i=c\sum E_iA_i,$$

since E is proportional to J, as indicated in an earlier part of this paper, for all J in a single pattern for which $V=$constant. The equation above was solved for the factor c, after which it was possible to find J at any point from the corresponding value of E. The total emitting area A, where $A=\sum A_i$, included that part of the measured emitting surface whose current density exceeded 1 percent of the maximum current density. Although this figure was quite arbitrary, it was found that emission in the border region of the visible pattern was so slight that the choice of outer boundary within reasonable limits made no appreciable difference in the results.

The areas A_i were marked on the map in such a way that each was bounded by two values of θ, the polar angle measured from the emitter apex, and two values of γ, the azimuthal angle. Since electron micrographs of the field emitter indicated that the emitting area could be very closely approximated by a part of a spherical surface,[10] the areas A_i were calculated by the spherical formula

$$A=r^2(\gamma_2-\gamma_1)(\cos\theta_1-\cos\theta_2),$$

where r was the radius of the emitter as obtained from its electron micrographs. Values of θ were readily obtained from the known angular differences between crystallographic directions associated with the pattern;[1] extreme values ranged from about 60° for direct current patterns to more than 90° for some patterns obtained during pulse operation. Values of γ were measured directly upon the map.

One immediate product of this analysis was the measurement of the fraction of the total current obtained from the most strongly emitting areas. Figure 5 is a cumulative emission *vs* area graph for several emitters. The location of each symbol represents the corresponding fractions of area and emission for a

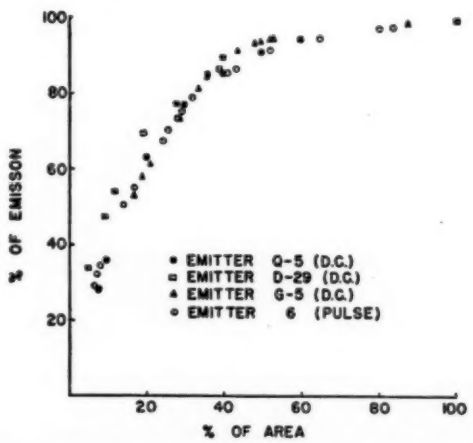

FIG. 5. Cumulative emission *vs* area graphs for several typical field emitters.

region A_i added to similar fractions from all the regions of higher current density than A_i. It is notable that about half of the emission came from regions totalling about one-fifth of the area, and 90 percent from regions totalling about half of the area. The regions near the (310) crystal faces emitted most strongly in all cases studied.

Certain information about the variation of work function with crystallographic direction was obtained by analysis of the graphs of Fig. 6, which show the variation of relative current density across various single azimuths of the indicated emission pattern. The automatic densitometer was well suited for the preparation of that figure. Near the apex region of the emitters, where the field was approximately constant,[10] the variation in J was ascribed primarily to the differences in work function ϕ associated with the various crystal directions. Nichols[11] gave values of ϕ for several directions for clean tungsten; some of his work was checked by Wilkinson[15] as a part of his study. Although Nichols did not measure ϕ_{310}, he did measure $\phi_{116}=4.35$ ev, and repeated comparisons in the patterns of the present study have indicated nearly equal emission for these two directions. The use of $\phi_{310}=4.35$ ev and an average

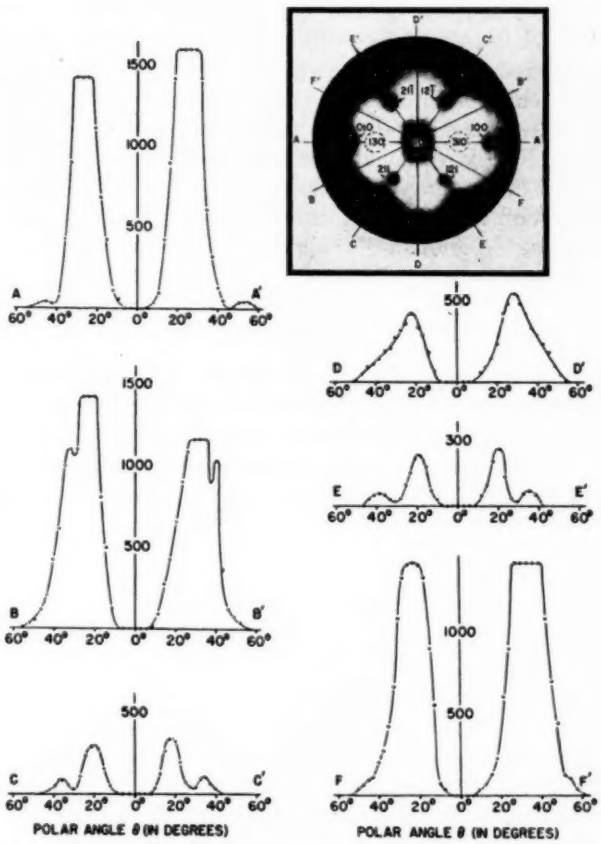

FIG. 6. Graphs showing the variation of current density J with polar angle θ for several azimuths of emitter Q5; vertical scale arbitrary. Upper right: emission pattern for same emitter, with identification of principal crystal faces and azimuths AA', etc., for the corresponding graphs.

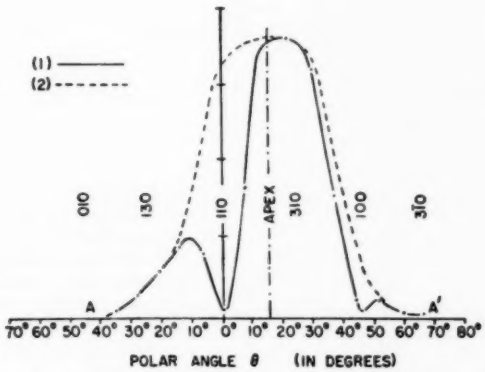

FIG. 7. Variation of current density J with polar angle θ for azimuth AA' of emitter D29; vertical scale arbitrary; (1) solid curve, experimental data; (2) dashed curve superimposed on experimental curve at crystallographically similar directions (130), (310) and (3$\bar{1}$0). Dashed curve shows probable dependence of J on θ for a constant work-function surface.

work function $\phi_{Av}=4.50$ ev, together with a value of the field $F=2.6\times10^7$ volts/cm derived from the electrical behavior of the emitter,[12] made it possible to compute by the field emission theory [Eq. (1)] a predicted ratio $J_{310}/J_{Av}=3.7$. Similar ratios obtained experimentally from the data of Fig. 8 were 2.8 if J was averaged over the "constant field region" described below, and 4.2 for J averaged over the whole emitting area. Allowing for a possible error[12] of 15 percent in F, the agreement is good.

Nichols' value of $\phi_{110}=4.65$ ev has been less universally accepted.[14,17] When the method of the previous paragraph was applied to the comparison of the highly contrasting (310) and (110) areas after painting out other parts of the pattern with Glydag as described above, the ratio of measured emission, $J_{310}/J_{110}=1600$, corresponded to $\phi_{110}=5.2$ ev for emitter Q5. For other emitters, the ratio led to values of ϕ_{110} in the range from 5.0 to 5.5 ev, in agreement with the estimate of Mueller.[14] Comparison without the Glydag treatment yielded values close to 5.0 ev, but in no case as low as Nichols' value of 4.65 ev. These results are not to be regarded as conclusive, but do suggest that the true value of ϕ_{110} is not likely to be less than 5.0 ev. The value may be increased if the presently recorded light intensities in the (110) areas at the phosphor are shown to be background illumination rather than the result of primary field electrons. The value may be altered by a more precise determination of the electric field which recognizes the effect of the small flat areas sometimes observed in electron micrographs of the emitter[12] and possibly associated with extension of the principal crystal faces.

The observed current-density distribution may be used to verify the field distribution reported earlier. In reference 10, the field distribution for a cathode similar to those used herein was used to calculate a current-density distribution from the theory in Eq. (1), assuming an average value of the work function

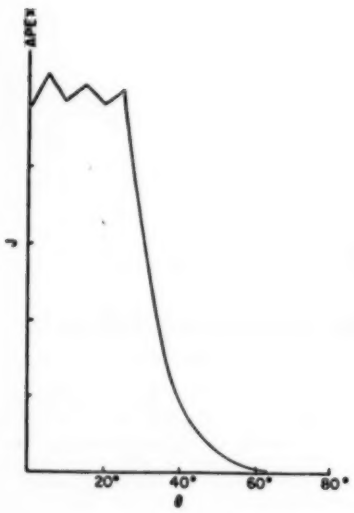

FIG. 8. Graph of current density J, averaged over all azimuths at successive values of polar angle θ, for emitter G5; vertical scale arbitrary.

$\phi=4.5$ ev for tungsten. In order to compare that calculated distribution with experiment, the variation of J with θ over azimuth AA' (Fig. 7) was obtained from emitter D29 whose surface was contaminated by residual gases in the experimental tube, thus increasing the uniformity of the work-function distribution. This emitter had the additional advantage that the apex coincided approximately with the strongly emitting (310) face. Other crystallographically symmetrical faces (130) and $(3\bar{1}0)$, assumed to have equal work functions, are included in azimuth AA'. The dashed curve is superimposed on the experimental curve at the points corresponding to the directions mentioned above and is an estimate, therefore, of the probable dependence of current density on polar angle for a surface of constant work function, that is, of the dependence due to change in field alone. The dashed curve in Fig. 7 is in good agreement with curve B, Fig. 8 of reference 10, thus confirming the predicted field distribution for a similar emitter. Since a decrease of 5 percent in F corresponds to a decrease of about 50 percent in J at the levels of operation here used, Fig. 7 may be interpreted as further evidence that the field is sensibly constant out to about 30° from the apex. Similar analysis of other emitters, not shown, led to essentially the same result.

An independent check on the same problem was made possible by the fortuitous circumstance that the apex of emitter G5 was located asymmetrically with respect to the crystal symmetry. Thus, it was possible to average the values of J over several azimuths at successive values of θ without encountering bias resulting from the usual symmetrical occurrence of regions of identical work function. The resulting graph of average current density *versus* polar angle is shown in Fig. 8. Here again it may be supposed, to a reasonable approximation, that the variation in J is due to field alone. The relatively constant value of J out to a polar angle of about 30° is evident, followed by an abrupt decline at greater angles.

Comparisons between experiment[4,12,13] and theory[7] have used an average value of the current density $\bar{J}=I/A$ where I is total current and A is emitting area. This method ignores the distribution in electric field[10] which varies by about 15 percent over the emitting area. It is now possible to restrict the comparison to the constant field region A' (described above for $\theta<30°$) and obtain for that region a new average current density $\bar{J}'=I'/A'$, where I' is the current emitted by the area A'. For emitter Q5, described in Fig. 6, the ratio $\bar{J}'/\bar{J}$ was 1.5, a difference which is not large compared to other uncertainties in the comparison between experiment and theory.[12] Since the area A' includes extreme values in the work-function distribution,[11,17] it is reasonable to assign the average value $\phi=4.5$ ev for tungsten to that area. Hence no significant correction is introduced into the previous comparisons between experiment[4,12,13] and theory[7] by the considerations in this paragraph.

ACKNOWLEDGMENTS

It is a pleasure to acknowledge the considerable technical assistance and helpful suggestions rendered by L. M. Perry, by Professors George Barnes and John L. Boling, and by student assistants Richard Strayer and Maridel Dyke.

JOURNAL OF APPLIED PHYSICS VOLUME 25, NUMBER 1 JANUARY, 1954

On the Summation of Infinite Series in Closed Form

ALBERT D. WHEELON*
Douglas Aircraft Company, Inc., Santa Monica, California
(Received May 28, 1953)

A direct approach to the problem of summing infinite series in closed form is described. This method is based on the parametric representation of the general term of a series, so as to produce either the geometric or exponential series inside one or more integral signs. Each of these may be summed in closed form, thereby permitting one to exhibit a given series as a combination of definite integrals. When the original series is summable, these integrations can be performed analytically and the sum presented in closed form. Such a procedure enjoys the evident advantage of exploiting the relative abundance of integral tables, while circumventing the need for extensive preparation in the field of infinite series. The relations of this development to other methods are indicated and a number of illustrative examples presented.

INTRODUCTION

CONSIDERABLE interest has been aroused quite recently in the applied aspects of infinite series. This has been prompted in part by the important role accorded series representations by ever-increasing analytical studies of physical and engineering problems. Since most series of physical interest converge very slowly,† one is urged to exploit closed expressions for summations whenever possible. Several current papers[1-5] discuss special techniques which may be used to derive closed expressions for particular types of series. Under the circumstances, however, one is encouraged to ask if a judicious combination of familiar operational methods might not provide a general approach to the problem. The present paper discusses such a technique and its applications.

A powerful method for obtaining closed expressions for infinite series has been devised which deals directly with the general term of the series. The fundamental operation is contained in the summation of both sides of a Laplace transform pair with respect to the transform variable (p), which is interpreted as the dummy index (n) of summation. This operation exhibits the desired sum as an integral of the geometric (I) or exponential (II) series, each of which may be summed in closed form (see below). In this way, one is able to express the series itself as a combination of real integrals, the evaluation of which depends only upon familiarity with integral calculus,

$$\sum_0^\infty a^n=\frac{1}{1-a}, \quad |a|<1; \tag{I}$$

$$\sum_0^\infty \frac{a^n}{(n)!}=e^a, \quad |a|<\infty. \tag{II}$$

This procedure is evidently well adapted to the characteristically sporadic applications, in that its sole requirements are: (1) table of Laplace transformations; (2) table of definite integrals; (3) the results (I) and (II).

Although the following presentation does not include a rigorous justification of the procedure, it is hoped that this technique will prove useful until such time as it may be established in a mathematically satisfying manner.

I. EXPOSITION

In developing a procedure for reducing complicated summations to integrals of simple series, one is led to the Laplace transform representation of a function $f(x)$;

$$F(p)=\int_0^\infty dx e^{-xp} f(x). \tag{1.1}$$

If one were to consider a series for which the function $F(p)$ represented the general term (or summand), one would be tempted to identify the transform variable (p) with the dummy index of summation (n) and sum both sides of (1.1) with respect to (n),

$$\sum F(n)=\sum \int_0^\infty dx e^{-xn} f(x)$$

$$=\int_0^\infty dx f(x) \sum (e^{-x})^n. \tag{1.2}$$

The second form follows from the important interchange of the summation and integration processes.‡ This exchange evidently produces the trivial geometric series, for which the summation is easily executed by (I).

A series of considerable historical interest first obtained in closed form by L. Euler serves to illustrate the

* Now at the Ramo-Wooldridge Corporation, Los Angeles 45, California.

† Thirty terms of the important series $\sum_1^\infty \frac{1}{n^2}$ give 1.612, in contrast to the exact value 1.645 computed from the closed form, $\pi^2/6$.

[1] G. G. Macfarlane, Phil. Mag. **40**, 188 (1949).
[2] L. A. Pipes, J. Appl. Phys. **21**, 298 (1950).
[3] I. F. Morrison, J. Appl. Phys. **21**, 939 (1950).
[4] M. R. Spiegel, J. Appl. Phys. **23**, 906 (1952).
[5] J. A. McFadden, J. Appl. Phys. **24**, 364 (1953).

‡ One might challenge such an inversion on the grounds that it apparently conceals the infinite value of an obviously divergent series such as $F(n)=1/n$. A short investigation, however, shows that such difficulties are conserved in the transformation and appear as divergencies in the remaining integral of (1.2).

fundamental idea,

$$\sum_1^\infty \frac{1}{n^2}=1+\frac{1}{4}+\frac{1}{9}+\frac{1}{16}\cdots=\frac{\pi^2}{6}. \tag{1.3}$$

Upon noting the Laplace transform pair,

$$\frac{1}{n^2}=\int_0^\infty dx e^{-xn}x, \tag{1.4}$$

and summing both sides with respect to (n),

$$\sum_1^\infty \frac{1}{n^2}=\int_0^\infty dxx\sum_1^\infty (e^{-x})^n$$

$$=\int_0^\infty \frac{dxx}{e^x-1}=\frac{\pi^2}{6}. \tag{1.5}$$

This example describes the simplest application of the pair

$$\frac{1}{(n+a)^k}=\frac{1}{(k-1)!}\int_0^\infty dxe^{-ax}x^{k-1}e^{-xn}. \tag{1.6}$$

One is evidently free to multiply both sides of this identity with any function $f(n)$ which does not spoil the convergence of the ensuing summation, so as to obtain more general series,

$$\sum\frac{f(n)}{(n+a)^k}=\frac{1}{(k-1)!}\int_0^\infty dxx^{k-1}e^{-ax}\sum f(n)e^{-xn}. \tag{1.7}$$

An additional parametric representation of $f(n)$ is usually required to bring the remaining summation to the standard form (I) or (II). We shall defer the details of these subversions and subsequent combinations§ until the parametrization of denominators has been further investigated.

II. REPRESENTATION OF DENOMINATORS

The integral parametric representation of an algebraic denominator of a summand is a relatively simple task, since every table of Laplace transforms includes numerous pairs leading to the reciprocals of algebraic functions.

(A) Rational Algebraic Functions

Series which contain second-degree polynomials in the denominator may be treated by noting the transform pair

$$\frac{1}{n^2-a^2}=\frac{1}{a}\int_0^\infty dxe^{-xn}\sinh(ax). \tag{2.1}$$

Thus,

$$\sum\frac{f(n)}{n^2-a^2}=\frac{1}{a}\int_0^\infty dx\sinh(ax)\sum f(n)e^{-xn}. \tag{2.2}$$

The corresponding series with (a) replaced by $(i\alpha)$ becomes

$$\sum\frac{f(n)}{n^2+a^2}=\frac{1}{a}\int_0^\infty dx\sin(ax)\sum f(n)e^{-xn}. \tag{2.3}$$

With these results and a single integration,¶ one may verify the interesting closed expressions given below:

$$\sum_0^\infty\frac{1}{n^2-a^2}=\frac{1}{a}\int_0^\infty\frac{du\sinh(au)}{1-e^{-u}}$$

$$=-\frac{1}{2a^2}[1+\pi a\cot(a\pi)]; \tag{2.4}$$

$$\sum_0^\infty\frac{1}{n^2+a^2}=\frac{1}{a}\int_0^\infty\frac{du\sin(au)}{1-e^{-u}}$$

$$=\frac{1}{2a^2}[1+\pi a\coth(a\pi)]. \tag{2.5}$$

These same results are easily deduced by Cauchy's method.[6]

A summation containing a quartic denominator may be calculated by noting the decomposition,

$$\sum\frac{f(n)}{n^4-a^4}=\frac{1}{2a^2}\left[\sum\frac{f(n)}{n^2-a^2}-\sum\frac{f(n)}{n^2+a^2}\right] \tag{2.6}$$

and inserting the appropriate lower-order results. Replacing (a) by $\alpha(-1)^{\frac{1}{4}}$ gives the corresponding series for $(n^4+\alpha^4)$. Higher-order denominators may be similarly discussed by employing partial fractions and/or factorizations.

(B) Linear Factors

When the denominator of a summand contains a product of two or more linear functions of (n), one is

§ The convolution theorem proves a powerful tool in effecting such unions.

¶ For example,

$$2\int_0^\infty\frac{du\sinh(au)}{1-e^{-u}}=\int_0^\infty du\frac{e^{au}}{1-e^{-u}}-\int_0^\infty du\frac{e^{-au}}{1-e^{-u}}$$

$$=\int_1^\infty\frac{dxx^a}{x-1}-\int_0^1\frac{dxx^a}{x(1-x)}$$

$$=-\int_0^\infty\frac{dx}{(1-x)x^{-a}}-\int_0^1 dxx^{a-1}$$

$$=-\left[\pi\cot(a\pi)+\frac{1}{a}\right].$$

The last integrals are given by H. B. Dwight [*Tables of Integrals and Other Mathematical Data* (Macmillan Company, New York, 1950), p. 197] for $|a|<1$. Other (non-integral) values are obtained by continuing the result analytically round its poles in the complex a plane.

[6] T. M. Macrobert, *Functions of a Complex Variable* (Macmillan and Company, Ltd., London, 1938), p. 113.

encouraged to exploit the convolution integral or Faltung theorem. Feynman[7] has given a particularly convenient form of this device,

$$\frac{1}{ab}=\int_0^1 \frac{du}{[a(1-u)+bu]^2}. \tag{2.7}$$

Repeated application of this relation yields the appropriate higher-order combinations

$$\frac{1}{abc}=2!\int_0^1 du\int_0^u dv \times[a(1-u)+b(u-v)+cv]^{-3}, \tag{2.8}$$

$$\frac{1}{abcd}=3!\int_0^1 du\int_0^u dv\int_0^v dw \times[a(1-u)+b(u-v)+c(v-w)+dw]^{-4}\cdots \text{ etc.} \tag{2.9}$$

When these expressions are combined with the inversion (1.6), one obtains the summation index (n) in the desired (linear) exponential form $e^{-\lambda n}$ inside an array of definite integrals. The function λ evidently depends linearly on the integration variables u, v, w, etc. The program is best illustrated by an example,

$$\sum_0^\infty \frac{1}{(3n+1)(3n+2)(3n+3)} =2\int_0^1 du\int_0^u dv\sum_0^\infty [3n+1+u+v]^{-3}. \tag{2.10}$$

The right-hand side follows from an obvious identification of a, b, and c in (2.8). The relation

$$\frac{1}{\lambda^3}=\frac{1}{2}\int_0^\infty ds s^2 e^{-s\lambda} \tag{2.11}$$

then leads to

$$\begin{aligned}\sum_0^\infty \frac{1}{(3n+1)(3n+2)(3n+3)} &=\int_0^\infty ds s^2\int_0^1 du\int_0^u dv e^{-s(1+u+v)}\sum_1^\infty e^{-3sn}\\ &=\int_0^\infty \frac{ds s^2 e^{-s}}{1-e^{-3s}}\int_0^1 du\int_0^u dv e^{-s(u+v)}\\ &=\frac{1}{2}\int_0^\infty \frac{ds e^{-s}}{1-e^{-3s}}[e^{-2s}-2e^{-s}+1]\\ &=\frac{1}{2}\int_0^1 dx\frac{(1-x)}{1+x+x^2}=\frac{1}{4}\left[\frac{\pi}{\sqrt{3}}-\log(3)\right],\end{aligned} \tag{2.12}$$

which corresponds to the result quoted by Adams.[8]

[7] R. P. Feynman, Phys. Rev. **76**, 769 (1949).

[8] E. P. Adams, *Smithsonian Mathematical Formulae and Tables of Elliptic Functions*, (Washington, 1947), p. 144.

(C) Irrational Algebraic Functions

The Laplace transformations of the various Bessel functions provide a wealth of irrational denominator expressions. Although such representations permit the summation to be performed exactly, it does not seem possible to carry out the ensuing integrations analytically in general. Such subversions, however, do provide rapidly convergent integral equivalents for slowly converging series,

$$\sum_1^\infty \frac{(-1)^n}{[n^2+a^2]^{\frac{1}{2}}}=\int_0^\infty du J_0(ua)\sum_1^\infty (-1)^n e^{-un} =-\int_0^\infty \frac{du J_0(ua)}{1+e^u}. \tag{2.13}$$

The latter expression converges rapidly in virtue of the bounded oscillations of $J_0(z)$ and the exponential increase of the denominator.

III. REPRESENTATION OF NUMERATORS

The presence of algebraic and transcendental functions in the numerator of the summand calls forth a variety of differential and integral representations. Since the devices to which one resorts in a particular problem depend primarily on the type of function encountered, the remaining discussion is organized according to types of numerators.

(A) Algebraic

Algebraic functions of (n) in the numerator of a series are most efficiently represented as combinations of the linear operator $(\partial/\partial\lambda)$ applied to an admixed exponential function $e^{-\lambda n}$. This term may be combined with the other exponentials arising from the parameterizations of the denominator and the resulting series summed exactly. The differentiations with respect to λ and parametric integrations may be performed in any convenient order. The variable λ is equated to zero, however, only after all operators $(\partial/\partial\lambda)$ have been applied. The following set of series is easily deduced by this means:

$$\begin{aligned}S_k&=\sum_0^\infty \frac{n^k}{(n)!}\\ &=\left[\frac{\partial^k}{\partial\lambda^k}\sum\frac{e^{\lambda n}}{(n)!}\right]_{\lambda=0}\\ &=\left[\frac{\partial^k}{\partial\lambda^k}\exp(e^\lambda)\right]_{\lambda=0} \quad \text{[by (II)]}.\end{aligned} \tag{3.1}$$

The indicated differentiations and subsequent limit

$\lambda \to 0$ confirm the known results,[9]

$$S_1 = e, \quad S_2 = 2e, \quad S_3 = 3e, \quad S_4 = 15e, \quad \text{etc.} \tag{3.2}$$

A more difficult example indicates the power of this representation,

$$\sum_1^\infty \frac{12n^2-1}{n[4n^2-1]^2} = \left(12\frac{\partial^2}{\partial\lambda^2}-1\right)\sum_1^\infty \frac{e^{-\lambda n}}{n(4n^2-1)^2}\bigg|_{\lambda\to 0}. \tag{3.3}$$

When the denominator is factored and the identity (2.8) differentiated once each with respect to a and b, there results a triple integral whose value confirms the known result: $2\log 2$.

The presence of irrational functions in the numerator may be circumvented by introducing the transforms of suitable Bessel functions. As noted previously, however, the ensuing integrals cannot be performed analytically in general.

(B) Exponentials

Linear exponential functions in the numerator pose no problem for summation. No parameterization is required and the integrals arising from the denominator are readily discussed when the united exponential is summed. A simple summation is embodied in

$$\begin{aligned}\sum_1^\infty \frac{e^{-an}}{n} &= \int_0^\infty du \sum_1^\infty e^{-n(a+u)}, \\ &= \int_0^\infty \frac{du}{e^{a+u}-1} = -\log[1-e^{-a}].\end{aligned} \tag{3.4}$$

Series containing factors of (e^{-an^2}) apparently lie outside the scope of the present methods.

(C) Trigonometric Functions

Trigonometric functions in the numerator correspond to ordinary Fourier series. These are most easily treated by representing $\cos(nx)$ and $\sin(nx)$ as the real and imaginary parts of (e^{inx}), respectively. A simple application of this idea is contained in

$$\begin{aligned}\sum_0^\infty a^n \frac{\sin(n\lambda)}{(n)!} &= Im\sum_0^\infty \frac{(ae^{i\lambda})^n}{(n)!}, \\ &= Im[\exp(ae^{i\lambda})] \quad \text{by (II)}, \\ &= e^{a\cos\lambda}\sin[a\sin(\lambda)].\end{aligned} \tag{3.5}$$

This device may also be combined with the inversions discussed previously to deal with trigonometric series containing algebraic denominators,

$$\begin{aligned}\sum_1^\infty \frac{(-1)^n\cos(n\lambda)}{n^2-a^2} &= Re\sum_1^\infty (-1)^n e^{in\lambda}\frac{1}{a}\int_0^\infty du e^{-un}\sinh(au) \\ &= Re\left[\frac{1}{a}\int_0^\infty du\sinh(au)\frac{-1}{e^{u-i\lambda}+1}\right] \\ &= Re\left[-\frac{1}{2a}\int_0^\infty du\frac{e^{au}-e^{-au}}{1+\zeta e^u}\right] \\ &= -\frac{1}{2a}Re\left[\int_1^\infty \frac{dw}{w^{1-a}}-\zeta^{-a}\int_0^\infty \frac{dww^a}{1+w}\right. \\ &\qquad \left.+\int_0^1 dww^a\left(\frac{1}{w+\zeta^*}-\frac{1}{w+\zeta}\right)\right],\end{aligned}$$

wherein we denote

$$\zeta = e^{-i\lambda}, \quad \zeta^* = e^{i\lambda},$$

$$\begin{aligned}\sum_1^\infty \frac{(-1)^n\cos(n\lambda)}{n^2-a^2} &= \frac{1}{2a}Re\left[\frac{1}{a}+e^{ia\lambda}\pi\csc(-a\pi)\right. \\ &\qquad \left.+2i\sin(\lambda)\int_0^1 dw\frac{w^a}{1+2w\cos(\lambda)+w^2}\right] \\ &= \frac{1}{2a^2}\left[1-\pi a\frac{\cos(a\lambda)}{\sin(a\pi)}\right].\end{aligned} \tag{3.6}$$

(D) Inverse Trigonometric Functions

The inverse trigonometric functions may be included in the present framework by employing the available decompositions of these functions,

$$\tan^{-1}\left(\frac{\alpha+\beta}{1-\alpha\beta}\right) = \tan^{-1}(\alpha)+\tan^{-1}(\beta), \tag{3.7}$$

before passing to integral transforms such as

$$\tan^{-1}\left(\frac{1}{\lambda}\right) = \int_0^\infty \frac{du}{u}\sin(u)e^{-\lambda u}. \tag{3.8}$$

An interesting example given by Knopp[10] is deduced from these two relations:

$$\begin{aligned}\sum_1^\infty \tan^{-1}\left(\frac{2}{n^2}\right) &= \sum_1^\infty \tan^{-1}\left(\frac{1}{n-1}\right)+\sum_1^\infty \tan^{-1}\left(\frac{-1}{n+1}\right) \\ &= 2\int_0^\infty \frac{du}{u}\sin(u)\sinh(u)\sum_1^\infty e^{-un} \\ &= \int_0^\infty \frac{du}{u}\sin(u)[1+e^{-u}] \\ &= \frac{\pi}{2}+\tan^{-1}(1) = \frac{3\pi}{4}.\end{aligned} \tag{3.9}$$

[9] Reference 8, p. 141.

[10] K. Knopp, *Theory and Application of Infinite Series* (Hafner Publishing Company, Inc., New York, 1928), p. 267.

(E) Logarithms

Series containing logarithms may be treated by employing the several pertinent Laplace transforms which exist. As an example, we record the pair

$$\log\left(1+\frac{a^2}{n^2}\right)=\int_0^\infty \frac{du}{u}e^{-un}2[1-\cos(au)]. \quad (3.10)$$

Upon summing both sides with respect to (n), one obtains

$$\sum_1^\infty \log\left(1+\frac{a^2}{n^2}\right)=2\int_0^\infty \frac{du}{u}[1-\cos(au)]\frac{1}{e^u-1},$$

$$=2\int_0^a d\phi\int_0^\infty du\,\frac{\sin(u\phi)}{e^u-1}. \quad (3.11)$$

The (du) integration is accomplished by methods similar to those employed in discussing (2.4),

$$\sum_1^\infty \log\left(1+\frac{a^2}{n^2}\right)=\lim_{\epsilon\to 0}\int_\epsilon^a d\phi\left[-\frac{1}{\phi}+\pi\coth(\pi\phi)\right]$$

$$=\log\left[\frac{\sinh(\pi a)}{\pi a}\right]. \quad (3.12)$$

This result is easily verified by taking the logarithm of the infinite product expansion for the hyperbolic sine.

(F) Legendre Polynomials

Series of Legendre polynomials do not seem well adapted to the Laplace transform method described previously. Instead, one is directed to work directly with the generating series for these functions,

$$\frac{1}{[1-2a\cos\phi+a^2]^{\frac{1}{2}}}=\sum_0^\infty a^nP_n(\cos\phi). \quad (3.13)$$

Differentiation and integration with respect to a produce a number of summable series. An example of interest is obtained by integrating (3.13) with respect to da from 0 to 1,

$$\sum_0^\infty \frac{P_n(\cos\phi)}{n+1}=\int_0^1 da[1-2a\cos\phi+a^2]^{-\frac{1}{2}}$$

$$=\log\left[1+\csc\left(\frac{\phi}{2}\right)\right]. \quad (3.14)$$

If two polynomials are present, one may square both sides of the expansion (3.13) and proceed with appropriate operations.

(G) Bessel Functions

In discussing series of Bessel functions, it proves desirable to supplement the Laplace transformation device with integral representations of these functions. The treatise by Watson[11] contains a lengthy discussion of such inversions as well as closed expressions for many series.

By way of example, one may recall the important integral representation

$$J_\mu(z)=\frac{1}{\pi}\int_0^\pi d\phi\cos[z\sin\phi-\mu\phi]. \quad (3.15)$$

This transformation permits one to sum the following series which contains the index of summation (n) as the argument of the function. If one denotes $\epsilon_0=1$, $\epsilon_n=2$, $n\geq 1$,

$$\sum_0^\infty \frac{\epsilon_n(-1)^nJ_0(n\pi)}{a^2-n^2\pi^2}$$

$$=\frac{1}{\pi}\int_0^\pi d\phi\sum_0^\infty \frac{\epsilon_n(-1)^n\cos(n\pi\sin\phi)}{a^2-n^2\pi^2}$$

$$=\frac{1}{a^2}-\frac{2}{\pi^3}\int_0^\pi d\phi\sum_1^\infty \frac{(-1)^n\cos(n\pi\sin\phi)}{n^2-(a/\pi)^2}. \quad (3.16)$$

The enclosed series was summed in the example of (3.6),

$$\sum_0^\infty \frac{\epsilon_n(-1)^nJ_0(n\pi)}{a^2-n^2\pi^2}$$

$$=\frac{1}{a^2}-\frac{2}{\pi^3}\int_0^\pi d\phi\left[\frac{1}{2(a/\pi)^2}-\frac{\pi}{2(a/\pi)}\frac{\cos(a\sin\phi)}{\sin(a)}\right]$$

$$=\frac{1}{\pi}\int_0^\pi d\phi\frac{\cos(a\sin\phi)}{a\sin a}=\frac{J_0(a)}{a\sin a}. \quad (3.17)$$

From this development, it should be clear how one is to deal with series containing $J_n(z)$ or $J_n(n\lambda)$ and the other kinds of Bessel functions.

IV. DOUBLE SERIES

Double series pose interesting theoretical questions, in that the order of summation may prove decisive in determining the result. The majority of problems encountered in practice are without ambiguity, although one must proceed cautiously. The following device proves useful in evaluating doubly convergent summations:

$$\frac{1}{\Lambda^{k+1}}=\frac{1}{(k)!}\int_0^\infty duu^ke^{-u\Lambda}. \quad (4.1)$$

This identity may be employed to evaluate the double

[11] G. N. Watson, *A Treatise on the Theory of Bessel Functions* (Cambridge University Press, Cambridge, 1952).

series,

$$\sum_1^\infty \sum_1^\infty \frac{1}{(4n-1)^{2m+1}}$$

$$= \sum_1^\infty \sum_1^\infty \frac{1}{(2m)!} \int_0^\infty du u^{2m} e^{-u(4n-1)}$$

$$= \int_0^\infty du e^u \left(\sum_1^\infty \frac{u^{2m}}{(2m)!} \right) \left(\sum_1^\infty e^{-4un} \right). \quad (4.2)$$

Upon comparison with (II), the series in the first bracket is easily recognized as the Taylor series for the hyperbolic cosine less one. The second series is given directly by (I), so that

$$\sum_1^\infty \sum_1^\infty \frac{1}{(4n-1)^{2m+1}} = \int_0^\infty du e^u [\cosh(u) - 1] \left[\frac{1}{e^{4u}-1} \right]$$

$$= \frac{1}{2} \int_0^1 dw w \frac{1-2w+w^2}{1-w^4}, \quad (4.3)$$

$$= \frac{\pi}{8} - \tfrac{1}{4} \log(2).$$

This result agrees with that of Bromwich,[12] and is representative of a number of double series.

A second example, discussed by Lord Kelvin in connection with the forces between charged spheres, is deduced by the original method.

$$\sum_1^\infty \sum_1^\infty \frac{nm(-1)^{n+m}}{(n+m)^2} = \int_0^\infty du u \sum_1^\infty \sum_1^\infty nm(-e^{-u})^{n+m}$$

$$= \int_0^\infty du u \left[\sum_1^\infty n e^{-un} (-1)^n \right]^2$$

$$= \int_0^\infty du u \left[-\frac{\partial}{\partial u} \sum_1^\infty (-1)^n e^{-un} \right]^2$$

$$= \int_0^\infty du u \left[\frac{-e^{-u}}{(1+e^{-u})^2} \right]^2. \quad (4.4)$$

Upon setting $w = e^{-u}$, one obtains the closed expression,

$$\sum_1^\infty \sum_1^\infty \frac{nm(-1)^{n+m}}{(n+m)^2} = -\int_0^1 dw \frac{w \log(w)}{(1+w)^4}$$

$$= \tfrac{1}{6}[\log(2) - \tfrac{1}{4}], \quad (4.5)$$

which agrees with the sum given in Bromwich.[13]

V. EVALUATION

A similar summation procedure has been developed by Macfarlane,[1] which depends upon the properties of the Fourier-Mellin transformation. We write a function in terms of its inverse in this notation as

$$f(z) = \frac{1}{2\pi i} \int_{\sigma-i\infty}^{\sigma+i\infty} ds z^{-s} F(s). \quad (5.1)$$

One is now directed to interpret (z) as the index of summation and sum both sides of this pair,

$$\sum_1^\infty f(n) = \frac{1}{2\pi i} \int_{\sigma-i\infty}^{\sigma+i\infty} ds F(s) \sum_1^\infty \frac{1}{n^s}. \quad (5.2)$$

The series included in the complex integrand defines the Riemann Zeta function for complex values of (s). The evaluation of the contour integral depends upon the analytic properties of this function[14] and the transform $F(s)$. Macfarlane has applied this method to several interesting examples.

The foregoing report describes an elementary technique which has been devised to obtain closed expressions for infinite series. The fundamental operation is contained in the summation of both sides of a Laplace transform pair with respect to the transform variable (p), which is interpreted as the (dummy) index (n) of summation. This operation has the effect of expressing the desired sum as the integral of a geometric or exponential series, which may be summed explicitly.

The present approach enjoys the evident advantage of presenting the summation as a combination of real integrals. The only required results of infinite series are given by (I) and (II). No new functions are introduced into the analysis, and the mathematical preparation and tables required are possessed by most engineers. To avoid recalculating familiar results, one may consult the foregoing references, or one of the available tables of summable series.[8,15,16]

[12] T. J. I'a. Bromwich, *Theory of Infinite Series* (Macmillan and Company, Ltd., London, 1947), p. 194.

[13] Reference (12), p. 90.

[14] E. T. Whitaker and G. N. Watson, *A Course of Modern Analysis* (Cambridge University Press, Cambridge, 1947), p. 265.

[15] L. W. B. Jolley, *Summation of Series* (Chapman and Hall, Ltd., London, 1925), (Out of print).

[16] A. D. Wheelon, "A Short Table of Summable Series," Report SM-14642, 1953, Douglas Aircraft Company, Inc., Santa Monica, California.

JOURNAL OF APPLIED PHYSICS VOLUME 25, NUMBER 1 JANUARY, 1954

On Reciprocity Theorems in Electromagnetic Theory*

T. H. CROWLEY
Antenna Laboratory, Ohio State University Research Foundation, Columbus, Ohio
(Received June 30, 1953)

Various forms of the reciprocity theorem arise in electromagnetic theory because of differences in the source of the fields. Five different types of sources are discussed briefly and the corresponding reciprocity theorem given.

THE fundamental role played by reciprocity theorems in electromagnetic theory has become even more important in recent years because of new methods of carrying out theoretical analyses.[1-3] The usefulness of such relations is considerably increased when the proper form is chosen for the particular problem under investigation. There are a good many forms available (depending mainly on the type of the sources of the fields), and the apparent differences between the forms are sometimes surprising.

The theorems under consideration are relations between an electromagnetic field ${}^aE$, ${}^aH$† and its source a and an electromagnetic field ${}^bE$, ${}^bH$ and its source b. It is assumed in every case that both these fields are monochromatic at the same frequency. For simplicity, it is further assumed that all media are isotropic. Various forms of the theorem arise because the form of the sources a and b may vary. Following is a partial summary of different forms for various sources a and b.

Let a be a volume distribution of sources for the field ${}^aE$, ${}^aH$; i.e.,

$$\nabla\times{}^aE+j\omega\mu{}^aH=-{}^aK,$$
$$\nabla\times{}^aH-j\omega\epsilon{}^aE={}^aJ,$$

where ${}^aK$ and ${}^aJ$ are a given volume distribution of magnetic and electric currents, respectively, and all sources are contained in a sphere of finite radius.

Let b be a similar source for the field ${}^bE$, ${}^bH$. We also require that both fields ${}^aE$, ${}^aH$ and ${}^bE$, ${}^bH$ satisfy the "radiation condition"[4] at infinity. Then it is easily shown[5] that‡

$$\int_{V_a}{}^aJ\cdot{}^bE-{}^aK\cdot{}^bH=\int_{V_b}{}^bJ\cdot{}^aE-{}^bK\cdot{}^aH, \qquad (1)$$

where V_a is any volume which contains a and V_b is any volume which contains b.

In particular V_a and V_b might be any volume V containing both a and b.

The special case in which one or both of the sources a and b reduces to a point source leads to a form which differs only in the fact that the integral signs do not appear. For example, when both are point sources, we have

$${}^aJ\cdot{}^bE-{}^aK\cdot{}^bH={}^bJ\cdot{}^aE-{}^bK\cdot{}^aH. \qquad (1a)$$

A greater difference in the form of the theorem occurs when the sources of the fields are surface distributions of current.

Let a be a surface distribution of sources for the field ${}^aE$, ${}^aH$; i.e.,

(I) $\nabla\times{}^aE+j\omega\mu{}^aH=0$ for every point not on the $\nabla\times{}^aH-j\omega\epsilon{}^aE=0$ closed surface Σ_a,

(II) ${}^aE$, ${}^aH$ satisfy the radiation condition at infinity,

(III) $n\times({}^aE_e-{}^aE_i)={}^aK$, $({}^aH_e-{}^aH_i)\times n={}^aJ$,

where n is the unit normal pointing to the side of Σ_a designated as the interior and ${}^aE_e({}^aE_i)$ designates the limit of ${}^aE(p)$ as p approaches Σ_a from the exterior (interior).

Let b be a surface distribution of sources for the field ${}^bE$, ${}^bH$.

Then it may be shown in a manner very similar to that used for theorem (1) that the following relations hold:

$$\int_{\Sigma_a}{}^aJ\cdot{}^bE_i-{}^aK\cdot{}^bH_i=\int_{\Sigma_b}{}^bJ\cdot{}^aE_e-{}^bK\cdot{}^aH_e. \qquad (2)$$

$$\int_{\Sigma_a}{}^aJ\cdot{}^bE_e-{}^aK\cdot{}^bH_e=\int_{\Sigma_b}{}^bJ\cdot{}^aE_i-{}^bK\cdot{}^aH_i. \qquad (2a)$$

Note that when the surfaces Σ_a and Σ_b are entirely different these two theorems are actually the same theorem and, more particularly, each is the theorem which is obtained by taking the limiting case of theorem (1) as the volume distributions approach surface distributions. Also when both sources consist only of electric currents or only magnetic currents, the theorems are the same. However, when both types of current are

* This work was carried out under Contract AF 18(600)-88 (E. O. No. 112-61 SR-6f4) Wright Air Development Center, Wright-Patterson Air Force Base, Ohio.

[1] H. Levine and J. Schwinger, Phys. Rev., **74** 958 (1948); **75**, 1423 (1949).

[2] Project Report 486-10 Antenna Laboratory, The Ohio State University Research Foundation, Columbus, Ohio.

[3] "Variational Impedance Calculations" Project Report 478-5, 16 July 1952, Antenna Laboratory, The Ohio State University Foundation, Columbus, Ohio.

† Printed E, H, K, J denote vectors. Script $\mathcal{E}_z$ denotes z component of E, etc.

[4] J. A. Stratton, *Electromagnetic Theory* (McGraw-Hill Book Company, Inc., New York, 1941), pp. 485-486.

[5] S. A. Schelkunoff, *Electromagnetic Waves* (D. Van Nostrand Company, Inc., New York, 1943), p. 477.

‡ For simplicity, the element of integration will not be indicated in any of the following formulas.

present and when $\Sigma_a \equiv \Sigma_b$ (or they have a common portion), these theorems are not only different, they are obtainable as a limiting case of theorem (1) only with some care and difficulty.

The combination of a surface distribution a and a volume distribution b gives a form which differs only slightly from theorem (1):

$$\int_{V_b} {}^bJ \cdot {}^aE - {}^bK \cdot {}^aH = \int_{\Sigma_a} {}^aJ \cdot {}^bE - {}^aK \cdot {}^bH. \quad (3)$$

Another type of source of some interest is the so-called line source. In this case there is a preferred direction which may be used as the z axis of a cylindrical coordinate system (ρ, θ, z). The (line) source a is then the source of the field ${}^aE$, ${}^aH$ when the following conditions are satisfied:

(a) All fields and sources vary with z as $e^{\gamma z}$, where γ is a complex constant.

(b) $\nabla \times {}^aH - jw\epsilon {}^aE = {}^aJ$ where ${}^aJ$ and ${}^aK$ are zero outside a cylinder of finite radius.
$\nabla \times {}^aE + jw\mu {}^aH = -{}^aK$

(c) The fields satisfy a radiation condition at $\rho = \infty$.

Then the following relation holds between two such sources:

$$\int_S {}^aJ \cdot {}^bE + {}^aK \cdot {}^bH - 2{}^a\mathcal{G}_z {}^b\mathcal{E}_z - 2{}^a\mathcal{K}_z {}^b\mathcal{H}_z = \int_S {}^bJ \cdot {}^aE + {}^bK \cdot {}^aH - 2{}^b\mathcal{G}_z {}^a\mathcal{E}_z - 2{}^b\mathcal{K}_z {}^a\mathcal{H}_z, \quad (4)$$

where S is any portion of the plane $z = 0$ outside of which all sources are zero.

Note that (4) differs in appearance considerably from all previous forms. In some special cases it reduces to a form more nearly like the previous ones, but it is worth noting that even in these cases the relation cannot be obtained easily from the previous relations (since the proofs given in those cases do not apply here).

If the line sources are contained on a closed curve instead of distributed over the surface S, forms analogous to theorem (2) are obtained:

$$\int_C {}^aJ \cdot {}^bE_s + {}^aK \cdot {}^bH_s - 2{}^a\mathcal{G}_z {}^b\mathcal{E}_{z_s} - 2{}^a\mathcal{K}_z {}^b\mathcal{H}_{z_s} = \int_C {}^bJ \cdot {}^aE_i + {}^bK \cdot {}^aH_i - 2{}^b\mathcal{G}_z {}^a\mathcal{E}_{z_i} - 2{}^b\mathcal{K}_z {}^a\mathcal{H}_{z_i}, \quad (5)$$

$$\int_C {}^aJ \cdot {}^bE_i + {}^aK \cdot {}^bH_i - 2{}^a\mathcal{G}_z {}^b\mathcal{E}_{z_i} - 2{}^a\mathcal{K}_z {}^b\mathcal{H}_{z_i} = \int_C {}^bJ \cdot {}^aE_s + {}^bK \cdot {}^aH_s - 2{}^b\mathcal{G}_z {}^a\mathcal{E}_{z_s} - 2{}^b\mathcal{K}_z {}^a\mathcal{H}_{z_s}. \quad (5a)$$

As before, special cases may result in simpler and more familiar looking relations.

Proofs of the foregoing theorems are not given here for several reasons. First, the only proofs known to the writer depend on knowing the form of the theorem in order to carry out the proof. Thus, they are of no assistance in determining the proper form of the theorem in other cases. Second, with suitably severe mathematical restrictions upon the form of the surfaces and curves involved, and upon the behavior of the sources and fields (such as continuity and differentiability) each of the theorems can be proved in essentially the same manner as theorem (1) (reference 5). A much more difficult and significant problem which is left unanswered here is involved in finding necessary and sufficient conditions which may be placed upon the surfaces and sources so that the theorems are valid.

The direction and aid of Professor V. H. Rumsey are acknowledged with pleasure.

JOURNAL OF APPLIED PHYSICS VOLUME 25, NUMBER 1 JANUARY, 1954

A Simplified Calculation for Dolph-Tchebycheff Arrays

G. J. VAN DER MAAS
Division of Radio and Electrical Engineering, National Research Council, Ottawa, Canada
(Received June 30, 1953)

A series is derived for the currents on the radiators of a Dolph-Tchebycheff array, which is more suitable for numerical calculation than the series given by Barbiere, when the number of radiators becomes large. The series is not alternating in character and is given in terms of a variable

$$\alpha=\tanh^2\left[\frac{\ln(r+(r^2-1)^{\frac{1}{2}})}{N-1}\right],$$

where r is the side-lobe ratio and N is the number of radiators. α is constrained to the interval $0\leq\alpha\leq 1$. The important practical case, when

$$\alpha\approx\frac{\ln^2(r+(r^2-1)^{\frac{1}{2}})}{(N-1)^2},$$

is approximated by a Bessel function. The calculations show that the currents on the two end elements of the array play a special role and that their adjustment should have due attention, whenever the inequality $\ln[r+(r^2-1)^{\frac{1}{2}}]<(N-1)^{\frac{1}{2}}$ is satisfied.

INTRODUCTION

THE methods given by Dolph[1,2] and Barbiere[3] for finding the currents in the radiators of a Dolph-Tchebycheff array require laborious calculations with numbers with many significant figures, even though only engineering accuracy may be required. The amount of computational labor becomes prohibitive when the number of radiators exceeds about twenty four. The main difficulty with Barbiere's series for the currents in individual elements, is the fact that the terms in the series are large and alternate in sign. Barbiere's series is given as a power series in a quantity z_0, which in terms of r and N is given by

$$T_{N-1}(z_0)=r, \tag{1}$$

where $T_{N-1}(z_0)$ is the Tchebycheff polynomial of degree $(N-1)$. In most practical arrays z_0 differs very little from unity, especially when N is large. This is another cause of the difficulties encountered in calculations when the number of radiators is large.

In this paper a series is derived, which is more suitable for numerical calculation than the series given by Barbiere. From this series and the differential equation in z_0 for the relative currents on the radiators, a formula is derived for the limiting case when N becomes large and z_0 differs very little from unity.

DERIVATION OF SIMPLIFIED SERIES FOR CURRENT DISTRIBUTION

If the N radiators are numbered from left to right 1, 2, $\cdots K$, $\cdots N$, the relative current in the Kth radiator, $I_N{}^K$, is given by the series

$$I_N{}^K=\sum_{s=0}(-1)^s\frac{(N-1)(N-2-s)!}{s!(N-K-s)!(K-s-1)!}z_0{}^{-2s}, \tag{2}$$

where z_0 is given by (1) in terms of r and N. The series ends for $s=N-K$, if $K\geq(N+1)/2$; and for $s=K-1$, if $K\leq(N+1)/2$ and is valid for odd and even values of N.*

The series (2) is written in a form somewhat different from that of Barbiere,[3] but it is seen very easily that the two series differ only by a factor $z_0{}^{N-1}$, which can be ignored, because only relative current values are of interest. It is seen that (2) satisfies the symmetry property

$$I_N{}^K=I_N{}^{N-K+1}, \tag{2a}$$

and it is noted for future reference that

$$I_N{}^1=I_N{}^N=1. \tag{2b}$$

It can be verified that $I_N{}^K$, as defined by (2), satisfies the differential equation in z_0

$$z_0{}^2y''+(2N-1)z_0y'+4(K-1)(N-K)(1-z_0{}^2)^{-1}y=0. \tag{3}$$

Because of (2a) and (2b), there is no loss of generality if K is restricted to the interval $2\leq K\leq(N+1)/2$ for the time being. Then let

$$I_N{}^K=z_0{}^{-2K+2}P_{K-1}(u), \tag{4}$$

where $u=z_0{}^2-1$. It is easily verified that $P_{K-1}(u)$ is a polynomial in u of degree $K-1$ and that the first term of $P_{K-1}(u)$ is $(N-1)u$. Now the function $-(N-1)^{-1}u^{-1}P_{K-1}(-u)$ satisfies the hypergeometric differential equation

$$u(1-u)y''+[2-(N-2K+4)u]y'+(K-2)(N-K+1)y=0. \tag{5}$$

Hence it follows that $P_{K-1}(u)$ can be written as

$$P_{K-1}(u)\equiv(N-1)uJ_{K-2}(N-2K+3;2;-u), \tag{6}$$

where $J_{K-2}(N-2K+3;2;-u)$ is a Jacobian poly-

[1] C. L. Dolph, Proc. Inst. Radio Engrs. **34**, 335 (1946).
[2] H. G. Riblet and C. L. Dolph, Proc. Inst. Radio Engrs. **35**, 489 (1947).
[3] D. Barbiere, Proc. Inst. Radio Engrs. **40**, 78 (1952).

* See Appendix.

nomial.[4] Now, $J_n(p;q;-u)$ can be developed into the series

$$J_n(p;q;-u)=\binom{p+n-1}{q-1}^{-1}(1+u)^n \times\sum_{s=0}^{n}\binom{n}{s}\binom{p+n-1}{q+s-1}\left(\frac{u}{1+u}\right)^s. \quad (7)$$

Expanding (6) with the aid of (7), substituting in (4), and making use of (2a) and (2b), the following series for I_N^K is obtained, in which the restriction $K\leq(N+1)/2$ can now be removed:

$$\left.\begin{aligned} I_N^K&=\frac{N-1}{N-K}\sum_{s=0}\binom{K-2}{s}\binom{N-K}{s+1}\alpha^{s+1} \\ &\qquad\text{for } K\neq 1 \text{ and } K\neq N, \\ I_N^K&=1 \text{ for } K=1 \text{ and } K=N, \end{aligned}\right\} \quad (8)$$

where

$$\alpha=z_0^{-2}(z_0^2-1)=\tanh^2\left[\frac{\ln(r+(r^2-1)^{\frac{1}{2}})}{N-1}\right]. \quad (8a)$$

The series ends for $s=K-2$, if $K\leq(N+1)/2$, and for $s=N-K-1$, if $K\geq(N+1)/2$.

It is obvious that series (8) is much better suited to numerical calculations than the series (2) of Barbiere, because it is not alternating in character and the variable α is always restricted to the interval $0\leq\alpha\leq 1$; while for the practical case when z_0 differs only very little from unity, α becomes very small. Special cases:

$\alpha=0$; all $I_N^K=0$ except $I_N^1=I_N^N=1$

$\alpha=1$; $I_N^K=\binom{N-1}{K-1}$ (binomial distribution).

For the sake of completeness the following two important recurrence relations for I_N^K, as defined by (8), are given:

$$\frac{1}{N-1}I_N^K=\frac{(N-K-1)}{(N-2)(N-2K+1)}I_{N-1}^K -\frac{(K-2)}{(N-2)(N-2K+1)}I_{N-1}^{K-1} \quad (9)$$

$$I_N^{K+1}=I_N^K+(N-2K)(1-\alpha)^K \times\int_0^\alpha\frac{I_N^K(\alpha)}{(1-\alpha)^{K+1}}d\alpha \quad (10)$$

valid for $2\leq K\leq N-2$. These relations can be derived from the recurrence relations for Jacobian polynomials. In using relation (9), α has to be treated formally as being independent of N. The "Pascal triangle," for the current distribution I_N^K up to $N=9$, is

$N=1$	1
2	1; 1
3	1; 2α; 1
4	1; (3α); (3α); 1
5	1; (4α); $(4\alpha+2\alpha^2)$; (4α); 1
6	1; (5α); $(5\alpha+5\alpha^2)$; $(5\alpha+5\alpha^2)$; (5α); 1
7	1; (6α); $(6\alpha+9\alpha^2)$; $(6\alpha+12\alpha^2+2\alpha^3)$; $(6\alpha+9\alpha^2)$; (6α); 1
8	1; (7α); $(7\alpha+14\alpha^2)$; $(7\alpha+21\alpha^2+7\alpha^3)$; $(7\alpha+21\alpha^2+7\alpha^3)$; $(7\alpha+14\alpha^2)$; (7α); 1
9	1; (8α); $(8\alpha+20\alpha^2)$; $(8\alpha+32\alpha^2+16\alpha^3)$; $(8\alpha+36\alpha^2+24\alpha^3+2\alpha^4)$; $(8\alpha+32\alpha^2+16\alpha^3)$; $(8\alpha+20\alpha^2)$; (8α); 1

LIMITING CASE FOR LARGE N AND SMALL α

Consider the limiting case, mentioned in the introduction, when N becomes large and α so small that it can be written as

$$\alpha=\tanh^2\left[\frac{\ln(r+(r^2-1)^{\frac{1}{2}})}{N-1}\right]\approx\frac{\ln^2(r+(r^2-1)^{\frac{1}{2}})}{(N-1)^2}.$$

In order to derive a formula for this case the differential equation in α is found, for I_N^K as defined by (8). Then, from Eq. (3),

$$y''+\frac{N-2}{1-\alpha}y'-\frac{(N-K)(K-1)}{\alpha(1-\alpha)}y=0. \quad (11)$$

Introducing a parameter

$$\xi=\frac{2K-N-1}{N-1}, \quad (12)$$

and a new variable v defined by

$$\alpha=\frac{v^2}{(N-1)^2},$$

and putting $y=vu$, Eq. (11) in y becomes the following

[4] E. Madelung, *Die Mathematische Hilfsmittel des Physikers* (Dover Publications, New York, 1943), p. 57.

differential equation in u:

$$u''+u'\left[\frac{1}{v}+\frac{2(N-2)v}{(N-1)^2\{1-[v^2/(N-1)^2]\}}\right]-u\left[\frac{1}{v^2}+\frac{1-\xi^2-2[(N-2)/(N-1)^2]}{1-[v^2/(N-1)^2]}\right]=0.$$

Now, for large N this equation becomes

$$u''+\frac{u'}{v}-u\left[\frac{1}{v^2}+(1-\xi^2)\right]=0, \tag{13}$$

with the general solution

$$C_1I_1[v(1-\xi^2)^{\frac{1}{2}}]+C_2K_1[v(1-\xi^2)^{\frac{1}{2}}].$$

This solution agrees with series (8) only when $C_2=0$ and $C_1=2v/(1-\xi^2)^{\frac{1}{2}}$. Hence, the limiting function $L(\xi)$, which the current distribution approaches under the stated conditions, is given by

$$\left.\begin{aligned} L(\xi)&\equiv\frac{2v}{(N-1)(1-\xi^2)^{\frac{1}{2}}}I_1[v(1-\xi^2)^{\frac{1}{2}}] \quad \text{for } |\xi|\neq 1\\ L(\xi)&=1 \qquad\qquad\qquad\qquad\qquad\quad \text{for } |\xi|=1\end{aligned}\right\}, \tag{14a}$$

or, if we normalize the function to 1 for $\xi=0$,

$$\left.\begin{aligned} L(\xi)&\equiv\frac{I_1[v(1-\xi^2)^{\frac{1}{2}}]}{(1-\xi^2)^{\frac{1}{2}}I_1(v)} \quad \text{for } |\xi|\neq 1\\ L(\xi)&=\frac{(N-1)}{2vI_1(v)} \qquad\qquad\quad \text{for } |\xi|=1\end{aligned}\right\}, \tag{14b}$$

where $I_1(x)=j^{-1}J_1(jx)$s a modified Bessel function of the first order. For practical side-lobe levels ($10<r<100$), function (14) is a good approximation even for arrays with as few as 20 radiators.

It is seen from (14) and (8) that the currents on the end elements, $I_N{}^1$ and $I_N{}^N$, play a special role in the current distribution. With the introduction of a new parameter

$$p=(N-1)^{\frac{1}{2}}/\ln[r+(r^2-1)^{\frac{1}{2}}], \tag{15}$$

it can be shown for large N and small α, that the end element currents will "fit" smoothly into the current distribution for the rest of the elements, only if $p=1$; and that these currents will be larger or smaller than those on the neighboring elements, when $p>1$ or $p<1$, respectively. Thus p is a quality factor determining the behavior of the end elements. The influence of the end elements on the field pattern is considered next.

FIELD PATTERN ANALYSIS FOR LARGE N AND SMALL α

It is well known that the field pattern for a Dolph-Tchebycheff array is given by

$$E=T_{N-1}[z_0\cos(\psi/2)], \tag{16}$$

with

$$T_{N-1}(z_0)=r \tag{1}$$

and

$$\psi/2=(\pi d/\lambda)\sin\vartheta. \tag{17}$$

Now $T_n(1+x)$ can be developed into the series

$$T_n(1+x)=\sum_{s=0}^{n}\frac{n(n+s)!}{(n+s)(2s)!(n-s)!}(2x)^s.$$

By assuming $1+x>0$ and approximating $(n+s)!$ and $(n-s)!$ with the Stirling formula for large n, it is found that $T_n(1+x)$ can be approximated by the function $\psi_n(x)$, defined by

$$\left.\begin{aligned} \psi_n(x)&=\cosh[n(2x)^{\frac{1}{2}}] \quad \text{for } x>0\\ \psi_n(x)&=\cos[n(-2x)^{\frac{1}{2}}] \quad \text{for } -1<x<0\end{aligned}\right\}. \tag{18}$$

This formula can be interpreted as follows. Write

$$\begin{aligned} 1+x&=\cos\chi \quad \text{for } -1<x<0\\ 1+x&=\cosh\chi \quad \text{for } x>0.\end{aligned}$$

Then

$$\begin{aligned} T_n(1+x)&=\cos n\chi \quad \text{for } -1<x<0\\ T_n(1+x)&=\cosh n\chi \quad \text{for } x>0,\end{aligned}$$

for all values of n. But for large n, according to (18),

$$\begin{aligned} T_n(1+x)&=\cos n[2(1-\cos\chi)]^{\frac{1}{2}}\\ T_n(1+x)&=\cosh n[2(\cosh\chi-1)]^{\frac{1}{2}}.\end{aligned}$$

This means that for large n, χ may be treated formally as such a small quantity, that $\cosh\chi$ may be replaced by $1+(\chi^2/2)$ and $\cos\chi$ by $1-\chi^2/2$, and vice versa.

With this interpretation of (18), it is readily shown, that for large N and z_0 near to unity, (16) can be written as

$$\left.\begin{aligned} E&\approx\cosh\left[v^2-(N-1)^2\frac{\psi^2}{4}\right]^{\frac{1}{2}} \quad \text{for } \left|\frac{\psi}{2}\right|<\frac{v}{N-1}\\ E&\approx\cos\left[(N-1)^2\frac{\psi^2}{4}-v^2\right]^{\frac{1}{2}} \quad \text{for } \left|\frac{\psi}{2}\right|>\frac{v}{N-1}\end{aligned}\right\}, \tag{19}$$

where again $v=\ln[r+(r^2-1)^{\frac{1}{2}}]$. On the other hand, it is known that the relation between field pattern and current distribution in the normalization used in this section is given approximately by

$$E(\omega)=\frac{N-1}{4}\int_{-1}^{+1}L(\xi)\cos\omega\xi d\xi, \tag{20}$$

where $\omega=(N-1)\psi/2$. Substituting the current distribution (14a) for $L(\xi)$ in (20), $E(\omega)$ becomes

$$\begin{aligned} E(\omega)&=\cos[\omega^2-v^2]^{\frac{1}{2}}-\cos\omega, \quad v<\omega\\ E(\omega)&=\cosh[v^2-\omega^2]^{\frac{1}{2}}-\cos\omega, \quad v>\omega.\end{aligned}$$

But the end elements, instead of having approximately zero value, actually have the value 1, and so contribute an extra $\cos\omega$. Thus, the field pattern becomes

$$E=\cos[\omega^2-v^2]^{\frac{1}{2}}, \quad v<\omega$$
$$E=\cosh[v^2-\omega^2]^{\frac{1}{2}}, \quad v>\omega$$

in agreement with (19).

Now suppose that the currents on the end elements have amplitudes a instead of 1, then the field pattern will change by an amount $\Delta E=(a-1)\cos\omega$. Thus an erroneous "fit" of the end element currents with the rest of the current distribution would give a change in the field pattern of the amount

$$\Delta E=\left(\frac{v^2}{N-1}-1\right)\cos\omega.$$

If $v=(N-1)^{\frac{1}{2}}$ this will not change the field pattern but, if v is smaller, it will influence the field pattern and cause the main beam to become broader and the side-lobes to taper, while the ratio between amplitude of main beam and first side lobes becomes smaller. For $v^2/(N-1)\ll 1$ it becomes almost half the original value r. For large values of $(N-1)$, the currents in the end elements become large compared with the currents in the rest of the elements, and the field pattern becomes very sensitive to changes in the excitation of the end elements. This sets a practical upper limit to the number of elements which can be used in a Dolph-Tchebycheff array and so a lower limit to the width of the main beam. Thus the parameter $p^2=(N-1)/v^2$, being a measure for the ratio of the currents in the end elements to the currents in the neighboring elements, is apparently a quality factor for a Dolph-Tchebycheff array. This is the same parameter as introduced in the preceding section on the current distribution.

For a given side-lobe ratio r, the number of elements should be chosen at least large enough to make $p=1$, i.e., $(N-1)^{\frac{1}{2}}=\ln[r+(r^2-1)^{\frac{1}{2}}]$, because there are no physical difficulties in obtaining this value; but values of p exceeding 1 by very much, though they would still make the main beam narrower, will be hard to realize in practice.

ACKNOWLEDGMENT

The author wishes to thank Dr. H. Gruenberg of the National Research Council for bringing this problem to his attention and also for suggesting the possibility of the existence of a limiting excitation function for arrays of practical lengths and side-lobe ratios.

APPENDIX

Series (2) can be derived very quickly as follows: Write the formal series

$$\left.\begin{aligned} &N \text{ even: } T_{N-1}(z_0x)\\ &=I_N{}^{N/2+1}(z_0)T_1(x)+I_N{}^{N/2+2}(z_0)T_3(x)\\ &\qquad +I_N{}^{N/2+3}(z_0)T_5(x)\cdots+I_N{}^{N}(z_0)T_{N-1}(x)\\ &N \text{ odd: } T_{N-1}(z_0x)\\ &=\frac{I_N{}^{N+1/2}(z_0)}{2}+I_N{}^{N+3/2}(z_0)T_2(x)\\ &\qquad +\cdots+I_N{}^{N}(z_0)T_{N-1}(x) \end{aligned}\right\}. \quad (21)$$

Develop $T_{N-1}(z_0x)$ in the power series:

$$T_{N-1}(z_0x)=\tfrac{1}{2}\sum_{s=0}\frac{(N-1)(N-2-s)!}{s!(N-2s-1)!}\times(2x)^{N-2s-1}z_0{}^{N-2s-1}, \quad (22)$$

which terminates for $s=N/2-1$ if N is even, and for $s=(N+1)/2$ if N is odd. Substitute in this series, for the even and odd powers of $(2x)$, the series

$$\left.\begin{aligned} (2x)^{2M}&=2\left[\tfrac{1}{2}\binom{2M}{M}+\binom{2M}{M+1}T_2(x)\right.\\ &\qquad \left.+\binom{2M}{M+2}T_4(x)+\cdots\right]\\ (2x)^{2M+1}&=2\left[\binom{2M+1}{M+1}T_1(x)\right.\\ &\quad \left.+\binom{2M+1}{M+2}T_3(x)+\binom{2M+1}{M+3}T_5(x)+\cdots\right] \end{aligned}\right\}. \quad (23)$$

Then, by equating the coefficients of the Tchebycheff polynomials in the resulting equation with those on the right-hand side of Eq. (21), a series is obtained, which is identical with (2) except for a factor $z_0{}^{N-1}$. This factor can be ignored, because only relative currents are considered. The series for both odd and even N lead apparently to (2). This does not change by formal replacement of K by $N-K+1$. Thus the series (2) satisfies the symmetry condition (2a) automatically and is valid for even and odd values of N.

Letters to the Editor

Electrical Characteristics of MnSe and MnTe

WILFRED PALMER
Rice Institute, Houston, Texas
(Received July 10, 1953)

SAMPLES of MnSe and MnTe (prepared by Kelly[1]) consisting of dark gray powders with grains about 1 mm in diameter were available. Resistance measurements were made with a Wheatstone bridge on individual grains of the materials. Thin strips of ordinary solder fused to the specimen provided electrical contacts. Measurements of the Hall coefficient were made on individual grains fashioned into thin rectangular slabs. Here pressure contacts were used.

MnSe is a high-resistivity semiconductor: its resistivity at room temperature was roughly estimated at 3×10^3 ohm cm. Figure 1 shows how the resistance of one specimen depends on temperature. The path taken on the warming portion of the temperature cycle does not retrace the cooling curve. Thermal hysteresis of this kind has been found by Lindsay[2] in the susceptibility curves of MnSe over the same temperature range. Lindsay attributed the effect to a series of three crystal structures or phases which succeed one another in the cooling process and which are not re-established in precisely the same manner upon warming. The hysteresis exhibited in Fig. 1 may be due to the same sort of lattice modifications. Experiments with various specimens indicated that hysteresis becomes greater as the loop is extended to lower temperatures. The activation energy at room temperature from the cooling curve of the specimen shown is 0.125 electron volt. This quantity becomes much smaller at lower temperatures. Another specimen exhibited a room temperature activation energy of only 0.071 electron volt and a more pronounced flattening of the resistance curves at low temperatures. These disparities suggest that the specimens were not identical combinations of manganese and selenium. The Hall coefficient was too small to be measured. It was less than 90 cm³/coulomb. Magnetoresistance measurements made in a field of 7500 gauss indicated that the fractional change of resistance must be less than 2×10^{-5} both at room temperature and at −196°C.

The resistivity of MnTe was estimated at 1.0 ohm cm. As may be seen from Fig. 1, the temperature coefficient is positive over the range investigated. This fact can probably be regarded as evidence that MnTe is a degenerate semiconductor throughout this temperature region. Results obtained by Squire[3] indicate that the temperature coefficient becomes negative at temperatures above about 280°K. Measurements of the Hall coefficient yielded a value of +0.6 cm³/coulomb at room temperature and +2.6 cm³/coulomb at −196°C. The sign of the Hall coefficient indicates that the compound is predominantly a *p*-type semiconductor between these two temperatures. Magnetoresistance measurements in a field of 7500 gauss indicated that the fractional resistance change is less than 1.2×10^{-4} at room temperature and less than 4×10^{-4} at −196°C.

The author wishes to thank Professor C. W. Heaps for his generous advice and assistance.

[1] K. K. Kelly, J. Am. Chem. Soc. **61**, 203 (1939).
[2] R. Lindsay, Phys. Rev. **84**, 569 (1951).
[3] C. F. Squire, Phys. Rev. **56**, 960 (1939).

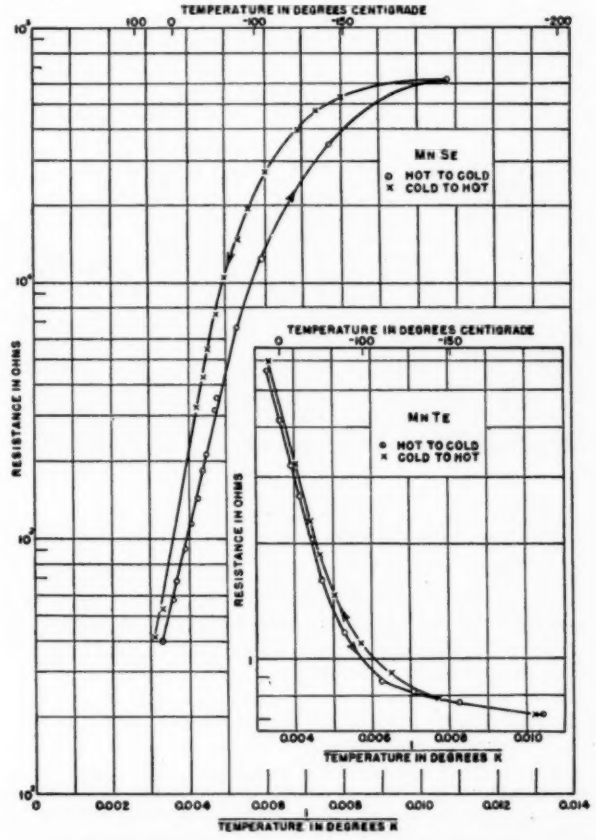

FIG. 1. The resistance of a specimen of MnSe and (inset) a specimen of MnTe as a function of the inverse of the temperature in degrees K. Arrows indicate the direction of the temperature cycle.

Sudden Change in the Arrangement of Crystallites in Thin Evaporated Bismuth Films*

LORN L. HOWARD
Conducting Thin Films Laboratory, Department of Electrical Engineering, University of Illinois, Urbana, Illinois
(Received September 30, 1953)

SOME of the effects of the electron-microscope beam and temperature on thin evaporated metal films have been examined by numerous investigators.[1–7] During recent experimental work with thin bismuth films, additional effects were observed for brief periods immediately following the exposures of individual film specimen areas to the electron beam.

The microscope specimen upon which these effects were observed was taken from a thin film of bismuth which had been evaporated in 3 sec onto a 0.04μ-thick substrate of cellulose nitrate. The evaporation pressure was 3×10^{-5} mm with an evaporation distance of 30 cm. This bismuth film was approximately 100A thick and had an initial resistance per square of 220 ohms before admission of air to the evaporation chamber and 240 ohms after the admission of air.

Although similar observations have been made previously on film specimens in the Philips microscope and the RCA model EMB microscope under different conditions of both voltage and current, the photographs reproduced herewith were made of the phenomenon as it occurred in the RCA model EMT microscope operating at approximately 48 kv, 25 μa, and 3000× magnification.

It is often noticed in this equipment that immediately after the appearance on the fluorescent screen of the image of a specimen such as described above there appears to be a great amount of activity in the specimen. The individual crystalline granules appear alternately light and then dark, and there is a slight shifting of position and some turning in position of the granules. This activity proceeds for perhaps 5 sec and then stops completely. It almost never resumes, even when the same specimen area is brought into the beam several times in succession. The accom-

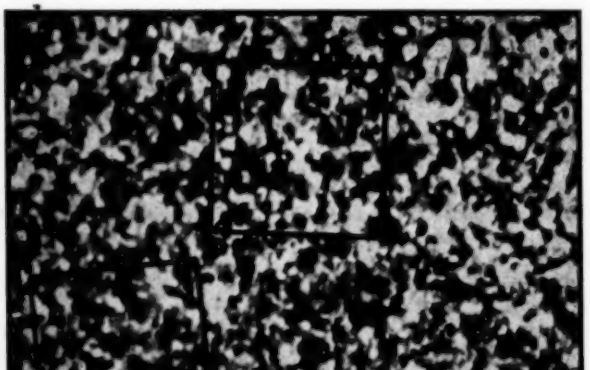

(a)

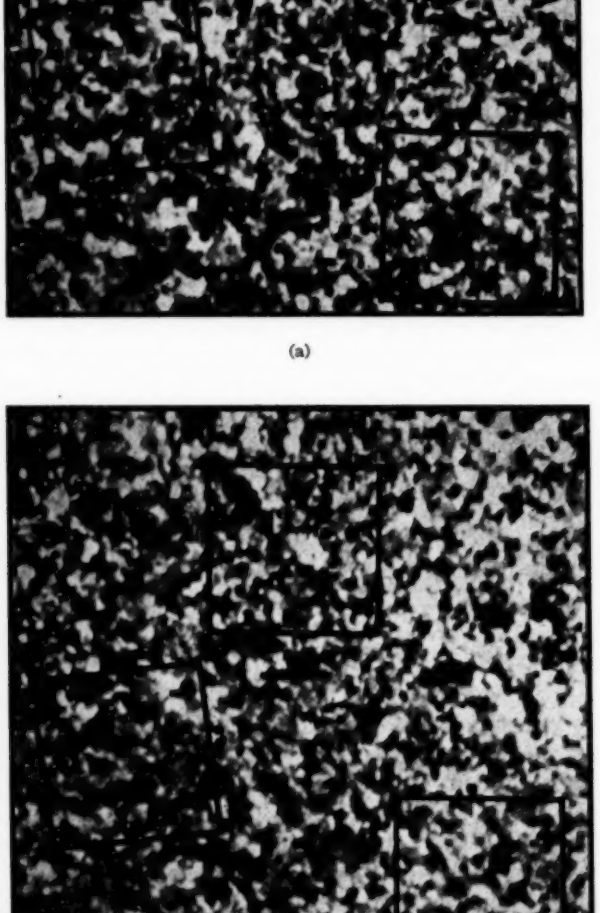

(b)

FIG. 1. Electron micrograph of evaporated bismuth film: (a) before the final shift of particles; (b) after the final shift of particles. (10 500×)

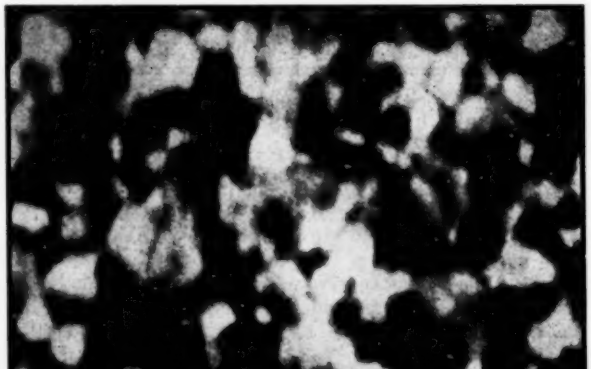

(a)

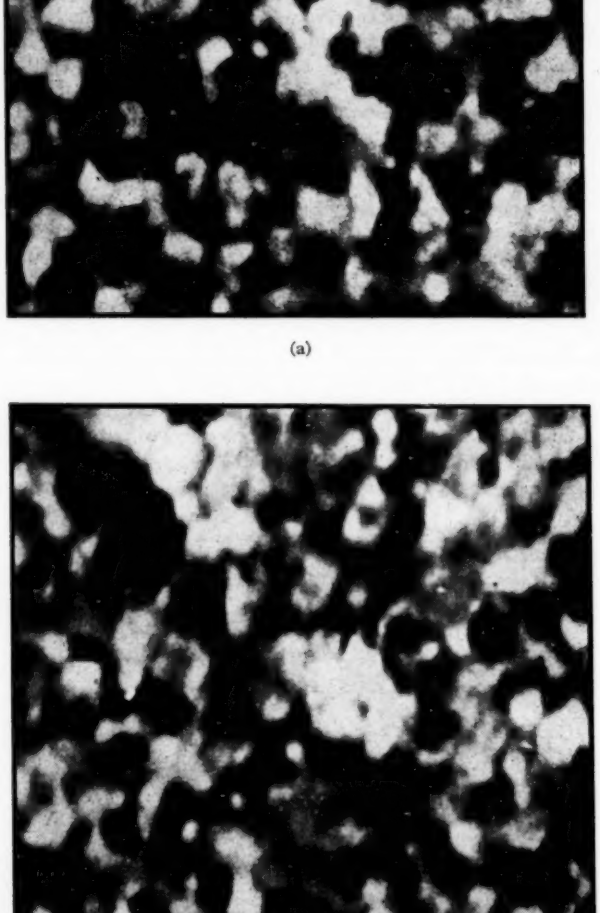

(b)

FIG. 2. Typical area (top center) of bismuth film in Fig. 1(a) and Fig. 1(b): (a) before the particle shift; (b) after the particle shift. (36 000×)

panying photographs were made before and after a rare occasion when the activity resumed for an instant after once ceasing. On this occasion there was a cessation of activity after the initial exposure of the area to the electron beam, following which the picture in Fig. 1(a) was made. The beam was turned on this same area again after replacement of the photographic plate. A few seconds later there appeared to be one simultaneous shift of a large number of crystallites, and then all activity ceased. The resulting rearrangement is shown in Fig. 1(b).

Figures 1(a) and 1(b) have been divided into squares as indicated, and the top center squares have been enlarged to show greater detail. Figure 2(a) presents the enlarged top center square before the final shift of the crystallites. Figure 2(b) shows the same square after the final shift of the crystallites. The activity as indicated by the changes in the photographs includes: (1) a change of the appearance of crystallites from black to gray or white; (2) a change of the appearance of crystallites from gray to black or white; (3) a change of the appearance of crystallites from white to gray or black; (4) a change in the distance between some of the crystallites; and (5) a slight rotation of some of the crystallites in the plane of the photograph. The other squares marked off in Figs. 1(a) and 1(b) surround areas where these same changes are noticeable and where the activity may be followed in detail.

A normal appearance for a bismuth film of this thickness, either with or without this crystallite activity might be that of either

Fig. 1(a) or 1(b), and this is similar to the appearance of a bismuth film of approximately six times this thickness, as shown by Williams and Wyckoff.[8] The changes indicated in (1), (2), and (3) above are probably caused by a tilting of the various crystallites with respect to their original positions under either the direct or indirect action of the electron beam. That such tilting of the crystallites would yield these results was suggested by Kirchner[9] and has been investigated and verified further by others.[10–14] The initial cause for the tilting is not clear at this stage of the investigation. In the case of indirect action by the electron beam, if one assumes a temperature-rise effect, the activity could be due to substrate contraction or to a "drifting" movement such as suggested by Eckardt,[15] in which the activity is an attempt to readjust to stresses and stretchings as a result of energy absorption. Such an explanation would also account for the activity described in (4) and (5) above. It is expected that further results will be reported upon later.

The author wishes to thank Professor Carl E. Drumheller for his encouragement and Albert E. Vatter, Jr., for his interest in this work.

* This work was supported in part by the U. S. Air Research and Development Command under Contract No. AF33(038)-21255.

[1] K. R. Dixit, Phil. Mag. **16**, 1049 (1933).
[2] E. N. da C. Andrade and J. G. Martindale, Trans. Roy. Soc. (London) **A235**, 69 (1935).
[3] E. T. S. Appleyard, Proc. Phys. Soc. (London) **49** (Extra Part), 118 (1937).
[4] D. A. Was, Physica **6**, 4, 390 (1939).
[5] R. G. Picard and C. S. Duffendack, J. Appl. Phys. **14**, 291 (1943).
[6] H. Levinstein, J. Appl. Phys. **20**, 306 (1949).
[7] R. S. Sennett and G. D. Scott, J. Opt. Soc. Am. **40**, 203 (1950).
[8] Robley C. Williams and Ralph W. G. Wyckoff, J. Appl. Phys. **15**, 712 (1944).
[9] K. Kirchner, Ann. Physik **13**, 38 (1932).
[10] H. Boersch, Ann. Physik **26**, 631 (1936).
[11] Manfred von Ardenne, Z. Physik **116**, 736 (1940).
[12] B. von Borries and E. Ruska, Naturwissenschaften **28**, 366 (1940).
[13] J. Hillier and R. F. Baker, Phys. Rev. **61**, 722 (1942).
[14] R. D. Heidenreich and L. Sturkey, J. Appl. Phys. **16**, 97 (1945).
[15] A. Eckardt, Optik **3**, 53 (1948).

Further Remarks on the Nature of the Statistical Observer

DAVID MIDDLETON
Cruft Laboratory, Harvard University, Cambridge, Massachusetts
(Received July 6, 1953)

IN several recent articles[1,2] the author has discussed three classes of optimum statistical procedures for the (incoherent) detection of pulsed carriers in normal random noise. These procedures provide tests of the statistical hypothesis (in terms of which the detection problem is properly formulated), *viz.*, "yes" or "no," for the presence or absence of a signal in the background noise. Two types of error can occur, the results of noise and finite observation time: a type I error, of probability α, of calling noise a signal when really only noise exists in the system; and a type II error, whose probability is β, of calling signal and noise, noise alone when actually a signal is being received. The details of the test determine the type of statistical observer. For instance, one who fixes α beforehand and then minimizes β is called a Neyman-Pearson observer. In a similar fashion, Siegert's ideal observer (see reference 1, paper I) minimizes the total probability of an incorrect decision, while the Sequential observer belongs to still another, somewhat more general class, where α and β are predetermined and the sample size (or integration time) is variable.[3]

The purpose of the present note is to emphasize (perhaps more succinctly than in references 1 and 2) the operational distinction between observers and to modify the comments and some of the conclusions[4] regarding the relative merits of the Ideal and Neyman-Pearson procedures.

We remark again that it is the external constraints (α, β, integration time, etc.) which effectively select our optimum observer. For example, since in many radar cases very small values of α are required (e.g., long false-alarm times), the Neyman-Pearson observer is a logical choice. On the other hand, although we may still require the total error of decisions to be minimized, for some operations this is to be done in such a way that the errors are equally shared between types I and II: we do not wish to weight unduly type I against type II and vice versa. The Ideal observer is then a natural choice. Finally, the Sequential observer may be used in either capacity, since we may set $\alpha=\alpha_{NP}$ and $\beta=\beta_{\min}$ for the Neyman-Pearson case, or arrange that the total error of decision equal that of the Ideal observer, for the corresponding operations, inasmuch as α and β are at our disposal here. Integration time, however, is not, but this is *on the average* as favorable or more so (e.g., smaller samples), than for either of the two fixed-sample tests discussed here.

A comparison of the Neyman-Pearson and Ideal observers is given in Sec. 7F, reference 1, and requires some amendment. First, if p and q are respectively the *a priori* probabilities that any given trial contains signal and noise, or noise alone, there the Ideal observer *by definition* is one who minimizes $\beta p+q\alpha$,[5] *not* $\beta+\alpha$, as incorrectly stated in reference 1 (unless $p=q=\frac{1}{2}$). (The analysis already includes the proper terms, and is unchanged.) Second, it is not true that the Neyman-Pearson observer is better than the Ideal, when compared using the *unnormalized* betting curve[6] for the same total error of decision, since the latter by definition is one which maximizes the probability of a correct decision.[7] This can be seen at once, for example, from Fig. 8 (reference 1, paper II). The curve for the Neyman-Pearson case ($\alpha=0.05$) in Fig. 7, however, is lower by about 0.5 db, which represents the effects of the different normalizations, [see Eqs. (7.7), reference 1, paper II]. For a more complete account of the comparisons see the discussion in the accompanying letters. Finally, we remark that the studies of references 1 and 2 represent but one case in the complete theory of the detection process, which is now being completed by the author.[8]

[1] D. Middleton, "Statistical criteria for the detection of pulsed carriers in noise I, II," J. Appl. Phys. **24**, 371, 379 (1953).
[2] D. Middleton, "Statistical methods for the detection of pulsed radar in noise"—see proceedings of a symposium (London, September, 1952) on *Applications of Communication Theory* (published in the United States by Academic Press, Inc., New York).
[3] For details, see reference 1, Secs. 1 and 2.
[4] See reference 1, especially p. 388.
[5] See reference 1, Eq. (1.1).
[6] See reference 1, pp. 373 and 381.
[7] See reference 1, abstract of paper II.
[8] For a résumé of some of the principal results see David Middleton, "The statistical theory of signal detection," paper presented at a Symposium on Information Theory, Berkeley, California, August 17 and 18, 1953.

Information Loss Attending the Decision Operation in Detection*

DAVID MIDDLETON†
Cruft Laboratory, Harvard University, Cambridge, Massachusetts
(Received August 8, 1953)

THE detection process in communication theory, when properly formulated, is basically the problem of testing the statistical hypothesis (H_1) of a signal (in noise) against the (null-) hypothesis (H_0) of noise alone.[1] Application of suitable tests[1] determines for us the presence or absence of a signal, subject to two classes of error: the Type I error (of probability α), of calling noise a signal when really only noise is present: and the Type II error (probability β), of calling signal and noise, with noise alone. In practical situations, these probabilities (α, β) are different from zero, since noise accompanies the signal in some manner, and the observation time is finite. Information is necessarily lost when a definite decision "yes," a signal, or "no," no signal, is made under these circumstances. It is the purpose of this note to provide a measure of this information loss, and to discuss its relation to the type of statistical test employed in the detection process.

Let $\mathbf{x}=(x_1, \cdots, x_n)$ be a set of possible signal values, in the unperturbed state, and let $\mathbf{y}=(y_1, \cdots, y_n)$ be a corresponding

set of possible, *received* signal values, after interaction with the noise. The amount of information H_T actually conveyed by the definite decision "yes," or "no," is given by the well-known[2] expression

$$H_T = H(\mathbf{x}) - H(\mathbf{y}|\mathbf{x}), \tag{1}$$

where $H(\mathbf{x})$ is the information content of the original, input $\mathbf{x}$, and $H(\mathbf{y}|\mathbf{x})$ is the conditional entropy, or uncertainty in $\mathbf{x}$ based on knowledge of the received wave $\mathbf{y}$, i.e., the *equivocation*. If p and q are, respectively, the *a priori* probabilities of signal and no-signal, e.g., $p+q=1$, it is clear that

$$H(\mathbf{x}) = -p\log p - q\log q, \quad (\ )/\text{indication}, \tag{2}$$

the units of information being (bits/indication or decision) if 2 is chosen as the base of the logarithm, in the usual way. (For $p=q=\frac{1}{2}$, $H_{\max}(\mathbf{x})=1$ bit/indication.)

The equivocation may be calculated as follows: let x_1 be a value of x associated with a signal; x_2, with no signal; and y_1, a value of the received wave, associated with a "yes" decision; y_2 is associated with a "no" decision. The probabilities of the various possibilities indicated above then are, if we remember that there are two types of error that can occur in any decision,

$$\begin{aligned} &P(x_1, y_1) = p(1-\beta); \quad P(x_1, y_2) = p\beta; \\ &P(x_2, y_1) = q\alpha; \qquad\quad P(x_2, y_2) = q(1-\alpha), \end{aligned} \tag{3}$$

and the equivocation is

$$H(\mathbf{y}|\mathbf{x}) = -\sum_{k,j=1}^{2} P(x_j, y_k)\log\left[\frac{P(x_j, y_k)}{P(y_k)}\right]. \tag{4}$$

The marginal probabilities needed here are: $P(y_1)=p(1-\beta)+q\alpha$; $P(y_2)=p\beta+q(1-\alpha)$. The equivocation becomes explicitly

$$\begin{aligned} H(\mathbf{y}|\mathbf{x}) = H(\mathbf{x}) &- [p(1-\beta)\log\{(1-\beta)/[p(1-\beta)+q\alpha]\} \\ &+ p\beta\log\{\beta/[p\beta+q(1-\alpha)]\} + q\alpha\log\{\alpha/[p(1-\beta)+q\alpha]\} \\ &+ q(1-\alpha)\log\{(1-\alpha)/[p\beta+q(1-\alpha)]\}]. \end{aligned} \tag{5}$$

One easily shows that the equivocation is a *maximum* when $\alpha+\beta=1$, and in fact is equal to $H(x)$, which is not unreasonable, as with completely wrong decisions no information remains upon detection, i.e., $H_T=0$, Eq. (1). One does better to guess on the basis of the *a priori* probabilities. At the other extreme, if $\alpha=\beta=0$, $H_T=H(\mathbf{x})$; as expected, no information is lost, since there is no error in decision.

Two cases of particular interest arise: (a) when α is very small, in the radar problem (small false-alarm times), and (b) when $\alpha=\beta$, in the many situations where there is no reason to weight errors of the second kind more heavily than the first.[3] We have

$$(\alpha \doteq 0;\ \beta > 0):\ H(\mathbf{y}|\mathbf{x}) \doteq -q\log q - p\beta\log p\beta + (p\beta+q)\log(p\beta+q), \tag{6}$$

$$(\alpha=\beta):\ H(\mathbf{y}|\mathbf{x}) = H(\mathbf{x}) - (1-\alpha)\log(1-\alpha) - \alpha\log\alpha + \sum_{k=1}^{2} P(y_k)\log P(y_k). \tag{7}$$

As an example, let us compare the Neyman-Pearson and Ideal observers[1] in two instances, assuming equal *a priori* probabilities in both cases, and equal input signal-to-noise ratios (i.e., the constraints on the channel for both observers are the same). The probabilities of Type I and Type II errors are, of course, different in general. From the data of Figs. 4 and 5 of reference 1 (Paper II), and with the help of (6) and (7), (1) and (2), we may tabulate the important quantities, remembering [see (2)] that $H(\mathbf{x})=1$ bit/indication when $p=q=\frac{1}{2}$.

The Ideal observer, for the same input signal-to-noise ratio (a_0^2), and integration time ($\sim n$), is seen to be better than the Neyman-Pearson observer in the same circumstances: less information is lost when the decision is made (larger H_T) and this in turn is reflected in the smaller probability of an incorrect decision $(\alpha+\beta)/2$, $p=q=\frac{1}{2}$ [from the unnormalized betting curves, see Sec. (4)–(6) of reference 1]. [For normalized betting curves, $\alpha+\beta$ represents the total probability of an incorrect decision here ($p=q=\frac{1}{2}$).] That the Ideal observer is better than the Neyman-Pearson is consistent with the definition of the former as minimizing the total probability of wrong decisions (for the same integration time and input ratio a_0^2).[1,4] Another comparison, on the basis of *equal* probabilities of error, confirms the superiority of the Ideal observer from the point of view of signal threshold. From the second and third rows of Table I, we find that the Neyman-Pearson observer loses less information in decision by 0.043 bit/indication than does the Ideal, but requires at the same time a threshold signal (if the noise background and integration time are held constant) 2.0 db [$=10\log_{10}(5.0/3.15)$] stronger. Finally, we note that the Sequential observer,[1] for the same values of α, β chosen for the Ideal or the Neyman-Pearson cases, yields the same equivocations as indicated above, see Table I and (5), with the same comparisons on that score, but always on the average for *smaller* ratios of $a_0^2(n)^{\frac{1}{2}}$. Thus, for the same input ratios $a_0^2\sqrt{n} = a_0^2\langle n\rangle^{\frac{1}{2}}$, α and β, and hence $H(\mathbf{y}|\mathbf{x})$ will be correspondingly smaller. A detailed study of the interdependence of threshold, integration time, α and β, and information loss is being prepared.[5]

TABLE I.

Observer	Threshold constant (weak signal)	α	β	Total prob. of error $(\alpha+\beta)/2$	$H(\mathbf{y}\|\mathbf{x})$	H_T
Neyman-Pearson	$a_0^2\sqrt{n}=3.15$	10^{-4}	0.73	0.365	0.850 bit	0.150 bit
Ideal	3.15	0.05	0.05	0.05	0.285	0.715
Neyman-Pearson	$a_0^2\sqrt{n}=5.0$	10^{-4}	0.10	0.05	0.242	0.758
Ideal	5.0	0.01	0.01	0.01	0.080	0.920

* The research reported here was done by the author as a consultant to the Lincoln Laboratory, The Massachusetts Institute of Technology (Cambridge, Massachusetts), and is published by permission, which is gratefully acknowledged. The research in this document was supported jointly by the U. S. Army, Navy, and Air Force under contract with the Massachusetts Institute of Technology.

† Consultant, Lincoln Laboratory, Massachusetts Institute of Technology.

[1] D. Middleton, J. Appl. Phys. **24**, 371, 379 (1953); also "Statistical methods for the detection of pulsed radar in noise," proceedings of a symposium (London, September, 1952) on *Applications of Communication Theory* (Academic Press, Inc., New York, 1953).

[2] C. E. Shannon, Bell System Tech. J. **27**, 379, 623 (1948).

[3] Reference 1 and D. Middleton, J. Appl. Phys. (Letter to the Editor, to be published).

[4] D. Middleton, Letter to the Editor, J. Appl. Phys. (to be published).

[5] D. Middleton, "The Statistical Theory of Detection, III; Entropy Changes and Information Loss," a Lincoln Laboratory report.

Discussion of "Statistical Criteria for the Detection of Pulsed Carriers in Noise I, II"

D. MIDDLETON, *Cruft Laboratory, Harvard University, Cambridge, Massachusetts*

AND

W. W. PETERSON AND T. G. BIRDSALL, *Engineering Research Institute, University of Michigan, Ann Arbor, Michigan*

(Received September 12, 1953)

THESE papers[1] represent the first unified presentation of the application of several types of statistical tests to the important problem of detection in communication theory. However, we feel that the comparison of tests considered in paper II is of somewhat limited scope and that a clearer and more complete account of the author's methods of comparison is needed.

A comparison of statistical observers may be made in a number of ways: in fact, we observe first that in many situations there is no necessity for comparing the Neyman-Pearson, Ideal, and Sequential observers[2]—each is an optimum procedure for the problem at hand.[3,4] However, our choice of observers in some instances may be based on which is the best *for a given total*

probability $(\alpha q+\beta p)$ *of decision error*. Then the comparisons discussed at length in paper II, reference 1, follow. (We recall that α and β are, respectively, the probabilities of a Type I and a Type II error, and that p and q are the *a priori* probabilities associated with signal plus noise, and noise alone.[2])

Two possibilities exist under this condition: (1) the comparison is made on the basis of the unnormalized betting curves W; (2) the comparison is given in terms of *normalized* betting curves,[5] with the best observer defined in each instance as the one giving the largest value of the betting curve for a given threshold (a_0^2)

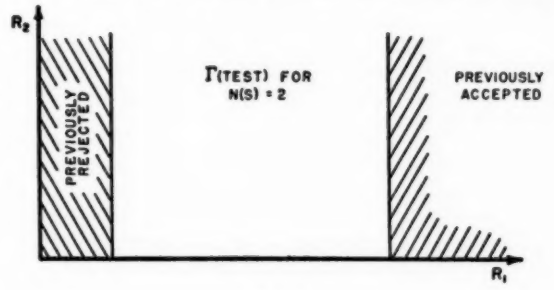

FIG. 1.

and observations time (n) (or equivalently, the same value on the betting curve for the smallest threshold). Paper II considered case (2) only and did not emphasize the normalized character of the betting curves under comparison. Accordingly, we include a short table (Table I), comparing the Neyman-Pearson and Ideal observers, subject to the same value of the sum $\alpha q+\beta p$. (The equal signs mean "equally good;" $\gtrless$ indicate "better than" or "worse than," and p, q, n are held fixed for any particular comparison.)

The tests are identical (for fixed a_0, n, p, q) when $\alpha_{NP}=\alpha_{I(\min)}$, and thus $\beta_{NP(\min)}=\beta_{I(\min)}$, and $K=1$, [see Eqs. (4.5) and (4.6), reference 1]. When the tests are not identical, $\alpha_{NP}\neq\alpha_{I(\min)}$, etc., then *by definition* the Ideal observer is best, in the sense of the *unnormalized* comparison, since he minimizes the total probability of decision error, while the Neyman-Pearson observer has α_{NP} already fixed, and can only minimize β. On the basis of normalized betting curves, however, the Neyman-Pearson observer is sometimes better than the Ideal. This is the result of the normalization procedure. This explains why the former gives a smaller minimum detectable signal than the latter (same $\alpha q+\beta p$), as shown in Fig. 7, $\alpha=0.05$ (reference 1), and why in Fig. 8, $\alpha=0.05$, the reverse

TABLE I.

	Conditions	Unnormalized	Normalized
I	$\alpha p \doteq 0$	$NP=$Ideal	$NP\doteq$Ideal
$\alpha_{NP}=\alpha_I$; $\beta_{NP}=\beta_I$ (Identical tests)	$\alpha(p-q)\doteq 0$ other αp, $\alpha(p-q)$	$NP=$Ideal	$NP>$Ideal
II	$W_{NP}<W_I<\dfrac{W_{NP}-\alpha_{NP}(2q-p)}{1-\alpha_{NP}}$ $(q<p)$ (Nearly-identical tests)	$NP<$Ideal	$NP>$Ideal
III $\alpha_{NP}\neq\alpha_{I(\min)}$; $\beta_{NP}\neq\beta_{I(\min)}$ (and not II) (Non-identical tests)		$NP<$Ideal	$NP<$Ideal

situation appears. (For a brief mention, see reference 4.) The normalization also accounts for the apparently greater amount of information following the decisions operation for the Neyman-Pearson observer, as shown in the comparison of lines 2 and 3 (Table I), in a recent "Letter to the Editor."[6] We remark, finally, that the Sequential observer, for the same α, β, p, q, will yield a lower threshold for the same average integration time, or equivalently, for the same threshold, a shorter average observation period, than either the Neyman-Pearson or the Ideal observers.

The indicated calculation of the betting curves in reference 1 for the Sequential observer, Eqs. (6.2), (6.5), is not correct, although Eq. (6.1) is valid, provided we determine P_n and Q_n properly. Unfortunately, we cannot find P_n and Q_n as was done for the fixed sample tests (Neyman-Pearson, etc.), in as much as the Sequential observer deals at any stage n (before a decision is reached at $n=n(s)$) *only* with those signals which have not been previously accepted or rejected. The remaining signals will yield distributions of the logarithm of the likelihood ratio (the P_n, Q_n) quite different from the distributions derived on the basis of all possible signals, on which the calculations [Eq. (4.12)] for the Neyman-Pearson and Ideal observers are based. Thus, instead of (4.3) or (4.12) we have for the distributions of the logarithm (x) of the likelihood ratio, expressions of the type

$$P_{n(s)}(x;a_0)=c_{n(s)}\int_{\Gamma(\text{test})}\cdots\int W_{n(s)}(R_1\cdots R_{n(s)}|a_0)dR_1\cdots dR_{n(s)}\delta(x-\log\Lambda_{n(s)}), \quad (1)$$

$$Q_{n(s)}(x;a_0)=d_{n(s)}\int_{\Gamma(\text{test})}\cdots\int W_{n(s)}(R_1\cdots R_{n(s)}|0)dR_1\cdots dR_{n(s)}\delta(x-\log\Lambda_{n(s)}), \quad (2)$$

where $c_{n(s)}$ and $d_{n(s)}$ are constants such that

$$\int_{-\infty}^{\infty}P_{n(s)}(x;a_0)dx=1=\int_{-\infty}^{\infty}Q_{n(s)}(x;a_0)dx, \quad (3)$$

and the test region $\Gamma(\text{test})$ consists of all envelopes $(R_1\cdots R_n\cdots\times R_{n(s)})$ such that

$$\frac{\beta}{1-\alpha}\leq\Lambda_n(R_1\cdots R_n)\leq\frac{1-\beta}{\alpha}\text{ for all }n<n(s). \quad (4)$$

This makes the explicit evaluation of P and Q technically quite complicated. For example, in the very simple case where $\log\Lambda_{n(s)}$ is proportional to the sum of the squares of the envelope samples,

$$\log\Lambda_n=g(n)\sum_1^n R_i^2, \quad (5)$$

for $n(s)=2$ the test region $\Gamma(\text{test})$ is all (R_1, R_2) that satisfy condition (4), namely,

$$\log\frac{\beta}{1-\alpha}\leq g(1)R_1^2\leq\log\frac{(1-\beta)}{\alpha}, \quad (6)$$

and is shown graphically in Fig. 1. For $n(s)=3$, the test region is all (R_1, R_2, R_3), satisfying both Eqs. (6) and (7),

$$\log\frac{(1-\alpha)}{\beta}\leq g(2)[R_1^2+R_2^2]\leq\log\frac{(1-\beta)}{\alpha}. \quad (7)$$

The reason for this is that at the second stage those (R_1, R_2) in the test region that satisfy

$$g(2)[R_1^2+R_2^2]>\log\frac{1-\beta}{\alpha} \quad (8)$$

are accepted, and those in the test region that satisfy

$$g(2)[R_1^2+R_2^2]<\log\frac{\beta}{1-\alpha} \quad (9)$$

are rejected (leading to the conclusion that only noise was present). Therefore, the test region for the next (3rd) stage is all those (R_1, R_2, R_3) that satisfy (7) but not either (8) or (9), and is the infinite cylinder with base as in Fig. 2. Clearly the test region becomes more complex at each step, and it appears to be a very difficult task to describe the test region and calculate the integrals (1) and (2) for all values of $n(s)$.

When (1) and (2) have been found, Eq. (6.3) may then be used to obtain the mean betting curve, which results when we average over all possible $n(s)$ for which the test just terminates. The discrepancy between the calculations for the Sequential observer

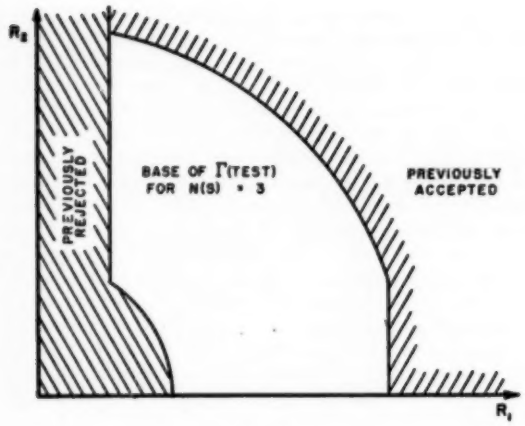

FIG. 2.

shown in Figs. 8 and 9 and the expected superiority of this observer over the others for the same controls is explained primarily in terms of the foregoing error, The necessarily crude approximations to the distribution of sample size, as originally indicated in paper II, also plays a part in this discrepancy.

[1] D. Middleton, J. Appl. Phys. **24**, 371 (I), 379 (II) (1953). Also, a condensed account of this work appears in *Applications of Communications Theory*, edited by Willis Jackson (Academic Press, New York, 1953).
[2] For a description, see reference 1, paper I.
[3] W. W. Peterson and T. G. Birdsall, "The theory of signal detectability," Technical Report No. 13, Electronic Defense Group, Engineering Research Institute, Department of Electrical Engineering, University of Michigan, discuss in detail the Neyman-Pearson and Ideal observers on this basis.
[4] D. Middleton, J. Appl. Phys., **24**, 127(L) (1953), also mentions some specific applications where the type of observer is specified beforehand by the problem in question.
[5] The specific normalizations are indicated in Eqs. (7.7a-c), reference 1.
[6] D. Middleton, "Information loss attending the decision operation in detection" J. Appl. Phys. **24**, 127(L) (1953).

A Method for Generating Strong Shock Waves

A. HERTZBERG AND W. E. SMITH
Cornell Aeronautical Laboratory, Inc., Buffalo, New York
(Received September 30, 1953)

EXPERIMENTAL research into the physical phenomena associated with hypersonic flow[1] and high-temperature gas dynamics[2] is characterized by its dependence currently upon successful generation of shock waves whose strengths correspond to Mach numbers greater than ten. To this end, attention has been directed toward development of suitable techniques involving either explosive charges,[3] electrical discharge tubes,[4] or especially high-pressure-ratio shock tubes.[5] The shock tube excels in its simplicity and versatility. The present note is to discuss a simple modification of the operation of the combustion-powered, high-pressure-ratio shock tube which permits extension of its range.

The tendency has been to employ as driver a gas, or gases, whose temperature is high and whose molecular weight is low, so that the corresponding acoustic velocity is maximized. The influence of the acoustic velocity in the driver gas is illustrated in Fig. 1, where the diaphragm pressure ratio required to produce a certain shock strength is given for various speed-of-sound ratios. A simple method for obtaining a high acoustic velocity in the driver is by burning a combustible gaseous mixture in the driver chamber at constant volume. Unfortunately, the maximum temperature to which the driver can be heated is limited by the onset of molecular dissociation. Its molecular weight is likewise limited by practical combustion mixtures. In general, it is not feasible to operate a shock tube in which the speed-of-sound ratio exceeds 6.6 (approximately). Thus, the shaded area in Fig. 1 is unavailable to the experimenter employing a constant-volume combustion cycle.

To drive a shock wave through air, a stoichiometric mixture of oxygen and hydrogen diluted with 80 percent helium has been adopted at Cornell Aeronautical Laboratory. Shock Mach number of about 17 with a pressure ratio of 17 200 may be obtained from this mixture. To maintain appreciable densities in the low-pressure chamber, however, high pressures in the driver chamber are required. To accommodate a significant volume within a large-bore shock tube, then, the structural problems become prohibitive. Methods for obtaining effectively higher driver speeds must be developed if the application of the shock tube in the Mach-number range above ten is not to be severely limited.

In the course of hypersonic-flow investigations with the combustion-powered shock-tube facility at Cornell Aeronautical Laboratory, it has been discovered that higher shock speeds than can be explained by the theory of constant-volume burning are obtained under certain conditions. The anomalous results, although at first dismissed as being due to experimental error arising from the instrumentation, were eventually shown to be unexplainable by any orthodox analyses. Furthermore, in every case, the unexpected "efficiency" was correlated with the application of diaphragms (separating high- and low-pressure regions) which were accidentally weaker than those designed to withstand complete combustion at constant volume. As a consequence, a subsidiary investigation was launched. Diaphragms of varying thickness to withstand pressures corresponding to the full range of possible completion of combustion (from none to fully complete) were tested while holding fixed the initial (pre-ignition) pressures of the driver and driven gases. The test results are shown in Fig. 2.

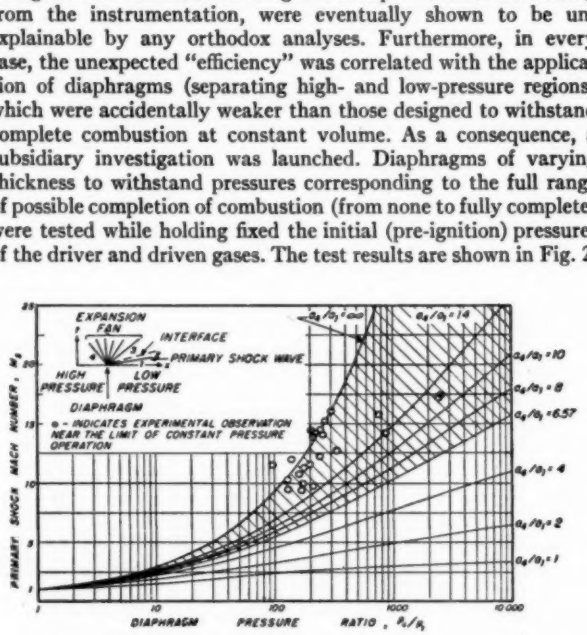

FIG. 1. Shock-tube performance curves and test data. p_1, p_4 are total pressures acting on the diaphragm at instant of failure. a_1, a_4 are sound velocities in the high and low pressure regions after combustion at constant volume is completed and before the diaphragm bursts. The adiabatic exponents, γ_1 and γ_4, are each taken to be 1.40. Because of the limitation on a_4, the shaded region is inaccessible for constant volume operation.

The excessive scatter arises largely from practical difficulties involved in determining the shock Mach number, for the shock front may consist of multiple shock waves for several tube diameters downstream of the diaphragm.

It is seen that the shock Mach number varies *inversely* as the measured bursting pressure of the diaphragm. Thus, the highest shock strength is realized when the diaphragm is destroyed immediately after ignition. In this case, the combustion proceeds within the driver gases as they issue forth at constant pressure into the low-pressure chamber. Should the diaphragm fail after combustion is partially completed, the shock strength is intermediate between the limits represented by constant pressure and constant volume cycles. Multiple shock fronts are characteristic phenomena of these "in-between" cycles. It has been demonstrated by carefully recording and analyzing the pressure history within the burning gases that detonation phenomena are absent from the combustion processes here described. Preliminary data on operation near the constant-pressure limit are shown in Fig. 1 and indicate the extent to which the shaded area becomes accessible. It appears that for a given diaphragm pressure ratio the "constant pressure" process permits attainment of the limiting

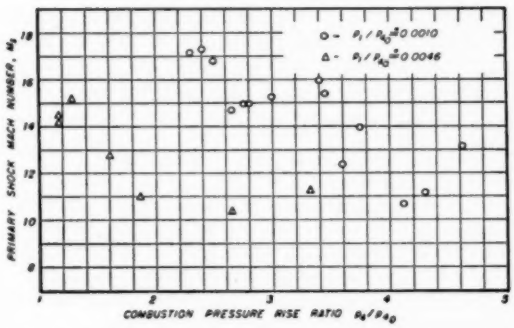

FIG. 2. Shock-tube test data. p_{40} is pressure in the high-pressure chamber before combustion. p_4 is pressure in the high-pressure chamber at instant of diaphragm failure. p_1 is pressure in the low-pressure chamber at instant of diaphragm failure.

shock strength, i.e., corresponding to an infinitely large sound speed in the driver.

The suggested method, then, for generating strong shock waves with apparatus whose physical strength is to be minimized is to pierce the diaphragm mechanically immediately following ignition of a combustible mixture. To calculate the performance of a shock tube using constant pressure combustion, it is sufficient to apply conventional theory and to assume the acoustic velocity in the driver to be infinitely large. The pressure ratio across the diaphragm at the instant of failure is consequently equal to the pressure ratio across the generated shock. The constant pressure-driving method is being explored further in relation to varying combustible mixtures and tube configurations.

[1] A. Hertzberg, J. Aeronaut. Sci. **18**, 803 (1951).
[2] Resler, Lin, and Kantrowitz, J. Appl. Phys. **23**, 1390 (1952).
[3] Koski, Lucy, Shreffler, and Willig, J. Appl. Phys. **23**, 1300 (1952).
[4] Fowler, Goldstein, and Clotfelter, Phys. Rev. **82**, 879 (1951).
[5] J. Lukasiewicz, National Aeronautical Establishment, Canada, Report No. 15 (1952).

Electrical Conductivity Induced by Ionizing Radiation in Some Polymeric Materials*

A. J. WARNER, F. A. MULLER, AND H. G. NORDLIN
Chemical-Physical Laboratory, Federal Telecommunication Laboratories, International Telephone and Telegraph Corporation, Nutley, New Jersey
(Received October 8, 1953)

WE have recently worked out a method of measuring the electrical conductivity of plastic insulating materials during irradiation with gamma rays, and using this method we have evaluated several of these materials. The method involves the use of a specially developed Wheatstone bridge[1] capable of measuring resistances up to 10^{17} ohms. Disk-type samples are used that have an electrode-area-to-dielectric-thickness ratio of about 10^4 cm, so that the measurable range of resistivity extends up to 10^{21} ohm-cm. The samples are placed in an evacuated desiccator during measurements; it was empirically determined that if the residual air pressure is reduced to less than 7 microns, the electric current through the air becomes negligible. The effects of stray leakage currents are eliminated by the use of guard electrodes on the sample and on the leads to the sample.

To allow polarization currents to fall to negligibly small values, the measuring voltage is applied before the start of each experiment and maintained uninterruptedly all through the test. In some samples of very pure polystyrene, the polarization current was found to decay to a value equivalent to a conductivity of 10^{-20} mho/cm within three-quarters of an hour after beginning electrification; whereas after forty-five hours, the equivalent conductivity of polyethylene was not as low as 10^{-19} mho/cm, although still decreasing at a rate approximately inversely with the square root of time. The other materials tested were between these two extremes with respect to the decay of polarization currents.

Samples are irradiated from a source consisting of a nominal one Curie of cobalt-60 with a beta-ray filter interposed, so that the radiation is essentially monochromatic gamma rays having a photon energy of about 1.2 Mev. The samples are placed at a distance of about four inches from the source so that the irradiation intensity will be 100 roentgens per hour.

After electrifying each sample in the evacuated desiccator for a sufficient length of time, the gamma-ray source is suddenly brought into position close to the sample and conductivity measurements are simultaneously begun. The results of conductivity as a function of time of irradiation for seven synthetic plastic materials are shown in Fig. 1. The curve labeled "copolymer" refers to a copolymer of styrene and parachlorostyrene. The curves shown for polystyrene, polyethylene, Teflon, and Kel-F are representative of more than one sample.

The earliest reading that can be obtained is 1 or 2 minutes after the start of exposure, and during this time the conductivity has already increased by a factor of more than 10, except for polyvinylchloride in which the factor is only about 2. During the course of the experiment, the conductivity in most cases is seen to continue to increase for a long time. In all materials tested except Kel-F and polyvinylchloride, the conductivity eventually decreases again, although this does not show very clearly in the graph. The conductivity of polyparachlorostyrene has already passed its maximum value by the time the first reading can be obtained.

Other data of this type, involving irradiation at different rates, and of the conductivity *vs* time after irradiation ceases, suggest

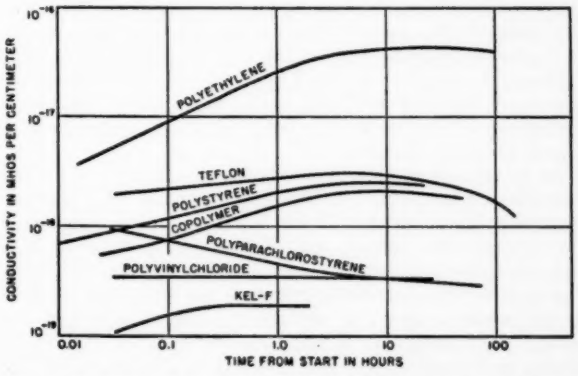

FIG. 1. Variation of electrical conductivity as a function of time for various synthetic plastics irradiated at a rate of 100 roentgens per hr from a cobalt-60 source of gamma rays.

that the slow increase is associated with a corresponding accumulation of ions that are predominantly univalent. The subsequent decrease is believed to result from physical degradation that is accompanied by the formation of molecular dipoles acting as traps for the ions.

A full account of this work will be published elsewhere.

* This work was supported by the Signal Corps Engineering Laboratories.
[1] A. J. Warner and H. G. Nordlin, *Annual Report of the 1951 Conference on Electrical Insulation* (National Research Council, 1952).

The Dispersion Formula for Plasma Waves

L. R. WALKER
Bell Telephone Laboratories, Murray Hill, New Jersey
(Received August 27, 1953)

IF plane longitudinal electromagnetic waves of small amplitude varying as $\exp j(\omega t-\beta z)$ propagate in a homogeneous plasma possessing at every point the same total electron density ρ_0 and

the same normalized velocity-distribution function, $f(u, v, w)$, for the three velocity components, u, v, and w, then a well-known relation connects ω and β.[1] This may be written

$$\frac{1}{\omega_p^2}=\int_{-\infty}^{+\infty}\frac{f_s(w)dw}{(\omega-\beta w)^2}, \tag{1}$$

where

$$\omega_p^2=\eta\frac{\rho_0}{\epsilon_0} \quad \text{and} \quad f_s(w=)\int_{-\infty}^{+\infty}du\int_{-\infty}^{+\infty}dvf(u,v,w);$$

η is the charge to mass ratio of the electron and ϵ_0 the permittivity of free space. At the 1949 Institute of Radio Engineers Conference on Electron Devices the writer described a simple method which may give information about the roots β of (1) for real ω. The method will be outlined here since it does not seem to be generally known.

In (1) put $\omega/w=t$ and $f_s(\omega/t)=g(t)$, so that $g(t)$ is normalized to unity if f_s is. Note that for real ω, if β is a root of (1), so is β^*, its complex conjugate. Consider then the equation satisfied by β^*, which is

$$\int_{-\infty}^{+\infty}\frac{g(t)dt}{(t-\beta^*)^2}-\frac{\omega^2}{\omega_p^2}=0.$$

Integrating by parts, one has

$$\int_{-\infty}^{+\infty}\frac{(dg/dt)dt}{t-\beta^*}-\left[\frac{g(t)}{t-\beta^*}\right]-\frac{\omega^2}{\omega_p^2}=0, \tag{2}$$

where the term in square brackets indicates the sum of the values of the enclosed term evaluated (with the signs appropriate to the integration) at all the finite discontinuities of $g(t)$, say $t_1, t_2, \cdots, t_n$. Inspection shows that the three terms of (2) may be interpreted successively as the complex electric field (E_x+jE_y) at the point $\beta=x+jy$ because of a surface distribution of line charges of density dg/dt at $x=t$; lumped charges $\pm g(t_r)$ at $x=t_1, t_2, \cdots, t_n$ and a uniform field $-\omega^2/\omega_p^2$ in the x direction; y may be assumed positive. If, then, $\beta=x+jy$ is a neutral point of this electrostatic system, β^* is a root of (2). It should be remarked that the total charge on $y=0$ is zero and the field due to the charges must then vanish at large distances.

As an example of the use of this analog consider a distribution which is zero except for $0<t_1<t<t_2$ and let it be flat or monotone or have a single maximum in this interval. For such distributions the corresponding charge distribution, including any lumped charges, consists of a single positive region and a single negative region with the former lying entirely to the left of the latter. The electric vector at β is now easily seen to lie to the left of a line joining β to the point of separation of positive and negative charge and thus its component normal to this line is always in the same direction as that of the component of the field, $-\omega^2/\omega_p^2$. There can therefore be no neutral point for $y\neq 0$. It follows that a minimum in $g(t)$ or $f_s(w)$ is a necessary condition for a complex root of (2). By considering E_x along $y=0$ it is clear that a pair of roots exists for real β, one on each side of the charge distribution.

Consider now a case in which $f_s(w)$ is symmetrical about a maximum at $w=0$. Any three-dimensional distribution which is symmetrical in u, v, and w will lead to such an $f_s(w)$. For this case $g(t)$ is monotone decreasing (increasing) for t negative (positive) if f runs from $w=-\infty$ to $w=+\infty$; if the distribution is finite, lying between $w=-w_0$ and $w=w_0$, $g(t)$ follows the above rule, except in the range $-\omega/w_0<t<\omega/w_0$, where it is zero. By symmetry the field E_y vanishes generally only on $y=0$; in addition it is zero for the finite distribution on $y=0$ for $-\omega/w_0<x<\omega/w_0$. Along $x=0$ the field E_x is positive and increases as y decreases. If $E_x(0,0)>\omega^2/\omega_p^2$ or $\omega_p^2>(\omega^2/E_x(0,0))$, there will be a purely imaginary root (cut off). If $E_x(0,0)<\omega^2/\omega_p^2$ there can be no root at all in the unbounded case, but for the finite distribution, since $E_x(x,0)$ increases from $E_x(0,0)$ to infinity as $|x|$ goes from 0 to ω/v_0, there will be a pair of symmetrically disposed roots in this range.

In this analog, single velocity beams are represented by dipoles, as may easily be seen if they are considered to be the limit of narrow rectangular distributions, since the latter are to be represented simply as a pair of lumped charges at the ends of the distribution. The existence of double stream gain for sufficiently strong pairs of dipoles and the behavior of the gain as a function of separation and so forth are readily discussed qualitatively.

[1] See, for example, D. Bohm and E. P. Gross, Phys. Rev. 75, 1851 (1949).

Comments on Summation of Slowly Converging Series

JULIAN H. BRAUN
U. S. Naval Gun Factory, Washington, D. C.
(Received September 23, 1953)

IN a letter[1] to the editor published in this Journal in August, 1953, Gumowski develops a formula for the rapid summation of slowly converging series. We wish to point out that although his formula is independently derived, it is not a really new result, being, in essence, equivalent to the process of adding up the first few terms of the series and applying Euler's summation formula adapted to a converging series to the succeeding terms.

Euler's formula[2] is

$$f_0+f_1+\cdots+f_s=\int_0^s f(x)dx+\tfrac{1}{2}(f_s+f_0)+\sum_{k=1}^{\lambda}\frac{B_{2k}}{(2k)!}D^{2k-1}(f_s-f_0)+R_\lambda \tag{1}$$

where

$$R_\lambda=\int_0^s P_{2\lambda+1}(x)f^{(2\lambda+1)}(x)dx,$$

$$P_{2\lambda+1}(x)=(-1)^{\lambda-1}\sum_{i=1}^{\infty}\frac{2\sin 2i\pi x}{(2i\pi)^{2\lambda+1}},$$

and B_{2k} are the Bernoulli numbers. For convergent series we have that $\lim_{s\to\infty}(D^m f_s)=0$ for m, a non-negative integer. In Eq. (1) set $f_i=a_{n+i}$, $p'(n)=a_n$ and let both s and λ "go to infinity." In making these substitutions note that

$$\int_0^\infty f(x)dx=\int_0^\infty a_{n+x}dx=\int_n^\infty a_x dx.$$

We obtain for *convergent* series

$$\sum_{i=0}^{\infty}a_{n+i}=\int_n^\infty a_x dx+\tfrac{1}{2}a_n-\sum_{k=1}^{\infty}\frac{B_{2k}}{(2k)!}D^{2k}p(n)+R_\infty, \tag{1'}$$

where

$$R_\infty=\lim_{\lambda\to\infty}\int_n^\infty P_{2\lambda+1}(x)p^{(2\lambda+2)}(x)dx;$$

but

$$\lim_{\lambda\to\infty}P_{2\lambda+1}(x)=\lim_{\lambda\to\infty}(-1)^{\lambda-1}\sum_{i=1}^{\infty}\frac{2\sin 2i\pi x}{(2i\pi)^{2\lambda+1}}=0,$$

and since also $\lim_{\lambda\to\infty}p^{(2\lambda+2)}(x)$ is finite for $0<n\leqq x\leqq\infty$ (for convergent series) we have that $R_\infty=0$. Thus, substituting $R_\infty=0$ in (1') and substituting the result in the identity

$$\sum_{k=1}^{\infty}a_k=\sum_{k=1}^{n}a_k+\sum_{i=0}^{\infty}a_{n+i}-a_n,$$

we obtain

$$\sum_{k=1}^{\infty}a_k=\sum_{k=1}^{n}a_k+\int_n^\infty a_x dx-\tfrac{1}{2}a_n-\sum_{k=1}^{\infty}\frac{B_{2k}}{(2k)!}D^{2k}p(n). \tag{2}$$

This is Gumowski's formula with some changes in notation. From the definition of b_m in the cited letter[1] it follows that $b_m=B_m/m!$ for $m>1$. Further, $B_3=B_5=B_7=\cdots=0$. The equivalence of (2) with Gumowski's formula is now clear. (The usage of $a_x dx$ instead of $a_n dn$ avoids a slight ambiguity, *viz.*—the lower limit on the integral is a chosen constant, n, whereas the "n's" in $a_n dn$ are obviously not meant to be constant.)

[1] I. Gumowski, J. Appl. Phys. 24, 1068 (1953).
[2] See, for example, K. Knopp, *Theory and Application of Infinite Series* (Blackie and Son, Ltd., Glasgow, 1951), p. 524.

Further Comments on Summation of Slowly Converging Series

IGOR GUMOWSKI
Université Laval, Quebec, Canada
(Received October 24, 1953)

I ADMIT readily that once the result of my paper is known, it is possible to show that a formally equivalent, but not a fundamentally identical, expression can be deduced from Euler's summation formula. However, this result was not established rigorously before the publication of my paper, as can easily be seen by checking the published literature.

By consulting K. Knopp [*Theory and Application of Infinite Series* (Blackie and Son, Ltd., Glasgow, 1951)], who is an authority on series, it can be noted that my result differs essentially from Euler's formula as the latter is rigorously stated, both in form and in the type of series to which it applies. In fact, Euler's formula cannot be used for summing series whose general term is of the type $f_n=1/n^k$, $k>0$, because at least one of the following integrals,

$$\int_0^n f(x)dx \quad \text{or} \quad \int_0^n P_{2k+1}(x)f^{2k+1}(x)dx,$$

diverges in the Riemann sense. *No transformation of Euler's formula can change this fact.*

On the contrary, the result of my paper is especially adapted to series of the type $f_n=1/n^k$, $k>0$, because only the existence of $\int_n^\infty f(x)dx$ is required.

However, if a series S not summable by Euler's formula is split up, there results

$$S=\sum_{k=1}^{\infty} a_k=\sum_{k=1}^{n} a_k+\sum_{k=n+1}^{\infty} a_k=\sum_{k=1}^{n} a_k+\sum_{p=1}^{\infty} a_{p+n}.$$

It usually happens that the series

$$S'=\sum_{p=1}^{\infty} a_{p+n},$$

having for general term $f_p=a_{p+n}$, *is* summable by means of Euler's formula. Thus, the sum of the series S can be expressed in terms of the sum of the essentially different series S', which amounts to *changing the series* to which Euler's formula is applied. This result is, however, a new and original contribution.

To illustrate the above point on a concrete example, let us consider the series

$$S=\sum_{n=1}^{\infty}\frac{1}{n^2}$$

which obviously is not summable by Euler's formula. Splitting up S at the nth term, there results

$$S=\sum_{k=1}^{n}\frac{1}{k^2}+\sum_{k=1}^{\infty}\frac{1}{(k+n)^2}.$$

Now, the series

$$S'=\sum_{k=1}^{\infty}\frac{1}{(k+n)^2}$$

is summable by Euler's formula; therefore,

$$S=\sum_{k=1}^{n}\frac{1}{k^2}+S'.$$

Of course, this result has to be formally equivalent to the result of my paper, because it represents the sum of the same series, but it is by no means identical *in principle*.

As far as I know, the suggestion leading to the above reasoning was first made by C. E. Sunborn and R. A. Mugele of the Shell Development Company, Emeryville, California, and it is to them that should be given the credit for making possible the proof of the formal equivalence (but not the identity in principle) of Euler's formula and the result of my paper.

Mr. J. H. Braun does not seem to bring out the really significant aspects of the problem. In the sentence "For convergent series we have that $\lim_{n\to\infty}(D^m f_n)=0$ for m a non-negative integer," he supposes that f_n is the general term of the series to be summed. But for a series which violates the validity conditions of Euler's formula, his subsequent relation

$$\int_0^\infty f(x)dx=\int_0^\infty a_{n+x}dx=\int_n^\infty a_x dx$$

becomes meaningless, because the integral on the left side diverges.

Note on Helix Impedance Measurements Using an Electron Beam

D. A. WATKINS, *Stanford University, Stanford, California*
AND
A. E. SIEGMAN, *Hughes Research and Development Laboratories, Culver City, California*
(Received October 28, 1953)

IN connection with our recent paper in this journal,[1] two items of correction or addition have come to our attention as follows:

(1) Dr. R. Kompfner of the Bell Telephone Laboratories has suggested to us that the mysterious backward wave labeled "?" in Fig. 5 of the paper could be the result of our signal generator having third-harmonic output. The experiment has been repeated with a similar signal generator, and Dr. Kompfner's postulate verified. Thus Fig. 5 would correctly represent our experimental findings if the component labeled "?" were not shown.

(2) Although Fig. 10 is substantially correct, it is somewhat misleading. The figure shows two curves—one is the computed impedance of the (-1) space-harmonic component at the helix radius *versus* $ka\tan\psi$, and the other is the *measured* impedance converted to the *mean* helix radius *versus* the same variable. The large discrepancy between the two is a result of the finite thickness of the tape used in the experimental helix. If the measured impedance is converted to the *inside* radius of the helix rather than the *mean* radius, the discrepancy between the computed and measured curves is less than 17 percent over the entire range, and most of the remaining discrepancy can be attributed to effects of space charge on the measured curve at the low-frequency end.

This experimental result is of some practical importance in connection with the design of helix-type backward-wave oscillators. Thus, if we are interested in the impedance at some radius within a helix wound of tape with finite thickness, the theoretical impedance given by Eq. (8) or the dashed line of Fig. 10 of the paper should be considered to exist at the inside radius of the helix rather than at its mean radius. A similar rule applies to the region outside. This must of course be regarded as an approximation for tapes of finite thickness since the additional energy stored in the fields between the wires must actually lower all of the space-harmonic impedances somewhat. This reduction should be very small for relatively thin tapes.

[1] D. A. Watkins and A. E. Siegman, J. Appl. Phys. **24**, 917 (1953).

Comment on "The Summation of Series Involving Roots of Transcendental Equations and Related Applications"*

G. KUERTI
Case Institute of Technology, Cleveland, Ohio
(Received October 12, 1953)

PROFESSOR Spiegel's aim, to present in this paper a "quite general method by which the summation of such series may be obtained," has not been achieved, in my opinion. Four well-known examples are given, and the impression is created that the method is safe in all cases where "the transcendental function has real zeros" only. Actually, the applicability of the procedure,

which was extensively used by Euler and Jacobi, depends in no way on the reality of the zeros, but it is a simple matter to give sufficient conditions which cover the four examples in the paper and may hold in many other practically important cases. To arrive at these conditions, we have to quote two theorems.

I.[1] If $\sum_1^\infty c_n$ is *absolutely* convergent, then the product $\prod_1^\infty (1+c_n z)$ is an integral function, and the coefficients α_n of its Taylor expansion about $z=0$, *viz.*, $1+\sum_1^\infty \alpha_n z^n$, are related to the zeros of Π, $-c_n^{-1}$, in the same way that holds for finite products, that is, $\alpha_n=\Sigma c_{\nu_1}c_{\nu_2}\cdots c_{\nu_n}$.

II.[2] Every integral function $f(z)$ of finite order, ρ, can be represented in the following form:

$$f(z)=z^k \exp Q_m(z)\cdot \prod_1^\infty (1-u_n)\exp\left(u_n+\frac{u_n^2}{2}+\cdots+\frac{u_n^p}{p}\right), \quad (1)$$
$$u_n=z/z_n,$$

where the z_n are the zeros of $f(z)$; they contribute to (1) according to their multiplicity, and $z_0=0$ has been put in evidence as a k-fold zero. $Q_m(z)$ is a *polynomial* of *degree* m, and p is the *smallest integer* for which $\prod_1^\infty$ will converge everywhere. [p may be zero; in this case we re-define (1), omitting the factors $\exp(u_n+\cdots)$.] The *order*, ρ, introduced above is the smallest number for which

$$|f(z)|<A\exp r^{\rho+\epsilon}, \quad r=|z| \quad (2)$$

is true for any positive ϵ, A being a constant which in general depends on ϵ. We finally need the *exponent of convergence*, ρ_1, being the smallest number for which

$$\sum_1^\infty |z_n|^{-(\rho_1+\epsilon)}, \quad (3)$$

is convergent for any positive ϵ. Only the following results of the factorization theory are important for our purpose:

$$m\leqq\rho, \quad p\leqq\rho_1\leqq\rho, \quad (4)$$

and

$$\rho_1=\rho, \quad \text{if} \quad m=0. \quad (5)$$

Even if $p=0$, it is often quite difficult to determine $Q_m(z)$ for a given $f(z)$, and it is the presence of the factor $\exp Q_m(z)$, which in this case makes (I) in general inapplicable. Consider e.g., $f(z)=\exp z^2 z^{-1}\sin z$. The zeros are, of course, not affected by the factor $\exp z^2$, but the Taylor expansion starts now with $1+5z^2/6+\cdots$, and, according to Professor Spiegel's argumentation, this would imply $\Sigma 1/n=-5\pi/6$.

In the case $\rho<1$, however, we can definitely state $m=0$, $p=0$ as consequences of (4), and therefore $\rho_1=\rho$ by (5). This immediately implies the applicability of Theorem I.

But in practical problems one often meets $\rho=1$. All four examples given by Professor Spiegel are of this nature. This would seem to make the search for the factor $\exp(az+b)$ indispensable, were it not for the fact[3] that the Taylor series in the first three examples has the form $1+\Sigma\alpha_n z^{2n}$ and the form $1+\Sigma\alpha_n z^{4n}$ in the fourth. Thus $f(z)$ is an integral function of $t=z^2$ with order $\frac{1}{2}$ in the first three cases, and of $t=z^4$ with order $\frac{1}{4}$ in the fourth case, and we have $m=p=0$ for the canonical representation in the variable t. The exponent of convergence ρ_1 equals $\frac{1}{2}$ (or $\frac{1}{4}$, respectively). With $t_n=z_n^2$ (or z_n^4, respectively), the sums $\Sigma|t_n|^{-(1+\epsilon)}$ (or $\Sigma t_n^{-(1+\epsilon)}$, respectively) converge, and the sums $\Sigma|t_n|^{-1}$ do so *a fortiori*. Thus Theorem I applies.

This result may be formulated in the following way. Let $f(z)=0$ be a transcendental equation and let $f(z)$ be regular everywhere and have the order

$$\rho<1 \quad (a)$$

or

$$\rho\geqq 1 \text{ } \textit{and} \text{ the Taylor expansion } 1+\sum_1^\infty \alpha_n z^{kn} \text{ with } \rho/k<1. \quad (b)$$

Then the "usual algebraic relations" will hold in case (a) between the coefficients α_n and the roots, and in case (b) between the coefficients α_n and the kth powers of the roots; but in this case each *group of k roots*

$$z_{n+\lambda}=z_n\exp(2\pi i\lambda/k), \quad \lambda=0, 1, 2, \cdots, k-1,$$

contributes only *once*.

[*] M. R. Spiegel, J. Appl. Phys. **24**, 1103 (1953).
[1] See e.g., K. Knopp, *Theory and Application of Infinite Series*, translated from the second German Edition (London & Glasgow, 1928), Sec. 254.
[2] Hadamard's canonical representation. See e.g., E. C. Titchmarsh, *The Theory of Functions* (London, 1939), Second Edition, Sec. 8.24–8.26.
[3] This idea is implied in a remark by E. Borel: *Leçons sur les fonctions entières* (Paris, 1921), Second Edition, p. 83.

Metal Whiskers

S. Eloise Koonce and S. M. Arnold
Bell Telephone Laboratories, Murray Hill, New Jersey
(Received September 30, 1953)

In the earlier work with filamentary growths on metal surfaces,[1-3] the whiskers quite generally were observed to be approximately 2 microns in diameter. Since then many more specimens have been examined and we have found that a greater variation in whisker size is possible, not only on different but even on the same specimens.

In Fig. 1, two tin whiskers may be seen with approximate diameters of 5.8 and 0.05 microns, respectively. A satisfactory formulation of the growth mechanism must take into account a variation of this order and at the same time explain the fact that a large part of the filaments are approximately 2 microns in diameter. Two published articles regarding possible growth mechanisms[4,5] have not been concerned with actual limits as to whisker size. Frank,[6] proposing that an oxidation process occurring at a dislocation is responsible for growth, infers whisker diameters of the order of 2 microns.

Further, during the earlier work referred to, the whiskers were found to be generally straight. Recently we have observed a few which show an offset, apparently at some stage developing at an angle to the axis of the whisker for a short distance and then reverting to the original growth direction. The change in direction

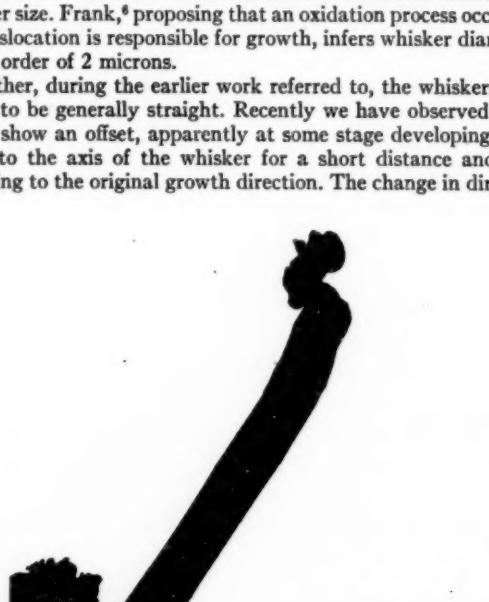

FIG. 1. Electron micrographs of silhouettes of tin whiskers illustrating size range.

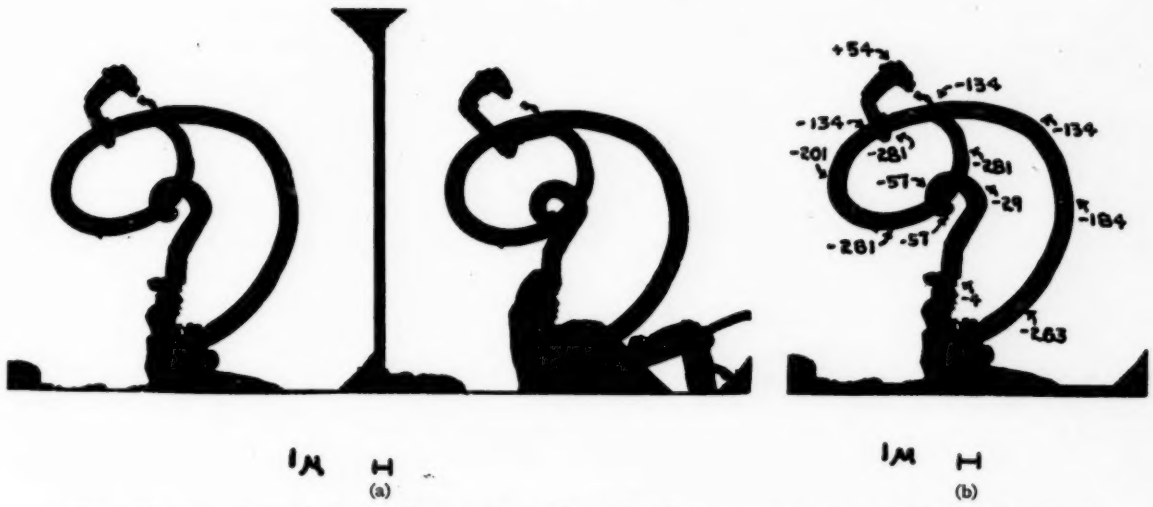

FIG. 2. (a). Stereomicrograph showing silhouettes of spiraled growths. (b). The numbers indicate the relative displacement of sections of the whiskers along a line perpendicular to the plane of the figure. (2250×).

may be a result of twinning, and its significance must be determined.

Spiraled growth forms also have been found. Observed in three dimensions by means of a stereoviewer, it can be seen that the configuration is not planar but deviates from the plane of the figure in the manner shown in Fig. 2.

[1] Compton, Mendizza, and Arnold, Corrosion **7**, 327 (1951).
[2] C. Herring and J. K. Galt, Phys. Rev. **85**, 1060 (1952).
[3] S. E. Koonce and S. M. Arnold, J. Appl. Phys. **24**, 365 (1953).
[4] M. O. Peach, J. Appl. Phys. **23**, 1401 (1952).
[5] J. D. Eshelby, J. Appl. Phys. **24**, 176 (1953).
[6] F. C. Frank, Phil. Mag. **44**, 854 (1953).

Some Remarks on Thermal Effect in an Electron Beam on the Gain of Traveling-Wave Tubes

KANEHISA UDAGAWA AND MASAO SUMI
Electrical Communication Laboratory, Tokyo, Japan
(Received August 17, 1953)

RECENTLY Parzen and Goldstein[1] pointed out that the small velocity spread in an electron beam appears to cause a decrease in gain of a traveling wave tube. In their paper the ratio of gain for the case with and without the velocity spread is plotted against μ.[2] However, they treated the ratio for the growing wave alone whereas it is actually the ratio of the corresponding attenuation constants. Consequently, the ratio of the overall gain is, as will be shown later, less than that given by these workers and is, therefore, not solely dependent on μ. After careful investigation on the performance of traveling-wave tubes under various small-signal operating conditions, it has been found that the limiting condition of amplification will only become important for the case when the thermal motion of the electrons has to be taken into consideration. In particular, when the operation of low-noise tubes is to be investigated, the region near the limit mentioned above should be examined more closely.

Let us make use of the equations for an electron beam, i.e., Eqs. (14) and (15) in reference 1, and the equation of propagation along the transmission circuit

$$\frac{\partial^2 V}{\partial x^2}-\frac{1}{v_0^2}\frac{\partial^2 V}{\partial t^2}=\frac{eZ_c}{v_0}\frac{\partial^2 n}{\partial t^2}, \tag{1}$$

where V is the voltage, v_0 the phase velocity of propagation, and Z_c the characteristic impedance of the circuit. Taking the propagation constant as $\Gamma=j(\beta+\xi)$, where $\beta=\omega/v_0$ and $|\xi|\ll\beta$, and assuming $v_0\doteqdot u_0$, we get an equation of the third order in ξ as follows:

$$\xi^3-\alpha\beta^2\xi+(\beta/2)K=0, \tag{2}$$

where $K=en_0\omega^2Z_c/(2v_0V_0)$. It can readily be seen that Eq. (2) is equivalent to Eq. (22) in reference 1. Solving (2) for ξ, the attenuation constant γ, the imaginary part of ξ, is derived:

$$\gamma=-6.13\times10^{-5}(\omega/V_0)\sigma\{[1+(1-\kappa^2)^{\frac{1}{2}}]^{\frac{1}{3}}+[-1+(1-\kappa^2)^{\frac{1}{2}}]^{\frac{1}{3}}\}, \tag{3}$$

where $\sigma=[I_0V_0^{\frac{1}{2}}Z_c/(2e/m)^{\frac{1}{2}}]^{\frac{1}{3}}$ and $\kappa=9.44\times10^{-5}(kT_0/\sigma^2)$. Let us denote the value of γ as γ_0 when $\kappa=0$ or $kT_0=0$, as given by Pierce. Then the ratio γ/γ_0 shows the same behavior against κ as $G(\mu)/G(0)$ against μ, where κ is the normalized constant of μ. Consequently, the over-all gains G and G_0 with and without the velocity spread, respectively, are given in decibels:

$$G=8.69(-\gamma x)-9.54, \tag{4}$$

and

$$G_0=8.69(-\gamma_0 x)-9.54. \tag{5}$$

When the increasing wave alone exists, the gain-ratio G/G_0 can be uniquely determined by either μ or κ. On the contrary, such a simple relation does not hold for the over-all gain, and this can be determined as a function of three variables, σ, ω/V_0, and kT_0. When $\gamma/\gamma_0=\frac{1}{2}$, the value of the gain-ratio as given in reference 1 will also become $\frac{1}{2}$ whereas the ratio of the over-all gain, G/G_0, varies appreciably with the value of $-\gamma_0$, even when $\gamma/\gamma_0=\frac{1}{2}$.

More reduction of gain may be expected than that for the case given by Parzen and Goldstein. When $\gamma/\gamma_0=\frac{1}{2}$ and the tube length is 25 cm, the following results are obtained:

$-\gamma_0$	27.6	18.4	13.8
G/G_0	1/2.5	1/2.9	1/3.7
G(db)	20.6	10.6	5.6.

Figure 1 shows the relation between the overall gain G *versus* σ for the case when the tube length is 25 cm, ω/V_0 and kT_0 as parameters. From this the following conclusions can be reached: When the effect of thermal motion in an electron beam is taken into account, the overall gain G of a traveling-wave tube begins to build up at σ_0, the limiting value of σ, which depends only on kT_0 and is independent of ω/V_0. The value of G approaches asymptotically with increasing σ to that of the overall gain, corresponding to a given value of ω/V_0, with the thermal motion neglected. The larger ω/V_0 becomes, the more the gain corresponding to a definite value of σ is reduced as compared with that given by Pierce. In the latest low-noise tubes the value of ω/V_0 is, in fact, so large that σ must approach the limiting value σ_0 in order to attain an appreciable gain. The gain attainable

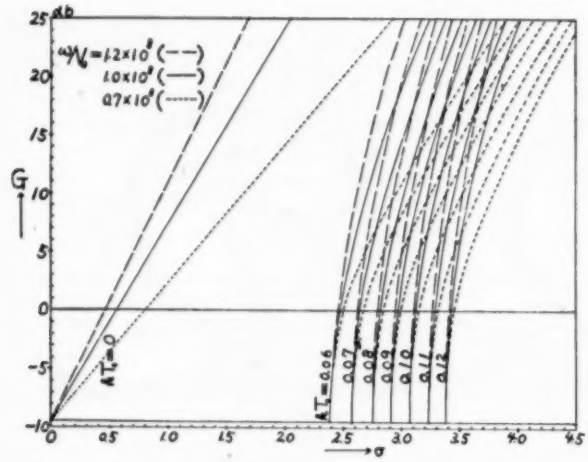

FIG. 1. Over-all gain G *versus* σ, ω/V_0, and kT_0 as parameters when tube length is 25 cm.

deviates remarkably from that derived by Pierce's theory and is found to be considerably changed with the variations of I_0, V_0, and kT_0.

For example, let the frequency 6200 Mc/sec, dc voltage $V_0=390$ volts, dc current $I_0=60$ microamperes, and the characteristic impedance of the circuit $Z_c=15$ ohms[3] for the low-noise tube, we get $\sigma=3.06\times10^{-3}$ and $\omega/V_0=1\times10^8$. When the beam temperature is raised, the gain obtained will be reduced as follows: 20 db at $kT_0=0.06$ volt, 15.5 db at 0.07 volt, 11 db at 0.08 volt, and 5 db at 0.09 volt. It drops suddenly to -9.54 db at 0.10 volt. The sudden drop is due to the fact that the value of σ is below the limiting value $\sigma_0=3.07\times10^{-3}$, where no growing wave can exist. On the other hand, the gain at $kT_0=0$ as given by Pierce will become 41.5 db which is far greater than the reasonable value.

[1] P. Parzen and L. Goldstein, J. Appl. Phys. **22**, 398 (1951).
[2] The notations used here are the same as those in reference 1 unless otherwise stated.
[3] This value is believed to be reasonable because the value of Z_c is greatly reduced in the presence of glass supports and electron beam.

Erratum: Thermal Effects in Point Contact Rectifiers

[J. Appl. Phys. **24**, 1332 (1953)]

H. L. ARMSTRONG
Radio and Electrical Engineering Division, National Research Council, Ottawa, Canada

EQUATION (2) should read

$$(2\pi r^2 g/\theta)(d\theta/dr) = -iv,$$

and the line below it

g/θ is the thermal conductivity, etc.

Erratum: A Note on the Analysis of First-Order Glow Curves

[J. Appl. Phys. **24**, 1306 (1953)]

LEONARD I. GROSSWEINER
Chemistry Division, Argonne National Laboratory, Lemont, Illinois

EQUATION (3): Interchange limits on integral.

Equation (8): Should read as follows:

$$(E/k)(1/T'-1/T^*)-0.693=[skT^{*2}\exp(-E/kT^*/E\beta] \times[1-(T'/T^*)^2\exp\{-(E/k)(1/T'-1/T^*)\}].$$

Errata: A Study of the Propagation Mode for Metallic Vapors in Shadow Casting by Vacuum Evaporation of Au^{198} and Cr^{51}

LUTHER E. PREUSS
Edsel B. Ford Institute for Medical Research, Detroit 2, Michigan
[J. Appl. Phys. **24**, 1402 (1953)]

CONCURRENT with recent data[1] columns 7 and 8 of Table I should read:

	Energy (Mev) Beta	Gamma
Au^{198}	0.963	0.412
	0.290	0.676
	1.37	1.09
Cr^{51}		0.330
		K capture

[1] Hollander, Perlman, and Seaborg, Revs. Modern Phys. **25**, 469–651 (1953).

Erratum: On the Propagation Constant in Gentle Circular Bends in Rectangular Wave Guides—Matrix Theory

A. T. DE HOOP
Technological University, Delft, Netherlands
[J. Appl. Phys. **24**, 1325–1327 (1953)]

AN error has been noticed by the author in one of the principal formulas on page 1327. Equation (2.18) should read as follows:

$$\gamma_m^2=\gamma_{mn}^2=\Gamma_{mn}^2+(\xi^2/4\alpha^2)[3-(\Gamma_{mn}\alpha/\pi m)^2(10+\pi^2m^2) +(\Gamma_{mn}\alpha/\pi m)^4(7+\pi^2m^2/3)], \quad m>0. \quad (2.18)$$